

CHEMICAL REVIEWS

Self-Assembly of Colloidal Nanocrystals: From Intricate Structures to Functional Materials

Michael A. Boles,^{†,‡} Michael Engel,^{‡,§,¶} and Dmitri V. Talapin^{*,†,||}

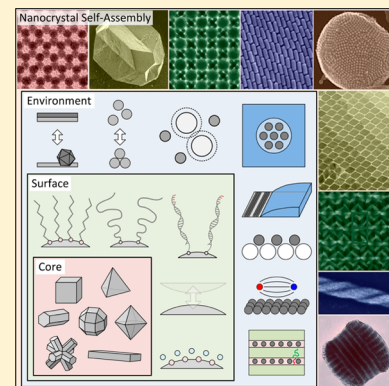
[†]Department of Chemistry and James Franck Institute, University of Chicago, Chicago, Illinois 60637, United States

[‡]Institute for Multiscale Simulation, Friedrich-Alexander University Erlangen-Nürnberg, 91052 Erlangen, Germany

[§]Department of Chemical Engineering, University of Michigan, Ann Arbor, Michigan 48109, United States

[¶]Center for Nanoscale Materials, Argonne National Lab, Argonne, Illinois 60439, United States

ABSTRACT: Chemical methods developed over the past two decades enable preparation of colloidal nanocrystals with uniform size and shape. These Brownian objects readily order into superlattices. Recently, the range of accessible inorganic cores and tunable surface chemistries dramatically increased, expanding the set of nanocrystal arrangements experimentally attainable. In this review, we discuss efforts to create next-generation materials via bottom-up organization of nanocrystals with preprogrammed functionality and self-assembly instructions. This process is often driven by both interparticle interactions and the influence of the assembly environment. The introduction provides the reader with a practical overview of nanocrystal synthesis, self-assembly, and superlattice characterization. We then summarize the theory of nanocrystal interactions and examine fundamental principles governing nanocrystal self-assembly from hard and soft particle perspectives borrowed from the comparatively established fields of micrometer colloids and block copolymer assembly. We outline the extensive catalog of superlattices prepared to date using hydrocarbon-capped nanocrystals with spherical, polyhedral, rod, plate, and branched inorganic core shapes, as well as those obtained by mixing combinations thereof. We also provide an overview of structural defects in nanocrystal superlattices. We then explore the unique possibilities offered by leveraging nontraditional surface chemistries and assembly environments to control superlattice structure and produce nonbulk assemblies. We end with a discussion of the unique optical, magnetic, electronic, and catalytic properties of ordered nanocrystal superlattices, and the coming advances required to make use of this new class of solids.



CONTENTS

1. Introduction	11221	4.6. Contributions to Free Energy of Nanocrystal Solutions	11232
2. Preparation of Nanocrystal Superlattices	11222	5. Self-Assembly of Hard Particles: Entropy Maximization and Dense Packings	11232
2.1. Experimental Approaches To Prepare Nanocrystal Superlattices	11222	5.1. Entropy Maximization Principle for Hard Particles	11232
2.2. Evaporation-Based Nanocrystal Self-Assembly	11225	5.2. Dense Packings as Candidate Structures for Nanocrystal Superlattices	11233
2.3. Destabilization-Based Nanocrystal Self-Assembly	11225	5.3. Dense Packings of Binary Hard Particle Mixtures	11234
2.4. Kinetics of Nanocrystal Self-Assembly	11225	5.4. Cataloging Stable Phases of Hard Polyhedra	11235
3. Characterization of Nanocrystal Superlattices	11226	6. Self-Assembly of Soft Particles: Internal Surface Area Minimization	11236
3.1. Real-Space Superlattice Characterization	11226	6.1. Hard and Soft Particles Are Two Extremal Models for Nanocrystals	11236
3.2. Reciprocal-Space Superlattice Characterization	11227	6.2. Area-Minimization Principle and Tetrahedral Close-Packaging	11237
4. Nanocrystal Interactions and Thermodynamics	11228	6.3. Area-Minimization Principle for Hydrocarbon-Capped Nanocrystal Superlattices	11238
4.1. Interparticle Potentials at the Ordering Transition	11228		
4.2. van der Waals Forces between Nanocrystal Cores	11229		
4.3. Steric Stabilization	11230		
4.4. Hydrocarbon Ligand Packing in Nanocrystal Solids	11230		
4.5. Electrostatic Stabilization	11231		

Special Issue: Nanoparticle Chemistry

Received: March 26, 2016

Published: August 23, 2016

7. Self-Assembly of Hydrocarbon-Capped Nanocrystals	11238	12.4. Multicomponent Assemblies for Synergistic Effects	11267
7.1. Quasi-Spherical Nanocrystals	11239	12.5. Beyond Quantum Phenomena: Classical Transport and Mechanical Properties	11269
7.2. Rod-Shaped Nanocrystals	11240	13. Conclusion and Outlook	11269
7.3. Platelet-Shaped Nanocrystals	11241	Author Information	11271
7.4. Polyhedral Nanocrystals	11242	Corresponding Author	11271
7.5. Branched and Multicomponent Nanocrystals	11243	Author Contributions	11271
7.6. Sphere + Sphere Nanocrystal Mixtures	11245	Notes	11271
7.7. Nanocrystal Shape Mixtures	11247	Biographies	11271
8. Defects in Nanocrystal Superlattices	11248	Acknowledgments	11271
8.1. Zero-Dimensional Defects: Vacancies, Interstitial and Substitution Sites	11248	References	11271
8.2. One-Dimensional Defects: Dislocations, Disclinations, and Vortices	11249		
8.3. Two-Dimensional Defects: Stacking Faults and Grain Boundaries	11251	1. INTRODUCTION	
8.4. Three-Dimensional Defects: Voids, Cracks, and Precipitates	11251	Self-assembly is the process by which individual components arrange themselves into an ordered structure. While sufficiently broad to include crystallization of atomic solids, the term is generally reserved for building blocks not linked together via covalent bonds but ordered through weak forces (e.g., van der Waals, hydrogen bonding) or hard-particle (e.g., excluded volume) interactions. ¹ Following this classification, examples of self-assembled structures include DNA, ² proteins, ³ lipid vesicles, ⁴ block copolymer melts, ⁵ opals, ^{6,7} and nanocrystal superlattices. ^{8,9} Self-assembly can also make use of external forces such as electric/magnetic fields or fluid flows, but the term does not extend to serial manipulation of building blocks (e.g., dragging individual particles into position). In this review we focus on nanocrystal self-assembly, covering the techniques for preparation and characterization of nanocrystal superlattices and other superstructures, the range of building blocks and accessible architectures, factors governing the assembly process, potential applications of ordered nanocrystal solids, and current challenges facing the field. This work aims to build upon the body of literature including reviews from the early days ^{10–14} and recent years, ^{15–23} highlighting new developments over the past decade made possible by a rapid expansion of nanocrystal shapes, surface chemistries, and assembly techniques.	
9. Self-Assembly Driven by Chemical Processes at Nanocrystal Surfaces	11251	Nanocrystals are fragments of semiconductor, metal, or dielectric crystals, protected by a layer of surface-bound molecules (ligands), and able to be dispersed in solution. A couple decades of research has revealed that decomposition of precursors in the presence of organic surfactants is an effective approach to prepare size- and shape-uniform nanocrystals. ²⁴ The capping layer protecting the nanocrystal surface is similar to organic–inorganic interfaces formed by self-assembled surfactant monolayers adsorbed on planar crystalline surfaces, ^{25–28} exemplified by the well-studied system of monolayers of thiols on gold, ^{29,30} the <i>Drosophila</i> of surfactant monolayers. By adjusting synthetic parameters (e.g., precursors, surfactants, reaction temperature, and time), crystalline, monodisperse particles have been synthesized in a variety of shapes and sizes. ³¹ In addition, postpreparative improvements in homogeneity made possible by size-selective precipitation, ^{20,24} digestive ripening, ³² and chromatography ³³ techniques further facilitate access to a uniform collection of particles.	
9.1. Partial Desorption of Native Hydrocarbon Ligands	11251	An ensemble of colloidal nanocrystals can be encouraged to self-assemble into an ordered superlattice (Figure 1) by, for example, evaporation of carrier solvent. The complex phase behavior (Figure 2 and Table 1) observed for even the simplest (e.g., spherical) building blocks, contributed in part by the nonadditivity of nanoscale interparticle interactions, ³⁴ has presented an intriguing puzzle to those working in the field.	
9.2. Homopolymer Surface Ligands	11252		
9.3. Block Copolymer Surface Ligands	11253		
9.4. Coarse-Grained Models for Ligand-Tethered Nanocrystals	11253		
9.5. Capping Layers Containing Two or More Ligand Species as Patchy Particles	11254		
9.6. Charged Aliphatic Surface Ligands and Charged Nanocrystal Cores	11255		
9.7. DNA-Based Surface Ligands	11256		
9.8. Toward Biologically Inspired Self-Assembly	11257		
9.9. Molecular Switches as Surface Ligands	11258		
10. Role of the Environment in Directing Nanocrystal Self-Assembly	11258		
10.1. Self-Assembly on Flat Surfaces	11258		
10.2. Self-Assembly on Patterned Surfaces	11259		
10.3. Self-Assembly Aided by Curved Surfaces	11260		
10.4. Self-Assembly under Spherical and Other Confinement	11260		
10.5. Self-Assembly in Structure-Directing Media	11261		
10.6. Depletion-Driven Self-Assembly	11261		
10.7. Self-Assembly in External Electric, Magnetic, or Electromagnetic Field	11262		
10.8. Temperature Control of Nanocrystal Self-Assembly	11263		
11. Mesoscale Patterns Arising from Nonequilibrium Drying Effects	11264		
11.1. Drying-Mediated Assembly: Vapor Phase Nucleation and Domain Coarsening	11264		
11.2. Rings and Networks: Visualizing Experimental Drying Dynamics	11265		
11.3. Striped Nanocrystal Films: Controlled Contact Line Instability	11265		
12. Unique Properties of Ordered Nanocrystal Solids	11266		
12.1. Controlled Mixing of Nanocrystal Electronic States	11266		
12.2. Orientational Ordering of Nanocrystals for Luminescence Applications	11267		
12.3. Plasmon Resonance under Electromagnetic Excitation	11267		

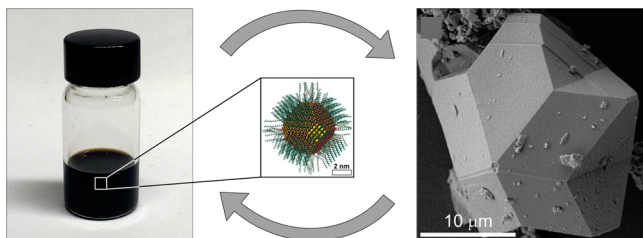


Figure 1. Self-assembly of colloidal nanocrystals. Individual nanocrystal building blocks prepared by colloidal chemistry techniques (left) are integrated into ordered arrays, or superlattices (right), without external direction, by the process of self-assembly. Since they are held together by weak forces, superlattices may be redissolved back into constituent building blocks upon exposure to solvent. Shown here: 7-nm-diameter PbS nanocrystals capped with oleic acid surface ligands self-assemble into a close-packed superlattice array. Adapted with permission from ref 36. Copyright 2014 American Association for the Advancement of Science. Adapted from ref 37. Copyright 2009 American Chemical Society.

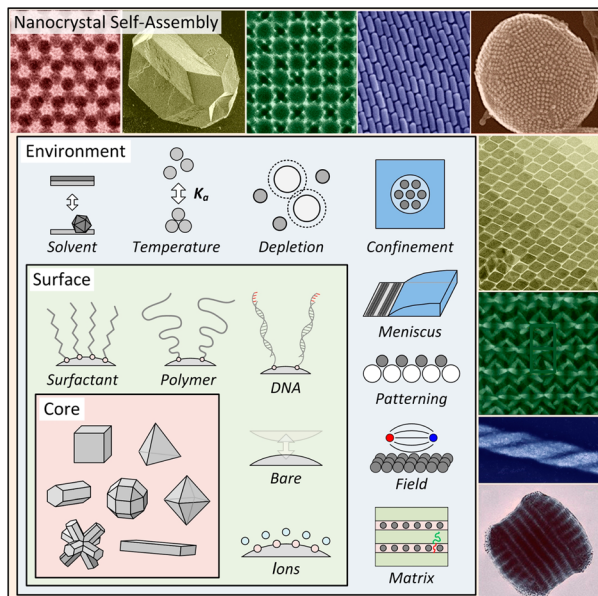


Figure 2. Nanocrystal self-assembly is a process that involves control over several length scales. The nanocrystal core (typically 1–100 nm across) is surrounded by a layer of surface ligands (with length typically between 1 nm and up to tens of nanometers). The assembly environment can be used to control interparticle interactions and impart geometric constraints with characteristic length scale exceeding nanocrystal size. The resulting superstructures are typically produced with domain size falling between 1 μm and several millimeters. Details about the nanocrystal composition, assembly conditions, and references for the systems shown in this figure are given in Table 1.

More practically, the flexibility of superlattice composition and structure suggests that controlled nanocrystal self-assembly could be an important enabler of next-generation materials design. Furthermore, while top-down techniques (e.g., electron beam lithography, dip-pen nanolithography³⁵) for nanoscale patterning require elaborate facilities and permit only successive iterations of two-dimensional structure design, nanocrystal synthesis and self-assembly is carried out with comparatively basic equipment and enables production of complex, three-dimensional patterns of arbitrary functional materials in a single step, often with subnanometer precision.

A nanocrystal superlattice is an array of inorganic objects separated by layers of surface ligands. Expanding the set of ligands with the goal of targeting desired superlattice structures and properties (section 9) enables novel biomedical and optoelectronic applications and is a subject of current research.³⁸ One approach aims for structure-dependent properties that emerge if the interparticle matrix facilitates electronic communication between particles. Because typical organic ligands amenable to nanocrystal synthesis and self-assembly prevent overlap of electronic wave functions of proximate nanocrystals in the superlattice, optoelectronic properties of nanocrystal superlattices are often similar to those of isolated building blocks. Recently developed compact inorganic ligands^{39–42} offer delocalization of electronic states in nanocrystal solids.^{43,44} Furthermore, varying the ligand chemistry using DNA strands⁴⁵ or polymer brushes⁴⁶ receives much attention because it promises access to a variety of programmable superlattices with properties not otherwise achievable. Even so, the traditional surface ligands (e.g., oleic acid) often considered a barrier to practical application of superlattices can impart useful optical⁴⁷ and mechanical⁴⁸ properties to the nanocrystal solid.

Several challenges must be addressed before the promise of bottom-up nanomaterials design^{23,57} is realized. For one, a robust link between properties of individual nanocrystals (composition, shape, size, surfaces), the environment (solvent, substrate, temperature, external fields), and the self-assembly product has yet to be fully elucidated, hampering targeted design of nanocrystal solids. Additionally, comparable free energies of superlattice polymorphs can result in undesired formation of competing structures. New trends in nanocrystal self-assembly include the incorporation of complex ligand chemistry, structure tuning by variation of environmental parameters, and low-dimensional superstructures (e.g., strings, sheets, vesicles), leaving the door wide open for new developments in optical, electronic, and mechanical applications of nanocrystal assemblies. Future progress will require a concerted effort to advance both experimental techniques and theoretical understanding beyond the state of the art laid out in this review.

2. PREPARATION OF NANOCRYSTAL SUPERLATTICES

Preparation and structural characterization of superlattices are the foundation of experimental nanocrystal self-assembly investigations. In this section we only give a brief overview and focus on some recent developments. For more details we refer the reader to other sources.^{6,10}

2.1. Experimental Approaches To Prepare Nanocrystal Superlattices

Ordered arrays of colloidal nanocrystals may be prepared by evaporation or destabilization of a nanocrystal solution.⁵⁸ Evaporation-based assembly typically leads to superlattice thin films and takes place at the late stages of solvent drying when particles find themselves in crowded solution. Often, addition of excess surfactant can assist in the formation of long-range-ordered superlattices by repassivating bare nanocrystal surfaces, preventing solvent dewetting of the subphase, and inducing depletion attraction.⁵⁹ There are a few methods to prepare nanocrystal superlattices via solvent evaporation (Figure 3, left). One approach is to simply drop cast a small volume (about 10 μL) of dilute nanocrystal solution onto solid support and allow it to dry over a couple of minutes. For hydrocarbon-

Table 1. Sample of Structural Possibilities Afforded by Nanocrystal Self-Assembly^a

self-assembled structure (sections 5–10)	nanocrystal core (sections 5, 7)	surface ligands (sections 6, 7, 9)	assembly technique (sections 2–4, 10, 11)	reference
close-packed thin film	spherical 4.5 nm Au	octadecanethiol	solvent evaporation	section 7.1, ref 49
faceted three-dimensional superlattice	spherical 8 nm PbS	oleic acid	solvent destabilization	section 7.1, ref 37
binary superlattice thin film	spherical 10 nm PbS and 3 nm Au	oleic acid and dodecanethiol	solvent evaporation	section 7.6, ref 50
smectic-like superlattice	rod-shaped 14 nm × 35 nm Au	cetyltrimethyl ammonium bromide	solvent evaporation	section 7.2, ref 51
icosahedral cluster	spherical 9 nm CoFe ₂ O ₄	oleic acid	confinement in emulsion droplet	section 10.4, ref 52
two-dimensional monolayer	plate-shaped 35 nm × 2 nm GdF ₃	oleic acid	liquid–liquid interface	section 7.3, ref 53
interlocking network	octapod-shaped 70 nm CdSe–CdS	octadecylphosphonic acid	solvent destabilization	section 7.5, ref 54
chiral one-dimensional helices	cubic 13 nm Fe ₃ O ₄	oleic acid	solvent evaporation in magnetic field	section 10.7, ref 55
cylinder with two spherical caps	rod-shaped 30 nm × 7 nm CdSe–CdS	octadecylphosphonic acid	decomposition of surfactant micelles	section 7.2, ref 56

^aThese examples highlight the diversity of strategies and techniques employed to achieve ordering of nanocrystals, such as varying the nanocrystal core geometry, the chemistry of surface ligands, and the assembly conditions and environment. Corresponding electron microscopy images are contained in Figure 2. The table lists these examples clockwise from the top left in the image.

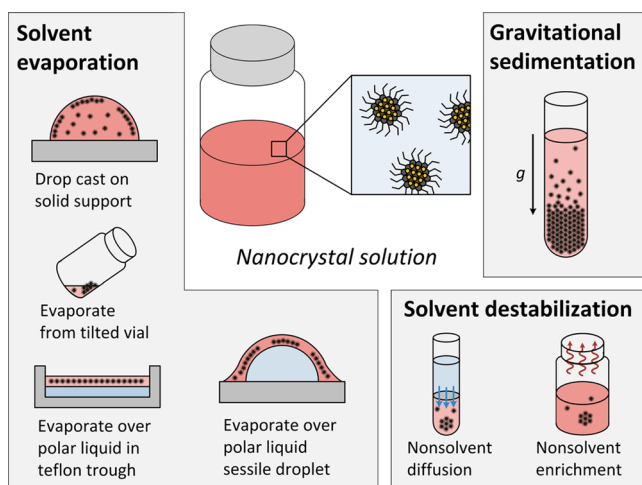


Figure 3. Experimental approaches to prepare nanocrystal superlattices include various evaporation techniques (left), which produce thin film superlattices, and destabilization or sedimentation techniques (right), which lead to three-dimensional superlattices.

capped nanocrystals, a mixture of hexane and octane (9:1 by volume) has been effective in producing long-range ordered superlattices.⁶⁰ Similarly, gentle deposition of a droplet of nanocrystal solution upon a surface enables assembly via particle trapping at the air–liquid interface, forming extended two-dimensional superlattice membranes.⁶¹ Evaporation-based assembly can also be carried out in a small vial, permitting tilting of the substrate contained within and resulting in control over the direction of meniscus movement.⁶² Spreading of nanocrystal solution over large substrate areas can be facilitated by doctor blade casting.⁶³ Along the same lines, polar liquids (e.g., diethylene glycol) immiscible with nonpolar nanocrystal solvents have been used as a platform for nanocrystal assembly, resulting in extended superlattice thin films which can be subsequently transferred to solid support for characterization.⁶⁴ Such an approach may be combined with Langmuir–Blodgett setup to impose lateral surface pressure and controllably

condense nanocrystal monolayers ordered over wafer-scale areas.⁶⁵

Destabilization-based assembly (Figure 3, lower right) exploits attractive interactions between nanocrystals when solvent intermingling in nanocrystal capping layers becomes less favorable than overlap of ligands between neighboring nanocrystals, promoting gradual clustering of nanocrystals in solution. For hydrocarbon-capped nanocrystals, slowly increasing polarity of the solution by controlled diffusion of nonsolvent is effective in inducing flocculation. In practice, this may be accomplished by placing a layer of nonsolvent above a nanocrystal solution contained in a test tube (e.g., ethanol above toluene), while avoiding significant intermixing of the two liquids during the transfer.^{57,66} Slow intermixing of the miscible liquids over several days induces controlled precipitation of faceted nanocrystal superlattices subsequently collected as sediment from the bottom of the tube. Alternatively, slow destabilization may be carried out by heating a premixed solvent/nonsolvent mixture to enrich the higher-boiling nonsolvent component (e.g., octane and 1-octanol).⁵⁸

A less common approach to assembling nanocrystal superlattices exploits gravitational sedimentation (Figure 3, upper right). Since gravity biases thermal motion of nanocrystals with diameter approaching 1 μm, or nanocrystal core materials comprised of high-density metals, crowding-induced self-assembly can occur via sedimentation of nanocrystals in the bottom of solvent. The propensity for particles to accumulate in the bottom of a solution under the influence of gravity can be evaluated by comparing the relative size of thermal energy $k_B T$ and the gravitational potential energy mgd required to raise a particle of mass m by its own diameter d in Earth's gravity g .⁶⁷ The ratio of $k_B T$ to mgd scales as d^{-4} and for 10 nm nanocrystals, for example, is approximately 10^6 , while for micrometer-sized particles it is below 1. Accordingly, even in the presence of repulsive interparticle interactions, the largest nanoobjects (100–1000 nm) are expected to sediment under the force of gravity in all but the densest of liquids.⁶⁸ Particles in this size regime exceed the 100 nm boundary set by the community (according to the ISO/TS 80004-2:2015 stand-

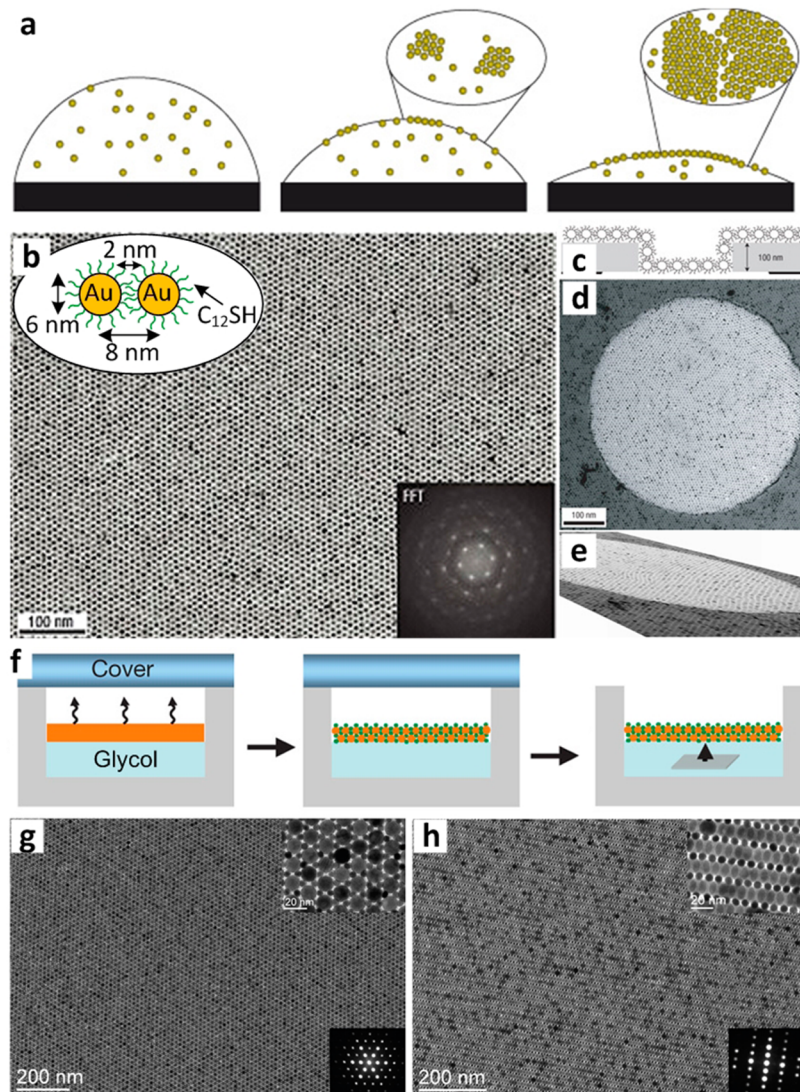


Figure 4. Self-assembly of colloidal nanocrystals at the air–liquid interface leads to superlattices with uniform thickness and large domain size. (a) Schematic illustration of Au nanocrystals captured by a quickly receding interface leading to monolayer island growth. (b) TEM overview of a long-range-ordered monolayer with hexagonal symmetry formed by rapid evaporation of a sessile toluene droplet containing 6 nm dodecanethiol-capped Au nanocrystals. Top inset: sketch of a pair of hydrocarbon-capped nanocrystals introducing nanocrystal diameter, ligand length, and interparticle separation. Bottom inset: fast Fourier transform (FFT) of the superlattice. Adapted with permission from ref 61. Copyright 2006 Nature Publishing Group. (c) Sketch of the freestanding superlattice membrane formed by evaporation over a polar liquid subphase. (d) TEM image of a superlattice membrane draped over a 0.5-μm-diameter hole, and (e) tilted projection of the same image. Adapted with permission from ref 72. Copyright 2007 Nature Publishing Group. (f) Schematic illustration of nanocrystal interfacial assembly and the substrate transfer process. TEM overview of (g) (100) projection and (h) (110) projection of an AlB₂ binary nanocrystal superlattice. Top insets: zoom of the structures. Bottom insets: electron diffractograms. Adapted with permission from ref 64. Copyright 2010 Nature Publishing Group.

ard⁶⁹) to distinguish nanoparticles from coarser particulate matter. In fact, most of the nanocrystals discussed in this review fall comfortably below this limit and exhibit assembly behavior not significantly influenced by gravitational forces. Such emphasis primarily reflects that of the self-assembly literature, a result of the availability of synthetic protocols for producing uniform particles at the lower end of the nanoscale, fundamental interest in quantum size effects, and the ease with which smaller nanoparticles diffuse, explore configurational space, and ultimately adopt equilibrated structures than their larger counterparts.

Akin to the art of protein crystallization,⁷⁰ nanocrystal self-assembly is sensitive to several factors beyond the quality of the starting material. For instance, the choices of solvent,

temperature, and substrate (section 10) play a role in the ordering of nanocrystal superlattices. Undesired flocculation of particles in solution before triggering assembly by evaporation or destabilization can suppress ordering. As such, use of a good solvent for aliphatic capping ligands (e.g., hydrocarbon liquids such as hexane, octane, or toluene; chlorinated hydrocarbons such as chloroform, tetrachloroethylene, chlorobenzene) promotes dispersal of the colloid and is a good starting point for assembly experiments. Gentle heating of the assembly solution facilitates ordering of nanocrystals in superlattices. Because nanocrystals experience a thermodynamic drive to eliminate surface area if provided sufficient thermal energy to coalesce, thermal decomposition of the material presents a practical upper limit to assembly temperature.⁶² In addition, the

solvent vapor pressure is an important parameter for evaporative self-assembly experiments. Because the ordering process requires particles to diffuse through solution and sample various positions, use of volatile solvents may condense particles too rapidly to allow for self-assembly. Furthermore, the choice of support (i.e., solid or liquid subphase) influences the assembly outcome, setting dimensions and orientation of nanocrystal superlattices.

2.2. Evaporation-Based Nanocrystal Self-Assembly

Evaporating a nanocrystal solution over a solid or liquid subphase typically produces two-dimensional superlattice thin films. Depending on the initial concentration of the nanocrystal solution and the area over which it is spread, such films may be deposited at submonolayer coverage and up to several unit cells thick. Typical individual grain sizes reach up to hundreds of micrometers.⁷¹ Maximizing superlattice domain size seems to require conditions that minimize interaction between nanocrystals and support during self-assembly. Along these lines, long-range-ordered hexagonal monolayers of dodecanethiol-capped Au nanocrystals have been assembled by evaporation of sessile droplets of nanocrystals dispersed in toluene (Figure 4a,b).⁶¹ In this approach, early stage evaporation traps particles at the air–liquid interface, with subsequent nucleation and growth proceeding in two dimensions (Figure 4c–e). An alternative technique employs a pair of immiscible liquids, for example, a polar subphase of ethylene glycol supporting a nonpolar hexane solution of nanocrystals on top (Figure 4f–h).⁶⁴

2.3. Destabilization-Based Nanocrystal Self-Assembly

Destabilizing solutions of spherical nanocrystals produces close-packed superlattices not as thin films but as platelets, polyhedra, or spheres. In this case, gradual onset of attractive interactions between dispersed nanocrystals induces slow clustering of particles in the solution bulk. For example, transferring a layer of nonsolvent above a solution of nanocrystals (Figure 5a) leads to the self-assembly of nanocrystals into flat platelets (Figure 5b–d) or multiply twinned polyhedra (Figure 5e–g) depending on particle size.³⁷ This general approach⁶⁶ has also been used to assemble nanorod⁷³ and nanoplatelet⁷⁴ superlattices. Along these lines, functionalizing nanocrystal surfaces with light-triggered molecular switches⁷⁵ results in colloid destabilization and similar polyhedral superlattices (section 9.9). Another destabilization-based technique for achieving three-dimensional superlattices involves inducing solvophobic interactions by disrupting a surfactant bilayer.⁷⁶ In this approach, dodecyltrimethylammonium bromide (DTAB) surfactant is used to hydrophilize organic-capped nanocrystals, forming a bilayer held together by van der Waals forces between aliphatic chains (Figure 5h). Subsequent exposure to polymer-containing ethylene glycol solution at 80 °C decomposes the bilayer and leads to the formation of round superlattices with face-centered-cubic (fcc) internal packing structure (Figure 5i–l). This approach has also been used to make spherical and needle-shaped superlattices of nanorods.⁵⁶

The shape (morphology) of the superlattice polyhedron that results from destabilization-based self-assembly can be rationalized using thermodynamic principles. Like any finite-size solid, including the nanocrystal itself, a nanocrystal superlattice has facet-specific surface energies arising from the reduced coordination of the particles at the surface as compared with those in the superlattice bulk.⁶⁶ While nanocrystals have 12 nearest neighbors in the interior of a close-packed superlattice,

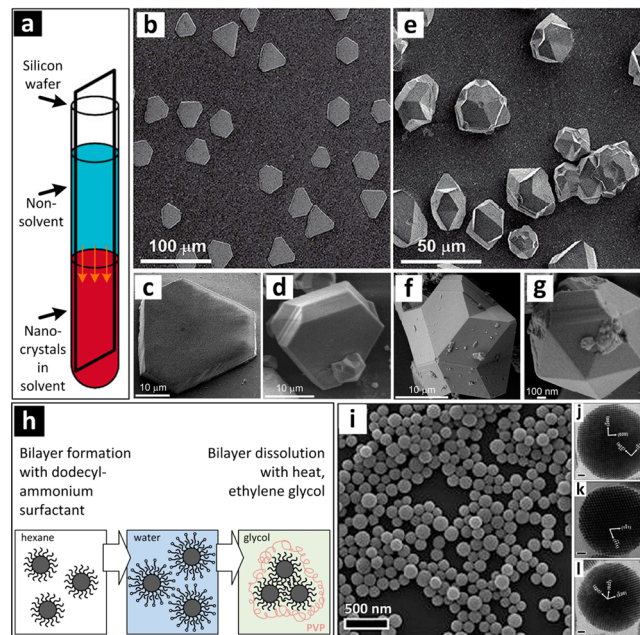


Figure 5. Destabilization-based assembly of spherical nanocrystals. (a) Schematic of self-assembly by slow diffusion of the nonsolvent into the dispersed nanocrystal colloid. (b) SEM overview of platelet-shaped superlattices formed from destabilization of a toluene solution of 3 nm PbS nanocrystals. (c, d) SEM zoom of individual platelet superlattices. (e) SEM overview of multiply twinned superlattices with icosahedral or pentagonal (5-fold) symmetry formed from destabilization of toluene solution of 8 nm PbS nanocrystals. (f, g) SEM zoom of individual polyhedral superlattices. Adapted from ref 37. Copyright 2010 American Chemical Society. (h) Schematic of self-assembly by decomposition of the surfactant bilayer. (i) SEM overview of spherical superparticles produced as shown in (h). (j–l) TEM zoom of individual superparticles with internal fcc crystallographic assignment. Scale bars, 20 nm. Adapted from ref 76. Copyright 2007 American Chemical Society.

nanocrystals at the surface have eight nearest neighbors on (100), seven on (110), and nine on (111) facets (Figure 6a–c). By simply counting the number of broken bonds, it is possible to predict that the surface energy of these facets increases as $E_{111} < E_{100} < E_{110}$. A surface energy minimizing polyhedron (known as the Wulff polyhedron) of a solid with fcc or hcp internal structure then has facet surface areas increasing as $A_{111} > A_{100} > A_{110}$ (Figure 6d). Alternatively, by incorporating low-energy twin plane defects (section 8) within the interior, polyhedral superlattices may present exclusively (111) facets with icosahedral shape (Figure 9a).³⁷

2.4. Kinetics of Nanocrystal Self-Assembly

The equilibrium (or near-equilibrium) aggregation of nanocrystals into a superlattice is a phase transition that proceeds via nucleation and growth. Because nucleation is sensitive to impurities in the system, it is important to distinguish between homogeneous nucleation and heterogeneous nucleation. Homogeneous nucleation occurs in solution and requires overcoming a nucleation barrier. Reducing solvent quality or increasing particle volume fraction by evaporation increases the nucleation rate by lowering the nucleation barrier. Rapid evaporation or destabilization can lead to barrierless aggregation via spinodal decomposition⁷⁷ into nanocrystal-rich and nanocrystal-poor areas similar to demixing observed upon cooling two fluids below the critical temperature of

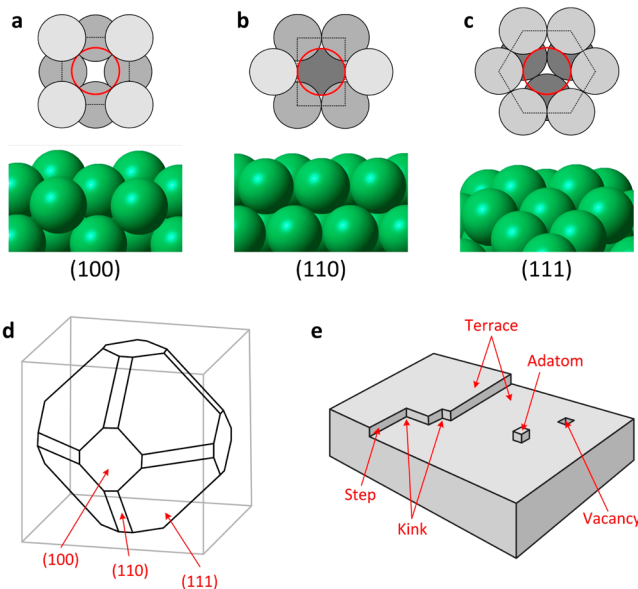


Figure 6. Surface area and broken contacts at the superlattice surface determine facet surface energy and the morphology of superlattices formed with destabilization-based assembly. Here we show the fcc lattice as an example. (a) A (100) surface nanocrystal (red circle) has eight nearest neighbors, four in-plane (light gray) and four below (dark gray). Modeled three-dimensional structure shown underneath. (b) A (110) surface nanocrystal has seven neighbors, two in-plane and five below. (c) A (111) surface nanocrystal has nine neighbors, six in-plane and three below. (d) A superlattice seeks to minimize the total surface energy by adopting a shape that preferentially expresses low-energy facets. Shown here: polyhedron with relative facet areas $A_{111} > A_{100} > A_{110}$. (e) Illustration of the step-terrace-kink model for monomer addition to a growing crystal.

miscibility. However, such far-from-equilibrium processes typically produce disordered nanocrystal solids.

Heterogeneous (templated) nucleation near an interface (wall) can be significantly faster than homogeneous nucleation because the presence of a surface naturally preorders the colloid. After nucleation, growth proceeds via addition of individual nanocrystals or groups of nanocrystals to the growing seed. Growth speed is limited by the availability of nanocrystals from solution and the energetics of surface defect formation. A simple model for surface defect formation is the terrace–ledge–kink model (Figure 6e), which predicts that nanocrystal integration into a growing superlattice is influenced by the number of bonds formed upon attachment. Under attractive interparticle interactions, growth proceeds quickly at vacancies and kinks, which establish many new nanocrystal–nanocrystal contacts. On the other hand, steps and terraces are comparatively stable due to fewer contacts gained upon nanocrystal adsorption.

To minimize total surface energy, a collection of nanocrystals that finds itself in the absence of good solvent prefers the aggregation into a single Wulff polyhedron. In practice, however, solvent destabilization allows multiple nucleation sites and produces many superlattice domains from a collection of particles. This leaves more surface area (broken bonds) than if all particles incorporated themselves in a single superlattice. Larger aggregates move slower in solution than individual nanocrystals or small aggregates, inhibiting coalescence of superlattice domains. However, their mass promotes large superlattices to sediment in the bottom of the container,

assisting densification.⁷⁸ The barrier to nucleation by solvent destabilization is thus sufficiently low, and the barrier to merging of domains sufficiently high, such that many nuclei form but cannot completely coalesce (Figure 7, left pathway). In contrast, evaporation-based self-assembly often nucleates superlattices under thin-film confinement, for example at the air–liquid interface,⁶¹ and in the absence of significant attractive interparticle interactions, producing two-dimensional films (Figure 7, right pathway). These films will typically start out polycrystalline but can improve by defect repair and healing of internal interfaces given sufficient time during a slow enough evaporation protocol.⁷⁹ Such analysis underscores the fact that, in practice, superstructures produced by nanocrystal self-assembly are equilibrated only within the pathway taken by the system.

3. CHARACTERIZATION OF NANOCRYSTAL SUPERLATTICES

Characterization techniques determine nanocrystal position and orientation within a superlattice, the size and orientation of superlattice domains, the presence of crystal defects, and the existence of secondary structures. Imaging (real-space) and scattering (reciprocal-space) techniques represent a complementary set of approaches for collecting local- and ensemble-structural information. While superlattice preparation requires only basic laboratory supplies typically including solvent, pipet, and a solid substrate (e.g., carbon or silicon), superlattice characterization is often carried out using sophisticated technology such as an electron microscope or a synchrotron facility.

3.1. Real-Space Superlattice Characterization

Transmission electron microscopy (TEM) is a common method of probing superlattice structure. This technique sends an electron beam through a thin sample specimen, magnifying and focusing the transmitted electrons onto a detector screen, subsequently displayed on a computer as a digital image. TEM images represent a two-dimensional projection of a three-dimensional structure. Because electron scattering increases with atomic number, TEM image quality is

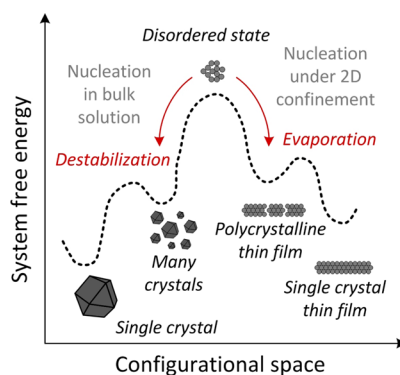


Figure 7. Superlattice morphology and free energy landscape of nanocrystal self-assembly at the disorder–order transition. A collection of nanocrystals transitions from the disordered state with high free energy (top) to an ordered state with lower free energy. Polyhedral superlattices form if nucleation occurs in the absence of boundary conditions (left pathway), while thin film superlattices result under geometric confinement (right pathway). Note that a part of the system free energy scales with the surface area, or the number of broken bonds, left behind after assembly.

best for high atomic number contrast between sample and support (e.g., PbS nanocrystals on carbon, Figure 8a). For this reason, imaging the nanocrystal hydrocarbon capping layer can be challenging; however, the use of ultrathin or holey support (i.e., imaging arrays resting on graphene or suspended over a hole) enables partial visualization of the surface-bound molecules (Figure 8b). A key strength of TEM for superlattice characterization is the ability to image a nanocrystal assembly along various crystallographic directions. In this approach, a series of images of a single domain is collected by tilting the sample holder with respect to the incident electron beam, enabling systematic characterization⁸⁰ of superlattices for which

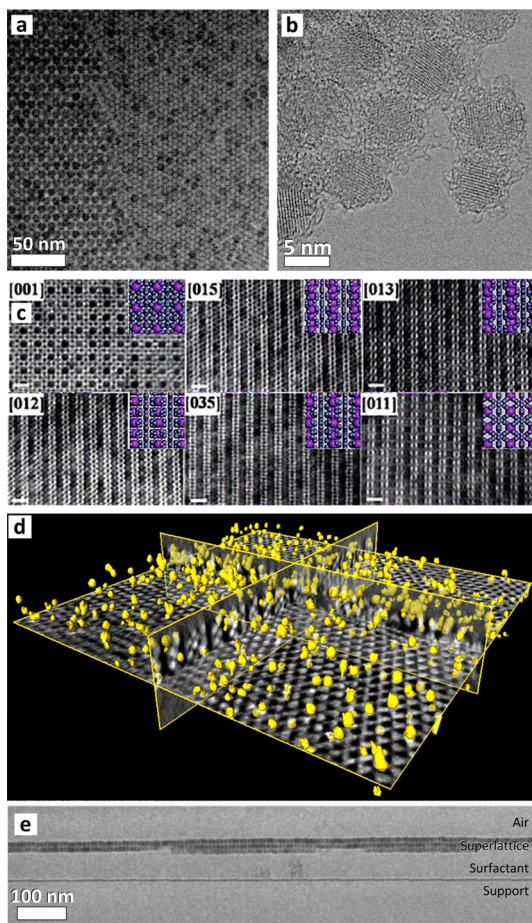


Figure 8. Transmission electron microscopy (TEM) characterization of nanocrystals, surface ligands, and self-assembled superlattices. (a) TEM image of hcp and fcc packing of 7 nm PbS nanocrystals capped with oleic acid surface ligands. Taken from ref 50. (b) TEM image reveals dodecene ligands at the surface of Si nanocrystals suspended over a hole in the graphene support. Adapted from ref 86. Copyright 2012 American Chemical Society. (c) TEM tilting experiments performed on NaZn₁₃ binary superlattices of two sizes of Fe₃O₄ nanocrystals reveal six different projections of the same structure (scale bars, 20 nm). Adapted from ref 80. Copyright 2010 American Chemical Society. (d) Tomographic reconstruction of a CdSe superlattice containing Au nanocrystals (highlighted in yellow) distributed randomly as substitutional dopants throughout the structure. Adapted from ref 85. Copyright 2015 American Chemical Society. (e) Cross-sectional TEM image of superlattice of 11 nm CoFe₂O₄ nanocrystals obtained by focused ion beam slicing of silica-encapsulated nanocrystal thin film. Adapted from ref 63. Copyright 2010 American Chemical Society.

an analysis of the normal projection alone may fail to provide an unambiguous assignment (Figure 8c). Furthermore, such a tilt series can be fed into iterative tomographic reconstruction software to obtain a three-dimensional rendering of the imaged superlattice (Figure 8d), including reconstruction of slices perpendicular to the plane of the support.^{81–85} Alternatively, such slices may be directly imaged in TEM by physically cutting the superlattice with a focused ion beam (Figure 8e).

Because TEM requires the sample to be introduced into a vacuum chamber, characterization of superlattices has typically been performed ex situ on dry samples. Such an analysis is helpful for establishing the arrangement of nanocrystals after evaporation but does not shed light on the self-assembly pathway. Over the past few years, liquid-cell TEM techniques⁸⁷ have been developed, enabling wet samples to be introduced into the instrument vacuum chamber. In this approach, encapsulation of small (microliter) volumes of nanocrystal solution between silicon nitride or graphene layers allows visualization of single nanocrystals in solution. Recently, liquid-cell TEM has uncovered important information concerning interparticle interactions and crystallite atomic structure by following the motions of single nanocrystals or small groups of nanocrystals in solution. It was also possible to observe the formation of nanocrystal superlattices in situ.^{88–90} As imaging techniques continue to improve, it will be interesting to compare the kinetics during the ordering transition with that known for micrometer-sized colloidal particles,⁹¹ where direct imaging is already well-established.

A useful complement to TEM is scanning electron microscopy (SEM), which scans an electron beam in raster fashion across the sample surface, detecting backscattered electrons. This technique probes the specimen surface, enabling imaging of nanocrystal superlattices that are too thick to permit electron transmission. SEM has been used to image, for example, three-dimensional polyhedral superlattices produced by solvent destabilization (Figure 9a). In addition, SEM is a convenient tool for probing the surface structure of superlattice thin films (Figure 9b). Similarly, scanning probe microscopy techniques⁹² such as atomic force microscopy (AFM) are a tool to characterize the surface of nanocrystal superlattices (Figure 9c). In this case, a probe tip is rastered across the sample surface, providing quantitative topographic information.

3.2. Reciprocal-Space Superlattice Characterization

To obtain structural information averaged over a large sample volume, and to analyze complex nanocrystal superlattices, it is helpful to examine the structure in reciprocal space. One way to do this is to perform a fast Fourier transform (FFT) on a real-space image, an operation available in common image analysis software packages and numerical libraries. The Fourier transform is a plot of spatial frequencies in a periodic image, with each spot in reciprocal space corresponding to a lattice spacing in the real-space image. Analogously, the electron diffraction pattern of a nanocrystal superlattice, obtained by collecting transmitted electrons in the TEM diffraction plane, is used to distinguish between similar-looking arrangements in real space (Figure 10a,b). In addition to characterizing the position of nanocrystals within a superlattice at small scattering angles, FFT or electron diffraction data at high angle offers information concerning the orientation of nanocrystal inorganic atomic planes. Such analysis helps in identifying packings with orientational registry of inorganic cores (Figure 10c).

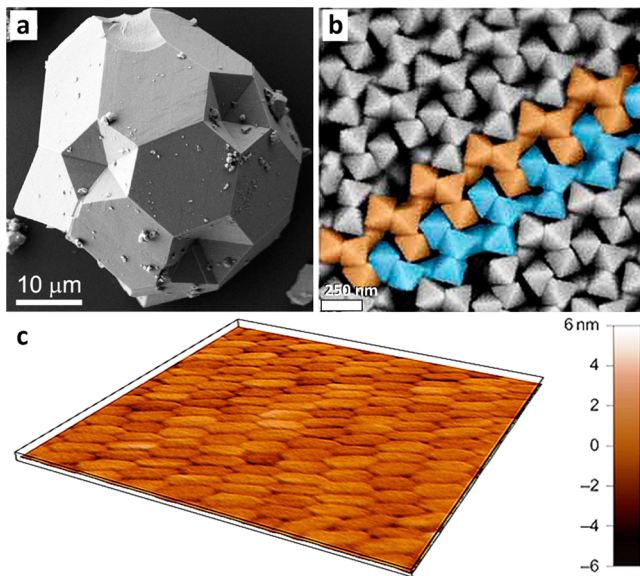


Figure 9. Characterization of the superlattice morphology and surface structure using scanning electron microscopy (SEM) and atomic force microscopy (AFM) techniques. (a) SEM image of a twinned three-dimensional superlattice of PbS nanocrystals formed by solvent destabilization. Adapted from ref 37. Copyright 2010 American Chemical Society. (b) Silver octahedra assemble into a complex superstructure that consists of tetramer motifs (accented with false color) as elucidated by high-resolution SEM. Adapted with permission from ref 68. Copyright 2011 Nature Publishing Group. (c) Height profile of a liquid crystalline array of Au nanorods revealed by AFM. Adapted from ref 93. Copyright 2013 American Chemical Society.

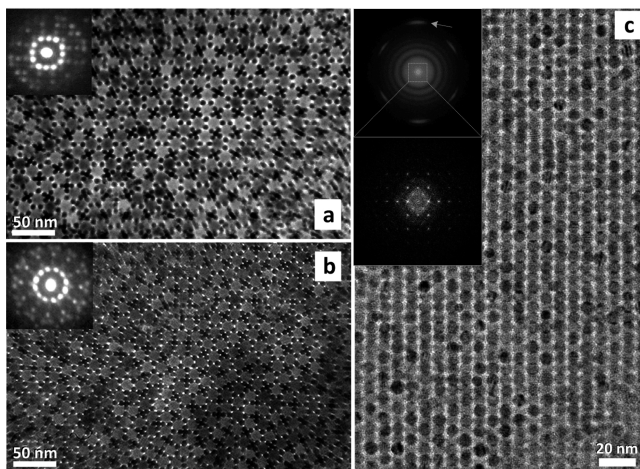


Figure 10. Reciprocal-space analysis of superlattice thin films. (a) TEM overview of an Archimedean tiling binary superlattice comprised of Au and Fe_3O_4 nanocrystals. Inset: electron diffractogram reveals 4-fold rotational symmetry. (b) TEM overview of a dodecagonal quasicrystal binary superlattice assembled from the same nanocrystals. Inset: electron diffractogram reveals 12-fold rotational symmetry. Note the clear difference in reciprocal space despite similar appearance of both structures in real space. Adapted with permission from ref 94. Copyright 2009 Nature Publishing Group. (c) bcc superlattice of PbS nanocrystals. Upper inset: FFT shows high-frequency arcs (indicated by arrow) arise from atomic lattice fringes, suggesting orientational registry of the inorganic nanocrystal cores. Lower inset: zoom into the FFT center shows spots corresponding to superlattice periodicity (small angle). Taken from ref 50.

Small-angle X-ray scattering (SAXS) is another powerful tool for characterizing nanocrystals in solution and nanocrystal superlattices.⁹⁵ SAXS measurement involves elastic scattering of X-radiation (photons of subnanometer wavelength) collected at a two-dimensional detector (Figure 11a). The intensity of X-rays scattered off a nanocrystal ensemble is determined by two parameters: the form factor, which takes into account particle shape and size, and the structure factor, which depends on the spatial arrangement of particles. The form factor dominates SAXS measurement for nanocrystals dispersed in solution, enabling estimation of average particle size and shape as well as their distributions (Figure 11b).^{96,97} When nanocrystals are packed into an ordered arrangement, the SAXS pattern shows off-center spots corresponding to Bragg reflections from superlattice planes. Structural data can be collected in transmission (TSAXS, Figure 11c) or reflection (grazing incidence, or GISAXS, Figure 11d) modes. Like FFT or electron diffraction, wide-angle reflections probe nanocrystal orientation within the superlattice. Furthermore, performing the measurement at ambient pressure enables monitoring the self-assembly process *in situ* as nanocrystals move reversibly between dispersed, colloidal crystalline, and dry states upon solvent evaporation or condensation.^{98,99}

4. NANOCRYSTAL INTERACTIONS AND THERMODYNAMICS

Self-assembly brings a set of particles from a dilute state to one in which particles are contacting their nearest neighbors. As such, it is important to consider the various contributions to the nanocrystal–nanocrystal interaction throughout the self-assembly process. These interactions include van der Waals forces between inorganic cores and between surface ligands as well as osmotic, electrostatic, and elastic contributions. The combination of the interactions is commonly described by an effective interparticle pair interaction.

4.1. Interparticle Potentials at the Ordering Transition

Colloidal nanocrystal solutions remain in the dispersed state as long as the pair potential is dominantly repulsive (Figure 12a, darkest trace). Tethering molecular chains (e.g., hydrocarbon surfactants or neutral polymers) to the nanocrystal surface enables steric stabilization of nanocrystals, while adsorption of charged species leads to electrostatically stabilized colloids (Figure 12b,c). These cases form two fundamentally different mechanisms to colloidal stabilization and provide complementary approaches to disperse nanocrystals in nonpolar and polar solvents, respectively. Such mechanisms need not be mutually exclusive. Chains with ionizable groups allow for both to be combined together in the special case of electrosteric stabilization using polyelectrolyte ligands.¹⁰¹

Aggregation of nanocrystals can be induced by, for example, removal of solvent, reduction of solvent quality via nonsolvent addition or cooling the solution, and desorption or cross-linking of capping ligands. During this process, the effective interparticle interaction changes from repulsive to attractive. In the dried state, nanocrystals are linked firmly together by the interparticle matrix comprised of surface ligands. Complete removal of solvent freezes a collection of nanocrystals into a superlattice with interparticle separation set by the balance between ligand elastic repulsion and van der Waals attraction forces. Associated nanocrystals then sit in a deep potential well that far exceeds the characteristic thermal energy ($k_{\text{B}}T$) of the system (Figure 12a, lightest trace).

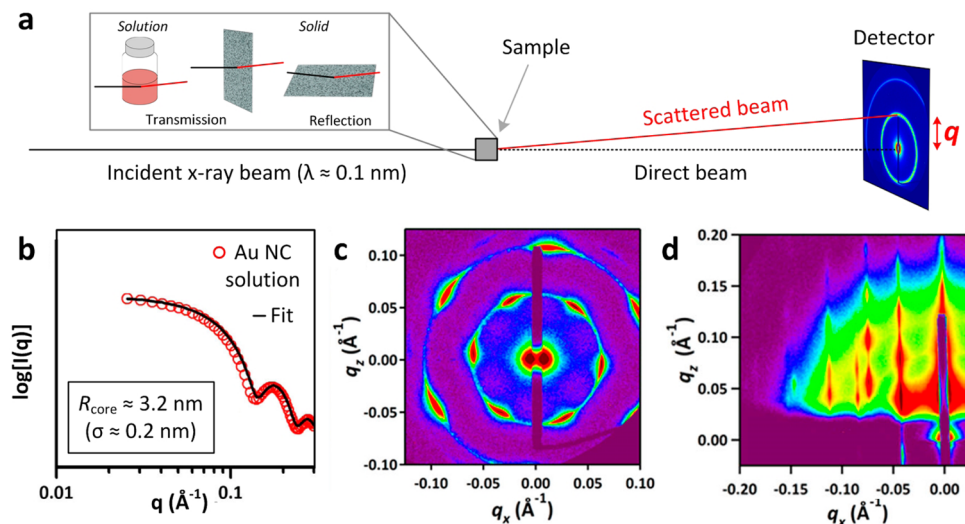


Figure 11. Small-angle X-ray scattering (SAXS) analysis of nanocrystal solutions and superlattice thin films. (a) Sketch of the SAXS experimental setup. (b) Radial profile of SAXS measurement of Au nanocrystals in solution (red circles) with fitted form factor for spheres (black trace). Such an analysis allows for estimation of average core size and standard deviation. Adapted from ref 100. Copyright 2015 American Chemical Society. (c) Transmission SAXS measurement shows reflections off superlattice planes within a single domain of close-packed CoFe₂O₄ nanocrystals. Red pixels denote areas with highest detected counts. (d) Grazing-incidence SAXS measurement of AlB₂ binary superlattice comprised of Bi and Au nanocrystals. Adapted from ref 71. Copyright 2014 American Chemical Society.

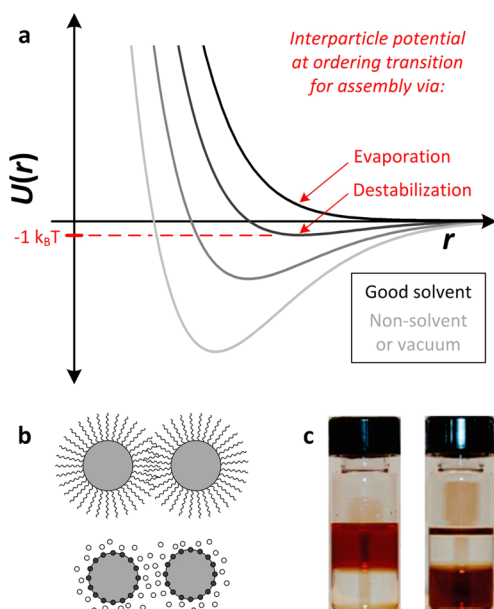


Figure 12. Pair interactions of nanocrystals in the dispersed state and the assembled state. (a) Evolution of the effective pair interaction potential U at interparticle separation distance r for nanocrystals from the beginning (darkest trace, dispersed state) to the end point (lightest trace, close-packed state) during the self-assembly experiment. This plot was constructed using 6–12 power-law potentials and serves only as a qualitative representation of nanocrystal pair interactions. (b) Sketch of a pair of interacting nanocrystals with hydrocarbon (top) and ionic (bottom) surface ligands. (c) Sterically stabilized solution of oleate-capped CdSe in nonpolar toluene phase (left photo, upper layer). Exchange of oleate ligands to potassium sulfide results in a phase transfer of the nanocrystals to the polar formamide phase (right photo, bottom layer). Adapted from ref 41. Copyright 2011 American Chemical Society.

Rapid destabilization results in uncontrolled, out-of-equilibrium growth of disordered nanocrystal aggregates producing dendrites¹⁰² or gel networks.¹⁰³ On the other hand, faceted,

polyhedral superlattices can be obtained by assembly near equilibrium conditions,³⁷ where interparticle attractions remain comparable to $k_B T$ for a sufficiently long time to allow nanocrystals to sample multiple sites on the superlattice surface before irreversible attachment.

4.2. van der Waals Forces between Nanocrystal Cores

The van der Waals interaction between inorganic cores stems from transient fluctuations in the distribution of electrons. It is typically attractive and favors flocculation of the colloid. In general the theory of the interatomic van der Waals attraction at the nanoscale is complex¹⁰⁴ but for the purpose of a coarse-grained description may be expressed as an effective pair potential

$$U_{vdW}(r) = -\frac{C\rho_1\rho_2}{r^6} \quad (1)$$

where ρ_1 and ρ_2 are the number of atoms per unit volume in two interacting bodies and the constant C is the coefficient in the interparticle interaction. This constant is large for materials with free electrons (e.g., metals). The total van der Waals energy of attraction between two particles with volumes V_1 and V_2 can be obtained by pairwise summation of van der Waals interaction between all atoms in the constituent particles

$$U_{vdW} = - \int_{V_1} dV_1 \int_{V_2} dV_2 \frac{C\rho_1\rho_2}{r^6} \quad (2)$$

This integral can be solved analytically¹⁰⁵ for two spherical nanocrystal cores with radii R_1 and R_2

$$U_{vdW}(r) = -\frac{A}{3} \left[\frac{R_1R_2}{r^2 - (R_1 + R_2)^2} + \frac{R_1R_2}{r^2 - (R_1 - R_2)^2} \right] + \frac{1}{2} \ln \left(\frac{r^2 - (R_1 + R_2)^2}{r^2 - (R_1 - R_2)^2} \right) \quad (3)$$

with Hamaker constant $A = \pi^2 C \rho_1 \rho_2$. A good approximation at close contact, $d = r - R_1 - R_2 \ll \min(R_1, R_2)$, is

$$U_{\text{vdW}}(d) = -\frac{A}{6d} \frac{R_1 R_2}{R_1 + R_2} \quad (4)$$

Equation 4 forms the basis of the Derjaguin approximation,¹⁰⁶ which estimates the van der Waals energy between two particles of arbitrary shape from the curvature of their surfaces and integration of the interaction energy of infinite parallel plates.

4.3. Steric Stabilization

The van der Waals interactions between nanocrystal cores can be sufficiently screened by the ligand shell to impart predominantly repulsive interactions and maintain stable colloidal solutions of even strongly interacting materials (e.g., metals with large Hamaker constant A). Osmotic and elastic repulsion between chains in good solvent form the basis of steric stabilization of hydrocarbon- and polymer-capped nanocrystals and beads, as well as solutions of surfactant, dendron, and polymer micelles. In this case, good solvent implies negative free energy of chain–solvent mixing.¹⁰⁷ An osmotic term resulting from unfavorable exclusion of solvent molecules within the ligand interaction region acts upon a pair of particles as soon as their ligand coronas begin to overlap. This effect occurs over the whole range of steric interaction, beginning at interparticle distances d lower than twice the width L of the capping layer ($d < 2L$). Compression of the ligand chains results in an elastic contribution to the potential at smaller surface separations. Because this elastic component quickly exceeds thermal energy, the predominant region sampled during a Brownian collision is the moderate interpenetration ($L < d < 2L$) domain.¹⁰⁸

In the interpenetration domain, the free energy of interpenetration of two chains tethered to the nanocrystal surfaces brought from infinite separation together in volume dV may be expressed with the Flory–Krigbaum theory¹⁰⁹ as

$$\Delta G = 2k_B T \frac{v_s^2}{v_i} \left(\frac{1}{2} - \chi \right) \int_V \varphi_1 \varphi_2 \, dV \quad (5)$$

where v_s , v_i , and χ are the Kuhn segment volume, solvent molecular volume, and Flory–Huggins chain–solvent interaction parameter, respectively. The segment density distribution functions φ_1 and φ_2 are derived from the geometry of a cone-shaped available ligand volume and can be evaluated numerically. Accordingly, in good solvent ($\chi < 1/2$), intermingling of hydrocarbon segments from neighboring nanocrystals is penalized ($\Delta G > 0$), and particles experience repulsion upon contact. On the other hand, clustering of nanocrystals is favorable in poor solvent (for $\chi > 1/2$, $\Delta G < 0$).

From this analysis it can also be seen that the steric repulsion strength depends on grafting surface curvature.¹¹⁰ On highly curved surfaces, found for example on small nanocrystals or the tips of pointy nanocrystals, each ligand enjoys access to a large cone-shaped volume. In this case, the segment density φ rapidly decays away from the grafting surface. The spatial concentration of ligand segments given by the overlap integral $\int_V \varphi_1 \varphi_2 \, dV$, and thus the free energy change upon corona interpenetration, is small. In contrast, for nearly flat surfaces, the overlap integral, and thus $|\Delta G|$, is large. Such logic predicts increasing per-ligand repulsion energy with decreasing surface curvature and might account for the counterintuitive propensity

of smaller nanocrystals to form clusters in solution.¹¹¹ Although not treated in the simple steric barrier model, significant melting enthalpy of solid ligand bundles (particularly for long-chain *n*-alkanes) has recently been uncovered as an important factor working against nanocrystal solubility.^{112,113}

Importantly, the total steric interaction energy between two particles is the sum of individual ligand–ligand potentials given in eq 5. For the case of the nanocrystal diameter greatly exceeding the thickness of the ligand capping layer, accurate estimation of interparticle interaction can make use of the Derjaguin approximation. However, this approach overestimates the steric repulsion between particles with stabilizing shell thickness on the order of the particle diameter (e.g., sub-10-nm nanocrystals capped with C₁₈-length hydrocarbons), where tilting of chains away from the contact axis can be significant.¹¹⁴ Modeling steric interaction between particles with comparable diameter and corona thickness remains an area of active research.¹¹⁵

Enhancing steric stabilization is a strategy to improve self-assembly success. One possibility is introducing unsaturation along the hydrocarbon backbone (e.g., *cis*-9-octadecyl chains of oleic acid or oleylamine) to suppress the tendency of long-chain saturated (e.g., stearic acid or octadecylamine) ligands to crystallize on the nanocrystal surface, promoting chain–solvent mixing and nanocrystal solubility. Tethering end-functionalized polymers¹¹⁶ to the nanocrystal surface is another possibility. Such chains can be considered entropic springs with elastic response from both stretching and compressive deviations from random-walk dimensions.¹¹⁷

4.4. Hydrocarbon Ligand Packing in Nanocrystal Solids

At the late stage of drying a nanocrystal solution, or upon nonsolvent addition, interpenetrating coronas are no longer swollen with solvent molecules and begin to freeze together under the influence of attractive van der Waals interactions between hydrocarbon chains. The attraction experienced by two parallel chains¹¹⁸ scales with the length L of overlap and decays quickly with backbone separation x as

$$U_{\text{vdW}}(x) = -A \frac{3\pi}{8\lambda^2} \frac{L}{x^5} \quad (6)$$

where λ is the sp³ carbon–carbon bond length ($\lambda \approx 0.15$ nm) and A is the Hamaker constant ($A \approx 0.1$ kcal/mol) for attraction between methylene units whose centers are separated by roughly 0.5 nm in the close-packed ligand bundle.

Saturated hydrocarbon chains tethered to a flat surface readily crystallize into an all-parallel backbone arrangement.^{119,120} Predictions from molecular dynamics simulations and experimental analysis using vibrational spectroscopy indicate that bundles of parallel ligand chains can form on the surface of nanocrystals in the absence of good solvent.^{121,122} Such bundling is most common for longer (C₁₂–C₁₈) chains tethered to the surface of larger-diameter particles. On the other hand, vibrational spectroscopy has revealed that ligands in nanocrystal solids have a significant concentration of *gauche* defects in the chain ends, which propagate toward the interior with increasing temperature.¹²³ Upon addition of nonsolvent to the nanocrystal solution, coronas contract to reduce contact with poor solvent and nanocrystals cluster for the same reason. Upon evaporation of a nanocrystal solution, however, hydrocarbon coronas are swollen with solvent when nanocrystals are initially crowded together. As a result, interparticle separations

are typically about 33% larger for evaporation-based assembly than for destabilization-based assembly.¹²⁴

The packing of hydrocarbon chains between nanocrystal cores and the resulting interparticle separations (Figure 13a) has not only been treated with molecular dynamics simulations but also using simple geometric models. These models postulate space-filling of ligands along the bond axis (optimal packing model (OPM),¹²⁵ Figure 13b) or space-filling of ligands within the entire volume of the corona overlap (overlap cone model (OCM),¹²⁶ Figure 13c). Experimental separations measured from TEM images of hexagonally ordered monolayers of alkanethiol-capped Au nanocrystals are consistent with the first model (Figure 13d,e).⁴⁹ However, they also confirm the existence of many-body interactions between nanocrystal capping layers predicted by the second model, which cause the effective corona thickness to vary with nanocrystal coordination number (Figure 13f,g). Together, molecular dynamics simulations and experimental data suggest that the nanocrystal ligand corona is a deformable surface coating that can support a variety of chain packing structures in the nanocrystal superlattice depending on chain length, surface curvature, and coordination state. Structural analysis of liquid crystals has recently inspired a conceptual framework to treat corona

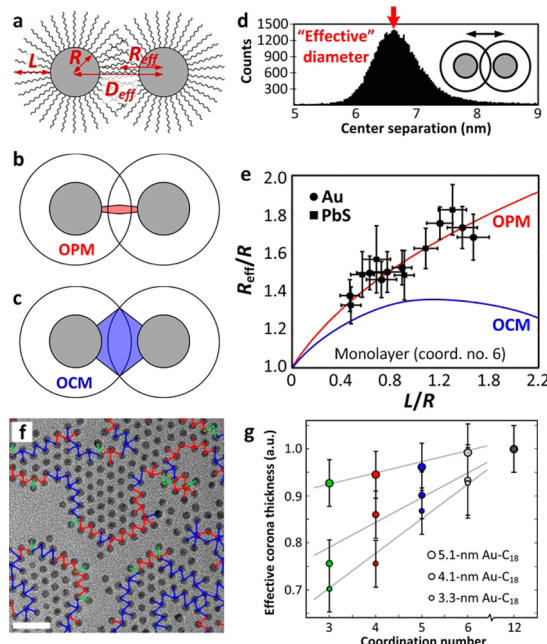


Figure 13. Packing of hydrocarbon ligands in nanocrystal superlattices. (a) Sketch of interdigitating hydrocarbon coronas between a nanocrystal pair showing core radius R , ligand length L , and effective radius R_{eff} . (b) Illustration of the optimal packing model (OPM) prediction of a small axial volume of space-filling hydrocarbons between nanocrystal cores. (c) Sketch of the overlap cone model (OCM) prediction of a larger overlap volume with space-filling hydrocarbons. (d) Histogram plot of the reduced separations measured from TEM images of a hexagonally ordered monolayer of alkanethiol-capped Au nanocrystals. (e) Summary of the TEM measurements collected from several ligand length–core radius combinations using Au and PbS nanocrystals. (f) TEM image showing various coordination states of nanocrystals deposited at submonolayer surface coverage. (g) Deformability of the hydrocarbon corona revealed by the measured reduction in effective nanocrystal size in low-coordination position. Adapted from ref 49. Copyright 2015 American Chemical Society.

deformation as a set of topological defects (e.g., vortices or disclinations) constrained by the geometry of the grafting surface. This approach has yielded a ligand packing model (the orbifold topological model, or OTM¹²⁷) which anticipates the relative stability of candidate binary superlattices in good agreement with an experimental phase diagram of binary mixtures of nearly spherical, hydrocarbon-capped nanocrystals.

All-atom or united-atom molecular dynamics simulations with classical or coarse-grained force fields investigated the ligand shells of nanocrystals and estimated effective interparticle potentials. The interaction can be quantified by calculating the potential of mean force between nanocrystals.¹¹⁵ Recent studies suggest that the ligand capping layer structure, and thus ligand-mediated interparticle interactions, is sensitive to factors such as solvent,^{128,129} temperature and bonding strength,^{130,131} grafting surface curvature,^{132,133} coating thickness,¹³⁴ core size,¹³⁵ and facet dimensions.^{136,137} However, there is no attempt to strictly separate the factors in these works, and in practice they all compete.

4.5. Electrostatic Stabilization

Adsorption of charged ions enables dispersion of nanocrystals in polar solvent (Figure 12b, bottom, and Figure 12c, right). Such surfaces may be obtained by ligand exchange of hydrocarbon-capped nanocrystals³⁸ or by synthesizing nanocrystals directly in polar medium (e.g., citrate-capped Au¹³⁸ or thioglycolic acid capped CdTe nanocrystals¹³⁹). The nanocrystal surface charge is then balanced by oppositely charged counterions surrounding the particle. Solvents with high dielectric constant (e.g., water, formamide) efficiently screen the electrostatic attraction between surface-bound ions and charge-neutralizing counterions, promoting the formation of an electrical double layer. Close approach of charge-stabilized nanocrystals in polar solution results in the overlap of counterion clouds, inducing a local osmotic pressure between surfaces, which causes an effective repulsion. Reducing the dielectric screening of the solvent by addition of less polar liquids (e.g., toluene, acetonitrile) induces collapse of the counterion cloud, enabling close approach of nanocrystal surfaces and promoting flocculation.

The interaction potential between a pair of charge-stabilized nanocrystals, including both electrostatic repulsion and van der Waals core–core attraction, is often treated in a first approximation using the Derjaguin, Landau, Verwey, and Overbeek (DLVO) theory.¹⁰⁷ The repulsive term decreases approximately exponentially with particle separation and can be estimated using the Derjaguin approximation at small separations and linear superposition at larger distances.¹⁴⁰ Analytical approximations provide an alternative to numerical integration. For example, the screened Coulomb (Yukawa) repulsive potential for two spheres of charge Z_1 and Z_2 in solution, separated by distance $r < \kappa^{-1}$, is given by

$$U_{\text{sc}}(r) = \frac{Z_1 Z_2 \lambda_B}{(1 + \kappa R_1)(1 + \kappa R_2)} \frac{\exp(-\kappa(r - R_1 - R_2))}{r} \quad (7)$$

Here κ^{-1} is the Debye screening length, $\lambda_B = e^2/(4\pi\epsilon_0\epsilon_r k_B T)$ is the Bjerrum length, and charge is expressed in units of the elementary charge e . The total DLVO interaction energy is then the sum of the repulsive electrostatic (Coulombic) and attractive van der Waals terms.

4.6. Contributions to Free Energy of Nanocrystal Solutions

Nanocrystal self-assembly is affected by the interplay of many chemical and physical forces. The equilibrium superlattice structure is the one that minimizes the system free energy (F), expressed in terms of energetic (U) and entropic (S) components as $F = U - TS$. Similarly, the free energy change ΔF upon self-assembly provides the driving force for ordering and results from corresponding changes in system internal energy and entropy, $\Delta F = \Delta U - T\Delta S$.

The internal energy change of the assembling system can be broken down approximately into core and ligand contributions, $\Delta U \approx \delta U_{\text{cores}} + \delta U_{\text{ligands}}$, as can be entropy, $\Delta S \approx \delta S_{\text{cores}} + \delta S_{\text{ligands}}$. Energetic interactions between nanocrystal cores are described by the set of van der Waals interactions, $\delta U_{\text{cores}} \approx \delta U_{\text{vdW}} \approx \delta U_{\text{London}} + \delta U_{\text{Keesom}} + \delta U_{\text{Debye}}$. The first term, the London dispersion attraction¹⁴¹ between instantaneously induced dipoles, is present for all nanocrystal core materials. The second and third terms are dipole-induced dipole and dipole-dipole interactions, respectively, which relate to materials with permanent electric dipole moments (e.g., CdSe). The combined strength of all three is described by the Hamaker constant A (section 4.2). In the general case, magnetic dipole moments (e.g., Fe₃O₄) and Coulombic interactions between charged particles may also be present. For charged nanocrystals there exist additional contributions from charge-charge, charge-dipole, and charge-induced dipole to the system internal energy.¹⁴² On the other hand, particle core entropy has configurational, translational, and rotational terms, $\delta S_{\text{cores}} \approx \delta S_{\text{conf}} + \delta S_{\text{trans}} + \delta S_{\text{rot}}$. The first term is related to rearrangements of the particles in the system ignoring local effects. In the superlattice it counts the number of ways to exchange particles. The other two terms handle local motions only, such as individual or collective fluctuations about equilibrium positions and orientations.

When sterically stabilized particles contact in good solvent, densification of ligand segments results in an osmotic penalty, $\delta S_{\text{ligands}} \approx \delta S_{\text{osmotic}}$.¹⁰⁷ Similarly, for charge-stabilized nanocrystals dispersed in polar solvent, condensation of counterion clouds gives rise to osmotic pressure between surfaces. In addition, upon interpenetration of hydrocarbon coronas, compression or extension of the backbone can distort torsion angles along the chain and introduce *gauche* defects, giving rise to elastic energetic penalty upon contact.¹⁴³ In the absence of good solvent, this elastic resistance to chain deformation balances the attractive London dispersion interaction between aliphatic chains: $\delta U_{\text{ligands}} \approx U_{\text{elastic}} + \delta U_{\text{London}}$.

While the above considerations give a rough idea of various factors governing nanocrystal self-assembly, other terms might be present depending on the chemistry of the system and the experimental setup.^{1,15,144} The abundance of contributing elements to the interparticle potential, unknown relative weights of each term, nonlinear and nonadditive coupling and evolution during self-assembly, the finite size of solvent molecules and solvated ions, inhomogeneity of the nanocrystal and its surroundings, and other effects make devising an accurate expression for the total free energy of the system extraordinarily complicated.³⁴ At present, the treatment of nanocrystal self-assembly in theory and simulation requires simplifying assumptions concerning particle shape (i.e., perfect spheres, cubes, etc.) and interactions at the disorder-order transition (purely repulsive, attractive, or absent). Fortunately, fundamental factors (such as nanocrystal core geometry) often dominate the formation of superlattices, allowing coarse-

grained models to explain many of the outcomes of self-assembly experiments.

5. SELF-ASSEMBLY OF HARD PARTICLES: ENTROPY MAXIMIZATION AND DENSE PACKINGS

Predicting the self-assembly of nanocrystals into ordered superlattices requires comparing the relative stabilities of candidate structures. In general, taking into account all energetic or entropic contributions present in the system is not possible. Approximations are necessary to estimate free energies numerically. Yet, just as Pauling's rules proved useful in understanding the structure of ionic compounds in the early days of crystallography,¹⁴⁵ rather general considerations help to clarify fundamental factors, such as the role of particle shape,¹⁴⁶ and elucidate the relationship between the geometry of building blocks and the superlattice into which they assemble.¹⁴⁷ The hard particle model is well-suited for such a study and a good approximation for nanocrystals with predominantly repulsive interactions or with only weak attraction over short distances.

5.1. Entropy Maximization Principle for Hard Particles

It was established in the 1950s that crystallization of particles can occur even when energetic interactions are entirely absent. Entropy-driven crystallization of hard spheres, the so-called Kirkwood–Alder transition, was predicted theoretically^{148–150} and subsequently observed in concentrated solutions of micrometer-sized colloidal beads with steep repulsive (i.e., nearly hard) interactions (Figure 14a).^{151,152} Such particles experience strong repulsion upon contact and are well described by the hard sphere model (Figure 14b). Hard particles interact solely through excluded volumes. They strive to minimize the Helmholtz free energy $F = -TS$ under the condition of constant volume V , and minimize the Gibbs free energy $G = PV - TS$ under the condition of constant pressure P . Importantly, the most stable phase of a hard particle system at a given volume corresponds to the phase maximizing the total entropy of the system.

By measuring all energies and pressure in units of $k_B T$, the phase behavior of a hard particle system becomes independent of temperature and only dependent on the particle volume fraction (Figure 14c). The volume fraction (also called packing density or packing fraction) $\phi = NV_0/V$ is the ratio of the average particle volume $V_0 = \sum_i V_i/N$ to the volume V/N available to each particle in the system. Dimensionless free energy and pressure are then defined as $F^* = F/k_B T$ and $P^* = PV_0/k_B T$, respectively.

When suspended in fluid at high volume fraction, a collection of hard particles has greater total entropy in an ordered crystal than as a disordered fluid (Figure 14d,e). Specifically, the configurational entropy loss incurred by collective ordering of mean particle positions (loss of configurational entropy) is more than offset by extra free volume ("wiggle room") afforded to particles for local vibrations around their equilibrium lattice positions and rotations about their average orientations in the colloidal crystal (gain of translational and rotational entropy). In other words, the increase in visible order is associated with an increase in microscopic disorder.¹⁵³

The entropy of N particles may be expressed using free volume theory¹⁵⁴ in terms of the volume fraction ϕ and the structure-dependent jamming limit ϕ_c

$$S \approx k_B fN \ln\left(\frac{\phi_c}{\phi} - 1\right) + S_c \quad (8)$$

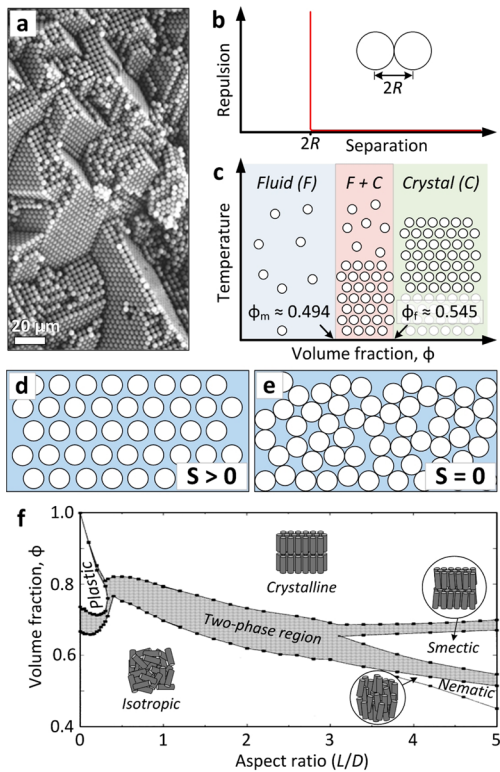


Figure 14. Entropy-driven crystallization of hard spheres and hard spherocylinders. (a) SEM image of close-packed spherical colloidal beads. Adapted from ref 168. Copyright 1999 American Chemical Society. (b) Hard sphere interaction potential. (c) Phase diagram of noninteracting spheres showing fluid phase at low density, crystal at high density, and coexistence of the two phases over an intermediate density range. Adapted with permission from ref 169. Copyright 2002 Nature Publishing Group. (d, e) The accessible free volume available to each particle increases upon adoption of an ordered colloidal crystal state (d) instead of a jammed state (e). In this schematic we ignore rattlers, which sets $S_c = 0$. (f) Phase diagram of noninteracting spherocylinder rods as a function of shape anisotropy and density. Adapted with permission from ref 170. Copyright 1997 AIP Publishing.

where f is the effective number of degrees of freedom per particle and S_c is an additive constant due to collective excluded volume effects. The jamming limit is defined as the density that can be reached with rapid compression avoiding crystallization. While free volume theory is only an approximation, eq 8 becomes exact at high density, i.e., close to ϕ_c . This means the densest phase is then thermodynamically favored. Only if several configurations have the same density does the additive factor S_c matter. Thus, because spheres can be packed in fcc up to $\phi_c \approx 0.74$ before jamming, fcc must be more stable than a disordered collection of spheres that only accommodates spheres up to a limit of $\phi_c \approx 0.64$ before becoming jammed.

Entropy-driven ordering is predicted for mixtures of two sizes of hard spheres.¹⁵⁵ Similarly, noninteracting anisotropic particles (e.g., rods or plates) at sufficiently high volume fraction may align, generating a discontinuous phase transition from isotropic solution to a liquid crystalline state (Figure 14f).¹⁵⁶ This process, known as the Onsager transition,¹⁵⁷ increases translational entropy at the expense of rotational entropy, and is predicted for ellipsoids of length-to-breadth ratio of more than 2 or less than 0.5.¹⁵⁸ For polyhedral

particles, entropy maximization leads to complex phases including entropically driven solid–solid phase transitions.¹⁵⁹

Several methods have been proposed to identify entropy-maximizing configurations for various hard particles.¹⁶⁰ Stochastic sampling via modern Monte Carlo simulation tools¹⁶¹ or solving Newton's equations of motion via event-driven molecular dynamics simulation^{162,163} are brute-force methods that directly emulate aspects of the experiment and do not require a priori assumptions about the ordered phases. Candidate phases can also often be guessed using small systems, for example via the floppy-box Monte Carlo simulation.¹⁶⁴ Once candidate phases are known, direct free energy calculation is possible to high precision via thermodynamic integration or Frenkel–Ladd integration.^{165,166} Given a sufficiently large set of candidate structures, these powerful techniques are almost arbitrarily accurate (limited only by compute power) and rely on numerically tracking thermodynamic parameters such as pressure (or density) during slow, continuous variation of other parameters such as density (or volume, or particle interactions, e.g., from hard to soft). For example, the change in Helmholtz free energy during a density change from ϕ_1 to ϕ_2 is

$$F^*(\phi_2) - F^*(\phi_1) = N \int_{\phi_1}^{\phi_2} \frac{P^*(\phi)}{\phi^2} d\phi \quad (9)$$

Other similar formulas can be derived starting from the fundamental thermodynamic relation. Special precaution is necessary when handling partially disordered phases¹⁶⁰ and symmetry-equivalent particle orientations in an ordered phase.¹⁶⁷

5.2. Dense Packings as Candidate Structures for Nanocrystal Superlattices

One assumption has routinely been invoked for predicting the outcome of nanocrystal self-assembly: dense packings are favored. Dense packings appear for hard particles in the high-pressure/high-density limit where the PV term in the Gibbs free energy dominates the entropy term TS . A densest packing (minimal V) will eventually be the maximum entropy state and therefore be the most stable. This can be seen directly from free volume theory, eq 8. Densest packings have the same meaning for hard particle systems as thermodynamic ground states for systems of interacting particles: they are the states reached when all dynamics of the system has ceased and entropy can be ignored. Finding the densest packing for a given shape is thus a natural starting point for predicting the structure of self-assembled nanocrystal superlattices.

Packing shapes has a long history that goes back to ancient Greece, at which time Plato developed a polyhedron-based theory of matter (fire is comprised of tetrahedra; air, octahedra; earth, cubes; water, icosahedra). In 1900, David Hilbert challenged mathematicians as part of the 18th of his 21 problems¹⁷¹ to find the optimal way to “build up space from congruent polyhedra”. This plain wording, however, belies its complexity. More than a century after Hilbert's proposal, it has been proven for only one shape, the sphere. The Kepler–Hales theorem states that face-centered cubic (fcc), hexagonal close-packed (hcp), and other stacking variants of hexagonal layers are the densest packings for spheres (Figure 15a,b), filling $\phi_{\text{fcc}} = \pi/\sqrt{18} = 74.04\ldots\%$ of space.¹⁷² Resolving the entropy difference between these two phases requires high-precision free energy calculations. The outcome of the calculation is a small entropic preference of $\Delta s = 0.001164(8)k_B$ per sphere for

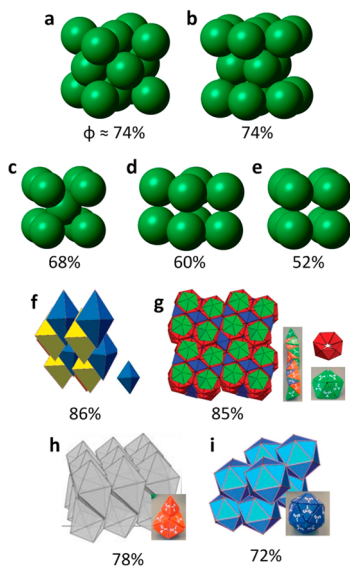


Figure 15. Dense and less dense crystalline packings of spheres and tetrahedra. (a) Unit cell of spheres in fcc packing. (b) Structural motif of spheres in hcp packing. (c) Unit cell of spheres in bcc packing. (d) Unit cell of spheres in simple hexagonal packing. (e) Unit cell of spheres in simple cubic packing. (f) Double dimer (densest known) tetrahedron packing. Adapted with permission from ref 177. Copyright 2002 American Physical Society. (g) Quasicrystalline tetrahedron packing. Adapted with permission from ref 178. Copyright 2009 Nature Publishing Group. (h) Wagon wheel (nonamer) tetrahedron packing. Adapted with permission from ref 179. Copyright 2008 Springer. (i) Icosahedron (20-mer) tetrahedron packing. Adapted with permission from ref 180. Copyright 2009 Nature Publishing Group.

fcc¹⁷³ over hcp due to phonon contributions.¹⁷⁴ Optimal packings for space-filling solids (the cube, for example, and several other polyhedra^{167,175}) are also known and represent trivial Hilbert solutions.

Nowadays, searching for the densest packing is a special case of a mathematical optimization problem. Only with the advent of modern computers it became possible to study the packing of a wide range of shapes numerically. Many solutions have been found that are believed to be optimal or at least near optimal. Yet, due to the complexity of the packing problem, searching for new rigorous mathematical results has turned out to be extremely difficult even in simple situations. Small steps forward thus represent significant mathematical advancements.¹⁷⁶

For hard spheres, the ordered phases observed in the Kirkwood–Alder transition coincide with the densest packing of spheres, yielding primarily fcc or hcp packings. Alternative candidate structures such as bcc, simple hexagonal (sh), and simple cubic (sc) (Figure 15c–e) have packing densities of 68, 60, and 52%, respectively, leaving more void space in the lattice than fcc and hcp (Figure 15f). Such arrangements of hard spheres are not stable, because they provide less free volume for local translations in the colloidal crystal than fcc and hcp packing.

The packing of polyhedra is particularly relevant in the context of nanocrystal self-assembly because polyhedral nanocrystals are frequently encountered as energy-minimizing Wulff shapes comprised of an atomic single crystal or twinned polycrystal.¹⁸¹ Densest packings of most regular convex¹⁵⁹ and concave^{164,182} polyhedra, as well as families of polyhedra,^{183–185} have been reported using numerical techniques.

The regular tetrahedron, for example, is the simplest Platonic solid. It has pyramid shape with four equilateral triangle sides. In one of the earliest recorded mistakes in the history of mathematics, Aristotle suggested that copies of the regular tetrahedron fill space completely.¹⁸⁶ In fact, no such arrangement is possible, although a series of recent works^{179,180,187–189} demonstrated that there exist several ways to pack tetrahedra more densely than spheres (Figure 15f–i). Self-assembly of tetrahedrally shaped colloids mediated by excluded volume interactions can be expected to produce such arrangements in the high-pressure limit.

5.3. Dense Packings of Binary Hard Particle Mixtures

The search for dense packings of two sizes of spheres was encouraged by the discovery of gem opals comprised of bidisperse silica beads.¹⁹⁰ Binary sphere mixtures often pack more densely than a single component alone, for example, by filling the voids in a close-packed sphere lattice with smaller spheres. When evaluating ways to densely pack sphere mixtures, there are two degrees of freedom that influence the maximally achievable packing density: the radius ratio (or size ratio), $\gamma = R_B/R_A$, and the stoichiometry, $x = n_B/(n_A + n_B)$, of the large (A) and small (B) spheres. Recent studies^{191–194} uncovered more than 15 unique binary sphere packings that exceed the densest single-component (fcc) arrangement (Figure 16). Such analyses provide a natural starting point for anticipating the structures formed by spherical nanocrystals that seek to maximize packing density at high particle volume fraction. However, in the limit of similar sphere radii ($\gamma > 0.66$), phase separation into separate fcc (or hcp) lattices of large and small spheres provides the densest packing, while in the limit of very disparate sizes ($\gamma < 0.2$) depletion effects (section 10.6) strongly disfavor the achievement of dense packings in experiment.

Beyond these space-filling considerations, configurational entropy and entropy of mixing provide an additional driving force for cocrystallization of two sizes of hard spheres at intermediate density. Such second-order effects can stabilize binary structures that compete with, but do not exceed, the

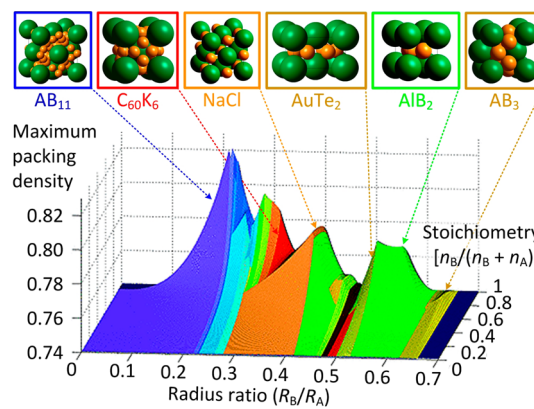


Figure 16. Summary of densest known binary sphere packings. Maximum packing density (z-axis) surface plot shown as a function of radius ratio (x-axis) and stoichiometry (y-axis). Unit cells or characteristic structural motifs for selected structures are shown above. The proposed maximum density is claimed by the AB_{11} structure, which fills space with about 82% efficiency at radius ratio close to 0.22. The radius ratio for which binary packings exceed single-component close packing is $\gamma < 0.66$. Adapted with permission from ref 194. Copyright 2012 American Physical Society.

density of phase-separated packings. Examples are the NaZn_{13} arrangement within size ratio range $0.54 < \gamma < 0.61$ (ref 155) and Laves phases within $0.76 < \gamma < 0.84$ (refs 195, 196). In this way, translational and configurational contributions to system entropy can stabilize a hard sphere binary crystal in some instances if its density is above about 65%. So far the complete phase behavior of binary sphere mixtures away from the limit of densest packings shown in Figure 16, and thus the role of entropy in the formation of binary sphere crystals, has not been investigated for all values of the radius ratio, stoichiometry, and packing density.

The phase diagram of mixtures of spheres and rods is even more complex because it contains the rod aspect ratio as a third parameter. Although the packing of rods and spheres has not been investigated in full generality, at least one binary structure of spheres and rods with aspect ratio 2 exceeds the density of demixed phases (Figure 17a). Closely related to the AlB_2 arrangement of spheres, this AB_2 binary phase has a stability range of $0.5 < \gamma = R_{\text{sphere}}/R_{\text{rod}} < 0.58$, similar to where an equivalent phase is found in a binary sphere mixture (Figure 17b). The rod–sphere system is an example where the densest packing is not the only ordered maximum entropy solution. At intermediate density, bulk demixing into rod-rich and rod-poor phases, and microphase separation into a variety of morphologies, has been predicted and observed in experiment (Figure 17c).^{197,198} Cococrystallization is expected if these competitor phases are avoided, as recently confirmed in an investigation of the experimental phase behavior of mixtures of rod-shaped and sphere-shaped nanocrystals.¹⁹⁹

5.4. Cataloging Stable Phases of Hard Polyhedra

Packing arguments²⁰⁰ and self-assembly studies may be extended to all manner of hard shapes to predict their phase

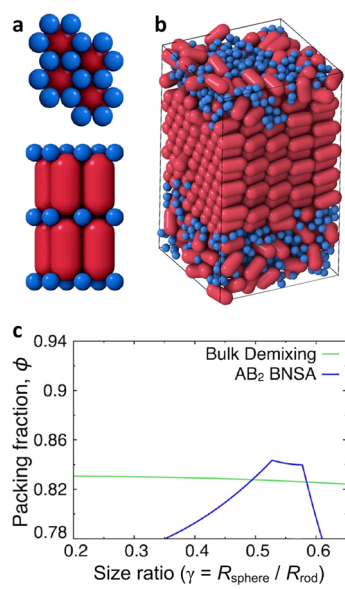


Figure 17. Packing rods and spheres. (a) Modeled AB_2 packing of rods and spheres at size ratio 0.56. (b) At intermediate volume fraction, simulations predict phase separation into rod crystal and mixed fluid. (c) Plot of packing efficiency of phase-separated (green trace) and AB_2 binary nanocrystal shape alloy (BNSA, blue trace) for simple hard rod (spherocylinder) and sphere shapes. Excluded volume (hard particle) interactions between rods and spheres stabilize dense binary structures at size ratios $0.50 < \gamma < 0.58$. Adapted from ref 199. Copyright 2013 American Chemical Society.

behavior and elucidate the relationship between particle shape and the stable phase. To this end, Monte Carlo simulations revealed a large diversity of ordered maximum entropy phases in systems of hard polyhedra belonging to Platonic, Archimedean, Catalan, and Johnson solid groups,¹⁵⁹ many of which are experimentally accessible for nanocrystals prepared by colloidal synthetic techniques. At intermediate density in the $0.5 < \phi < 0.6$ range, spontaneous ordering occurs for a majority of high-symmetry polyhedra. In this case, nucleation and growth leads to well-ordered superlattices and is generally fast. Lower-symmetry polyhedra, however, remained disordered even after prolonged simulation. On the other hand, particularly densely packing polyhedra (e.g., cubes and rhombic dodecahedra) order faster than spheres.

Three structural categories (Figure 18) were observed. One such category is that of the crystal phases, with both translational and orientational long-range order. The other two categories, intermediate between liquid and solid, are examples of mesophases,²⁰¹ with either orientational or translational order but not both. For instance, the roundest shapes often arrange themselves on a lattice without preference for particle orientation (plastic crystals or rotator crystals), while large zero curvature surfaces direct particles onto a lattice with orientational registry (nematic, smectic, and columnar/discotic liquid crystals), as shown in Figure 18b. The assembly behavior of polyhedra can be predicted from particle sphericity and local order in the fluid. Sphericity is measured by the isoperimetric quotient $36\pi V^2/A^3$ for a particle with volume V and surface area A (ref 159) or via the asphericity factor $\alpha = RA/3V$, where R is the mean radius of curvature. Both parameters are normalized such that they are 1 for a sphere. The asphericity factor appears in the second virial coefficient of hard particles which is known analytically, $B_2 = V(1 + 3\alpha)$ (refs 202, 203).

Ordered phases can be surprisingly complex, and include the close-packed sphere lattices fcc and hcp, the soft particle lattice bcc, the topologically close-packed (Frank–Kasper and pseudo-Frank–Kasper^{204,205}) phases γ -brass, β -Mn, and β -W (isostuctural to the A15 phase) for weakly faceted spheres, a few Bravais lattices, and a few others including diamond (Figure 18a). In addition to these single-polyhedron assemblies, the phase behavior of binary mixtures of polyhedra has recently been investigated.²⁰⁶ Such studies reveal packing complementarity for particular shape pairs. For instance, octahedra and tetrahedra, which necessarily leave gaps when phase-separated, can fill space when mixed in a 1:2 ratio provided they have identical edge lengths. Indeed, a binary phase of hard tetrahedra and octahedra has been observed in simulation.²⁰⁷

This notion of flat surfaces directing orientational registry of hard rods or plates (Figure 14, bottom) and faceted polyhedra (Figure 18b, center) has given rise to the concept of directional entropic forces.^{183,208} These entropic forces between anisotropic particles strive to maximize local dense packing by aligning faces and can be quantified by using the potential of mean force and torque.²⁰⁹ Under compression, the system shows a strong preference for coordination via centering the faces, for example of neighboring cubes irrespective of the presence of a high density of vacancies.²¹⁰ Directional entropic forces allow for the possibility of designing entropic assemblies by constructing entropically patchy particles²¹¹ or using shapes given by the Voronoi tessellation of the target crystal structure.¹⁶⁷ It is then possible to aim for novel entropically stabilized phases or specific symmetries by modifying the

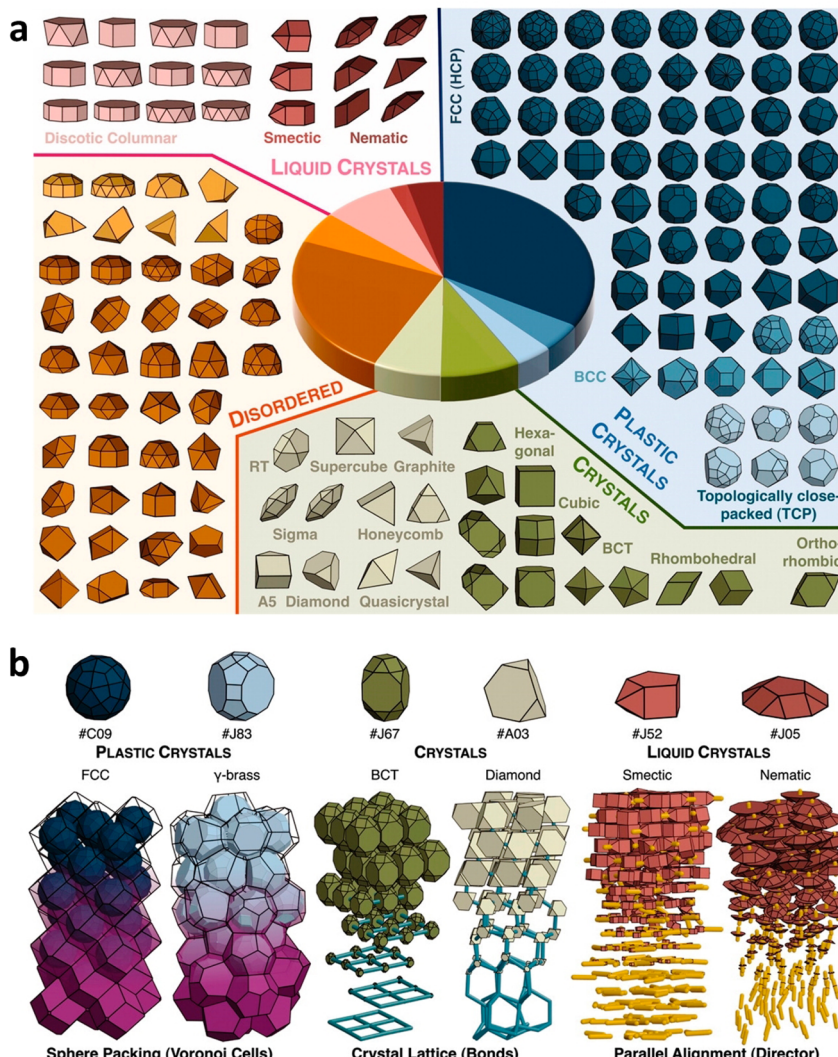


Figure 18. Cataloging the phases formed by Monte Carlo computer simulations of 145 convex polyhedra. (a) Illustrations of the polyhedra forming crystals, plastic (rotator) crystals, liquid crystals, and glasses. (b) Representative particle shapes that select one of the three phase families. Nearly spherical polyhedra rotate in the ordered phase forming plastic crystals, faceted polyhedra resemble covalent (directionally bonded) crystals, and highly anisotropic polyhedra only partially order their position forming liquid crystals. Adapted with permission from ref 159. Copyright 2012 American Association for the Advancement of Science.

attributes of building blocks.²¹² For example, particle shapes have been designed to yield chiral crystals²¹³ or cholesteric (chiral nematic) liquid crystals.²¹⁴ Advancements in the theoretical understanding of hard polyhedron crystallization, coupled with shape-controlled synthesis of colloidal nanocrystals,^{215–219} provides a blueprint for preparing novel superlattice structures via shape-directed nanocrystal self-assembly.

6. SELF-ASSEMBLY OF SOFT PARTICLES: INTERNAL SURFACE AREA MINIMIZATION

So far, we rationalized the phase behavior of nanocrystals by considering only the shape of the particle core in the hard particle model. However, after synthesis, colloidal nanocrystals are typically covered by a layer of hydrocarbon surface ligands. The presence of this corona of semiflexible “hairs” has two effects: it softens the interaction of the inorganic cores and, assuming uniform coverage, results in an effective nanocrystal shape that is always more spherical than the underlying core. These effects require a modification of the hard particle model when applied to surfactant-stabilized nanocrystals. The soft

particle model is a complementary approach to the hard particle model for studying the self-assembly of nanocrystals. It replaces the hard particle assumption of perfect particle rigidity by the assumption of perfect particle elasticity coupled with incompressibility. In other words, soft particles can deform as long as their volume does not change.

6.1. Hard and Soft Particles Are Two Extremal Models for Nanocrystals

The prime example of soft particles are block copolymer micelles. Block copolymers are a class of macromolecules with two or more chemically distinct polymer segments (blocks), which may be, for example, hydrophobic and hydrophilic (poly(styrene)-block-poly(ethylene oxide), PS-PEO). They adopt a number of ordered nanostructured phases including the spherical phase, which segregates the minority block into spheres surrounded by a corona of chains of the majority component.²²⁰ The polymer melts are easily deformable, but necessarily completely fill space because liquids do not support local density variations. Using this logic, block copolymer

micelles may be considered, in good approximation, as incompressible, deformable particles.

While the self-assembly of hard particles is driven by maximization of packing density in the limit of high pressure (section 5), soft particles strive to minimize contact area between particles in the limit of low temperature.²²¹ For block copolymer micelles, this minimization is caused by the conformational entropy penalty associated with elastic chain deformation. Density maximization and area minimization lead to different solutions. For example, while hard spheres frequently assemble into fcc and hcp arrangements, block copolymer micelles do not. Instead, these soft particles typically prefer to adopt bcc ordering.²²²

The combination of rigid inorganic core and soft organic corona naturally places colloidal nanocrystals between the hard and the soft particle models (Figure 19). Perhaps unsurprisingly, therefore, colloidal nanocrystals, often with 2–10 nm core diameter and C₈–C₁₈ (about 1–2 nm length) hydrocarbon surfactant shells, self-assemble into phases characteristic of both dense packings and contact area-minimizing configurations.²²³ Interestingly, the search for minimal-area soft particle phases, like the search for dense-packing hard particle phases and Hilbert's 18th problem, appears to conveniently intersect with another famous problem of mathematics.

6.2. Area-Minimization Principle and Tetrahedral Close-Packing

In 1887, Lord Kelvin asked the question: what regular partition of space into cells of equal volume has the smallest surface area of cells? This concept is also known as the internal surface area minimization principle (or in short, area-minimization principle). Kelvin proposed the bcc lattice to be the most area-minimizing structure. Indeed, bcc was considered optimal for more than 100 years until Weaire and Phelan uncovered a more efficient partitioning of space, the A15 phase.²²⁴ Isostructural with Cr₃Si and β -tungsten, the A15 structure features mutually orthogonal dimers centered on the faces of a bcc lattice (Figure 20a). It is a poor choice for efficient sphere packing, having a density similar to that of the simple cubic lattice (52%). However, A15 represents a partitioning of space with even less internal surface area than Kelvin's choice of bcc arrangement.

The property of efficiently partitioning space is captured by examining the shape of the Voronoi cell (also known as Wigner–Seitz polyhedron). The Voronoi cell is the space available to each particle on the lattice or, mathematically speaking, the volume that comprises all points in space that are closer to a given particle than to any other. An equivalent formulation of Kelvin's question is, which structure maximizes

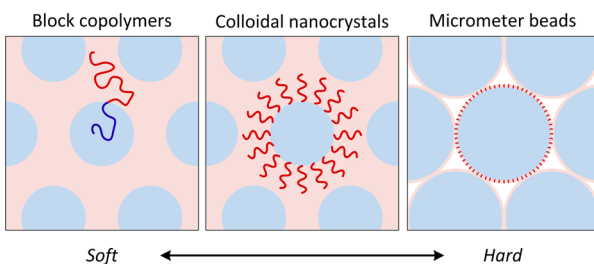


Figure 19. Schematic illustration of colloidal nanocrystals (middle) bearing similarity to both block copolymer systems (left, soft particles) and micrometer-sized colloidal beads (right, hard particles).

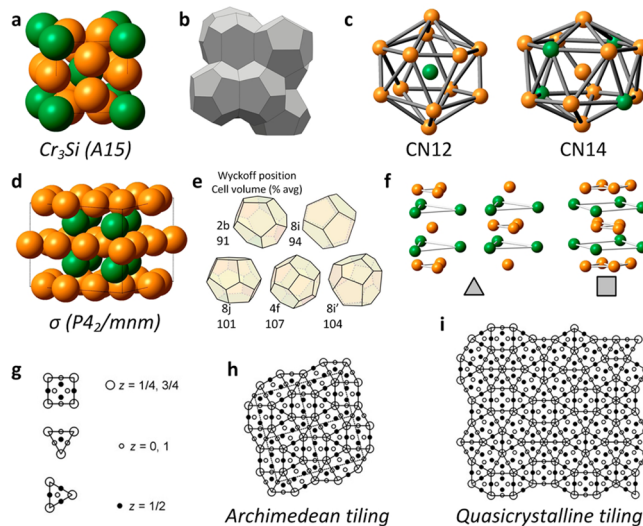


Figure 20. Frank–Kasper phases are tetrahedrally close-packed structures. (a) The A15 phase divides space into equal-volume partitions with minimal internal surface area. The unit cell is comprised of a bcc sublattice (green spheres) with face-centered sites (orange spheres) positioned along three mutually perpendicular, interlocking columns. (b) Dodecahedra and tetrakaidecahedra are the Voronoi cells of the A15 phase. Adapted with permission from ref 225. Copyright 2011 Nature Publishing Group. (c) Coordination polyhedra for sites in the A15 phase. Note that the polyhedra have exclusively triangular faces, which means A15 has only tetrahedral voids. (d, e) Relaxing the requirement for equal-volume partitions, the Frank–Kasper σ phase has even less internal surface area than the A15 phase. The σ phase unit cell is comprised of 30 spheres, with 8j particles forming tiling vertices highlighted in green. Adapted with permission from ref 226. Copyright 2010 American Association for the Advancement of Science. (f) Decomposition into triangle (left) and square (right) tiling units. (g) Space-filling polyhedra with volumes shown underneath. (h, i) Tiling from triangle and square units with only 3.4.3².4 vertices in the σ phase and by including other vertices in a dodecagonal quasicrystal. Adapted with permission from ref 227. Copyright 2004 Nature Publishing Group.

the average isoperimetric quotient for its Voronoi cells or minor modifications thereof? A15 (isoperimetric quotient 0.764) narrowly beats bcc (0.757), which in turn beats fcc (0.741). Since the pentagonal dodecahedral and tetrakaidecahedral Voronoi cells of A15 (Figure 20b) are more spherical than the truncated octahedral Voronoi cell of the bcc lattice, they require less deformation of a spherical soft hydrocarbon shell.

The Frank–Kasper phase family is defined to comprise all phases that feature exclusively tetrahedral voids (i.e., they are tetrahedrally close-packed, tcp).^{204,205} Notably, the A15 arrangement is an example of a Frank–Kasper phase. Only tetrahedral voids are present in A15, as evidenced by the coordination polyhedra with exclusively triangular faces (Figure 20c). One-third of the voids in the fcc lattice, by contrast, are octahedral. Frank–Kasper phases generally have Voronoi cells with high values of the isoperimetric quotient.

An arrangement with even less internal surface area emerges if Kelvin's requirement for equal-volume partitions is removed. The new optimal phase, the Frank–Kasper σ phase, isostructural with intermetallic Fe₄₆Cr₅₄, has an unusually large unit cell built from 30 particles (Figure 20d). The σ phase divides space into five distinct Voronoi polyhedra with about 15% spread in volumes (Figure 20e) and is comprised of

triangle (Zr_4Al_3 type) and square (Cr_3Si type) tiling units (Figure 20f,g). The two polygonal units ("squares" and "triangles") can be used to construct tilings of the plane. They can be arranged periodically in the $3.4.3^2.4$ Archimedean tiling (Figure 20h) with three triangles and two squares meeting at each vertex and no sharing of edges between squares. A quasicrystalline arrangement results by incorporating 3^6 vertices (six triangles meeting at a point, Figure 20i). The appearance of such complex phases is no complete surprise because tetrahedral local order is incompatible with long-range order and thus difficult to extend linearly.

Intriguingly, $A15$, σ , and quasicrystal phases are readily observed in soft matter systems such as micelle-forming block copolymers,^{226,228} dendrons,^{227,229} and surfactant solutions²³⁰ (Figure 21) and can even be targeted via precisely controlled positional interactions between micelles of giant macromolecular tetrahedra.²³¹ There is significant overlap between the phases observed for soft micelles and colloidal nanocrystals: for example, Frank–Kasper $MgZn_2$ ($C14$ Laves phase), σ , and quasicrystalline phases result from assembly of binary nanocrystal mixtures (section 7.6). The area-minimizing, tetrahedrally close-packed, and often complex arrangements like Frank–Kasper $A15$, σ , and quasicrystalline phases would not be uncovered by searching for efficient sphere packings but naturally arise when interactions between soft ligand shells are taken into account.

Simulations performed on modeled spherical micelles support the notion that complex arrangements can be stable for building blocks favoring regular tetrahedral interstices.²³² In this work, mobile surface entities and shape polydispersity are crucial for consistently assembling quasicrystals and/or approximants, indicating that polytetrahedral order is possible by appropriate particle functionalization and shape. Indeed, Frank–Kasper and related complex phases are often achieved by starting from hard spheres and introducing shape anisotropy.¹⁵⁹ In this way, imperfections in particle size and shape, as frequently found in nanocrystals, are analogous to an effective softness in the nanocrystal interaction and destabilize fcc/hcp lattices. Whenever disfavoring close-packing, for example by softening the interaction potential,²³³ structures corresponding to bcc and tetrahedrally close-packed lattices are

found to naturally appear. Quite general theoretical considerations suggest that while bcc is typically favored near the melting line, icosahedral local symmetries, as found in tetrahedrally close-packed lattices, are favored in amorphous solids.²³⁴ In similar fashion, more diverse phases and a richer phase diagram are also obtained in binary soft particle systems by varying the degree of softness away from pure excluded volume repulsion by changing the exponent of effective inverse power law interaction potentials.^{235,236}

6.3. Area-Minimization Principle for Hydrocarbon-Capped Nanocrystal Superlattices

Only some of the phases experimentally observed for nearly spherical nanocrystals are explained by hard-sphere-packing arguments. For example, the bcc phase is a suboptimal sphere packing arrangement (Figure 15) but is frequently observed upon evaporating solutions of quasi-spherical nanocrystals.²³⁷ Nanocrystal "softness", expressed as L/R , where L is the molecular length of the capping ligand and R is the radius of the inorganic core, plays a crucial role in selecting between close-packed and non-close-packed sphere arrangements: alkanethiol-capped metal nanocrystals experience an fcc-to-bcc transition for $L/R > 0.7$.^{223,238} Similar arguments also hold for DNA-mediated nanocrystal assembly into the bcc phase, where long linkers were identified as the cause for the deviation from close-packing.²³⁹

Along these lines, recent attempts to rationalize nanocrystal superlattice phase behavior have evaluated superlattice packings on the basis of an area-minimization principle. Assuming hydrocarbon chains must fill the interparticle matrix after solvent evaporation, the shape of the space afforded to each particle (Voronoi cell or Wigner–Seitz polyhedron) packed in fcc or bcc arrangements (Figure 22a,b) determines the extent to which ligands are forced to compress or expand to fill space (Figure 22c). Plotting the distance separating the polyhedron center and all points on its surface reveals a wider spread for the rhombic dodecahedron (fcc cell) than the cuboctahedron (bcc cell), implying a larger elastic penalty for hydrocarbon capping ligands packed in the fcc arrangement (Figure 22d). Accordingly, for nanocrystals with significant soft character contributed by surface-tethered hydrocarbon ligands, phase behavior reflects a contribution from both sphere packing and area-minimizing components. Such arguments have been extended to rationalize the recent experimental observation of the $C14$ Laves (Frank–Kasper) phase assembled from monodisperse 2 nm Au nanocrystals capped with hexanethiol ligands at $L/R \approx 0.84$.²⁴⁰ Furthermore, evidence of an area-minimizing contribution to nanocrystal assembly has been observed for the case of binary superlattices of spherical nanocrystals (section 7.6). In one notable example, solid-state binary assembly via Ostwald ripening of monodisperse nanocrystal superlattices heated above 120 °C yielded only Frank–Kasper or pseudo-Frank–Kasper binary structures.²⁴¹ In these cases, the absence of large octahedral voids in the tetrahedrally close-packed phases, and resulting minimal distortion of surface-bound hydrocarbon chains required to fill the interparticle matrix, may be the driving force to form such unusual sphere packing arrangements.

7. SELF-ASSEMBLY OF HYDROCARBON-CAPPED NANOCRYSTALS

In the following section, we highlight examples of superlattices formed by spherical and anisotropic nanocrystals and nano-

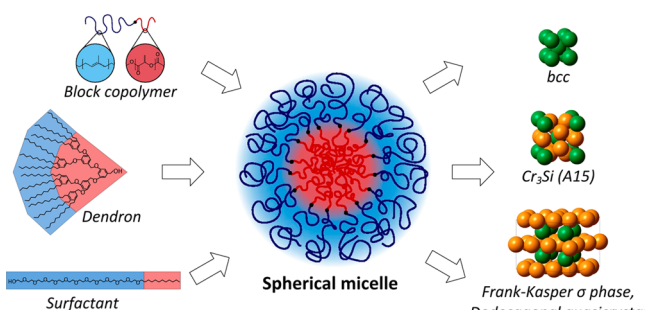


Figure 21. Experimental soft matter systems ordering onto area-minimizing lattices. Organic molecules such as block copolymers, dendrons, and surfactants (e.g., from top left to bottom left, polyisoprene-*b*-lactide, 3,4,5-tris(*n*-dodecyl)benzyloxy, and dodecyl-polyethylene glycol) assemble into hairy spherical micelles (center) with phase behavior reminiscent of nanocrystal superlattices, including tetrahedrally close packed Frank–Kasper σ phase, quasicrystal, and $A15$ (Weaire–Phelan) structure, as well as bcc phase. Center panel adapted with permission from ref 228. Copyright 2014 National Academy of Sciences.

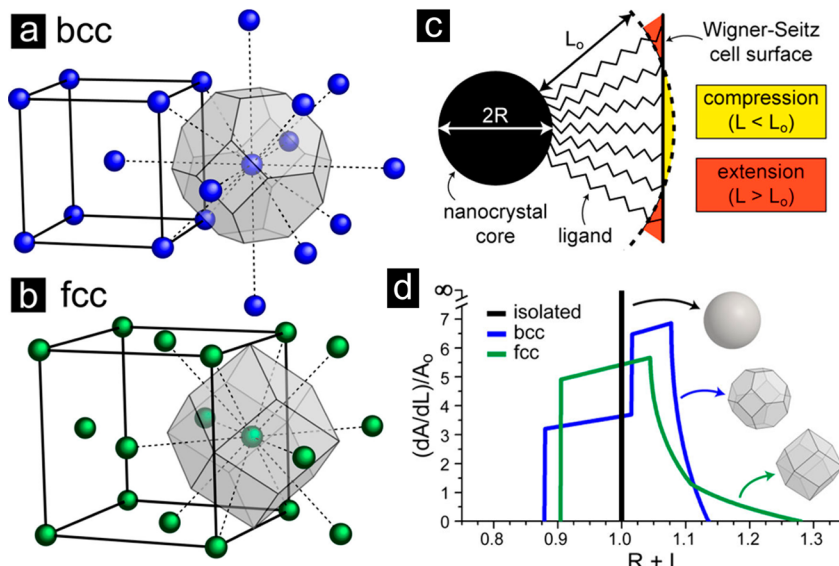


Figure 22. Wigner–Seitz evaluation of sphere packings. The bcc structure requires less distortion of the ligand corona than fcc arrangement. (a) bcc unit cell and the corresponding Wigner–Seitz polyhedron. (b) fcc unit cell and the corresponding Wigner–Seitz polyhedron. (c) Illustration of the compression and extension of hydrocarbon chains required to occupy the entire Wigner–Seitz cell. (d) Asphericity of both Wigner–Seitz cells. The spread in center-to-surface distances of the bcc Wigner–Seitz polyhedron (blue trace) is narrower than that of the fcc Wigner–Seitz polyhedron (green trace), and thus requires less distortion of capping ligands. Adapted from ref 242. Copyright 2015 American Chemical Society.

Table 2. Examples of Prior Work on Self-Assembly of Monodisperse Hydrocarbon-Capped Nanocrystals into Three-Dimensional Superlattices^a

core shape	core material	surface ligands	approx core size (nm)	self-assembled struct	lit. example
sphere	CdSe	C ₄ , C ₈ , C ₁₆	3–10	fcc, hcp	ref 58
	Au	C ₁₂	2–7	fcc, hcp, bcc	ref 223
	Pb(S,Se,Te)	C ₁₈	3–10	fcc, hcp, bcc, sh	refs 37, 243
cube	Pt	C ₇ , C ₈ , C ₁₂ , C ₁₆ , C ₁₈	2–10	sc, bct	refs 244, 245
	Fe ₂ O ₃	C ₆	8.5	bct	ref 246
	Pb(S,Se,Te)	C ₁₈	10	sc, bct, rh	refs 245, 247
octahedron	Pd	C ₁₂	10	sc, rh	ref 248
	Pt ₃ Ni	C ₁₈	10	bcc	ref 249
InCdO		C ₁₈	50	Minkowski	ref 250
tetrahedron	CdSe	C ₉ , C ₁₄ , C ₁₈	10	bco	ref 110
octapod	CdSe/CdS	C ₁₈	100	bct	ref 54
rod	CdSe, CdSe/CdS	C ₁₈	30 × 5	N, S, hcp	refs 73, 251
plate	GdF ₃	C ₁₈	20 × 2	C, L	ref 53

^aStructure key: fcc = face-centered cubic, hcp = hexagonal close-packed, bcc = body-centered cubic, sh = simple hexagonal, sc = simple cubic, bct = body-centered tetragonal, rh = rhombohedral, bco = base-centered orthorhombic, N = nematic, S = smectic, C = columnar, L = lamellar.

crystal mixtures capped with aliphatic surface ligands. We connect the observed superlattices to the physical concepts underlying the self-assembly of hard shapes (section 5) and soft shapes (section 6). An overview of self-assembled structures obtained for various nanocrystal shapes is provided in Table 2. Due to high chemical potential of high-curvature surfaces, anisotropic nanocrystals typically have rounded or truncated corners. Descriptions of an inorganic core shape as cube, octahedron, and tetrahedron in Table 2 should therefore be understood as slightly truncated/rounded versions of the shape.

7.1. Quasi-Spherical Nanocrystals

Self-assembly of nearly spherical (e.g., cuboctahedral, rhombicuboctahedral, or multiply twinned icosahedral²⁵²) nanocrystals by solvent evaporation often results in the formation of fcc or hcp superlattice thin films. Because superlattice domains are typically oriented with the close-packed plane making contact with the support, fcc and hcp phases are often observed to

assemble with the 3-fold axes parallel to the normal of the thin film. These phases are built up from hexagonally ordered monolayers with ABCA- or ABAB-type overlay pattern (Figure 23a, left and right insets). In line with hard sphere phase expectations, fcc and hcp are most common for particles with surface ligands that make a minimal contribution to total particle volume (small softness value L/R). The small free energy difference between fcc over hcp predicted for hard spheres¹⁷³ appears to be negligible in nanocrystal self-assembly experiments as both phases are commonly produced.

However, fcc and hcp are not always observed with equal probability. Experiments with 5-nm-diameter alkanethiol-capped Ag nanocrystals indicate that evaporation-based assembly from higher-boiling solvents (e.g., octane) favors hcp structure, while lower-boiling solvents (e.g., hexane) typically produce fcc superlattices.²⁵³ Along these lines, it has been hypothesized that solvent flow through the interstitial sites

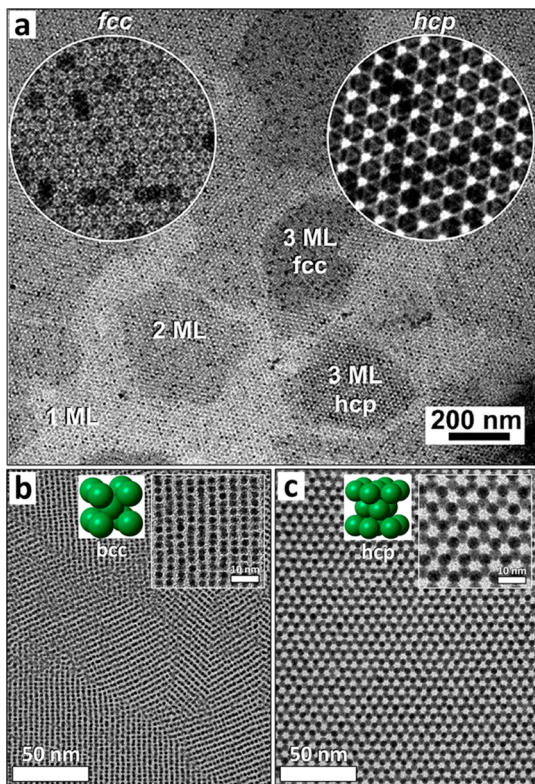


Figure 23. Assembly of quasi-spherical nanocrystals into fcc, hcp, and bcc superlattices. (a) Evaporating a dilute solution of 11 nm CoFe_2O_4 nanocrystals capped with oleic acid surface ligands frequently produces thin films with three or more monolayers (ML) of fcc (left inset) and hcp (right inset) packing arrangements. Adapted from ref 63. Copyright 2010 American Chemical Society. (b) The assembly of Au nanocrystal superlattices depends on the softness parameter L/R . Shown here: [110]-oriented bcc packing of 2.2 nm Au nanocrystals capped with octadecanethiol ligands ($L/R \approx 1$) and (c) [100]-oriented hcp of 4.5 nm Au nanocrystals with the same ligands ($L/R \approx 0.5$). Taken from ref 50.

of close-packed spheres may play a role in favoring fcc packing by directing the third layer of spheres toward the threefold sites open to solvent flux.^{254,255} Furthermore, dipole–dipole interactions between spherical nanocrystals favor antiferroelectric ordering of dipole moments and promote formation of phases that maximize dipolar energy. As a result, the alignment

of such particles along columns with head-to-tail dipole–dipole orientation can stabilize hcp or even simple hexagonal phases over fcc.²⁵⁶

Subtle differences in the shape of quasi-spherical metal nanocrystals influences the presence or absence of orientational registry in self-assembled superlattices. For example, typical syntheses of Au nanocrystals often result in a mixture of single-crystalline (cuboctahedral) and polycrystalline (multiply twinned icosahedral) nanocrystals. Slow destabilization of such colloids results in phase separation of the two components: the more spherical polycrystalline icosahedral nanocrystals assemble into rotationally degenerate fcc superlattices, while the larger facets of crystalline cuboctahedral nanocrystals direct formation of fcc superlattices with orientational registry between Au nanocrystal cores.²⁵⁷ But core–core registry need not result in identical nanocrystal orientations. Detailed structural analysis of fcc superlattices of PbS nanocrystals indicates that particles occupying corner sites of the unit cell can be oriented differently than those occupying the face-centered sites.²⁵⁸

Nanocrystals with significant soft character often assemble into bcc superlattices following the prediction of the soft particle model. The well-established phase behavior of alkanethiol-capped Au nanocrystals, for example, shows a critical softness value that serves to differentiate fcc from bcc forming Au nanocrystals at $L/R \approx 0.7$.²²³ Along these lines, installation of octadecanethiol (C_{18}) chains on 2-nm-diameter spherical Au nanocrystals ($L/R \approx 1$) yields bcc superlattices (Figure 23b), while the same ligands on 5-nm-diameter spherical Au nanocrystals ($L/R \approx 0.5$) yields hcp structures (Figure 23c). Such observations are consistent with the proposition that the geometry of the space available to a particle in the fcc/hcp arrangement deforms surface hydrocarbon chains more significantly than that of the bcc lattice, destabilizing fcc/hcp arrangements of nanocrystals with significant contribution from the soft ligand shell.

7.2. Rod-Shaped Nanocrystals

Rod- and platelet-shaped nanocrystals synthesized by colloidal chemistry approaches enable exploration of the self-assembly behavior of anisotropic particles. Besides the isotropic liquid (random position and orientation) and the crystalline solid (fixed position and orientation), there are two families of mesophases, or states of matter with characteristics of both solid and liquid phases (Figure 24, top). Rod-shaped particles

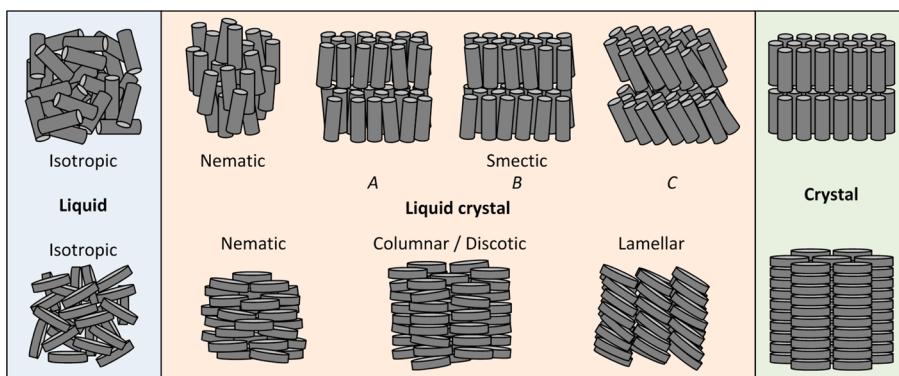


Figure 24. Liquid crystalline phases of rods and disks. Rods (top) and disks (bottom) adopt arrangements with (left to right) random particle position and orientation, ordering of particle orientation only, and ordering of both particle position and orientation. In the smectic B phase, rods remain free to rotate about their long axis. The crystal phase is characterized by orientational registry about all rod axes.

can adopt nematic (random position, fixed orientation) and smectic (fixed position in a plane only, fixed orientation) packings. In close analogy, platelet-shaped disks adopt nematic and discotic columnar (fixed position along one axis only, fixed orientation) mesophases (Figure 24, bottom).

Colloidal chemistry techniques have produced uniform collections of nanorods and nanowires which assemble into a number of ordered structures.^{259,260} For instance, metal (e.g., Au²⁶¹ and Ag²⁶²) nanorods grow from seeds in the presence of cationic surfactant (e.g., cetyltrimethylammonium bromide, CTAB) micelles. In such systems, optimizing surfactant mixtures has proven crucial to suppressing undesired shape byproducts. Exceptional size and shape uniformity of Au nanorods has recently been achieved using CTAB and sodium salicylate,⁵¹ CTAB and sodium oleate,²⁶³ and alkyltrimethylammonium chloride and sodium oleate.²⁶⁴ Furthermore, semiconductor (e.g., CdSe,²⁶⁵ CdSe–CdS²⁶⁶) nanorods can be prepared via high-temperature precursor decomposition in nonpolar solution.²⁶⁷ In this case, rapid monomer incorporation along weakly passivated nanocrystal surfaces induces unidirectional growth along a particular crystallographic axis. More recently, synthetic routes to two-dimensional semiconductor²⁶⁸ (e.g., CdS, CdSe, CdTe) and various oxide and fluoride²⁶⁹ (e.g., UO₂, LaF₃, etc.) nanoplates have been developed.

Evaporating a solution of colloidal nanorods yields superlattices in which the rods are highly aligned but exhibit some disorder in their position of rod centers (Figure 25a,b). Layers of similarly oriented rods (lamellae) often contain hexagonally close-packed rods (smectic B phase). Optical micrographs of nanorod liquid crystals show schlieren textures and disclinations common to conventional organic molecular liquid crystals.²⁷⁰ CTAB-capped Au nanorods sometimes assemble

tip-to-tip in a comparatively open superlattice structure not anticipated by simulations of hard rods. This behavior can be explained by recent *in situ* TEM experiments,²⁷¹ which provided evidence for anisotropic repulsion interaction resulting from reduced charge density at the tips of CTAB-stabilized Au nanorods in water. Self-assembly of uncharged nanorods (e.g., CdSe–CdS dot-in-rods capped with octadecylphosphonic acid, ODPA, ligands) by solvent evaporation produces smectic B superlattice films with either horizontal or vertical alignment (Figure 25c,d) depending on the choice of subphase (section 10.1).²⁵¹ The interplay between hexagonal close-packing within rod lamellae and the hexagonal cross section of wurtzite CdS rods facilitates orientational registry of the rods about their symmetry axes, maximizing cohesive interactions between flat rod faces after solvent evaporation (Figure 25d, inset).

Destabilization of the colloidal solution by nonsolvent addition,⁷³ depletant addition,²⁷² or micelle decomposition^{56,273} offers alternative routes to novel morphologies of rod assemblies. In one notable example, Cao and co-workers demonstrated that CdSe–CdS nanorods capped with ODPA surface ligands and water-solubilized by overcoating with dodecytrimethylammonium bromide (DTAB) surfactants controllably aggregate in ethylene glycol into nearly spherical (Figure 26a–c) or needle-shaped (Figure 26d–f) micrometer-sized colloidal superparticles. Detailed characterization revealed that the superparticles with >80 000 rods are comprised of a central cylindrical domain of close-packed rods (Figure 26c, red rods) capped by two domes (Figure 26c, blue rods). The amount of DTAB present in the aqueous nanorod solution controls the size of superparticles. An embryo growth mechanism was proposed, whereby small rod domains below the critical radius of stable nuclei coalesce into the capped cylinder shape. On the other hand, destabilization of the colloid by gradual diffusion of polar nonsolvent produces platelet-shaped nanorod assemblies (Figure 26d–h). In addition, flat sheets of hexagonally packed nanorods have been prepared by oleic acid addition, triggering nanorod assembly via depletion attraction (Figure 26i).

7.3. Platelet-Shaped Nanocrystals

Thermal decomposition of precursors in coordinating solvents has been applied to prepare two-dimensional nanocrystals (nanoplates) from cadmium chalcogenides²⁶⁸ and rare-earth halides.²⁶⁹ For colloidal nanoplates lacking uniform lateral dimensions, both solvent evaporation and destabilization approaches produce face-to-face stacks of ribbon-like one-dimensional superstructures.^{74,274,275} On the other hand, nanoplates with uniform size and shape, including circles, hexagons, rhombi, ellipses, and tripods, assemble into two- and three-dimensional superlattices. Slow evaporation of dilute solutions of nanoplates at the liquid–air interface induces self-assembly into area-tiling superlattices with the plate *c*-axis perpendicular to the support. Because the plate footprint determines the densest tiling arrangement, varying platelet shape leads to a variety of two-dimensional patterns including hexagonal, square, and rhombic tilings as confirmed by simulation²⁷⁶ and experiment²⁶⁹ (Figure 27a–d).

While entropy is a main driving force in larger, micrometer-sized colloidal plates such as Brownian squares²⁷⁸ and triangles,²⁷⁹ self-assembly of nanometer-sized plates can be understood from maximization of tiling density only to first approximation. For the case of irregular hexagonal DyF₃

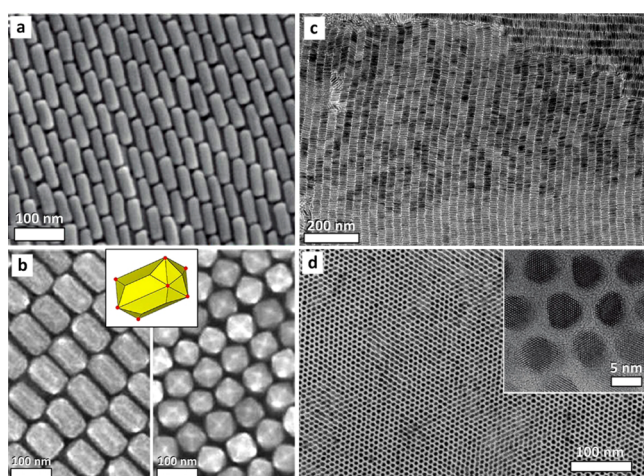


Figure 25. Self-assembly of nanorods. (a, b) SEM images of Au nanorods passivated with CTAB bilayers packed into superlattice with smectic ordering. Adapted from ref 51. Copyright 2012 American Chemical Society. Adapted from ref 263. Copyright 2013 American Chemical Society. (c) TEM overview of CdSe–CdS nanorods (6×28 nm) packed in smectic B superlattices with long axes lying parallel to the support. Adapted from ref 251. Copyright 2015 American Chemical Society. (d) TEM image of CdSe–CdS nanorods packed in smectic B superlattice with long axes perpendicular to the imaging direction. Inset: HRTEM confirms atomic registry of nanorods within the hexagonal packing. Adapted from ref 272. Copyright 2010 American Chemical Society.

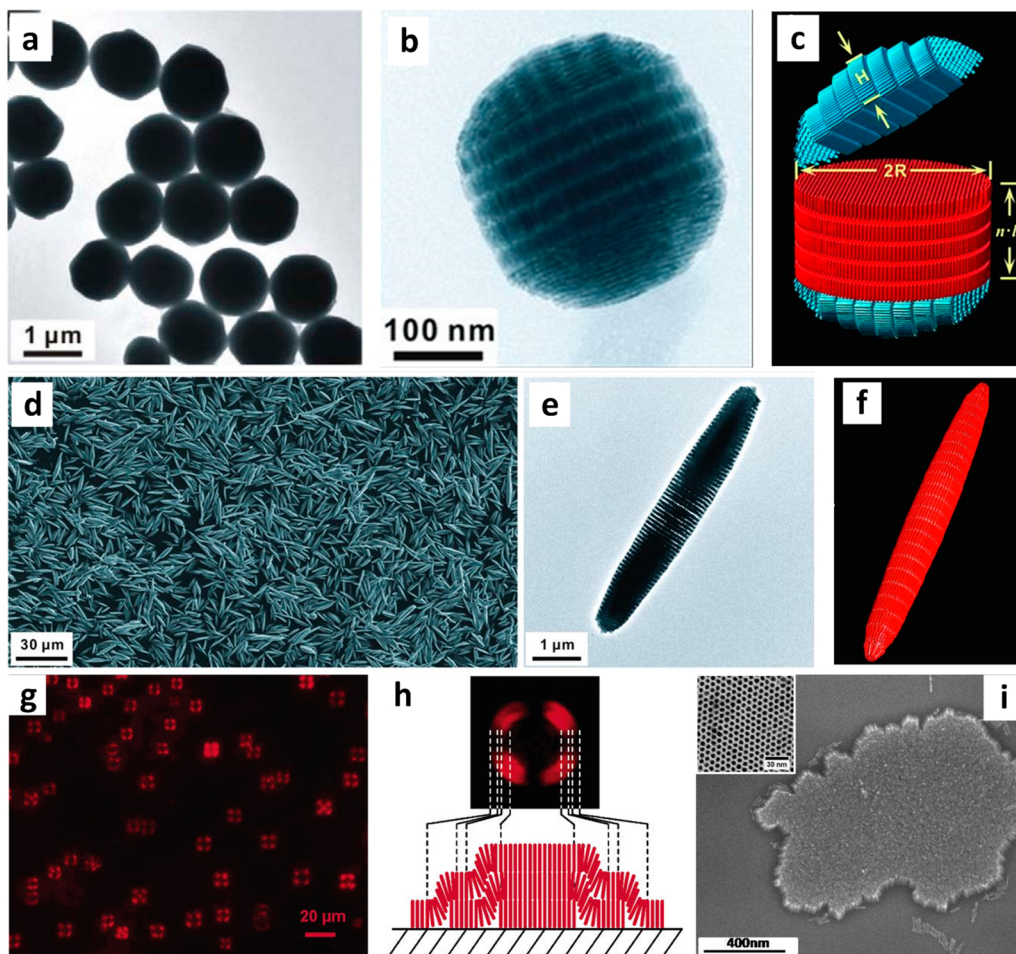


Figure 26. Superlattices formed by destabilization of nanorod colloids. (a) TEM overview of nearly spherical micrometer-sized superparticles comprised of CdSe–CdS dot-in-rods. (b) TEM zoom and (c) model of the superparticle microstructure revealing that rods are packed into a central cylindrical domain capped on either end by a multilayer dome. (d) TEM overview of single-domain elongated needles formed by preferential rod–rod attachment via highly solvophobic tips. (e) TEM zoom and (f) model of superparticle needles. Adapted with permission from ref 56. Copyright 2012 American Association for the Advancement of Science. (g) Destabilization of a CdSe–CdS nanorod solution by nonsolvent addition results in the precipitation of superparticle platelets onto the solid support exhibiting a Maltese cross luminescence pattern when viewed through crossed polarizers. (h) Proposed structure of the nanorod solids consistent with the optical signature. Adapted from ref 73. Copyright 2004 American Chemical Society. (i) Monolayer sheet of vertically oriented CdSe–CdS nanorods precipitated from solution by addition of excess oleic acid. Adapted from ref 272. Copyright 2010 American Chemical Society.

nanoplates, comprised of four (101) edge (“A”) facets at the tips and two (002) side (“B”) facets in the middle, an alternating arrangement resembling the herringbone packing is formed (Figure 27e). Geometric analysis reveals that while the alternating arrangement perfectly tiles a surface at intermediate plate aspect ratio (edge lengths, B/A), the parallel arrangement is area-tiling regardless of aspect ratio (Figure 27f). Because the alternating arrangement never covers a surface more efficiently than the parallel arrangement, this system requires an explanation beyond the entropy-maximizing perspective of efficient polygon packing. In fact, density functional theory calculations presented in the same work revealed that oleic acid surface ligands bind strongly to the (101) tip edge (A) facets and weakly to the (002) middle edge (B) facets. Assuming edge–edge attractions arising from ligand van der Waals interaction after solvent evaporation increases with the number of interacting alkyl chains, in-plane cohesion energy is greater for the alternating plate arrangement that avoids weakly interacting B–B contacts. Indeed, Monte Carlo simulations

incorporating such an edge-specific interaction asymmetry predict a stability range for the alternating arrangement.

In addition to tiling a flat surface, colloidal nanoplates also self-assemble into three-dimensional superlattices. Evaporating a hexane solution of rhombic GdF_3 nanoplates over glycol liquid support yields either columnar or lamellar structures (Figure 27g,h). Both columnar and lamellar plate phases feature face-to-face contacts between plates, an observation that may be rationalized based on Onsager-type entropic arguments as well as maximization of cohesive van der Waals interactions between the plates after solvent drying. One-dimensional lamellar superlattices of triangular Au nanoprisms featuring anomalously large interplate separations have been rationalized by treating the cetyltrimethylammonium bromide surfactant contribution to both attractive depletion forces and repulsive electrostatic forces.²⁸⁰

7.4. Polyhedral Nanocrystals

The body of knowledge collected by Monte Carlo simulations of phase behavior of hard polyhedra (Figure 18) serves as a logical starting point for considering the self-assembly of highly

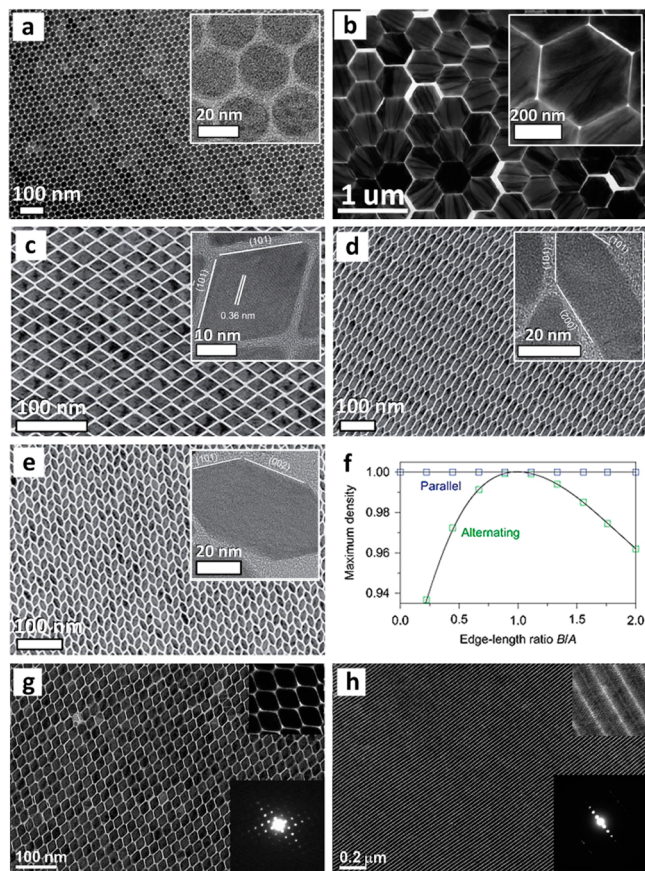


Figure 27. Two- and three-dimensional nanoplate superlattices. (a) TEM image of a two-dimensional hexagonal superlattice comprised of 20 nm diameter circular LiF₃ nanoplates. Insets: zoom of the plates. Adapted from ref 277. Copyright 2015 American Chemical Society. (b) TEM image of a hexagonal superlattice of hexagonal NaYF₄ nanoplates. Adapted with permission from ref 269. Copyright 2010 National Academy of Sciences. (c, d) TEM images of a rhombic superlattice of rhombohedral DyF₃ and irregular hexagonal EuF₃ nanoplates. (e) TEM overview of an alternating two-dimensional arrangement of DyF₃ nanoplates. The relative length of the (101) and (002) facets (A and B edges, respectively) determines the plate aspect ratio, B/A. (f) Area tiling fraction for parallel (blue) and alternating (green squares) plate arrangements for various aspect ratios. Adapted with permission from ref 93. Copyright 2013 Nature Publishing Group. (g, h) TEM images of columnar and lamellar three-dimensional nanoplate superlattices. Insets: zoomed TEM images in top left; small-angle electron diffraction pattern in bottom right. Adapted from ref 53. Copyright 2011 American Chemical Society.

faceted colloidal nanocrystals with regular polyhedral shape. Maximization of translational entropy in solution and interparticle cohesion after solvent evaporation both favor formation of dense polyhedron packings with a preference for face-to-face contacts. Rotational entropy, on the other hand, favors structures that assemble polyhedra in many orientations but leave space for particle reorientations. Indeed, Yang and co-workers demonstrated that 500 nm Ag polyhedra with adsorbed poly(vinylpyrrolidone) (PVP) ligands sediment from methylformamide (good solvent for PVP) under gravity (Figure 28a–c) to form densest packings known for cubes, cuboctahedra, and octahedra (Figure 28d,e). Similarly, 10 nm cubes of semiconductor,²⁸¹ metal,^{282,283} and metal oxide^{55,284} materials form close-packed arrangements with face-to-face contacts and cubic superlattice symmetry. Metal oxide

octahedra (edge length about 35 nm) assemble into the densest packing available to the shape,²⁵⁰ and metal oxide tetrahedra with similar edge lengths also readily establish face-to-face contacts.²⁸⁵ Even highly complex phases like the network phase isostructural with high-pressure lithium found for weakly rounded octahedra⁶⁸ (Figure 9b) can be explained within the hard particle model.¹⁸³

However, the entropy maximization principle is not sufficient to predict the self-assembly behavior of smaller particles. Octahedra and tetrahedra with comparatively short edge lengths on the order of 10 nm show phase behavior distinct from the expectations set by hard-particle studies and distinct from observed superlattices of analogous particles with size on the order of 100 nm. CdSe tetrahedra¹¹⁰ (Figure 29a,b) and Pt₃Ni octahedra²⁴⁹ (Figure 29c,d) in this size regime form superlattices with tip-to-tip contacts. Such tip-to-tip contacts preserve avoidable void space in the lattice, which is disfavored for hard object packings.

The superlattices of smaller polyhedral nanocrystals can be rationalized by considering the influence of surface curvature on repulsive ligand–ligand interactions during evaporation-based self-assembly. As nanocrystals are condensed into a small volume of solvent, overlapping ligand coronas experience unfavorable accumulation of hydrocarbon segments. The resulting repulsion energy depends on the geometry of the nanocrystal contact (Figure 29e). Overlap of face-bound ligands results in stronger spatial concentration of chain segments than overlap of ligands tethered to curved nanocrystal surfaces (Figure 29f). Accordingly, the osmotic penalty associated with unfavorable exclusion of good solvent gives rise to a significant difference in per-chain repulsion energy between face- and vertex-bound ligands (Figure 29g) favoring contact between nanocrystal tips in the crowded assembly solution. Besides this energetic argument, the effective rounding of vertices and edges decreases the facet area that can be in contact, weakening directional entropic forces.²⁰⁹ In addition, the sacrifice of two of the three rotational degrees of freedom upon establishment of face–face contacts further penalizes arrangements incorporating such geometry. Energetic and entropic factors can thus favor superlattice structures not anticipated by hard polyhedron packing arguments.

Just as in the case of rods (Figure 26b), application of the destabilization approach to assembling polyhedral nanocrystals leads to an intriguing set of superlattice shapes from nanocrystals with cubic, rectangular, rhombic dodecahedral, octahedral, and truncated octahedral core geometries.^{284,286,287} For example, aqueous precipitation of 40 nm polyhedral Au nanocrystals passivated with alkylammonium halide surfactant bilayers results in micrometer-sized superlattices with morphology that varies systematically with nanocrystal shape.²⁸⁸

7.5. Branched and Multicomponent Nanocrystals

Branched structures are yet another shape accessible to colloidal nanocrystals. CdSe–CdS tetrapods, for example, have been prepared by growth of four CdS arms extending from zinc blende phase CdSe seeds.²⁶⁶ Despite the prediction of stable liquid crystalline tetrapod phases,²⁸⁹ only disordered networks have been reported,²⁹⁰ perhaps because these nanostructures are susceptible to jamming at high densities.

On the other hand, CdSe–CdS branched octapods (eight arms) readily form superlattices under both evaporation- and destabilization-based self-assembly conditions. This unique nanocrystal morphology developed by Manna and co-workers

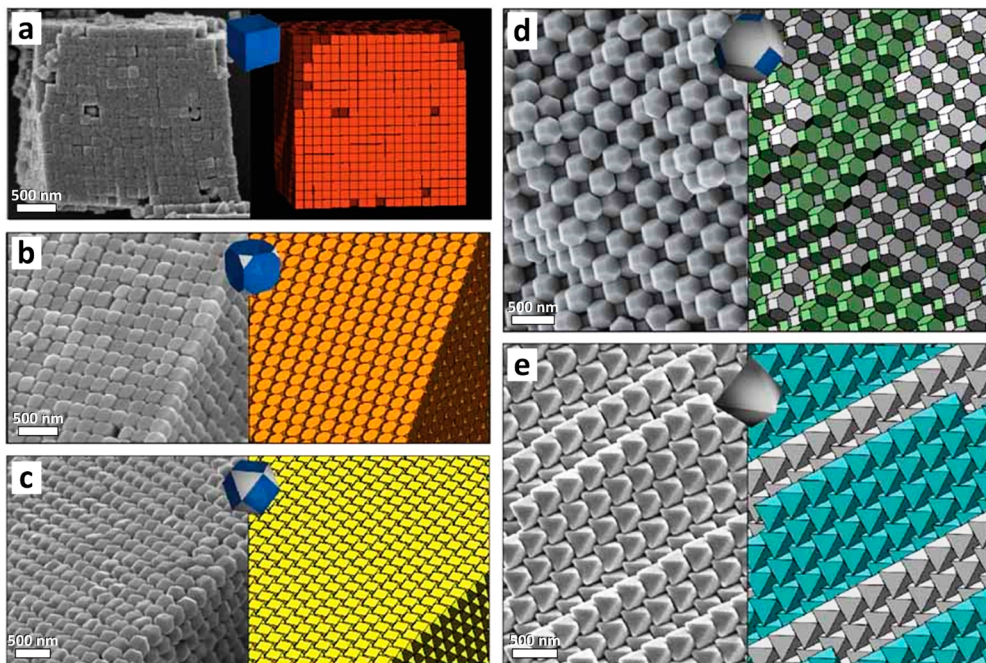


Figure 28. Self-assembly of densest polyhedron packings by gravitational sedimentation of polymer-stabilized, 500 nm Ag nanocrystals. (a–e) SEM images (left) and modeled structures (right) of dense polyhedron (cube, truncated cube, cuboctahedron, truncated octahedron, octahedron) packings. Adapted with permission from ref 68. Copyright 2011 Nature Publishing Group.

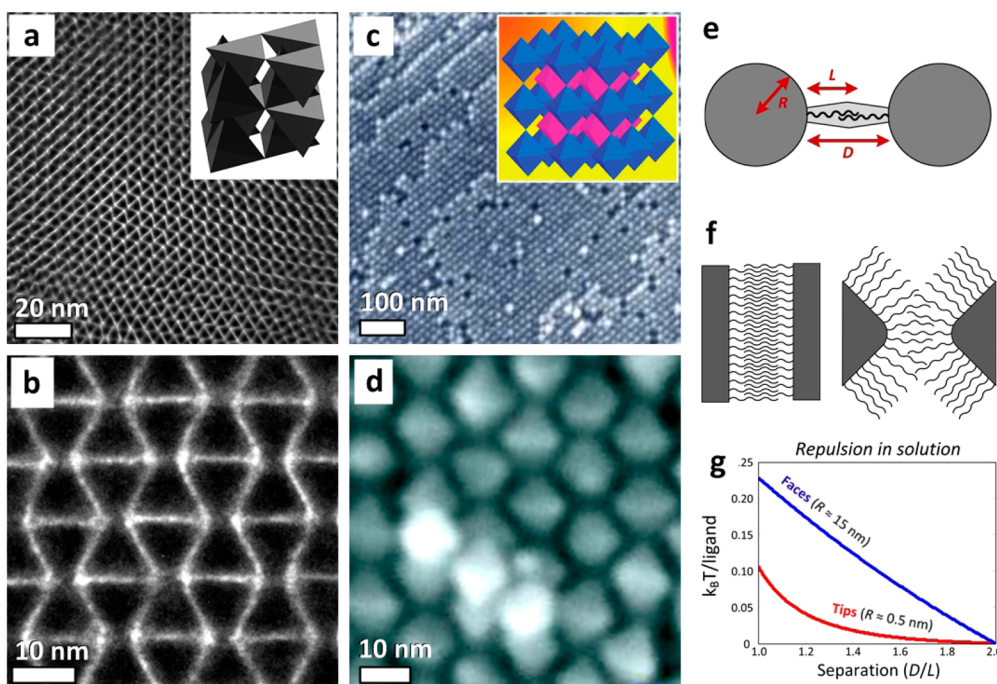


Figure 29. Open superlattices from polyhedral nanocrystals. (a) TEM image and (b) zoom of a superlattice of 10 nm tetrahedral CdSe nanocrystals capped with oleic acid ligands. Inset: modeled structure revealing contacts between tetrahedron tips. Adapted from ref 110. Copyright 2014 American Chemical Society. (c) SEM image and (d) zoom of a superlattice of about 10 nm octahedral Pt₃Ni nanocrystals capped with oleylamine ligands. Inset: modeled bcc packing featuring similar tip-to-tip contacts. Adapted from ref 249. Copyright 2011 American Chemical Society. (e) Sketch of the axial steric ligand interaction showing key parameters, surface curvature R , and extent of ligand overlap D/L . (f) Spatial overlap between the ligands involved in face–face (left) and tip–tip (right) contacts. (g) Osmotic repulsion calculated for the overlap of two ligands tethered to highly curved (red) or nearly flat (blue) nanocrystal surfaces. Adapted from ref 110. Copyright 2014 American Chemical Society.

has been achieved by transforming Cu_{2-x}Se seeds into the CdSe phase via cation exchange followed by overgrowth of CdS arms.²⁹¹ Colloidal octapods (60 nm center-to-tip distance, Figure 30a) are well-dispersed in chloroform but slowly form

interlocked linear oligomers with neighboring octapods mutually rotated by 45° (Figure 30b) in toluene. Upon addition of acetonitrile, octapods form long chains that subsequently pack into three-dimensional superlattices with

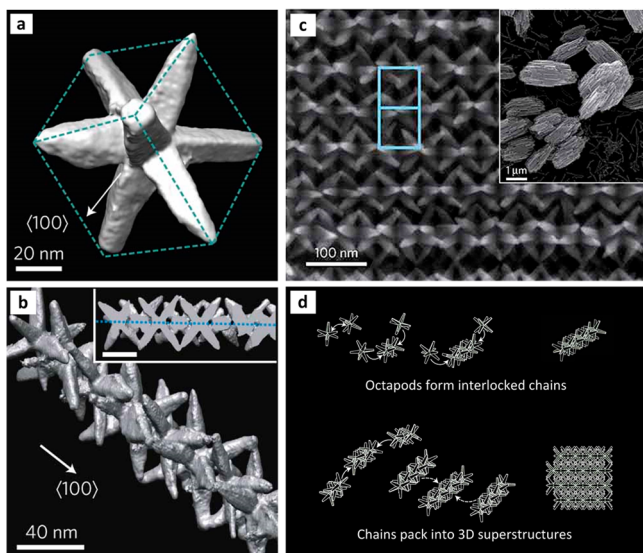


Figure 30. Hierarchical assembly of branched CdSe/CdS octapods into three-dimensional superlattices by colloid destabilization. (a) STEM reconstruction of a single branched nanocrystal (octapod). (b) Reconstruction of a chain of octapods revealing interlocking along the 4-fold direction. Scale bar, 40 nm. (c) SEM image of chain aggregates with half unit cells shown in blue. Inset, large-area SEM image with micrometer-scale aggregates. (d) Proposed mechanism of the octapod assembly. Chains form in toluene and aggregate upon nonsolvent addition. Adapted with permission from ref 54. Copyright 2011 Nature Publishing Group.

tetragonal crystal structure (Figure 30c,d).⁵⁴ The authors rationalize the one-dimensional octapod self-assembly via interlocked pair configuration by noting that the structure maximizes ligand cohesive interactions in the absence of good solvent. This nucleation and growth mechanism was subsequently confirmed by *in situ* TEM experiments.⁹⁰ Evaporation of the octapod solution over a solid support, in contrast, yields two-dimensional octapod assemblies. In this case, four of eight pods make contact with the substrate in a square lattice, an observation that has been rationalized by excluded volume interactions between octapods.²⁹² When drop-cast from solvent containing 1% by volume of polymer (poly(methyl methacrylate), PMMA, 120 kDa), only one of eight pods makes contact with the substrate, yielding hexagonally ordered monolayers partially embedded in the polymer melt.²⁹³

The CdSe–CdS branched nanocrystals highlighted above and the well-studied core–shell morphology are an example of nanoheterostructures featuring two or more chemical components joined within a single particle.^{294,295} Such mixed compositions, accessible by overgrowth²⁹⁶ or partial cation exchange,²⁹⁷ offer new approaches to nanocrystal assembly. For instance, semiconductor rods and tetrapods may be linked together by coalescence of Au domains localized at their tips.²⁹⁸ CdSe rods with a single Au tip form multiarmed star-like structures and elongated objects,²⁹⁹ while the same rods with two Au tips assemble side-by-side into smectic layers.³⁰⁰ Future work to improve size and shape uniformity of the starting material may enable self-assembly of extended arrays of complex nanocrystals mediated by interaction between distinct chemical components, possibly with chemically distinct ligand shells on each component.

7.6. Sphere + Sphere Nanocrystal Mixtures

In addition to superlattices formed by self-assembly of size- and shape-uniform nanocrystals, cocrystallization of two nanocrystal species is also possible.³⁰¹ Micrometer-sized spherical colloids have been shown to assemble, depending on size ratio, into a few phases of three-dimensional^{302,303} and two-dimensional^{304,305} binary superlattices that may be rationalized based on sphere packing principles. As in the case of octahedra (section 7.4), however, simple hard-shape phase behavior observed for micrometer-sized particles gives way to more complex superlattice structures at the sub-20-nm length scale. Along these lines, Murray and co-workers observed more than 15 unique binary nanocrystal superlattices (BNSLs) by evaporating a solution containing two sizes of quasi-spherical nanocrystals about a decade ago.¹⁴² Since then, the number of unique binary structures has continued to grow. Recent additions are a quasicrystalline BNSL,^{94,306} one isostructural with C₆₀K₆ (also called bcc-AB₆),³⁰⁷ one with A₆B₁₉ stoichiometry,⁸⁴ and the Li₃Bi structure.⁴⁹ More recent variations on this theme include ternary nanocrystal superlattices,⁸² two-dimensional BNSLs,³⁰⁸ BNSLs assembled from polystyrene-capped nanocrystals,⁴⁶ and BNSLs incorporating polyoxometallate clusters.³⁰⁹ Such diversity is often observed even within a single sample, which may present a few different binary structures together with phase-separated domains (e.g., AB_m + AB_n + fcc_A + fcc_B). In Figure 31 we show 16 unique BNSL structures assembled from quasi-spherical hydrocarbon-capped nanocrystals, and in Table 3 we tabulate, to the best of our knowledge, all binary structures observed to date.

Although the stability of some BNSL phases (e.g., NaCl, AlB₂, C₆₀K₆) can be rationalized as dense packings of a mixture of two sizes of spheres, most structures observed to date have lower sphere packing density as compared to the phase-separated fcc_A + fcc_B alternative (Figure 32). The treatment of nanocrystal self-assembly as a packing problem is exact only in the high-pressure limit, however. At finite pressure (i.e., intermediate particle volume fractions), the configurational contribution to total system entropy can stabilize lower-density phases with large and complex unit cells such as NaZn₁₃ and MgZn₂ (section 5.3). Thus, if the observed (dry) BNSL structures are a reflection of the stable phase in the colloidal (wet) crystal, only those with density above approximately 0.65 might be rationalized based on hard-sphere interactions.

Particularly for sub-10-nm nanocrystals, the application of packing arguments is further complicated by the presence of the hydrocarbon ligand shell. The ligand shell, which can make a significant contribution to the total particle size, can be accounted for by taking the effective size ratio to be the quotient of the effective diameters of large and small nanocrystals measured from center-to-center separations in phase-separated, close-packed films. The experimentally observed effective size ratio can be compared to the size ratio calculated as

$$\gamma_{\text{eff}} = \frac{D_B + 2L_B}{D_A + 2L_A} \quad (10)$$

where D_A (L_A) and D_B (L_B) are the core diameters (effective ligand thicknesses) of large and small nanocrystals, respectively.⁴⁹ However, even with this adjustment, experimental data conflicts with the stability range predicted from the hard sphere model. For example, NaZn₁₃ and MgZn₂ structures are observed across radius ratio ranges (0.46 < γ_{eff} < 0.74 and

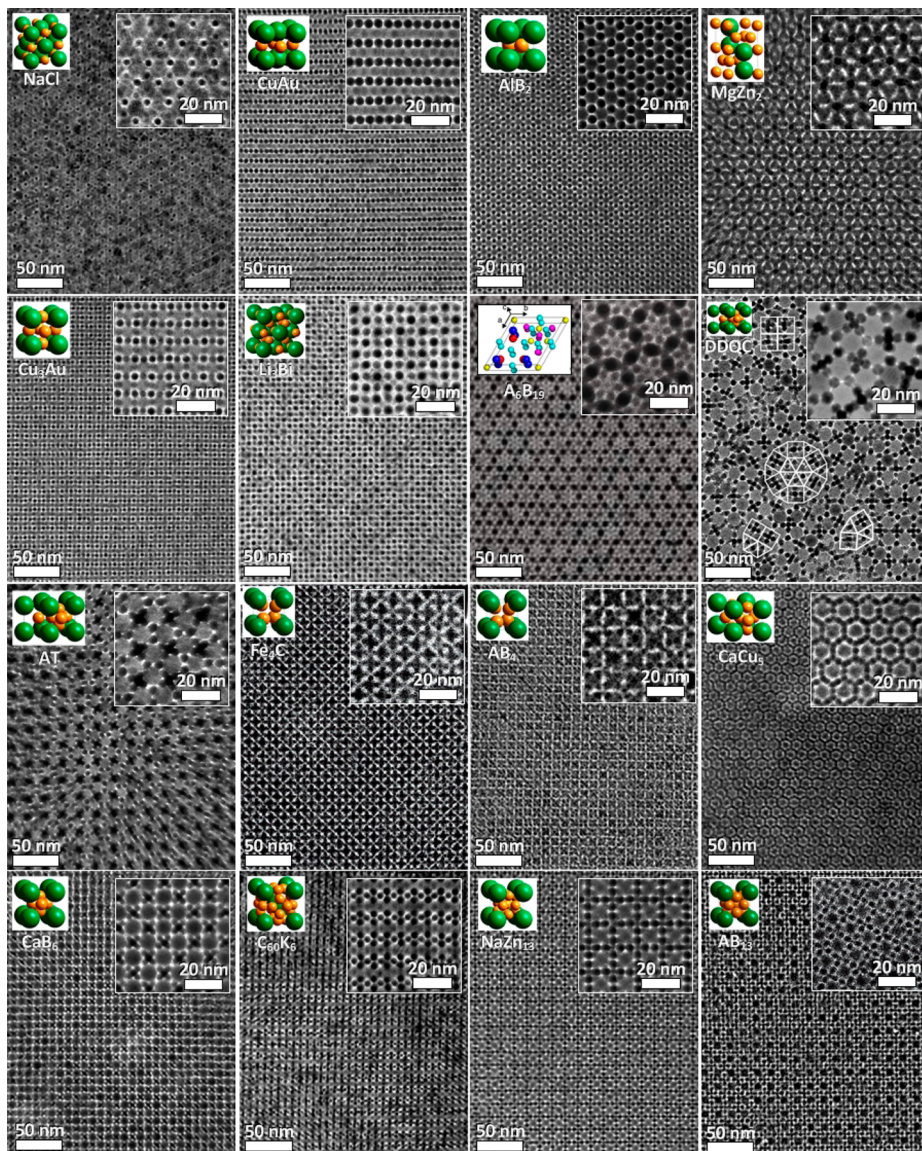


Figure 31. Assembly of a mixture of spherical nanocrystals with two sizes produces a wide range of binary superlattice structures. Each image shows large-area TEM overview of a structure. Inset: unit cell structure (left) and TEM zoom (right). Taken from ref 50. Adapted from ref 84. Copyright 2013 American Chemical Society. Adapted with permission from ref 94. Copyright 2009 Nature Publishing Group. Adapted from ref 310. Copyright 2006 American Chemical Society. Adapted from ref 62. Copyright 2010 American Chemical Society. Adapted from ref 311. Copyright 2005 American Chemical Society.

$0.65 < \gamma_{\text{eff}} < 0.81$, respectively, Figure 32b). These ranges lie outside the boundaries for which these hard sphere phases are predicted^{155,196} to be stable ($0.54 < \gamma < 0.61$ and $0.76 < \gamma < 0.84$, respectively).

It is tempting to explain the discrepancy between experimental BNSL phases and hard sphere predictions by considering the nanocrystal ligand corona. For example, particle tracking measurements of single-component and binary nanocrystal arrays reveal changes in the effective capping layer thickness for nanocrystals in various coordination environments.⁴⁹ From this data it was concluded that a difference in hydrocarbon segment density across asymmetric brush contacts leads to corona deformation. The deformation allows the softer component to fill space more efficiently than a rigid sphere placed in the same lattice site, increasing the density of the binary structure beyond that possible within the hard sphere approximation. Furthermore, unanticipated BNSL

structures may also incorporate area-minimizing character (section 6) that minimizes elastic deformation of surface-bound hydrocarbon chains by providing particles with more spherical Voronoi cells than those offered by the set of densest sphere packings. Indeed, the observation of tetrahedrally close-packed (tcp) structural motifs in several common BNSLs including Frank–Kasper MgZn₂ and pseudo-Frank–Kasper CaCu₅ and NaZn₁₃ phases is an indication that there exists some area-minimizing component to BNSL assembly.

Thermodynamic calculations confirm that short-range, soft repulsive potentials enrich the phase diagram beyond that of hard spheres by stabilizing many common BNSL phases including AlB₂, MgCu₂, CaCu₅, C₆₀K₆, and NaZn₁₃.²³⁵ Such soft repulsive potentials, explored in detail as effective interactions for star polymers and other soft matter systems,³¹⁵ mimic ligand–ligand steric interactions well.

Table 3. Overview of Self-Assembled Multicomponent Superlattices from Quasi-Spherical Nanocrystals (NCs) with Hydrocarbon Capping Ligands^a

structure	NC A: core, ligands	NC B: core, ligands	effective size ratio	ideal size ratio (packing density)	other notes	lit. example
NaCl	13.4 nm Fe ₂ O ₃ , C ₁₈	5.0 nm Au, C ₁₂	0.43	0.41 ($\phi = 0.79$)	B NCs in fcc octahedral voids	ref 310
AB orthorhombic	5.8 nm PbSe, C ₁₈	3.0 nm Pd, C ₁₂	0.55		pseudo-Frank–Kasper	ref 310
A ₂ B ₃	11.2 nm Fe ₃ O ₄ , C ₁₈	6.4 nm Au, C ₁₂	0.59		bilayer binary phase	ref 308
CuAu	7.0 nm PbS, C ₁₈	4.1 nm Au, C ₉	0.62	0.74 ($\phi = 0.73$)	NC _A orientational registry	ref 49
AB	16.5 nm Fe ₃ O ₄ , C ₁₈	6.4 nm Au, C ₁₂	0.43	0.41 ($\sigma = 0.92$)	monolayer	ref 308
AlB ₂	15.0 nm Fe ₃ O ₄ , C ₁₈	6.0 nm FePt, C ₁₈	0.44	0.52 ($\phi = 0.76$)	B NCs in trigonal prismatic voids	ref 64
AB ₂	16.5 nm Fe ₃ O ₄ , C ₁₈	3.1 nm FePt, C ₁₈	0.24	0.17 ($\sigma = 0.95$)	monolayer	ref 308
ABC ₂	(A) 16 nm, (B) 7.0 nm Fe ₃ O ₄ , C ₁₈	(C) 3.1 nm FePt, C ₁₈	0.46, 0.24		ternary bilayer phase	ref 308
MgZn ₂	7.8 nm PbSe, C ₁₈	5.8 nm CdSe, C ₈	0.75	0.81 ($\phi = 0.72$)	Frank–Kasper phase	ref 312
Cu ₃ Au	5.8 nm PbSe, C ₁₈	3.4 nm Ag, C ₁₂	0.64	0.41 ($\phi = 0.63$)	NC _A orientational registry	ref 310
Li ₃ Bi	10.2 nm Fe ₂ O ₃ , C ₉	4.1 nm Au–C ₁₈	0.56	0.21 ($\phi = 0.76$)	B NCs in fcc tetr and oct voids	ref 49
AB ₃	16.5 nm Fe ₃ O ₄ , C ₁₈	6.0 nm FePt, C ₁₈	0.44		binary bilayer phase	ref 308
A ₆ B ₁₉	6.5 nm PbSe, C ₁₈	3.4 nm CdSe, C ₈	0.67	0.63 ($\phi = 0.69$)	A NCs in Kagome layers	ref 84
DDQC (AB _{3.86})	13.4 nm Fe ₂ O ₃ , C ₁₈	5.0 nm Au, C ₁₂	0.43	0.42 ($\phi = 0.72$)	quasicrystal with AlB ₂ , CaB ₆ units	ref 94
3.4.3 ² .4 (AB ₄)	13.4 nm Fe ₂ O ₃ , C ₁₈	5.0 nm Au, C ₁₂	0.43	0.42 ($\phi = 0.72$)	crystal tiling with AlB ₂ , CaB ₆ units	ref 94
Fe ₄ C	5.8 nm PbSe, C ₁₈	3.0 nm Pd, C ₁₂	0.55		tetrahedral B-clusters	ref 310
AB ₄	7.7 nm PbSe, C ₁₈	3.4 nm Pd, C ₁₂	0.53		alternating B-tetrahedra	ref 62
ABC ₄	(A) 12 nm, (B) 7.9 nm PbSe, C ₁₈	(C) 5.8 nm CdSe, C ₈	0.65, 0.48		three-dimensional ternary phase	ref 82
CaCu ₅	7.0 nm CdTe, C ₁₈	4.4 nm CdSe, C ₁₈	0.71	0.65 ($\phi = 0.70$)	pseudo-Frank–Kasper phase	ref 313
CaB ₆	13.4 nm Fe ₂ O ₃ , C ₁₈	5.0 nm Au, C ₁₂	0.43	0.41 ($\phi = 0.75$)	octahedral B-clusters	ref 310
C ₆₀ K ₆	14.0 nm Fe ₃ O ₄ , C ₁₈	4.6 nm Au, C ₁₂	0.40	0.28 ($\phi = 0.76$)	B-occupied bcc tetrahedral voids	ref 307
NaZn ₁₃	11.0 nm Fe ₂ O ₃ , C ₁₈	6.0 nm PbSe	0.55	0.56 ($\phi = 0.74$)	pseudo-Frank–Kasper phase	ref 314
AB ₁₃	5.8 nm PbSe, C ₁₈	3.0 nm Pd, C ₁₂	0.55	0.57 ($\phi = 0.70$)	cuboctahedral B-cluster	ref 311

^aSuperlattices are ordered by stoichiometry from equal composition (AB) to significant surplus of the small species (AB₁₃). In columns 2 and 3, core material and diameter are listed. Ligands are described by length of hydrocarbon chains (e.g., oleic acid is C₁₈, dodecanethiol is C₁₂, etc.). In column 4, effective size ratio includes the ligand shell. In column 5, ideal size ratio is defined as the size ratio that maximizes density for the structure. Sphere packing fraction ϕ (or disk packing fraction σ for two-dimensional superlattices) values are provided in parentheses. In column 6, Frank–Kasper phases feature only tetrahedral voids. Pseudo-Frank–Kasper phases feature only tetrahedral voids between B nanocrystals.

Energetic interactions between particles may also contribute to formation of BNSL structures unanticipated for systems dominated by hard-sphere phase behavior. For example, self-assembly of PbSe and Pd nanocrystals from solutions between –20 and 85 °C was observed to produce seven different BNSLs across the temperature series.⁶² In this study, the BNSLs observed at low temperatures frequently incorporated clusters of metal nanocrystals (e.g., CaCu₅, NaZn₁₃), suggesting that cocrystallization under such conditions proceeds by integration of preassembled clusters of strongly interacting metal nanocrystals. In addition, electrostatic charging has also been implicated as a potential source for rich binary phase behavior.^{142,316} Indeed, complex binary structures reminiscent of BNSLs were observed in ionic colloidal crystals of oppositely charged particles,³¹⁷ and similarly rich binary phase diagrams have been calculated with addition of electrostatic interactions between nanocrystals.³¹⁶ Even so, the poorly screening nonpolar solvents in which hydrocarbon-capped nanocrystals are prepared and assembled (e.g., octadecene, octane, toluene, etc.) should be an unlikely environment to observe charge separation.

The preceding analysis reveals that, 10 years after its revelation, the surprising structural diversity of BNSLs has yet to be fully explained. Nevertheless, progress has been made toward uncovering potential sources of counterintuitive phase behavior including ligand corona deformability, elastic preference for area-minimizing lattices, and kinetic integration of preformed clusters. Combining any or all of the above effects with established principles of hard-sphere crystallization may be necessary to achieve de novo BNSL structure prediction.

7.7. Nanocrystal Shape Mixtures

The investigation of nanocrystal cocrystallization naturally extends to mixtures of nanocrystal shapes. Several permutations of shape alloys are possible, including spheres with rods,¹⁹⁹ spheres with plates,⁵³ rods with plates,²⁷⁷ plates with plates,^{318,319} and octopods with spheres.³²⁰ In several of these examples, cocrystallization is observed at size ratios for which phase separation could yield denser packing. For example, a system of hard spheres and hard rods is expected to phase separate at intermediate density,^{197,198} as observed in mixtures of cellulose nanorods and latex nanospheres,³²¹ but is nevertheless observed in experiment (Figure 33a–d). To replicate experimental miscibility, rod–sphere attraction must

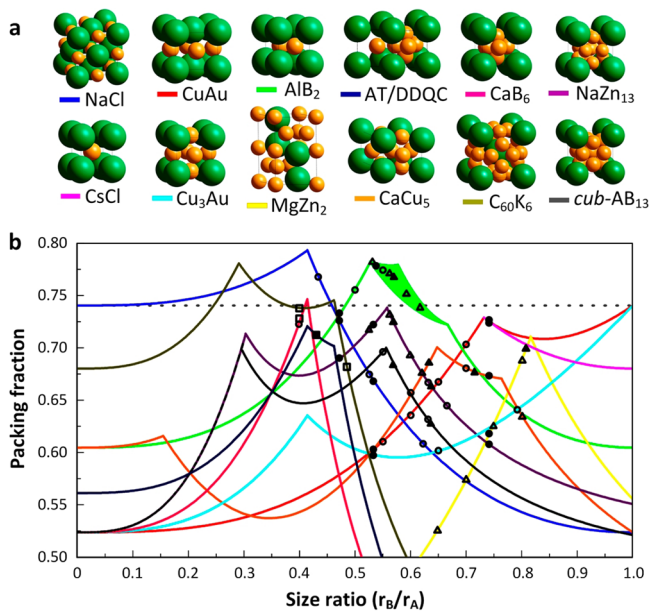


Figure 32. Structural diversity of binary nanocrystal superlattices and low packing density predictions. (a) Models of 12 commonly observed binary phases showing larger A-spheres in green and smaller B-spheres in orange. (b) Plot of packing fraction versus size ratio for spheres packed in these arrangements. Overlay: data points for phases observed in BNSL studies using the reported effective size ratios. Most observed BNSLs are open arrangements with lower density than close-packed monodisperse hard spheres (dotted line). Works cited: ○, ref 310; ●, ref 62; □, ref 307; ■, ref 94; △, ref 312; ▲, ref 313. Figure adapted from ref 49. Copyright 2015 American Chemical Society.

be incorporated into Monte Carlo simulations to extend the stability of the AB₂ binary crystal to conditions present during self-assembly in experiment.⁸⁹ The rod-with-disk shape mixture also forms binary superlattices, with size ratio setting the stoichiometry (either AB, AB₂, or AB₆) of resulting structures (Figure 33e–h),²⁷⁷ as anticipated by construction of dense circle tilings. Similarly, efficient packing explains cocrystallization of shape-complementary pairs of nanoplates with complementary surface curvature elements (Figure 33i–k).³¹⁸

8. DEFECTS IN NANOCRYSTAL SUPERLATTICES

In a perfect crystal the radial distribution function, or probability that the unit (atom, molecule, nanocrystal, bead, etc.) will be found at distance r from any other, is a periodic array of delta functions, indicating that order is deterministic and units are fixed at definite locations. In practice, however, thermal motion and crystal defects contribute structural disorder to crystals. The presence of defects increases the enthalpy H of the solid, since energy input is required to break bonds and accommodate strain. However, such defect incorporation can lower the total Gibbs free energy G of the solid by increasing configurational entropy S . As a result, free energy is minimized at finite temperature for nonzero defect concentration (Figure 34a).

The considerable effort recently invested in understanding the binary phase behavior of colloidal nanocrystals^{49,62,310} has created as a byproduct an extensive TEM library of BNSLs. Such images, in contrast to ensemble-level (i.e., scattering) data, provide microstructural information and serve as a convenient platform for the systematic characterization of defects in

nanocrystal superlattices,³²² mimicking the behavior of atomic and molecular crystals. Based on this analogy, four defect categories describe superlattice crystallographic imperfections according to the dimensionality of the defect region: point defects (zero-dimensional), line defects (one-dimensional), planar defects (two-dimensional), and volume defects (three-dimensional).

8.1. Zero-Dimensional Defects: Vacancies, Interstitial and Substitution Sites

Point defects cover a range of imperfections occurring at one point. They are by far the most common defects observed in BNSLs. A vacancy describes one missing nanocrystal (Figure 34b, “1”; Figure 34c), an interstitial defect is the insertion of a nanocrystal into a site not normally filled by the lattice (Figure 34b, “2”; Figure 34d), and substitutional defects involve the occupation of a lattice site by a different nanocrystal species (Figure 34b, “3” and “4”; Figure 34e).

8.2. One-Dimensional Defects: Dislocations, Disclinations, and Vortices

Line defects fall under the categories of dislocation or disclination. They are topological defects breaking translational symmetry (dislocation) or rotational symmetry (disclination) of the crystal. The line defects shown in Figure 35 run perpendicular to the imaging plane, and thus appear as a point in these two-dimensional projections.

The magnitude and direction of a dislocation is uniquely and unambiguously characterized by the Burgers vector, which corresponds to the additional translation required to complete a circuit around the dislocation line (red arrows, Figure 35a,b). The dislocation energy per unit length scales with the square of the Burgers vector magnitude. Depending on the orientational relationship between the direction of the Burgers vector and the dislocation line, one distinguishes edge dislocations (Burgers vector perpendicular to dislocation line) and screw dislocations (Burgers vector parallel to dislocation line). An edge dislocation is effectively the insertion of a half-plane into the lattice (Figure 35b). The formation of periodic arrays of half-planes inserted in BNSLs reflects the ability of such defects to relieve strain in superlattice domains growing at the curved solvent meniscus,³²³ similar to the stress relief on curved surfaces provided by grain boundary scars in spherical crystallography.^{324,325} Screw dislocations are difficult to observe in TEM, but can be recognized in SEM as an adlayer that appears to bury itself into a smooth surface (Figure 35c, bottom).

Disclinations effectively involve the insertion (or removal) of a wedge into (from) the lattice. Disclination strength, analogous to Burgers vector magnitude, is the extent to which a vector aligned along one of the crystallographic directions is rotated upon parallel transport along a closed path around the disclination (Figure 35d). Disclinations in a hexagonal array, for example, result in a point with 5-fold (−1) or 7-fold (+1) rotational symmetry, which often exist as tightly bound pairs in BNSLs (Figure 35e). In addition, superlattices comprised of anisotropic nanocrystals can contain additional defects resulting from the orientation of particles. For example, the vortex defect structure observed in liquid crystals^{326,327} and colloidal nanorods²⁵¹ (Figure 35f) results from violation of rotational symmetry featuring rod director varied around the defect center in a left- or right-handed fashion.

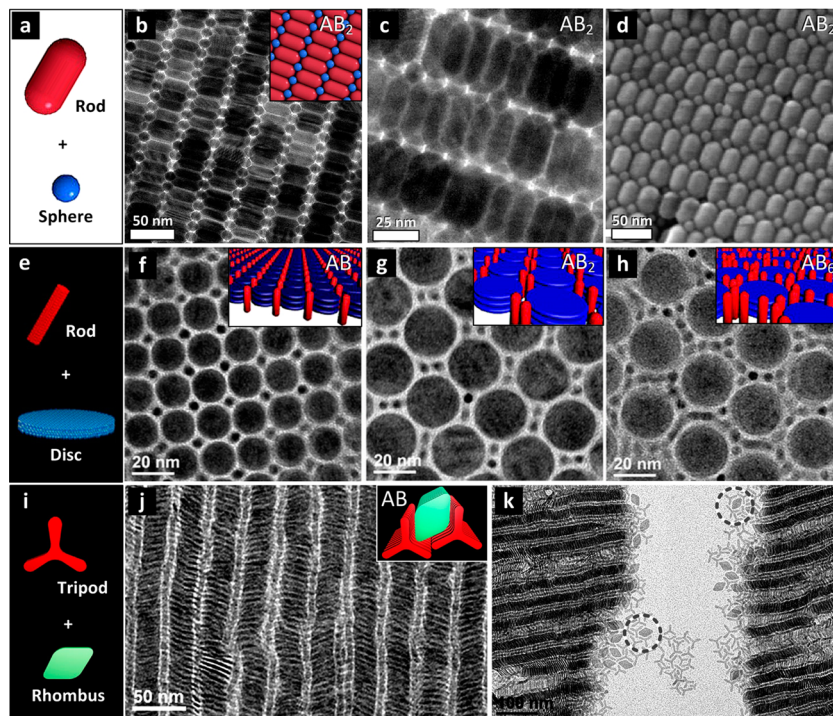


Figure 33. Shape alloy binary superlattices. (a) Evaporating a solution containing NaYF_4 rods and Fe_3O_4 spheres yields AB_2 binary superlattices revealed by (b, c) TEM and (d) SEM images. Inset: modeled shape alloy structure. Adapted from ref 199. Copyright 2013 American Chemical Society. (e) The same approach using CdSe/CdS rods and LaF_3 disks yields (f) AB , (g) AB_2 , and (h) AB_6 binary solids, depending on disk footprint size ratio, as shown by TEM images. Insets: modeled structures. Adapted from ref 277. Copyright 2015 American Chemical Society. (i) Flat tripod-shaped Gd_2O_3 and rhombus-shaped GdF_3 nanoplates cocrystallize into binary arrays as revealed by TEM zoom in (j). Inset: model showing complementarity of the shape alloy. (k) TEM overview of the tripod–rhombus shape alloy shows nanocrystals bound as complementary pairs (circled). Adapted from ref 318. Copyright 2015 American Chemical Society.

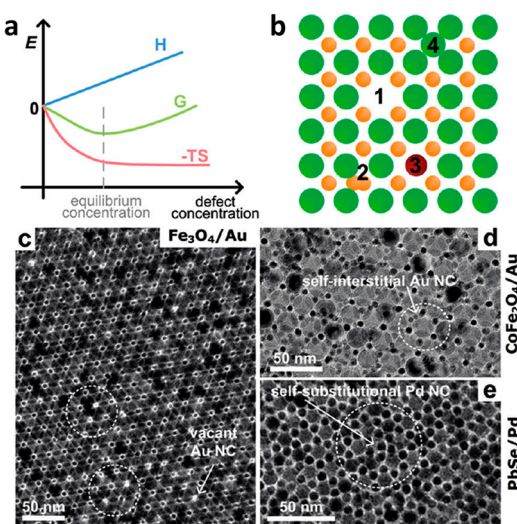


Figure 34. Zero-dimensional defects in binary nanocrystal superlattices. (a) Dependence of the crystal free energy on the concentration of point defects. (b) Illustration of typical point defects in binary superlattices: 1, vacancy; 2, interstitial; 3, impurity substitutional; 4, self-substitutional defect. (c) TEM image of a NaCl -type binary superlattice containing several octahedral site vacancies. (d) TEM image of the interstitial insertion of a nanocrystal in a normally unoccupied tetrahedral site of a large particle fcc sublattice. (e) TEM image of the substitution of a large nanocrystal for a smaller nanocrystal in the simple hexagonal sublattice of an AlB_2 binary superlattice. Adapted from ref 322. Copyright 2011 American Chemical Society.

8.3. Two-Dimensional Defects: Stacking Faults and Grain Boundaries

External and internal surfaces represent two types of two-dimensional defects in nanocrystal superlattices. Since no real crystals are infinitely large, surface termination is exhibited by all materials. As such, we restrict our discussion to internal surfaces. Internal surfaces are subdivided into stacking faults and several types of boundaries. These two-dimensional defects are readily observed when the interface lies perpendicular to the imaging plane (Figure 36). They may also run parallel to the imaging plane and thus remain buried within the crystal interior.

A stacking fault is a disrupted sequence of atomic planes. It is either an insertion or a removal of planes spanning less than a full period of the lattice. For example, the fcc stacking sequence $(\text{ABC})_n$ can be disrupted by inserting/removing any set of planes not encompassing a full ABC unit, i.e., $(\text{ABC})_m-\text{X}-(\text{ABC})_n$, where $\text{X} = \text{AB}, \text{BC}$, etc. A stacking fault is seen in the TEM image of an AlB_2 BNSL featuring one layer of large nanocrystals removed from the stacking sequence along the [110] direction (Figure 36a). If the internal interface separates two domains related by mirror reflection, the two-dimensional defect is referred to as a twin boundary. Using again the fcc example, a twin boundary is described as $(\text{ABC})_m-\text{X}-(\text{CBA})_n$, where $\text{X} = \text{A}$. Twin boundaries are low-energy defects commonly observed in atomic crystals and nanocrystal superlattices, as shown in the NaZn_{13} example presented in Figure 36b. Incorporation of such defects into three-dimensional superlattices produced via solvent destabilization reduces the surface-to-volume ratio of the Wulff polyhedron and

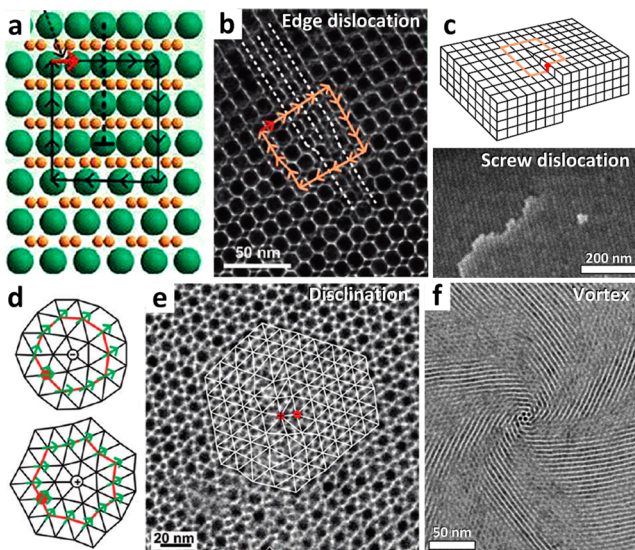


Figure 35. One-dimensional defects in nanocrystal superlattices. (a) Modeled structure of an edge dislocation, showing the inserted half-plane (dotted line), the Burgers circuit (black arrows), and the Burgers vector required to close the circuit (red arrow). (b) Example of an edge dislocation in the AlB_2 binary structure using the parameters described in (a). (c) Modeled structure (top) of a screw dislocation, showing the Burgers circuit (orange lines) closed by a Burgers vector (red) parallel to the dislocation line. (d) Two modeled examples of disclination defect, showing removal (top, “−”) and insertion (bottom, “+”) of wedge into a hexagonal lattice. (e) Tightly bound $+/-$ pair of disclination defects in the AlB_2 binary superlattice. Adapted from ref 322. Copyright 2011 American Chemical Society. (f) Vortex defect in vertically oriented smectic B superlattice of CdSe/CdS rods. Rod director is tilted away from vertical in a direction that varies continuously around the defect center. Adapted from ref 251. Copyright 2015 American Chemical Society.

increases the expression of low-surface-energy (111)-type facets.³⁷ Furthermore, in binary systems, there exists a special type of planar defect, the antiphase boundary, which involves swapping of positions by the two species on opposite sides of the defect plane. Such defects are commonly observed in CuAu-type BNSLs (Figure 36c). They translate the lattice by $(0, b/2, c/2)$, analogous to shearing the lattice by half a unit cell along the (011) cube diagonal.

The above examples of stacking faults, twin boundaries, and antiphase boundaries represent special cases of low-energy grain boundaries with high degrees of lattice fit and a small number of broken bonds. Such defects presumably form by minor perturbations during growth of a single superlattice domain. Two domains may also independently nucleate and grow until they establish contact with one another. In this case, reorientation of entire superlattice domains to optimize the structure of the interface is unlikely. Instead, superlattices remain fixed at random mutual orientations and individual nanocrystals must locally reposition themselves to minimize interfacial energy. The tilt boundary shown for CaB_6 BNSLs (Figure 36d) provides an example of two domains establishing contact at an angle that prevents the formation of a low-energy interface (e.g., twin plane), resulting instead in a small amorphous layer between the grains. The axis of rotation linking lattices across the defect lies within the boundary plane (Figure 36d, red arrow). A related defect, the twist boundary (shown with AlB_2 BNSL in Figure 36e), has an axis of rotation that passes through the boundary plane (red line). Here, the

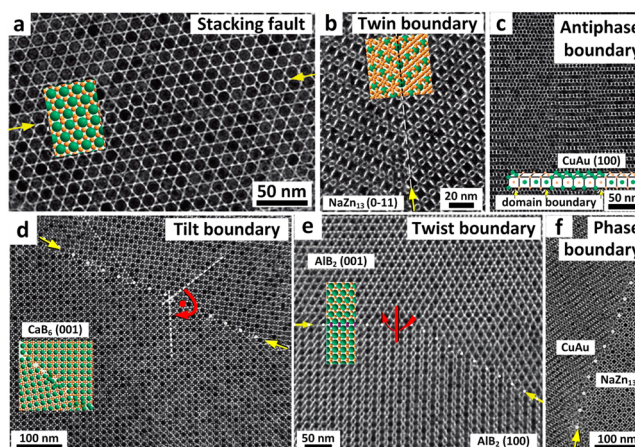


Figure 36. Two-dimensional defects in binary nanocrystal superlattices. (a) TEM image of a stacking fault in the AlB_2 BNSL with overlay of the modeled defect structure and yellow arrows highlighting defect plane. (b) TEM image showing different lattice orientations of the NaZn_{13} BNSL united by reflection across a twin plane. (c) TEM image of an antiphase boundary in the CuAu-type BNSL. The overlay shows swapping of nanocrystal species across defect planes. (d) TEM image of a tilt boundary between two domains of CaB_6 BNSLs. The axis of rotation relating grains is contained within the defect plane (red arrow and spot). Overlay: modeled structure of the tilt boundary showing disorder along the interface. (e) TEM image of a twist boundary between two domains of AlB_2 BNSLs. The axis of rotation (red line and arrow) penetrates the defect plane. (f) Phase boundary separating CuAu and NaZn_{13} BNSLs. Adapted from ref 322. Copyright 2011 American Chemical Society.

90° rotation about the twist axis enables coherent registry of domains across the defect plane. Such orientational registry is possible during growth by an abrupt change in crystallographic orientation with respect to the growth direction within a single superlattice or via gradual alignment of two grains by collective motion of dislocations during late stages of superlattice formation.

Finally, different phases of nanocrystal superlattices (particularly BNSLs) often nucleate and grow simultaneously on the same substrate. A phase boundary is formed when two distinct superlattice structures establish contact. This may come about two ways: by coalescence of independently nucleated domains or by epitaxial phase change during superlattice growth. The first case is highlighted in Figure 36f, showing contact between CuAu and NaZn_{13} BNSLs. The second case, phase boundary formation via epitaxial growth, is a low-energy defect, and provided a good fit between lattices on opposite sides of the defect plane.

A particularly intriguing illustration of the epitaxial phase boundary involves the interface between crystalline and quasicrystalline phases of BNSLs (Figure 37). Here, the quasicrystal comprised of square CaB_6 unit cells and triangular AlB_2 half-unit cells is bridged between pure-phase CaB_6 (analogously described as a 4^4 tiling) by a “wetting layer” containing vertices comprised of three triangles and two squares. The wetting layer is consistent with the $3^3.4^2$ Archimedean tiling motif (Figure 37, red trace). Several disclination quadrupoles (Figure 37, yellow areas) forming a special type of partial dislocation³²⁸ are found near the boundary, each containing two +1 and two -1 defect points. These disclination clusters are geometrically analogous to edge dislocations. Strings of edge dislocations are commonly

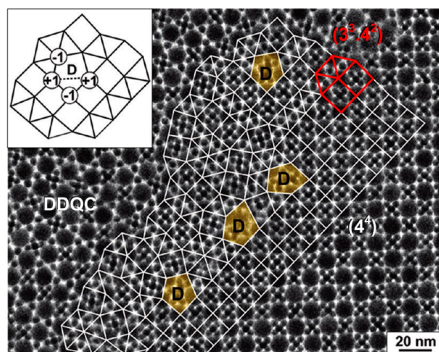


Figure 37. TEM zoom of epitaxial interface structure bridging crystalline and quasicrystalline binary nanocrystal superlattice domains. The periodic CaB_6 BNSL phase (right side) and the aperiodic dodecagonal quasicrystalline phase (left side) are joined by an Archimedean tiling wetting layer (red trace) and several clusters (highlighted in yellow) consisting of four tightly bound disclination sites. Adapted from ref 322. Copyright 2011 American Chemical Society.

observed at atomic small-angle grain boundaries and phase boundaries resulting from lattice orientation mismatch.

8.4. Three-Dimensional Defects: Voids, Cracks, and Precipitates

Bulk defects, including voids, cracks, and precipitates, involve large numbers of broken bonds and are thus the most energetically expensive class of crystallographic imperfections. A void is a three-dimensional piece of material missing from an otherwise coherent superlattice domain (Figure 38a). Voids may be templated by an impurity, for example accumulated excess organic ligands, or by nucleation of a vapor bubble, both of which prevent nanocrystals from accessing this space during superlattice growth. A related defect, the crack, is essentially a void that propagates in one direction (Figure 38b). Crack formation is a common strain release mechanism in nanocrystal assembly,³²⁹ where coherent contraction of superlattice dimensions upon solvent loss is opposed by pinning of domain edges to substrate surface at the late stages of drying. A third type of volume defect, the precipitate, involves not the absence of material within a domain but the inclusion of a solid with

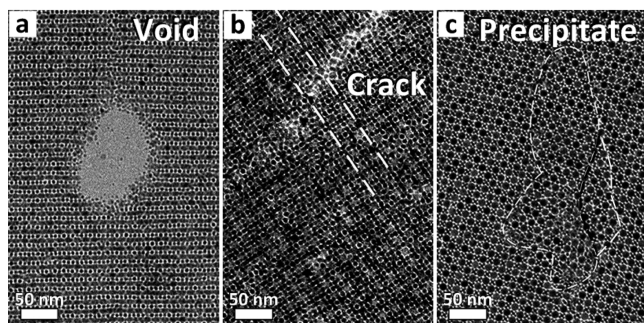


Figure 38. Volume defects in binary nanocrystal superlattices. (a) TEM image of a CuAu-type binary superlattice with a void comprised of several missing unit cells. (b) TEM image of a NaZn_{13} binary superlattice with a crack developed from lattice contraction during late-stage solvent drying. Dotted lines highlight the coherence of the superlattice across the crack. (c) TEM image of a CaB_6 binary superlattice with a precipitate inclusion featuring CaB_6 and quasicrystalline structure. Adapted from ref 322. Copyright 2011 American Chemical Society.

different phase or crystallographic orientation (Figure 38c). Such features develop if a growing superlattice encapsulates a group of nanocrystals that has already arrested into an ordered or disordered packing.

9. SELF-ASSEMBLY DRIVEN BY CHEMICAL PROCESSES AT NANOCRYSTAL SURFACES

As revealed in section 7, the organic surfactants that are optimized for nanocrystal synthesis (typically C_8 - to C_{18} -length aliphatic chains with Lewis basic anchoring headgroup) are also well-suited to order nanocrystals into superlattices. These native hydrocarbon ligands play a role in self-assembly by contributing to the effective nanocrystal size and shape. However, dramatically different phase behavior can be achieved by modifying nanocrystal surfaces after synthesis.

9.1. Partial Desorption of Native Hydrocarbon Ligands

Partial removal of native hydrocarbon ligands is often achieved, with or without intention, by washing and size-selective precipitation steps routinely performed after nanocrystal synthesis. The sensitivity of the nanocrystal capping layer to ligand removal is determined by chemistry of the anchor group.³⁸ For example, desorption of X-type ligands (e.g., carboxylates, thiolates, phosphonates) is electrostatically penalized in a nonpolar solvent, leading to a tightly bound capping layer that is relatively robust against ligand removal via repeated precipitation and redispersal steps. On the other hand, L-type ligands (e.g., amines, phosphines, carboxylic acids) are neutral species, more loosely bound to the nanocrystal surface and prone to establish a solution population upon each redispersal.

Somewhat counterintuitively, synthesis of nanocrystals in the presence of one surfactant species can produce particles with surface ligands in two distinct binding motifs. On PbS and PbSe nanocrystals prepared in the presence of oleic acid, for example, (111)-type surfaces are Pb -terminated and passivated by tightly bound X-type oleate ligands, while (100)-type surfaces have both Pb and S/Se surface atoms and are terminated by weakly bound L-type oleic acid ligands.³⁶ As a result, repeated washing and redispersal of quasi-spherical (i.e., cuboctahedral) PbS or PbSe nanocrystals lead to nearly ligand-free [100] nanocrystal facets. Such anisotropic surface protection strongly influences phase behavior, leading to flat-surface interactions and emergence of new superlattice phases. For example, minimally washed 7 nm PbS nanocrystals capped with oleic acid surface ligands self-assemble into orientationally random (plastic/rotator) phases of fcc/hcp structure (Figure 1). In contrast, additional precipitation and redispersal cycles cause the same nanocrystals to self-assemble into bcc superlattices with orientational registry between inorganic cores (Figure 39). Intriguingly, in situ SAXS experiments have also revealed that the assembly pathway of these bcc superlattices involves an fcc intermediate, suggesting screening of nanocrystal shape effects by solvent before complete drying.⁹⁸ Similarly, a bcc superlattice assembled from Pt_3Ni octahedra exhibits an orientational disordering transition when wetted with excess ligands and heated to 190 °C.³³⁰ BNSLs from quasi-spherical particles also incorporate orientationally registered nanocrystals, for example PbS/PbSe nanocrystals in CuAu and Cu_3Au BNSLs.^{49,310} The structural similarity between such BNSLs and the bcc SLs formed from PbS/PbSe nanocrystals after ligand loss³³¹ suggests weak passivation along particular crystallographic directions might play a crucial role.

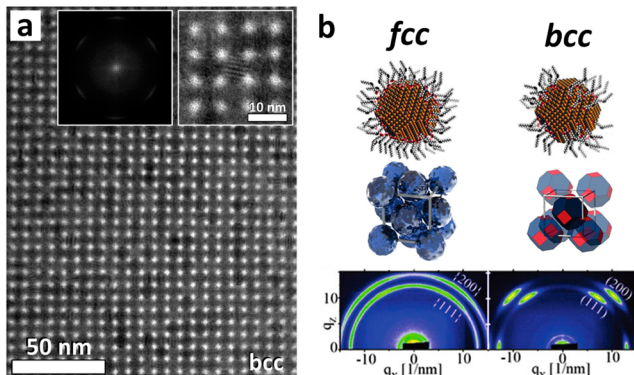


Figure 39. Effect of hydrocarbon ligand surface passivation on the phase behavior of 7.5 nm PbS nanocrystals capped with oleic acid surface ligands. (a) TEM image of well-washed PbS assembled into the bcc superlattices. This TEM image along the [100] projection of bcc packing shows a Moire pattern from the interference of atomic lattice fringes (right inset). The corresponding wide-angle lobe in FFT is shown in the left inset. Taken from ref 50. (b) Well-passivated 7 nm PbS nanocrystals assemble into the fcc structure. Wide-angle X-ray scattering (WAXS) reveals no orientational preference of the cores within the superlattice (left), while nanocrystals with an incomplete passivating layer assemble into the bcc superlattice with strong orientational registry between PbS inorganic cores (right). Adapted from ref 331. Copyright 2011 American Chemical Society.

In the extreme case, complete removal of hydrocarbon ligands leaves surfaces susceptible to reactions such as growth by coalescence³³² or oriented attachment,^{333–335} whereby two or more particles establish contact between inorganic cores and fuse into a continuously crystalline nanostructure, a process that can be studied using *in situ* electron microscopy.^{336–338} Lead chalcogenide nanocrystals have been a fertile testing ground for control over merging of nanocrystal cores into larger, often complex-shaped, nanostructures. The weakly passivated (100) and (111) facets are particularly prone to oriented attachment (Figure 40a–c). Merging of many nanocrystals in solution produces single-crystalline nanowires, nanorings,³³⁹ and nanosheets³⁴⁰ (Figure 40d–f). On the other hand, resting nanocrystal layers on glycol support leads to non-close-packed superlattices by oriented attachment of PbSe nanocrystals via (100) and (110) facets.³⁴¹ The glycol subphase facilitates desorption of oleic acid surface ligands and has been shown to produce single-crystalline buckled honeycomb superstructures analogous to silicene atomic sheets (Figure 40g,h).³⁴² In another example, control over oriented attachment of hydroxyapatite nanorods in either side-by-side or end-to-end fashion was achieved by selective ligand binding.³⁴³ Once grown, superlattices can be quite robust to the application of isotropic high pressure.³⁴⁴ Intriguingly, however, thermally induced merging of inorganic cores can be guided by preassembly of thermally labile nanocrystal species within a supporting lattice of a robust secondary component. For instance, when heated to 190 °C, CaB₆ BNSLs comprised of larger Fe₂O₃ nanocrystals and smaller PbSe nanocrystals were shown to transform to a CsCl-type binary structure via coalescence of the octahedral PbSe cluster.³⁴⁵

9.2. Homopolymer Surface Ligands

End-functionalized polymers may be tethered to the nanocrystal surface to tune effective building block softness, interparticle separation in close-packed arrays, and engineer hybrid materials.³⁴⁶ For example, thiol and carboxylic acid

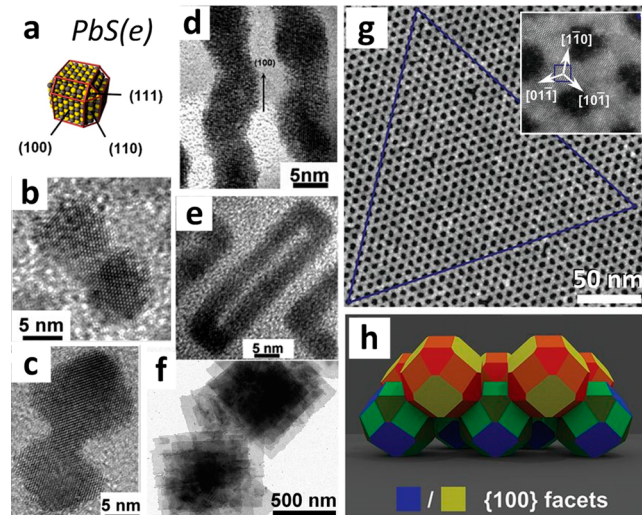


Figure 40. Oriented attachment of lead chalcogenide nanocrystals into single-crystalline nanostructures. (a) Modeled rock salt lead chalcogenide nanocrystal (top) with three distinct crystallographic facets shown. Controlled attachment of these units yields nanowires, sheets, and larger nanocrystals. (b) TEM zoom of a pair of PbSe nanocrystals joined along the (100) direction and (c) the (110) direction. (d) Nanowires formed by PbSe nanocrystals joined along the (100) direction. (e) PbSe nanorings formed by attachment of nanocrystals along (100) and (110) directions. Adapted from ref 339. Copyright 2005 American Chemical Society. (f) Nanosheets formed by joining PbSe nanocrystals through (110) facets. Adapted with permission from ref 340. Copyright 2010 American Association for the Advancement of Science. (g) HAADF-STEM image of a honeycomb structure with hexagonal symmetry highlighted by the equilateral triangle. Inset: zoom of the single-crystalline structure. (h) Plane view of the honeycomb superlattice with oriented PbSe building blocks attached along (100) facets. Adapted with permission from ref 342. Copyright 2014 American Association for the Advancement of Science.

terminated polystyrene chains with molecular weights ranging from 1 to >50 kDa (contour lengths ranging from 2 to >100 nm) are commercially available with narrow polydispersity. Exposure to an excess of such species can exchange the native capping ligands for end-tethered polymers. This exchange is driven by mass action and a difference in headgroup binding affinity. Nanocrystals capped with polystyrene ligands, for example, are dispersible in toluene and tetrahydrofuran, but no longer in hexane.¹¹⁶ Generally, increasing the polymer chain length results in decreased surface grafting density. This is because, while chain length does not alter the binding enthalpy of polymer anchoring to nanocrystal surface, it significantly influences the entropy loss upon confinement within a surface-tethered brush.¹¹⁷ As a result, grafting a long polymer incurs a more severe configurational entropic penalty unless confinement is relaxed by providing more space to the chain.

Although diminished interparticle ordering can accompany an increase in length of polymer ligands,³⁴⁷ long-range-ordered superlattices of polymer-capped nanocrystals are attainable. Perhaps surprisingly, replacing native ligands with much longer end-grafted polymer chains does not result in significant changes to the nanocrystal phase diagram for quasi-spherical nanocrystals. For example, it was recently shown that single-component arrays of very soft ($L/R \approx 5$) polystyrene-capped Au nanocrystals adopt bcc packings, just like the softer ($L/R > 0.7$) combinations of alkanethiol-capped Au nanocrystals.⁴⁶

Self-assembly of polystyrene-capped Fe_3O_4 and Au nanocrystals produced 10 BNSLs, all of which have been reported using nanocrystals capped with conventional aliphatic ligands (Figure 41). Apparently, the principles that dominate the phase behavior of moderately soft nanocrystals capped with typical native hydrocarbon ligands (e.g., oleic acid) also govern assembly of very soft polymer-capped nanocrystals.

Grafting of polymer chains to the surface of colloidal nanocrystals promotes dispersibility of such particles in polymer matrices, an important requirement of industrially relevant polymer nanocomposites.^{348–350} Incorporation of nanocrystals into a polymer matrix of the same chemical composition as the surface ligands (i.e., no interparticle energetic interactions) is accompanied by loss of conformational entropy of the matrix chains close to the particle surface. A common result is nanocrystal aggregation, which negates any benefits of the nanoscale dimensions of the building blocks. Grafting chains much longer than the matrix polymer at low density on the nanocrystal surface minimizes the matrix entropic effect that promotes phase separation.³⁵¹

Ligand chain length and grafting density can be used to tune the phase behavior of nanocrystals in polymers heated above the glass transition temperature. For example, the aggregation state of 14 nm spherical silica nanocrystals grafted with polystyrene and embedded in a polystyrene matrix has been controllably tuned from dispersed state to one-dimensional strings, two-dimensional sheets, and three-dimensional clusters by changing the molecular weight and surface density of grafted chains.³⁵² Along similar lines, nanocubes dispersed in a polymer host matrix may be controllably aggregated into strings with either face-to-face or edge-to-edge contacts depending on the length of the chain and its interaction strength with the particle surface.^{353,354} Uniaxial stretching of polymer composites above the glass transition temperature elongates matrix chains along the deformation axis, promoting alignment of anisotropic

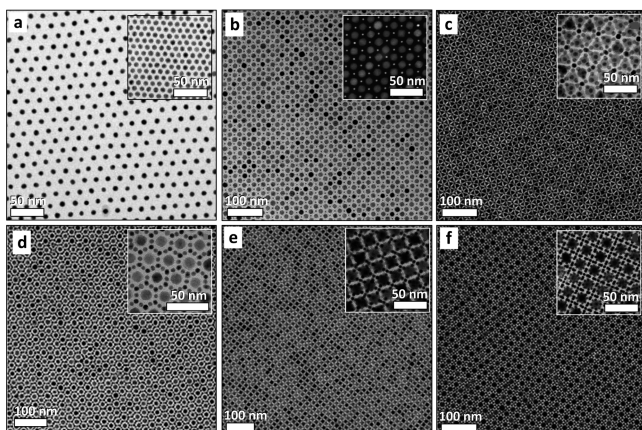


Figure 41. Evaporation-based assembly of two- and three-dimensional nanocrystal arrays with nanocrystal capping layers comprised of surface-grafted, end-functionalized polystyrene (PS) ligands. (a) TEM image of 7.6 nm Au nanocrystals capped with 11.5 kDa PS. Inset: the same nanocrystal cores capped with oleylamine before ligand exchange. (b) TEM image of an AB-type two-dimensional BNSL comprised of PS-capped Au and Fe_3O_4 nanocrystals. Inset: dark-field STEM zoom of the same structure. (c–f) TEM overviews and zooms (inset) of three-dimensional BNSLs comprised of PS-capped Au and Fe_3O_4 nanocrystals with (c) MgZn₂, (d) CaCu₅, (e) C₆₀K₆, and (f) NaZn₁₃ structures. Adapted with permission from ref 46. Copyright 2015 Nature Publishing Group.

particles contained within.³⁵⁵ Beyond polymers, the use of dendrimeric ligands has also been explored as a means to generate dense ligand shells.^{356–359}

9.3. Block Copolymer Surface Ligands

More unusual nanocrystal phases may be accessed by combining nanocrystals with block copolymers, which feature chemically incompatible segments that form separate nanoscale domains.^{360,361} For instance, addition of copolymer comprised of hydrophobic (polystyrene) and hydrophilic (poly(acrylic acid)) blocks (PS-*b*-PAA) enables encapsulation and dispersal of clusters of polystyrene-capped Au nanocrystals.³⁶² Alternatively, direct grafting of end-thiolated polystyrene-*b*-poly(ethylene oxide), (PS-*b*-PEO), copolymer to the surface of 14 nm Au nanocrystals yields a particle soluble in tetrahydrofuran (THF), a solvent compatible with both blocks.³⁶³ Evaporating a THF solution of these block copolymer-capped nanocrystals produces close-packed superlattices with unique properties: exposing the solid to water pulls hydrophilic ligand segments toward the solid–liquid interface, creating strain across the top nanocrystal layer that bends the sheet into spherical vesicles (Figure 42a). The walls of these vesicles are comprised of hexagonally close-packed Au nanocrystals glued together by hydrophobic polystyrene segments in the corona interior (Figure 42b,c) and can be opened and closed for controlled release.³⁶⁴ More recently it was shown that these nanocrystals can form strings,³⁶⁵ and that mixing unthiolated (free) block copolymer with the block copolymer-capped nanocrystals produces vesicles with nanocrystals localized only on one side of the sphere surface.³⁶⁶ More complex assemblies are on the horizon.³⁶⁷

9.4. Coarse-Grained Models for Ligand-Tethered Nanocrystals

Computationally modeling the self-assembly of nanocrystals with homopolymers, block copolymers, or other complex ligands is complicated by the multiscale nature of the problem.

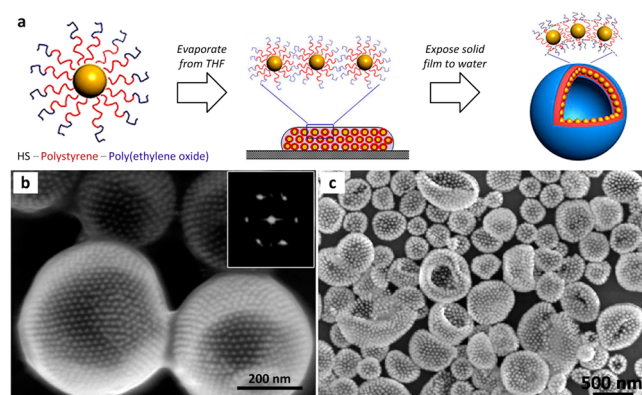


Figure 42. Self-assembly of Au nanocrystals capped with block copolymer ligands into spherical vesicles. (a) Schematic of vesicle preparation. Au nanocrystals with end-grafted hydrophobic–hydrophilic block copolymer chains (left) are soluble in tetrahydrofuran and assemble into close-packed arrays upon solvent evaporation (middle). Upon exposure to water, nanocrystal monolayers are bent into curved sheets that close into spherical vesicles (right). (b) SEM zoom of a pair of spherical vesicles with walls comprised of close-packed Au nanocrystals with block copolymer ligands. Adapted from ref 363. Copyright 2012 American Chemical Society. (c) SEM overview of spherical and collapsed vesicles. Adapted from ref 368. Copyright 2013 American Chemical Society.

Simulation methods have been developed on various scales employing particle-based and continuum methods.^{369–373} United-atom force-field simulations, dissipative particle dynamics simulations, and other models with comparable detail reproduce aggregation behavior^{374–378} and particle interaction with solvent and interfaces,^{379–383} but cannot yet achieve the time scales and system sizes necessary for the observation of spontaneous ordering. Another approach is self-consistent-field theory (SCFT), a mean field theory, which has been crucial to explaining phase behavior of block copolymers. Variations of SCFT are successful in situations that are well-suited to a continuum description,³⁶⁹ such as the formation of lamellae or cylinders,^{384,385} the estimation of the effective interaction between polymer-grafted particles in good solvent,¹¹⁴ or studying the elasticity of polymeric nanoparticles.³⁸⁶ Nevertheless, it is challenging to apply SCFT to nanocrystal self-assembly if the nanocrystal cores remain separated. In this case, the inclusion of discrete particle descriptions³⁸⁷ is desirable. Along these lines, the phase behavior of such systems has been analyzed with a mixed continuum and discrete particle treatment by combining a Cahn–Hilliard model for the polymer blend with a Brownian dynamics simulation for the rods.³⁸⁸ Another approach applies statistical associating fluid theory (SAFT) on polymer-grafted nanoparticles to predict dispersion and aggregation of systems with realistic interactions.³⁸⁹

Empirical particle-based models represent a versatile approach for studying colloidal nanocrystal assembly. Such models arrive at a coarse-grained description by reducing the particles to simple geometric shapes paired with physical and/or chemical intuition to select suitable interparticle interactions that reproduce essential features of the experiment. The hard particle model is the most radical simplification. Although it can be a useful approximation to understand nanocrystal assembly behavior in many cases, the hard particle model lacks the ability to account for occasionally important effects arising from the soft ligand shell or interparticle interactions. Two classes of particle-based models have been pioneered by Glotzer and co-workers as a stepping stone toward the rational design of nanomaterials: tethered particles with explicit ligands and patchy particles with implicit ligands.³⁷² These models alleviate the omissions of the hard particle model and reproduce many structures and phase behavior observed in self-assembly experiments.

A tethered nanoparticle consists of a soft or hard nanocrystal core grafted with one or several short bead strings, often spring chains of spheres (Figure 43a).³⁹⁰ The formation of lamellar,^{391,392} cylindrical,³⁹³ and gyroidal³⁹³ mesophases was reported with this model using only one tether. Mixing two types of polymer tethers³⁹⁴ or tethering two spheres together³⁹⁵ leads to phase behavior similar to that of block copolymers. This behavior also resembles that of very small nanoparticles, for example polyhedral oligomeric silsesquioxane (POSS) cubes,³⁹⁶ fullerenes (C_{60}), or other macromolecular giant molecules.³⁹⁷ End-tethered nanorods self-assembled into various phases, including a hexagonal chiral cylinder phase.³⁹⁸ Laterally tethered nanorods formed stepped-ribbon-like micelles³⁹⁹ and free-standing rafts with helices that can be switched by varying the solvent.⁴⁰⁰ By changing the geometry of the building blocks, transformations between thermodynamically stable structures could be enforced.^{401,402} Ordering is generally robust to the introduction of nanoparticle polydispersity of up to 15–30%.⁴⁰³

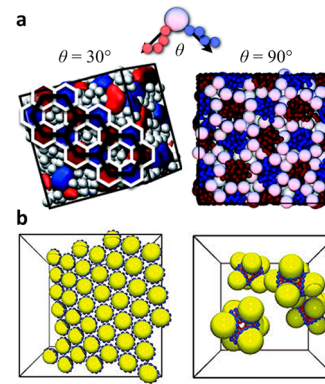


Figure 43. Modeling phase behavior of tethered and patchy particles. (a) Example of a tethered particle. Two chemically incompatible polymer segments (red and blue chains) are tethered to the surface of a spherical particle (top). The angle between grafting points controls microphase separation into different polymer–nanocrystal nano-composite morphologies (bottom). Adapted from ref 394. Copyright 2009 American Chemical Society. Adapted with permission from ref 372. Copyright 2015 Cambridge University Press. (b) Example of patchy particle assembly. The choice of the number and size of patches, as well as their distribution across the particle surface, can be used to tune phase behavior. Shown here: equatorial belts of attractive sites promote formation of hexagonal sheets (left), while translating the belt toward one of the sphere poles leads to the formation of six-membered square pyramid clusters (right). Adapted from ref 404. Copyright 2004 American Chemical Society.

Patchy particles have discrete attractive interaction sites (patches) at prescribed locations on the particle surface. They are a useful model to explore phase behavior of nanoparticles with highly anisotropic interactions and directional bonding (Figure 43b).^{404–407} In contrast to tethered nanoparticles, ligands are included implicitly. A popular implementation is the Kern–Frenkel interaction.⁴⁰⁸ Symmetric patchy particles with two patches on opposite sides favor the formation of chains,⁴⁰⁹ six patches arranged octahedrally stabilize a bcc lattice via contacts with second-nearest neighbors,⁴¹⁰ and four patches arranged tetrahedrally form the diamond structure.^{411–413} Such tetrahedrally patchy particles might be hard or even impossible to crystallize⁴¹⁴ and thus are ideal candidates to form stable gels. Assembly of patchy particles can also be kinetically hindered by rotational diffusion preventing stable interparticle patch alignment.⁴¹⁵ Recently, a relationship between polymer-grafted nanoparticles and patchy particles has been established, which maps the phase behavior of the two systems onto one another.^{416,417} Janus particles,^{418–420} named after the two-faced Roman god, are a special case of patchy particles with two patches occupying opposite hemispheres. Janus rod simulations found fibers, clusters, and bilayer⁴²¹ vesicles. In contrast, Janus spheres stabilize planar bilayers and three-dimensional networks,⁴²² possibly open to maximize entropy,⁴²³ and can form rings which may be useful as pores in “smart” membranes that have self-healing, breathable, or drug delivery functionality.⁴²⁴

9.5. Capping Layers Containing Two or More Ligand Species as Patchy Particles

Experimental demonstrations of patchy particle self-assembly used colloidal beads,^{425–432} triblock terpolymers,^{433–435} and compact molecular building blocks such as polyhedral oligomeric silsesquioxane (POSS) cubes,⁴³⁶ among other examples. Mesoscale smectic membranes are found with rod-shaped fd viruses that stick together on their sides⁴³⁷ and

exhibit shape-driven liquid–liquid phase separation.⁴³⁸ Likewise, significant control of Janus particle assembly has been achieved with particles at the larger end of the micrometer scale.⁴³⁹ Nevertheless, there has recently been significant effort in extending anisotropic shape and surface chemistry⁴⁴⁰ and thus patchiness to the self-assembly of colloidal nanocrystals. For instance, flat nanocrystal faces can already be considered a source of directional entropic patchiness,²¹¹ surface curvature¹¹⁰ can add enthalpic patchiness, and it is possible to combine both.⁹³

One promising approach to patch engineering is the use of mixed-ligand systems. Since the early days, nanocrystal syntheses have routinely made use of mixtures of surface-binding species such as alkylphosphines, phosphine oxides, phosphonic acids, and amines.^{24,441} Similar chemical compatibilities of various-length aliphatic tails, as well as significant differences in headgroup binding affinity, allow for neglecting the role of mixed-ligand composition within the capping layer on phase behavior of such nanocrystals. On the other hand, installation of ω -functionalized ligands alongside traditional aliphatic species (e.g., mercaptopropionic acid, HOOC–(CH₂)₂–SH, with octanethiol, CH₃–(CH₂)₇–SH) can lead to either intermixing or phase separation across the nanocrystal surface.^{442,443} However, unambiguous characterization of some mixed-ligand systems currently presents significant challenges.⁴⁴⁴

Mixed ligand systems can give rise to unique nanocrystal assembly phase behavior. Au nanorods selectively patterned with polystyrene tethers at their tips behave like metal–polymer analogues of amphiphilic triblock copolymers,⁴⁴⁵ assembling into nanorod chains and pom-poms⁴⁴⁶ (a term lent from branched polymers⁴⁴⁷) via reaction-controlled stepwise growth.⁴⁴⁸ These structural transitions result from competition between electrostatic repulsion and hydrophobic attraction, which can be controlled by solvent quality, salt concentration, and polymer ligand molecular weight.⁴⁴⁹ Similarly, spherical Au nanocrystals functionalized with dodecanethiol and mercaptoundecanoic acid aggregate in water into one-dimensional strings held together by hydrophobic bonds between contacting aliphatic surface groups,⁴⁵⁰ while Au nanorods stabilize free-standing arrays after selective ligand exchange⁴⁵¹ or chains when functionalized with polystyrene at the tips.⁴⁵² Janus-like behavior has been explored for polymer-grafted nanocrystals with two ligand species.^{453,454}

Side-by-side attachment is also possible with hydrophobic attraction of the cylindrical sections.⁴⁵⁵ Another example is the partial replacement of the native cetyltrimethylammonium bromide (CTAB) ligands with polystyrene on the tips of nanodumbbells, leading to the formation of cross-like dimers.⁴⁵⁶ In addition, mixing ligand species can add sensitivity to external stimuli. For example, partial incorporation of light-sensitive ligands into the corona of alkanethiol-capped Au nanocrystals promotes vesicle self-assembly via oxidative desorption of thiol anchor groups upon UV light irradiation.⁴⁵⁷

9.6. Charged Aliphatic Surface Ligands and Charged Nanocrystal Cores

Electrostatic interactions are well-suited to mediate the assembly of nanocrystals.¹⁴⁰ Kotov et al. investigated 2.5 nm CdTe nanocrystals that assemble into long pearl-necklace chains when functionalized with negatively charged (deproto-nated) thioglycolic acid⁴⁵⁸ but form large-area, free-floating sheets when functionalized with positively charged (proto-

nated) 2-(dimethylamino)ethanethiol.⁴⁵⁹ Simulations of this system confirmed that the sign of the charge and dipole direction are responsible for the different behavior.⁴⁶⁰ Spontaneous chain formation occurs if the attractive dipole–dipole and van der Waals interactions overcome the repulsive electrostatic forces, a process that has been visualized *in situ*.⁸⁹ The range of electrostatic forces and its competition with other forces depends on nanocrystal size and the surrounding medium. For example, repulsive electrostatic interactions weaken the strong van der Waals interaction between flat faces and facilitate the self-assembly of Au nanotriangles into superlattices.⁴⁶¹ On the other hand, switching the repulsive forces responsible for colloidal stabilization from long-range electrostatic to short-range steric can enhance solubility and improve self-assembly, as demonstrated for nanocrystals capped by chalcogenidometallate complexes.^{462,463}

The electrostatic charge of a nanocrystal can be determined from electrophoretic mobility measurements. Shevchenko et al. observed peaks in the mobility distribution curve of PbSe and Au nanocrystals in chloroform¹⁴² indicating the presence of integer multiples of elementary charge $-\epsilon$, 0, $+\epsilon$, and $+2\epsilon$. Addition of surfactants (e.g., carboxylic acids and tri-*n*-alkylphosphine oxides) changes the relative distribution of charge states. In contrast, no evidence for nanocrystal charging was observed in other nonpolar solvents (e.g., hexane, octane, and toluene) commonly used in nanocrystal self-assembly,^{62,93,94} allowing charging to be ruled out as the primary factor driving phase behavior of hydrocarbon-capped nanocrystals. On the other hand, a single micrometer-sized bead can support several hundred elementary charges across its surface, allowing electrostatic interactions between such particles to play an important role in colloidal crystal phase behavior. For instance, a binary system of oppositely charged poly(methyl methacrylate) (PMMA) spheres was observed to assemble into a CsCl-type superlattice.⁴⁶⁴ Many more such ionic colloidal crystals of oppositely charged spheres³¹⁷ occur as a function of the charge ratio Q and the Debye screening parameter κ , as confirmed by Monte Carlo simulations and Madelung energy calculations.⁴⁶⁵

Intentional, postsynthetic installation of charged ligands on the nanocrystal surface offers a strategy to target novel nanocrystal superlattice structures. Along these lines, equal-sized octahedral Au and Ag nanocrystals coated with ω -functionalized alkanethiols precipitate at the point of overall electroneutrality⁴⁶⁶ to self-assemble faceted, micrometer-sized, diamond-type crystals, in which each nanoparticle has only four oppositely charged neighbors.⁴⁶⁷ The fact that the thickness of the screening layer is commensurate with the dimensions of the assembling objects plays a key role in stabilizing the non-close-packed network. Alternative candidate structures (e.g., NaCl, CsCl) feature six- or eight-membered neighbor shells and thus large electrostatic repulsion between like charges within the coordination polyhedron. Necessary conditions for successful assembly in this work are a small charge asymmetry and a screening length κ^{-1} that is at least 100 times greater than the particle radius. Even like-charged particles can self-assemble into superlattices if conditions are tuned such that interparticle electrostatic repulsions are partly offset by attractive hydrogen bonding interactions.⁴⁶⁸

Interestingly, some polydispersity (up to 45%) in particle size has been reported to facilitate crystallization and improve ordering, although the size distributions of both species must overlap.⁴⁶⁹ A similar positive effect of polydispersity is observed

when particles cluster by a balance between electrostatic repulsion and van der Waals attraction. The self-assembly of CdSe nanocrystals with nonuniform size distributions into uniformly sized self-limiting supraparticles⁴⁷⁰ is even aided by the broad polydispersity of the nanoparticles.^{471,472} Along the same lines, balancing the charge of oppositely charged particles and using a combination of long-ranged attractive and repulsive interactions allows tuning the preferred number of neighbors. The result are finite-size binary colloidal clusters with similarity to molecules.⁴⁷³ An unusual idea is the use of charged nanocrystals as supramolecular surfactants for controlling the growth and stability of microcrystals.⁴⁷⁴

The interplay of polydispersity and electrostatic interaction has other unexpected consequences. Aqueous dispersions of colloidal silica with a broad monomodal size distribution (polydispersity, 14%; size, 8 nm) spontaneously split into different types of superlattices, which cooperate to make the best use of the whole population,⁴⁷⁵ a process called “fractionated crystallization”.^{476,477} The particles repel each other via a screened electrostatic interaction, with an effective Debye length of 2.5–4.5 nm and, as suggested by computer simulation,⁴⁷⁸ first form a bcc superlattice of the most abundant particles in the center of the size distribution. The leftover larger and smaller particles are then incorporated into a second superlattice of Laves MgZn₂ phase. In this work, the interparticle interactions are soft and may be described using a Yukawa potential. As a result, they exhibit high mobility and already assemble at low density, which might help speed up the sorting process. Details of the fractionated crystallization process are only starting to be understood.

Anisotropic particle shape or anisotropic surface chemistry can equip particles with directional electrostatic interactions. Protein cages (cowpea chlorotic mottle virus and ferritin cages) with negatively charged surface patches mixed with Au nanocrystals capped by ligands with terminal ammonium group form an AB₈ crystal structure.⁴⁷⁹ Au nanodumbbells show interplay between particle shape and local electrostatics: when acidic ligands are used, regions of the particle surface with different curvature become charged at different pH values of the surrounding solution.⁴⁸⁰ The particles form cross-stacks and open-lattice crystals, with pore sizes on the order of tens of nanometers. Positively charged Au nanorods can direct negatively charged nanospheres to rod sides or rod ends, depending on the rod size and resulting rod–sphere van der Waals interaction.⁴⁸¹

9.7. DNA-Based Surface Ligands

The topics outlined so far have primarily focused on relatively simple systems with one or two types of building blocks that readily form ordered structures. A qualitatively different approach to self-assembly involves particles with highly specific, orthogonal interactions via DNA linkers. DNA, a rigid polymer comprised of two helical chains held together by hydrogen-bonded base pairs, is perhaps the ultimate surface coating for targeted, programmable assembly.^{482,483} Nucleic acids, used by biological systems for hundreds of millions of years to store genetic information and catalyze cellular processes, are also ideal candidates for the self-assembly of three-dimensional structures.⁴⁸⁴ With the development of chemical methods for producing oligonucleotides of desired sequence, the application of this class of biopolymers as structure-directing nanocrystal surface groups has become an important topic in self-assembly research.

DNA-capped nanocrystals can be prepared by exchanging native surface ligands with end-functionalized oligonucleotides. Often, such nanocrystals are subsequently exposed to a DNA linker strand, which contains one region complementary to the nanocrystal-bound DNA and a second region with unhybridized dangling end that can be varied to control interactions between nanocrystals (Figure 44a). A special property of nanocrystals capped with DNA ligands is the sharp melting transition of interparticle bond formation/breaking during superlattice assembly/dissolution over only a few degrees Celsius.^{485,486} This unique transition, for which entropic factors play an important role,^{487,488} offers new opportunities to control the assembly process, for example for the formation of free-standing films of Au nanocrystals via a DNA-directed layer-by-layer approach.⁴⁸⁹ Phase behavior can also be directly programmed into the system with DNA strands that compete with grafted strands through strand displacement. Using strand displacement reactions, phase behavior not found in atomic systems, including reentrant melting,⁴⁹⁰ arbitrarily wide gas–solid coexistence, and reversible crystal–crystal transitions are possible.⁴⁹¹ After assembly, DNA bond strength can be increased using small molecule intercalators which enhance thermal stability.⁴⁹² In addition, Ag⁺ soldering is a technique to improve plasmonic coupling among nanocrystals.⁴⁹³

By designing a linker sequence with self-complementary sticky end, particles seek to maximize the number of nearest neighbors, favoring fcc or hcp phases (Figure 44b, left pathway). On the other hand, the use of a non-self-complementary linker requires a second type of linker to achieve nanocrystal assembly. In this case, the quasi-binary system maximizes the number of A–B contacts without allowing A–A or B–B contacts, demanding a more open first coordination shell with only eight nearest neighbors (i.e., bcc or CsCl-type packing; Figure 44b, right pathway).^{494–496} Recently, it was shown that hairpin loops formed by hybridization of two regions of the same strand can be used to hide sticky ends within the corona interior (Figure 44c, left).⁴⁹⁷ Upon exposure to a nucleotide sequence which binds the hairpin region, these ends are pushed to the corona exterior, enabling nanocrystal–nanocrystal binding events. Using this approach, selective exposure of self-complementary or non-self-complementary sticky ends enables toggling between fcc and bcc arrangements (Figure 44c, right). Similarly, diffusionless transformation between CsCl-type and CuAu-type packing of polymer microspheres with two-component DNA shells was demonstrated by changing temperature within a few degrees Celsius range.⁴⁹⁸

Novel superlattices have been obtained by replacing inorganic nanocrystals with hollow DNA “spacer” entities that are constructed to mimic the behavior of the nanoparticles they replace.⁵⁰² In another recent work, a three-dimensional lattice of DNA-coated nanocrystals has been switched from an initial “mother” phase (bcc, CsCl) into one of “multiple” daughter (fcc, hcp, CuAu, cluster state) phases by introducing different types of “input” DNA strands that link DNA shells at their ends.⁵⁰³ Furthermore, superlattices were made to reversibly contract and expand while preserving superlattice symmetry. Adding single-stranded DNA allows switching of interparticle distances by 15–25%,⁵⁰⁴ and dehydration and subsequent rehydration enable control of interparticle spacing over a 4–46 nm range.⁵⁰⁵ Finally, directionality (DNA patches) has been introduced via selective hybridization at a surface,⁵⁰⁶ aniso-

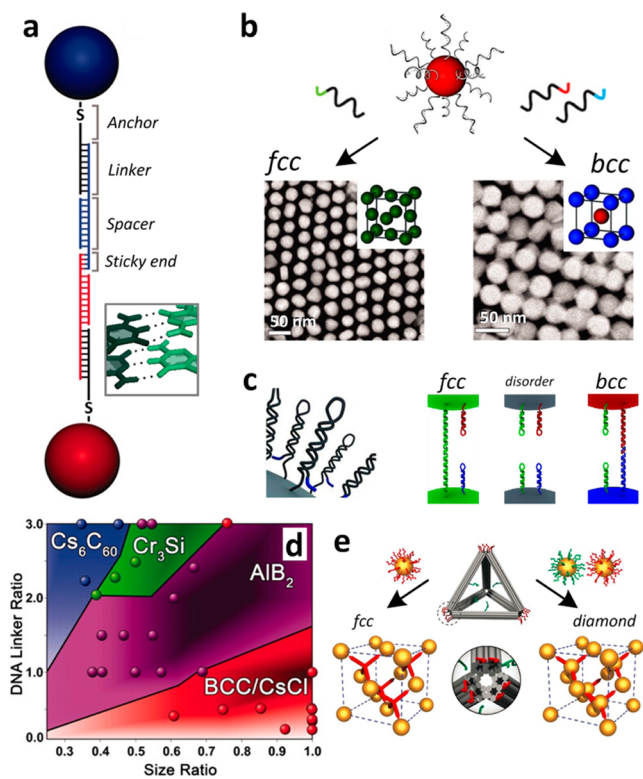


Figure 44. Programmable self-assembly of nanocrystals functionalized with DNA surface ligands. (a) Sketch of structural units of DNA-based ligands, including the alkanethiol anchor group and the 10-base nonbinding region, the recognition sequence that binds to DNA linker, the spacer sequence to control bond length, and the sticky end that drives nanocrystal assembly via hybridization. Inset: stick model of the G-C base pair interaction. Adapted with permission from ref 499. Copyright 2011 American Association for the Advancement of Science. Adapted with permission from ref 500. Copyright 2015 Nature Publishing Group. (b) Prototypical example of structure direction with DNA. Self-complementary linker strands drive the assembly of the fcc structure (left), while mixing two sets of nanocrystals with mutually complementary strands forces the formation of A-B contacts, leading to the bcc structure (right). Shown below are TEM images of the corresponding structures. Adapted with permission from ref 482. Copyright 2015 American Association for the Advancement of Science. Adapted with permission from ref 495. Copyright 2008 Nature Publishing Group. Adapted with permission from ref 499. Copyright 2011 American Association for the Advancement of Science. (c) DNA hairpin loops hide sticky ends (left), enabling the selective exposure of self-complementary and non-self-complementary oligonucleotide sequences, favoring the formation of fcc and bcc lattices (right). Adapted with permission from ref 497. Copyright 2016 American Association for the Advancement of Science. (d) Phase diagram of DNA-driven binary superlattices. Adapted with permission from ref 499. Copyright 2011 American Association for the Advancement of Science. (e) Combining DNA origami with DNA-capped nanocrystals enables structure direction via nanocrystal incorporation into preset DNA scaffold. Nanocrystal hybridization with tetrahedron vertices leads to the formation of the fcc structure (left), while addition of a second nanocrystal species localizing in the tetrahedron interior produces diamond-type superlattices. Adapted with permission from ref 501. Copyright 2016 American Association for the Advancement of Science.

tropic particle shape,⁵⁰⁷ or by using amphiphilic Janus particles as building blocks.⁵⁰⁸

Growth of DNA-functionalized nanocrystal superlattices proceeds along similar pathways as nanocrystals with traditional

ligands.⁵⁰⁹ Beyond fcc and bcc lattices, binary superlattices including structures with AB, AB₂, AB₃, and AB₆ stoichiometries have been accessed by combining nanocrystals with distinct hydrodynamic radii and/or DNA grafting density (Figure 44d).⁵¹⁰ The phase behavior in this case has been rationalized by a set of rules in the style of Pauling's rules for ionic (salt) crystals. In addition, combining DNA-capped nanocrystals with unbound DNA strands made rigid by staple segments (DNA origami^{482,511}) enables structure direction by placement of nanocrystals within a preset DNA scaffold,^{512–517} for example directing Au nanocrystals into tubular spirals,⁵¹⁸ into free-standing sheets,⁵¹⁹ and into planar shapes and periodic arrays.⁵²⁰ With this strategy it was also possible to link nanocrystals through tetrahedron vertices to produce extended fcc lattices, while modifying the same approach with a second nanocrystal species localized in the tetrahedron interior leads to occupation of half the tetrahedral voids in the fcc sublattice, producing diamond-type packing.⁵⁰¹ Nanocrystals have also been used as joints to combine DNA cages in a jigsaw-puzzle-like approach into larger assemblies.⁵²¹ Taking this idea to the extreme recently led to three-dimensional ordered nanoparticle–DNA frameworks.⁵²² DNA origami was applied to demonstrate the formation of an internal cavity that acts like a mold for the shape-controlled synthesis of Au nanocrystals.⁵²³ DNA functionalization has also started to be used to assemble anisotropic colloids. Shape and size complementarity coupled with DNA bonds leads to the alignment of nanorods⁵²⁴ and the cocrystallization of cubic particles and disks or spheres into bcc and simple cubic lattices through shape-induced directional bonding.^{500,525}

Theoretical work has created models of DNA-functionalized colloids that successfully reproduce many experimental findings.^{526,527} A particular focus lies in the modeling of the binding process, which is computationally demanding. Molecular dynamics simulations are able to produce general phase diagrams and evaluate the stability of previously overlooked crystalline phases.^{528,529} The optimal range of the DNA linker interaction strengths for a successful assembly is predicted to be $12\text{--}16k_{\text{B}}T$, the optimal mean lifetime of a DNA hybridization event is estimated at $10^{-4}\text{--}10^{-3}$ of the total time it takes to form a superlattice, and suitable DNA linker sequences have been proposed theoretically.⁵³⁰

9.8. Toward Biologically Inspired Self-Assembly

The above examples serve to highlight the tremendous potential of DNA-functionalized nanocrystal surfaces as customizable structure-directing agents. While there exist several obstacles to progress in this field, including the collapse of such structures in the absence of an interparticle filler (i.e., water or resin), DNA-programmable self-assembly promises a paradigm shift away from (passive) observation of superlattices formation toward (active) design of building blocks by encoding information into them about a desired target structure. In particular, DNA ligands are equipped with a sufficiently information-rich interaction as required for the self-assembly of complex structures. The resulting nanocrystals are informed components⁵³¹ with sufficient information capacity,⁵³² limited only by how many different types of DNA strands can be used per particle.⁵³³

Theoreticians are now dreaming of potential applications and new phase behavior made possible by DNA-terminated nanocrystal surfaces. Proposals range from open lattices,^{534,535} self-limiting^{536,537} and self-replicating⁵³⁸ colloidal clusters, to

the retrieval of several structures “stored” by the choice of specific interactions among many different types of components.⁵³⁹ Initial results suggest that it might in principle be possible to maximize yield⁵⁴⁰ and target almost arbitrarily complex equilibrium order from a large enough number of distinct component types,⁵⁴¹ possibly by exploiting a multistage hierarchical scheme.^{542–544} Although details how this might be achieved in practice remain vague, trying to narrow the gap between nanocrystals and biological self-assembly leading to the complexity of life certainly is a tempting endeavor.

9.9. Molecular Switches as Surface Ligands

Molecular switches are yet another promising class of nontraditional ligands for directing nanocrystal self-assembly. While they do not offer the promise of exquisite structural control like DNA, molecular switches (e.g., azobenzenes, spirobifluorenes, and dithienylethylenes^{545,546}) promise reversible, remote control over nanocrystal aggregation behavior via structural isomerization upon irradiation with light. Azobenzene ($C_6H_5-N=N-C_6H_5$), for example, is most stable in the *trans* isomer, although irradiation with UV light flips the molecule to the *cis* form (Figure 45a). The metastable *cis* state is converted slowly back to *trans* at room temperature, but this process can be accelerated by heat or blue light (Figure 45b). Crucially, such light-induced structural changes are accompanied by the appearance and disappearance of a significant dipole moment from electron density localized on nitrogen atoms (Figure 45b, inset). When azobenzene moieties are tethered to a nanocrystal surface binding group (e.g., thiols for gold nanocrystals or catechol for iron oxide nanocrystals), their attachment to the nanocrystal surface enables remote triggering

of nanocrystal assembly and redispersal. For instance, nanocrystals derivatized with alkanethiol-modified *trans*-azobenzene are soluble in toluene. Upon UV irradiation, however, dipole–dipole interactions between terminal *cis*-azobenzene groups encourage intermingling of ligand coronas, resulting in nanocrystal precipitation from solution (Figure 45c). Remarkably, this light-induced destabilization process can be carried out gently enough to form regular, faceted polyhedral superlattices (Figure 45d–f).

10. ROLE OF THE ENVIRONMENT IN DIRECTING NANOCRYSTAL SELF-ASSEMBLY

The different geometry of nanocrystal superlattices obtained by solvent evaporation (thin film) and destabilization (polyhedral cluster) discussed in section 2 illustrates an important concept of self-assembly: in addition to nanocrystal properties (size, shape, and surface chemistry, for example), the conditions under which particles are assembled play an important role. In this section we discuss how self-organization of nanocrystals may be guided by the presence of secondary species in solution, by surfaces, by encapsulation within structure-directing matrixes, and by assembly temperature and the presence of external electric or magnetic fields. Directed⁵⁴⁹ and templated⁵⁵⁰ self-assembly promise to be important for technological applications when a high level of control is required.

10.1. Self-Assembly on Flat Surfaces

Because characterization (e.g., TEM, SEM, AFM, SAXS) of nanocrystal assemblies typically requires immobilization of the superlattice on a solid support, it can be difficult to separate the role of the surface, if any, in influencing the structure formed. For this, theoretical investigation has been helpful in revealing some details of adsorption of hydrocarbon-capped nanocrystals at a solid interface. For instance, molecular dynamics simulation of 2 nm dodecanethiol-capped Au nanocrystals adsorbed on the basal plane of graphite predicts that hydrocarbon chains bend away from edges and corners of the underlying crystallite like “parting hair”.¹²¹ This nanocrystal–surface interaction favors edge orientation of nanocrystals to maximize London dispersion attraction between hydrocarbon chains and the smooth solid surface.

Passivated hydrocarbon monolayers serve to lubricate the interface between the inorganic nanocrystal core and the carbon surface, enabling mobility of single nanocrystals and groups of nanocrystals without solvent at modest temperatures.⁵⁵¹ Nanocrystal motions are characterized by Levy (long right-side tail) distribution, whereby long gliding trajectories are punctuated by sticking events.⁵⁵² Such observations suggest the possibility of structural rearrangement, or even self-assembly, in the absence of solvent. Along these lines, recent experiments heating thin films of close-packed, monodisperse metal nanocrystals constrained on a TEM grid have shown ripening and subsequent assembly of several common phases of BNSLs.^{241,553} Apparently, at elevated temperature, nanocrystal geometry can be sufficiently volatile, ligand chemistry sufficiently variable, and nanocrystal–nanocrystal friction sufficiently low for size evolution of nanocrystals through mass transfer via Ostwald ripening and superlattice structural transformations in the dried state.

Assembly at air–liquid and liquid–liquid interfaces is driven by a complex interplay of entropic⁵⁵⁴ and enthalpic forces influencing particle diffusion, crystallographic orientation, superlattice structure, and distribution of ligands within the

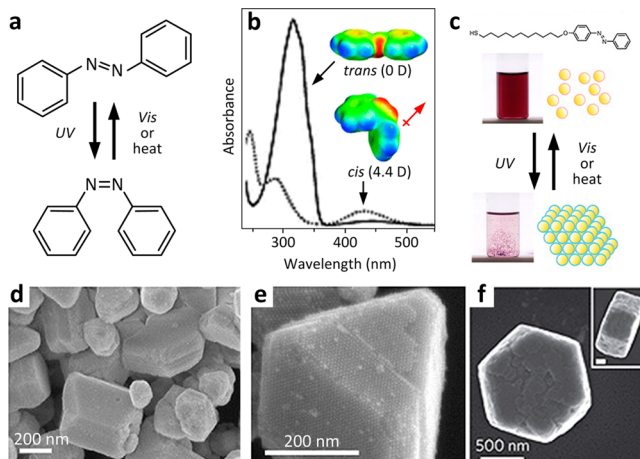


Figure 45. Reversible, light-triggered self-assembly of nanocrystals capped with surface ligands featuring azobenzene terminal groups. (a) Lewis structure of the azobenzene photoisomerization process. (b) Absorption spectrum for *trans* (solid trace) and *cis* (dotted trace) azobenzene isomers with calculated electron density maps inset. Adapted with permission from ref 547. Copyright 2011 Royal Society of Chemistry. (c) Molecular structure of an azobenzene switch tethered to alkanethiol nanocrystal surface binding moiety (top) and photos of the flocculation behavior of Au nanocrystals modified with such ligands. Adapted with permission from ref 75. Copyright 2007 National Academy of Sciences. (d–f) SEM images of faceted polyhedral superlattices obtained by irradiation of switch-functionalized Au nanocrystals. Adapted with permission from ref 75. Copyright 2007 National Academy of Sciences. Adapted with permission from ref 548. Copyright 2015 Nature Publishing Group.

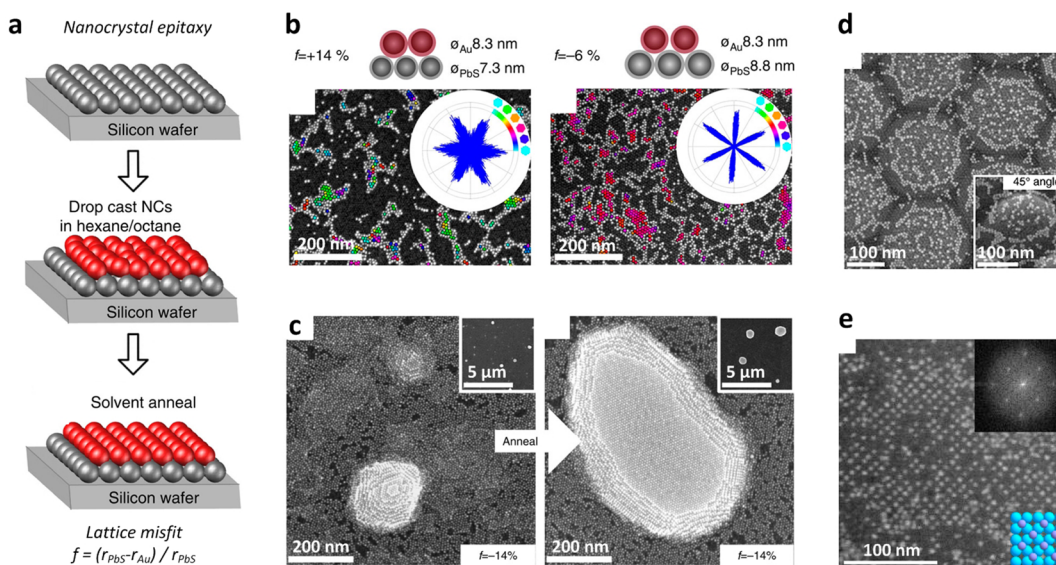


Figure 46. Nanocrystal epitaxy: assembly over patterned support. (a) Schematic showing the deposition of a base lattice (PbS nanocrystals, gray spheres) followed by an adlayer (Au nanocrystals, red spheres) and relaxation via solvent annealing. The difference in sizes of base layer and adlayer determines the epitaxial growth mode. (b) Tracked SEM images and bond angle plots (inset) reveal that adlayer alignment improves for small lattice mismatch and smaller adlayer nanocrystals. (c) Large lattice misfit favors island growth at submonolayer adlayer coverage. (d) PbS nanocrystal adlayer draped over 230 nm polystyrene beads forms a curved base layer. At low coverage, the Au adlayer nanocrystals are localized near areas with zero curvature in rings around the beads. (e) Deposition of Au nanocrystals over a square base lattice results in a $(\sqrt{2} \times \sqrt{2})R45^\circ$ surface reconstructed non-close-packed adlayer. Adapted with permission from ref 566. Copyright 2014 Nature Publishing Group.

assembly. Trapping micrometer-sized colloidal particles at an air–water interface creates thermally activated fluctuations leading to an unexpectedly large viscous drag, slowing down Brownian motion.⁵⁵⁵ In the case of assembly at a liquid–liquid interface, subphase polarity and surface tension have been shown to influence superlattice crystallographic orientation. For example, smectic B liquid crystals of CdSe/CdS nanorods may be assembled with the rod director in the substrate plane by using glycerol subphase, while diethylene glycol subphase shows a strong preference for perpendicular alignment with respect to liquid support.²⁵¹ Similarly, liquid crystals of GdF₃ nanoplates form a columnar phase with the nanocrystal flat surfaces contacting the interface (lying down) when tri- or tetraethylene glycol is used as liquid subphase, while ethylene and diethylene glycol subphases lead to the lamellar phase with nanocrystal edges contacting the liquid–liquid interface (standing up).⁵⁵³

Along these lines, the presence of excess surfactants was found to play a key role in setting the orientation of TiO₂ nanocrystals self-assembled into two-dimensional superlattices at the hexane–glycol interface.⁵⁵⁶ Similarly, ordering of hexagonal bipyramid- and bifrustum-shaped ZnS nanocrystals at the toluene–air interface results in two-dimensional superlattice sheets that both minimize interfacial free energy and maximize the surface tiling density.⁵⁵⁷ Furthermore, tuning the polarity of the ligand shell enables control over the superlattice structure of octahedral Ag nanocrystals assembled at a water–oil interface: with polar PVP ligands, densely packed monolayers assemble over a water subphase, while with nonpolar hexadecanethiol ligands, an open structure with minimal nanocrystal–water contact is formed.⁵⁵⁸ Manipulating the interfacial behavior of Ag nanocubes by controlling the ratio of hydrophilic/hydrophobic molecules added in a binary thiol mixture during the surface functionalization step allows continuous tuning of the nanocube orientation at an oil/

water interface from planar to tilted and standing configurations, leading to square close-packed and open linear and hexagonal superlattices.⁵⁵⁹ Finally, subphase polarity can influence even molecular details of the ligand shell: superlattice membranes assembled from hydrocarbon-capped Au nanocrystals on water surface concentrate methylene segments on the side opposite that exposed to polar subphase,⁵⁶⁰ causing the membrane to fold toward the water-exposed side following electron beam exposure.

10.2. Self-Assembly on Patterned Surfaces

The preceding treatment of assembly and interfaces discussed systems with flat surfaces. In this case surface tension favors a smooth interface between immiscible liquids, and atomic-scale roughness of solid supports is small compared to the diameter of typical nanocrystals. Evaporating a nanocrystal solution over a surface with texture size on the order of the particle diameter presents another strategy for structural control. For example, capillary forces may be used to trap solvated nanocrystals in the recessed regions of lithographically patterned templates.^{561–563} Such patterns control the position and number of nanocrystals within a cluster⁵⁶⁴ and selectively guide formation of contacts between nanocrystals of different shapes.⁵⁶⁵ In addition, sequential deposition of nanocrystal layers (nanocrystal epitaxy⁵⁶⁶) enables templated assembly without top-down lithographic pattern generation. In this approach, a base layer of nanocrystals immobilized by plasma treatment serves to guide the assembly of a second layer (Figure 46a). Adlayer registry with underlying pattern is determined by lattice misfit (Figure 46b), dewetting is favored for strongly interacting particles (Figure 46c), and sparse nanocrystal arrays may be patterned by using a curved (Figure 46d) or non-close-packed base layer (Figure 46e).

10.3. Self-Assembly Aided by Curved Surfaces

Assembly of colloidal particles on spherical surfaces is particularly rich, for example using the interface of emulsion droplets, among many other templating techniques.⁵⁶⁷ The resultant structures, first explored using micrometer colloids and then referred to as colloidosomes,^{568,569} are hollow, elastic shells with controlled permeability and elasticity. By varying the size and volume fraction of the nanocrystals and ligand chemistry, superlattices form at nonplanar interfaces where either enthalpy or entropy controls the resulting geometry.⁵⁷⁰ In Pickering emulsions, droplets are stabilized by the nanoparticles, which is possible even using anisotropic hematite microcrystals, which align depending on their shape.⁵⁷¹ The resulting microcapsules have unusual mechanical properties.⁵⁷² Toward higher density interfacial elastic instabilities occur,⁵⁷³ and crowding and jamming of nanocrystals⁵⁷⁴ stabilize liquid drops in nonequilibrium states.⁵⁷⁵ Nanocrystal monolayers have been desorbed mechanically from droplets within milliseconds using acoustic pressure generated from ultrasound,⁵⁷⁶ and nanofluidics can assist in the production of droplets.⁵⁷⁷ Highly stable vesicles of gold nanocrystals have been obtained by confinement on hydrophobic fullerene bilayers.⁵⁷⁸ Colloidosomes can also be formed with other shapes, might be only partially filled, and can be used as microreactors (or “colloidal eggs”) for superlattice growth.⁵⁷⁹ Similar yolk/shell assemblies occur when a binary mixture of Au nanocrystals (size ratio between 1:2 and 1:6) segregates such that the large particles are contained within a shell of small particles.⁵⁸⁰

Rod-like particles are also well-suited to form complex ordered patterns on spherical surfaces.⁵⁸¹ In past experiments, CuO nanoribbons have been shown to form dandelion-shaped structures,⁵⁸² vanadium pentoxide nanocrystals to form hollow microspheres,⁵⁸³ and two-segment gold-polypyrrole nanorods to assemble into kinetically controlled, shape-directed, shell-like superstructures.⁵⁸⁴ Fe-soc-MOF (metal–organic frameworks) assemble into partially ordered colloidosomes via a single-step emulsion-based approach.⁵⁸⁵ Aggregation on curved surfaces has also been coupled with subsequent growth to create new superparticles. The adsorption of positively charged ZnO nanocrystals onto the negatively charged surface of carboxylated polystyrene microspheres and growth of ZnO nanowires leads to hedgehog particles.⁵⁸⁶ Finally, polymer balls can be selectively loaded at the surface or in the core with nanocrystals to achieve diagnostically active nanodisco balls.⁵⁸⁷

10.4. Self-Assembly under Spherical and Other Confinement

The three-dimensional volume in which particles are immersed influences the assembly of nanocrystal clusters and superlattices.^{588,589} Analogous to guided monolayer assembly by nanocrystal confinement at a subphase surface, three-dimensional superlattices have been templated by confinement within emulsion droplets,⁵⁹⁰ nanoliter droplets inside a microfluidic capillary⁵⁹¹ or within evaporating droplets. Emulsification has been accomplished by mechanical shearing of water and nanocrystal solution in the presence of surfactant stabilizer.⁵⁹² Heating the emulsion removes low-boiling nonpolar phase, inducing superlattice assembly by increasing the nanocrystal volume fraction within the droplets. Using this approach, it was shown that entropy-driven assembly of nanocrystals, typically favoring formation of fcc arrays in extended superlattices, gives rise to multiply twinned superlattices with icosahedral

symmetry under three-dimensional confinement.⁵² Such multi-domain structures can be compared to polyhedral nanocrystal superlattices obtained by enthalpy-driven assembly³⁷ and small highly symmetric nanoassemblies stabilized by the competition of long-range hydrophobic attraction and short-range steric repulsion forces.⁵⁹³ Multiple-twinned clusters are the lowest energy states⁵⁹⁴ in systems of small gold nanocrystals⁵⁹² and close-packed zerovalent metal clusters (e.g., Au₅₅) comprised of a central atom encircled by n Mackay-cluster shells⁵⁹⁵ with the n th shell containing $(10n^2 + 2)$ spheres.⁵⁹⁶

Using 6 nm CoFe₂O₄ nanocrystals as a model system to study entropic self-assembly under spherical confinement, it was determined that the number of nanocrystals per cluster strongly influences the packing arrangement. The smallest clusters were found to be icosahedra consisting of 20 (111)-terminated fcc domains distorted slightly from tetrahedral geometry to share faces and fill the icosahedron interior (Figure 47a), while intermediate-sized clusters are rhombicosidodecahedra, built upon icosahedra by adding pentagonal and rectangular faces via surface reconstruction (Figure 47b). Because these two shapes are more spherical than the cuboctahedron (isoperimetric quotients of 0.83, 0.94, and 0.74), hard spheres enjoy access to more of the sphere interior when arranged in multiply twinned icosahedral clusters. However, when clusters contain a large number of particles, lattice strain associated with solid angle deficiency destabilizes icosahedral packing, driving the transition to the fcc structure found in nonconfined extended superlattices (Figure 47c). This phase behavior has been reproduced by simulations of hard spheres in spherical confinement (Figure 47d) and studied quantitatively using electron tomography.⁵⁹⁷

Polyhedra in spherical confinement exhibit a wide variety of symmetry point groups and high-symmetry, magic number clusters depending on particle geometry,⁵⁹⁸ while confined mixtures of nanoparticles can form binary superlattices and under pressure phase separate into Janus or core–shell supraparticles.⁵⁹⁹ Confinement is also possible in nonspherical geometries: Pt nanocrystals form rings around oblate droplets

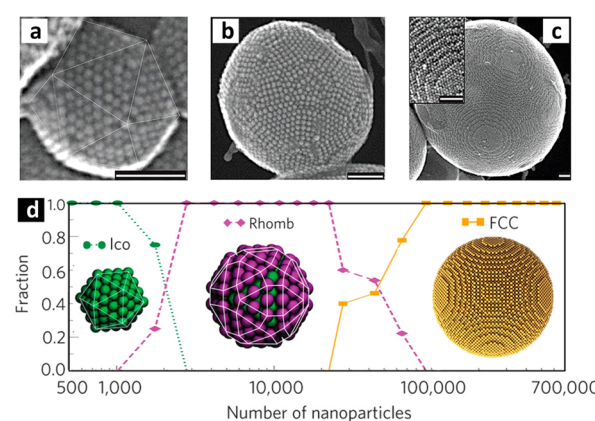


Figure 47. Self-assembly of polyhedral superlattice clusters by spherical confinement. (a) STEM image of multiply twinned icosahedral cluster containing fewer than 10^3 CoFe₂O₄ nanocrystals. (b) STEM image of multiply twinned rhombicosidodecahedral cluster containing on the order of 10^4 nanocrystals. (c) STEM image of single-crystalline fcc cluster containing more than 10^5 nanocrystals. (d) Size dependence of cluster structure obtained by simulations of hard spheres under confinement. Scale bars: 50 nm. Adapted with permission from ref 52. Copyright 2014 Nature Publishing Group.

of ethylenediaminetetraacetic acid (EDTA) dispersed in water.⁶⁰⁰ In this experiment, EDTA serves both as the ligands inhibiting nanocrystal aggregation and as the confining medium. An example of confinement in one-dimensional tubes is the ordering of nanorods within or in the matrix between cylindrical microdomains of block copolymer-based supramolecular assemblies.^{601,602} In addition, polystyrene-tethered gold nanocrystals in submicrometer-wide anodic aluminum oxide cylindrical nanopores assemble into regular and irregular strings.^{603,604} The defining parameter is the ratio of cylinder diameter to nanocrystal diameter, D_C/D_{NC} . The findings can be compared with densest packings of hard spheres in cylinders.⁶⁰⁵

10.5. Self-Assembly in Structure-Directing Media

In addition to direct attachment of polymer molecules to the nanocrystal surface (section 9), noncovalent approaches of interfacing inorganic particles with organic structure-directing matrixes⁶⁰⁶ are enabled by using (co)polymers^{607–609} or copolypeptides⁶¹⁰ containing segments that have affinity for nanocrystal ligands. Optimally, removal of native ligands is not necessary for producing such composites, since ligand exchange reactions can disrupt important properties of nanocrystals. Along these lines, block copolymer molecules with long aliphatic moieties, for example, polystyrene-*b*-poly(4-vinyl pyridine) (PS-*b*-P4VP) with 3-pentadecylphenol (PDP) attached via hydrogen bonding between alcohol and amine units (Figure 48a), have been used for such a purpose.⁶¹¹ Mixing this supramolecule with hydrocarbon-capped nanocrystals in chloroform, drop casting the solution, and annealing at 100 °C yield ordered block copolymer arrays with nanocrystals assembled at the center of P4VP-PDP nanodomains (Figure 48b,c). This block copolymer system has also been used to confine hydrocarbon-capped nanorods within cylindrical P4VP-PDP domains in end-to-end geometry.⁶⁰² While nanocrystal incorporation in the dilute limit can be treated as a small perturbation to block copolymer thermodynamic assembly, significant particle loading (>10% v/v) disturbs the ability of the polymer matrix to assemble into phases expected for pure copolymer melt (Figure 48d).⁶¹²

Alternative approaches to block copolymer-guided nanocrystal self-assembly are possible by exchanging native nanocrystal surface ligands for custom molecules with affinity for one of the polymer blocks,^{613,614} or by stripping ligands and coassembling using block copolymers with nucleophilic segments that bind to the bare nanocrystal surface.^{615,616} Such introduction of favorable enthalpic interactions represents an effective strategy for obtaining nanocomposites with high particle loading fraction. When assembled, either the nanocrystals or the polymer matrix can form the functional domain of the composite, while the other component fills the remaining space. Removal of organic component by thermal degradation⁶¹⁷ or solvent extraction⁶¹⁸ of polymer template enables production of ordered, nanoporous inorganic solids.

Liquid crystals (e.g., nematic-phase 4-cyano-4'-pentylbiphenyl) represent another class of structure-directing matrixes for nanocrystal self-assembly, enabling control over position, orientation, and aggregation behavior of plate-shaped nanocrystals.⁶¹⁹ Combining competing long-range elastic and electrostatic interactions in a nematic fluid host leads to triclinic pinacoidal lattices of orientationally ordered semiconductor nanorods.⁶²⁰ Their lattice periodicity can grow more than an order of magnitude larger than the nanocrystal size,

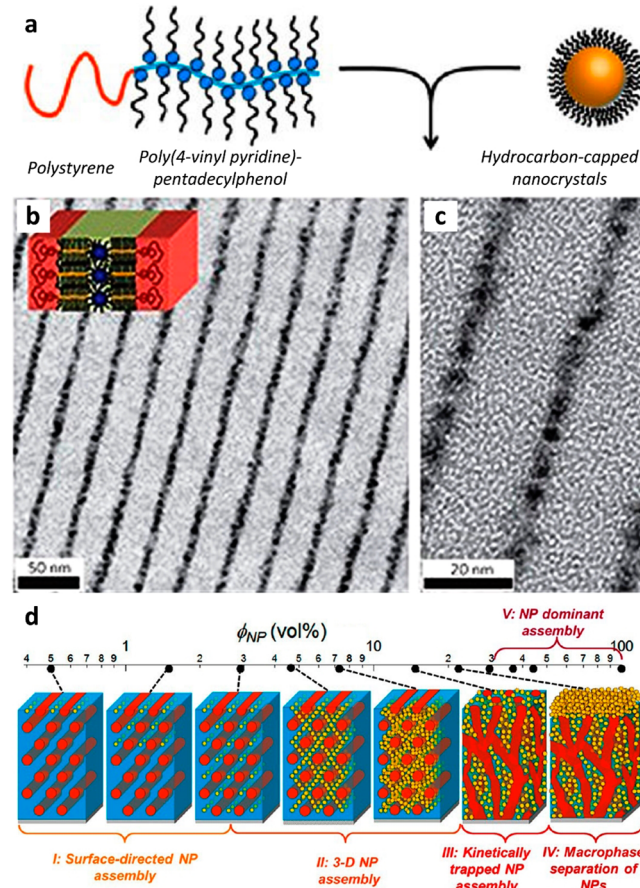


Figure 48. Self-assembly of hydrocarbon-capped nanocrystals guided by a diblock copolymer matrix. (a) Cartoon of a PS-*b*-P4VP(PDP) supramolecule (left) that features pentadecyl brush segments compatible with the native hydrocarbon ligands capping the surface of as-synthesized nanocrystals (right). (b) TEM overview and structural model (inset) of the nanocrystal-block copolymer composite produced by spin-casting a solution of block copolymer and CdSe nanocrystals in chloroform and subsequent solvent annealing of the deposited solid. (c) TEM zoom of (b) revealing nanocrystals confined within the center of P4VP-PDP lamellae. (d) Concentration dependence of composite phase behavior: nanocrystals minimally perturb the development of block copolymer nanodomains at low volume fraction (left), while higher loading prevents block copolymer-dominated assembly (right). Adapted with permission from ref 611. Copyright 2009 Nature Publishing Group. Adapted from ref 612. Copyright 2015 American Chemical Society.

which corresponds to a very low packing factor smaller than 1%. On a larger scale, micrometer-sized colloids have been shown to feel the directionality of the nematic liquid crystal and can assemble into crystals, bound by defects.^{621,622}

10.6. Depletion-Driven Self-Assembly

While destabilization-based assembly of nanocrystals has typically been carried out by introducing attractive interparticle interactions via reduction of solvent affinity for surface ligands, entropic destabilization is another means to direct superlattice formation. The depletion effect is achieved by adding small, noninteracting cosolutes (depletants) to the solution, which cause an attractive depletion force between large colloidal nanocrystals. This force arises because the depletant center of mass cannot access the solution within one depletant radius around the surface of an isolated nanocrystal (Figure 49a),

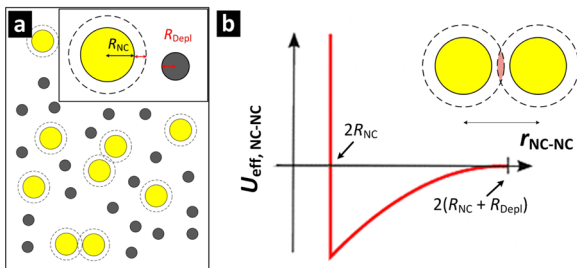


Figure 49. Entropic destabilization of nanocrystal colloids. (a) Cartoon of nanocrystals (yellow) and smaller species (gray) that cannot access the exclusion zone (dotted line) around the nanocrystal surface. Inset: key showing the relevant length scales of nanocrystal and depletant radius. (b) Effective interaction between nanocrystals immersed in a bath of depletants. At the onset of the exclusion zone overlap, nanocrystals experience an effective attraction (right side). Steric repulsion prevents the overlap of the cores upon contact between nanocrystal surfaces (left side of curve). Adapted with permission from ref 623. Copyright 2014 AIP Publishing.

inset). Overlap of such exclusion zones increases the volume of solution available to the depletants, lowering the free energy of the system by increasing the depletant translational entropy (Figure 49b). The result is an effective osmotic pressure of the solution inducing precipitation of the nanocrystals even in good solvent for the nanocrystal surface ligands. For example, phosphonate-capped CdSe/CdS nanorods have been assembled into superlattice sheets by addition of oleic acid (0.5–1.0 M) to an initially clear nanocrystal solution in toluene.²⁷²

According to the Asakura–Oosawa model,⁶²⁴ the potential energy arising from depletion of micelles between two particles at contact scales as the product of the excluded volume and concentration of micelles in solution. Geometrically speaking,

the excluded volume is greatest for large interparticle contact area, i.e., contact between low-curvature surfaces. As a result, the addition of depletants is an effective approach to separate size and shape impurities from a crude nanocrystal synthesis mixture.⁶²⁵ Depletion is also important for the self-assembly of binary nanocrystal mixtures. The addition of depletants stabilizes superlattices that maximize contact area and/or the number of contacts between larger species.

The manipulation of directional forces via surfactant micelle-induced depletion interaction aligns nanocrystal facets and leads to additional geometric control and tunability.^{208,280} It is also a pathway toward avoiding unwanted mechanical deformation. Depending on the thickness of PVP ligands, Pd cubes assemble into a superlattice that continuously transforms between a simple cubic phase and a rhombohedral phase.²⁴⁸ An effective rounding or truncation of cube edges and vertices causes a shear of the superlattice, as also found with platinum nanocubes,⁶²⁶ increasing the effective packing density.^{184,627–629} Adding poly(ethylene oxide) (PEO) depletants suppresses this shear, as demonstrated for micrometer-sized hollow silica cubes grown around hematite templates.⁶³⁰ Simulations suggest that leveraging the distribution of interparticle voids with polymeric additives can favor either of the two polymorphs, distinguishing the close-packed superlattices fcc and hcp or competing open superlattices.^{631,632} Finally, while the use of depletion is a purely physical effect that is based on entropy maximization, adding other additives allows controlling nanocrystal assembly chemically. For details and ideas we refer to a recent review.⁶³³

10.7. Self-Assembly in External Electric, Magnetic, or Electromagnetic Field

Another means of directing self-assembly of colloidal nanocrystals involves the use of external fields.⁶³⁴ In this case, the particles experience a rotational force (torque) favoring parallel

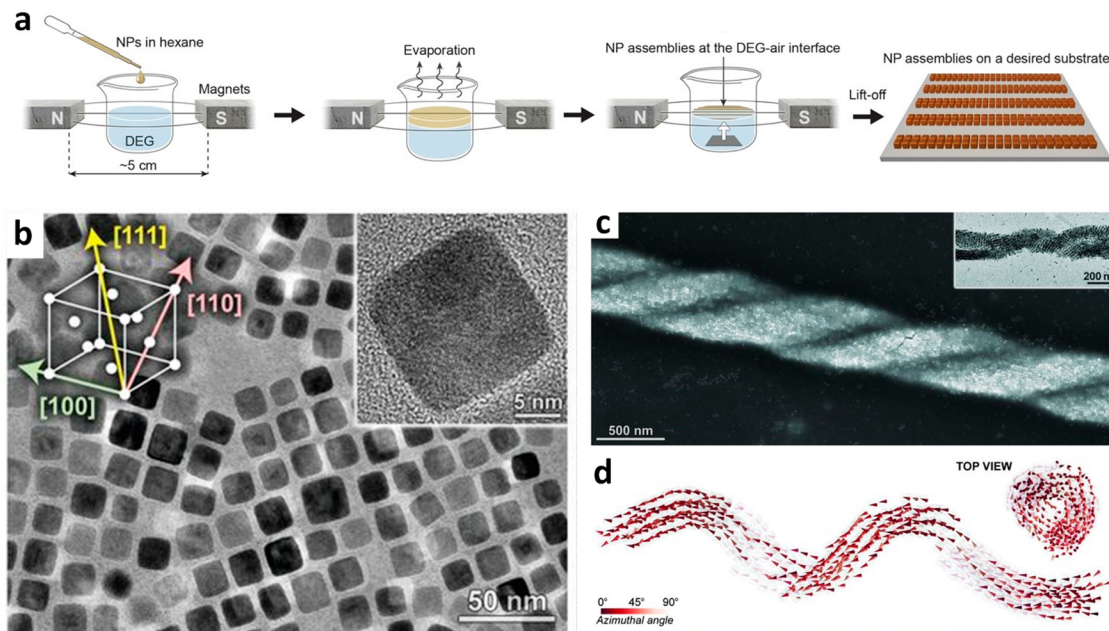


Figure 50. Self-assembly of magnetic nanocubes in external magnetic field. (a) Schematic of experimental setup, whereby a hexane solution of nanocrystals is evaporated between two magnets. (b) TEM image of 13 nm Fe_3O_4 rounded nanocubes used in assembly. The (111)-, (110)-, and (100)-crystallographic axes are easy, intermediate, and hard axes of magnetization, respectively. (c) SEM image of double helix, with TEM image inset. (d) Snapshots from Monte Carlo simulations of a one-dimensional belt folding into a helix. Adapted with permission from ref 55. Copyright 2014 American Association for the Advancement of Science.

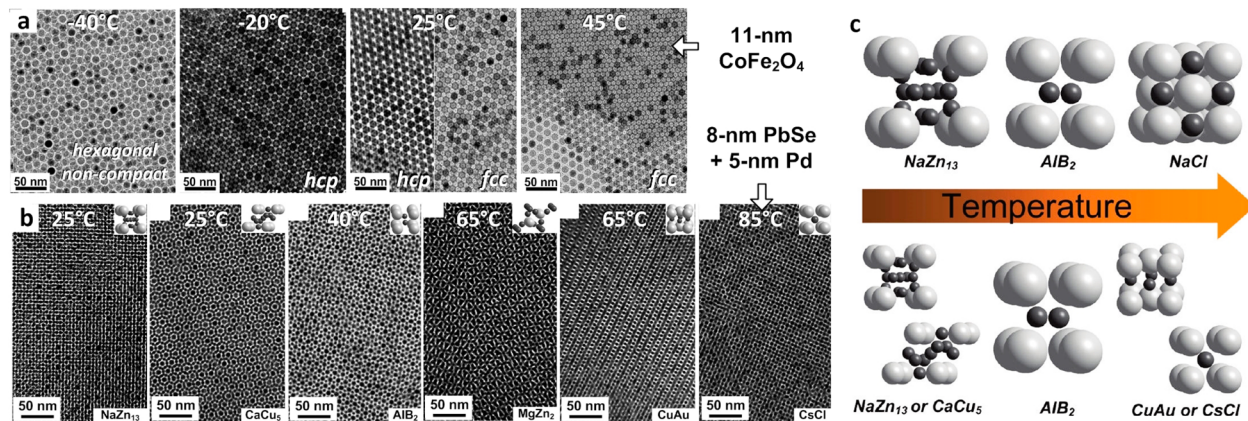


Figure 51. Temperature-dependent phase behavior of spherical nanocrystals. (a) Evaporating a solution of 11 nm CoFe_2O_4 nanocrystals at -40°C yields non-close-packed superlattices, while increasing the solution temperature during evaporation yields hcp or fcc arrangements. (b) Evaporating a binary solution of 7.7 nm PbSe and 4.9 nm Pd ($\gamma_{\text{eff}} = 0.74$) yields cluster phases (NaZn_{13} , CaCu_5) at low temperature and interstitial phases (CuAu, CsCl) at higher temperature. (c) Schematic illustration of the effect of temperature tuning on the binary phase behavior of a semiconductor–semiconductor system (top, TEMs not shown) and a semiconductor–metal system (bottom, corresponding TEMs shown in (b)). Adapted from ref 62. Copyright 2010 American Chemical Society.

alignment of the nanocrystal permanent electric or magnetic dipole moment with the external field. Evaporating a solution of nanocrystals in the presence of such a field condenses prealigned particles into superlattices with orientational registry of dipole moments. For example, drying a toluene solution of CdS nanorods spread between electrodes produces single-layer and multilayer smectic B liquid crystals with the rod long axis along the direction of the applied electric field.⁶³⁵ The application of an external field also aligns flat surfaces of the rods, facilitating close-packing. Micrometer-sized polyhedral metal–organic framework crystals align in an electric field into only one-dimensional locked chains that otherwise remain uncorrelated,⁶³⁶ an observation distinct from their behavior in the absence of the external field.⁶³⁷ Furthermore, particles have been guided into specific locations for assembly, for example via the use of positive ac dielectrophoresis into narrow gaps,⁶³⁸ a phenomenon also observed in simulation.⁶³⁹ With a spatially varying magnetic field Fe_3O_4 nanocrystals were aligned into parallel line patterns on the surface of a disk medium.⁶⁴⁰

When the nanocrystal dipole moment and close-packing direction are not aligned, complex superstructures can develop. For example, evaporation-based assembly of cube-shaped 13 nm Fe_3O_4 nanocrystals in the presence of an external magnetic field yields one-dimensional superlattice helices (Figure 50). Such braided, chiral structures appear to be a natural compromise between the system's entropic preference for face-to-face packing of cubes and the energetic drive to align the nanocrystal magnetic easy axis (cube diagonals) with the long dimension of the one-dimensional superstructure. Similar braided structures have also been found to assemble from aqueous dispersions of 4 nm CdTe truncated tetrahedra passivated with thioglycolic acid. In such systems, exposure to ambient light leads to photooxidation and attachment of particle surfaces, ultimately producing twisted ribbons with equal distribution of left- and right-handed chirality.⁶⁴¹ On the other hand, when a racemic dispersion of such particles is illuminated by circularly polarized light, enantioselective photoactivation takes place, resulting in the formation of chiral twisted ribbons with $\sim 30\%$ enantiometric excess.⁶⁴²

Helix formation even occurs without an external field in nanorods due to the solvent conditions,⁴⁰⁰ depletion,⁶⁴³ a

switch of interfacial tension,⁶⁴⁴ ligand interaction, template by peptides,⁶⁴⁵ or the chirality of the nanocrystal itself,⁶⁴⁶ or induced by racemic polymers through selective adsorption on the surface of nanocrystals.⁶⁴⁷ Several other, non-field-assisted methods exist to achieve one-dimensional assemblies.⁶⁴⁸

When the induced magnetic dipolar interaction and the interaction between the magnetic dipoles of cubes and the external field are small, on the order of the thermal energy and van der Waals forces, then other structures such as chains, ribbons, sheets, and large cuboids have also been observed.^{649–651} Buckling of chains⁶⁵² and cross-linking⁶⁵³ occurs only at sufficiently strong fields. Along these lines, fluctuating electromagnetic fields can induce a van der Waals torque, which leads to oriented attachment of cubic or spherical BaTiO_3 nanocrystals.⁶⁵⁴ Interestingly, light-controlled self-assembly is possible using nonphotoresponsive nanoparticles by using a photoswitchable medium that responds to light in such a way that it modulates the interparticle interaction.^{75,656}

10.8. Temperature Control of Nanocrystal Self-Assembly

Tuning solution thermal energy offers another route to control phase behavior of colloidal nanocrystals. For example, even in good solvent for ligands, formation of small nanocrystal clusters is common, particularly for strongly interacting (e.g., metal) core materials with high-curvature surfaces (i.e., small-diameter nanocrystals).¹⁴³ Because osmotic pressure from corona overlap increases with temperature, heating nanocrystal solutions encourages dispersal, and cooling induces flocculation. Along these lines, controlled chilling of nanocrystal solution is, to our knowledge, an unexplored technique for self-assembly, and might be expected to produce superlattices similar to the nonsolvent destabilization approach. On the other hand, tuning the temperature of evaporating nanocrystal solution has been shown to have a strong effect on superlattice phase behavior.⁶² For example, spherical nanocrystals evaporated from low temperature solution assemble into noncompact superlattices, while at elevated temperatures close-packed phases are observed (Figure 51a). Furthermore, the clustering of strongly interacting nanocrystals in solution at room temperature favors the formation of cluster-incorporating (e.g., NaZn_{13} or CaCu_5) BNSLs, while elevated temperatures

promote binary phases featuring metal nanocrystals occupying interstitial sites more evenly distributed (Figure S1b,c).

Thermal annealing can induce superlattice phase transitions even long after solvent drying. For example, Korgel and co-workers demonstrated that heating of monodisperse close-packed Au nanocrystals up to above 200 °C can result in Ostwald ripening, yielding bidisperse nanocrystal ensembles that self-assemble in the solid state into pseudo-Frank–Kasper CaCu₅ and NaZn₁₃ BNSLs.²⁴¹ In a similar follow-up work, Pileni and co-workers observed thermal-ripening-induced solid-state assembly at temperatures in the range 25–130 °C into, among other phases, the Frank–Kasper MgZn₂ structure.⁵⁵³ Such thermal coalescence of nanocrystal cores and concomitant structural changes are irreversible. On the other hand, fully reversible thermal toggling of superlattice structures was recently demonstrated by the Korgel group. In this intriguing experiment, a disordered solid of slightly polydisperse, octadecanethiol-capped Au nanocrystals was coaxed into adopting a bcc lattice at moderately elevated (60 °C) temperatures, while ordering was diminished again upon cooling back to room temperature.⁶⁵⁷ The authors proposed that the Au core polydispersity can be softened by the molten nanocrystal corona, facilitating ordering of the nanocrystals above the melting temperature of octadecyl chains. Freezing of chains upon superlattice cooling, however, induces formation of hydrocarbon bundles and prevents the necessary uniform distribution of segments throughout the superlattice matrix. Interestingly, the opposite trend is observed for polydisperse Ag nanocrystals capped with end-functionalized liquid crystal molecules: bcc superlattices undergo a reversible order–disorder transition order upon heating to 120 °C.⁶⁵⁸

11. MESOSCALE PATTERNS ARISING FROM NONEQUILIBRIUM DRYING EFFECTS

Rationalizing the behavior of colloidal nanocrystals as an equilibrium phase of hard or soft shapes presents a thermodynamic treatment of self-assembly. While such an approach offers valuable guidelines for anticipating the likely arrangement of particles within a superlattice domain, it makes no prediction of the mesoscale morphology of nanocrystal films formed by solvent evaporation. The patterns formed over several micrometers reflect the fact that initial and final states of self-assembly (i.e., particles immersed in fluid and immobilized in dried nanocrystal solid) are bridged by an intermediate stage where nanocrystals are deposited by the receding solvent front. As a result, formation and evolution of the liquid–solid–vapor contact lines across the support play an important role in determining the spatial patterns of nanocrystal solid left behind after solvent evaporation.

11.1. Drying-Mediated Assembly: Vapor Phase Nucleation and Domain Coarsening

Evaporative assembly has originally been explored for colloidal spheres with techniques such as capillary crystallization, which uses capillary forces to trap and organize particles in the recessed regions of a template,^{659,660} and more recently via convective steering,^{254,661–663} which employs convective flow induced by the evaporation of the solvent at the contact line. When using a solid substrate and in the presence of capillary flow, nonequilibrium effects can be dominant for large colloidal particles leading to aggregation at the contact line and irregular mesoscale morphologies.^{664,665} Similar, albeit weaker, crowding at the interface and ordering also occurs with nanocrystals

during rapid evaporation.^{574,666} However, provided nanocrystal diffusion is much faster than solvent evaporation (i.e., movement of the contact line), the particles are gathered in the areas of receding solvent. The patterns observed after evaporation are thus a reflection of the solvent drying history.⁷⁹

In the heterogeneous limit of solvent evaporation, vapor bubbles nucleate and grow on the surface of the support. On the other hand, rapid formation and coalescence of vapor phase occurs in the homogeneous limit. In this case, evaporation takes place by spinodal (i.e., barrierless) nucleation and coarsening of the vapor phase (analogous to quenching an Ising magnet below its critical temperature⁶⁶⁷) and leads to islands at low coverage, bicontinuous fingering networks at intermediate coverage, and voids (inverse islands) at high nanocrystal coverage (Figure 52a, left to right). The drive to shrink the total length of domain walls results in coarsening, whereby sharp features (e.g., small islands, high-curvature fingers) are straightened out by coalescence, increasing the characteristic length scale of the features (Figure 52b). This process occurs only if the domain boundaries remain wet with solvent, enabling the movement of particles across the interface. Coalescence of domains is halted after drying, freezing the

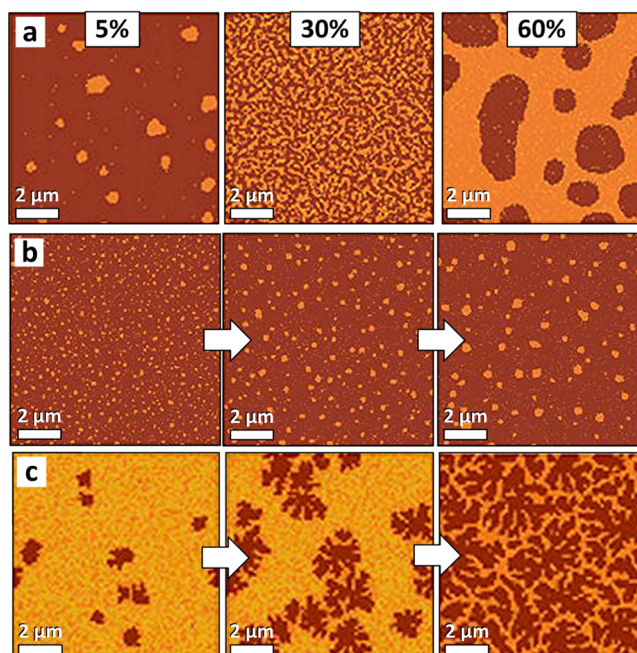


Figure 52. Spatial patterns resulting from Monte Carlo simulation of drying-mediated self-assembly of nanoparticles. (a) Influence of surface concentration (labeled at top) on drying pattern formed for a spatially uniform distribution of vapor nuclei (homogeneous evaporation) and nanoparticles remaining mobile at domain boundaries. At low concentration, disk-like islands are formed; at intermediate concentration, bicontinuous fingering patterns emerge; at high concentration, disk-shaped voids are observed. (b) Simulation trajectory of island growth by coalescence at 10% nanoparticle surface concentration under the same conditions of homogeneous evaporation and fluxional domain boundaries. (c) Simulation trajectory under heterogeneous solvent evaporation and with nanoparticles immobilized at domain edges. Such conditions favor growth of dendritic nanoparticle solids with fractal shapes. Each cell marks an independent nucleation event whose front pushes nanoparticles to boundaries of adjacent cells. Adapted with permission from ref 79. Copyright 2003 Nature Publishing Group.

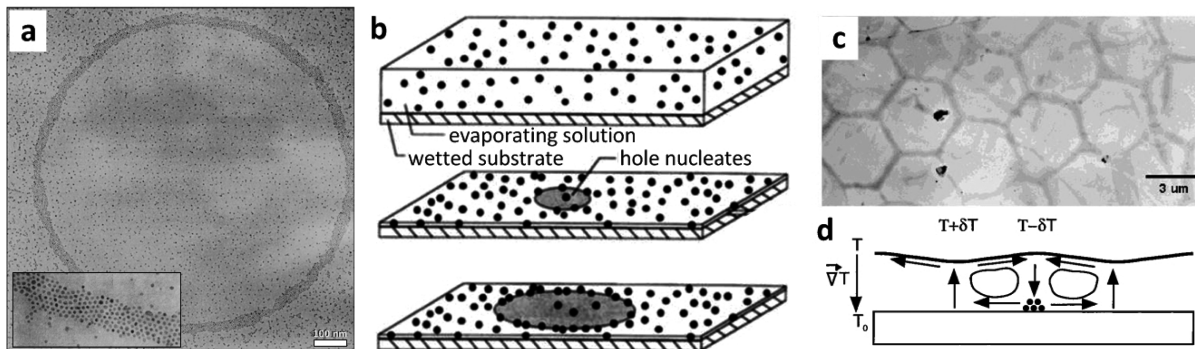


Figure 53. Assembly of ring patterns and hexagonal networks. (a) TEM overview of a 1- μm -diameter ring formed by evaporation of a hexane solution of 3 nm dodecanethiol-capped Ag nanocrystals. Inset: zoom of the annulus revealing particle ordering. (b) Sketch of the ring formation mechanism. Adapted with permission from ref 670. Copyright 1997 John Wiley and Sons. (c) TEM of a hexagonal network formed by evaporation of a dilute chloroform solution of 4 nm dodecanethiol-capped Au nanocrystals. Adapted from ref 671. Copyright 2001 American Chemical Society. (d) Sketch of the network formation mechanism. Adapted from ref 672. Copyright 2000 American Chemical Society.

system in its final state. However, if domain boundaries immobilize the peripheral particles, coarsening cannot occur. In this case, sharp features are preserved after solvent evaporation, resulting in branched fractal structures reminiscent of diffusion-limited aggregation (Figure 52c).¹⁰²

11.2. Rings and Networks: Visualizing Experimental Drying Dynamics

If the coarsening of features is prevented by rapid drying, the system can be frozen in a state that provides some clues about the dynamics of solvent evaporation. For example, rings of nanocrystals deposited by evaporation of nanocrystals in hexane point to solvent evaporation by nucleation and growth of vapor bubbles (Figure 53a,b). Similarly, water microdroplets that condense on the surface of nonpolar solvents from humid air have been used to template rings of gold nanorods.⁶⁶⁸ Rapid drying also gives rise to a temperature gradient, and thus a surface tension gradient, between the air–liquid and the liquid–substrate interface. When the resulting force exceeds solvent viscous forces, heat transfer from underlying warmer surface occurs no longer by diffusion but by convective motion of the liquid (the Marangoni effect). This instability in the fluid film can lead to steady-state flow pattern of hexagonally ordered convective cells, depositing nanocrystals at cell boundaries (Figure 53c,d). Recently, ultraviolet light has been used to exert spatial control over Marangoni flows circulating within a sessile droplet, enabling deposition of nanocrystals in predefined positions on the substrate.⁶⁶⁹

11.3. Striped Nanocrystal Films: Controlled Contact Line Instability

Harnessing such nonequilibrium effects for regular spatial patterning of nanocrystal films is of practical interest. To this end, unidirectional sweeping of the air–liquid–substrate contact line (meniscus) across a subphase is an effective approach to creating striped nanocrystal films. In one example, evaporation of a nanocrystal solution over a liquid subphase forms regularly spaced ridges of uniform height and pitch containing nanocrystals in close-packed arrangement (Figure 54a,b). The proposed mechanism for such a pattern formation is stick–slip motion of the meniscus. As the growing solid nanocrystal film slides across the liquid subphase, the contact line oscillates between stretched and relaxed states, resulting in rapid evaporation of solvent and deposition of ridge nanocrystals when the meniscus is stretched by a pinning force (Figure 54c). The stick–slip instability thus produces stripes

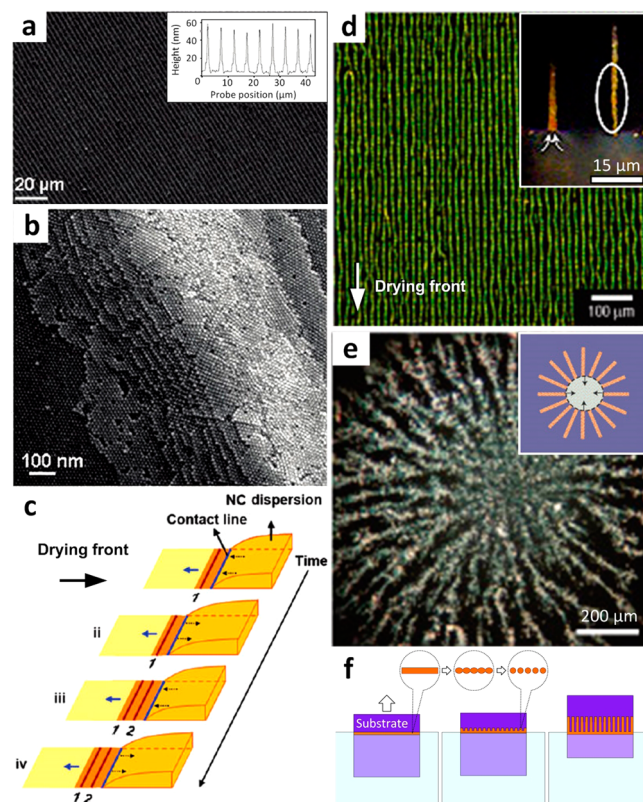


Figure 54. Deposition of striped nanocrystal films. (a) SEM overview of a striped film of 10 nm Fe_3O_4 nanocrystals formed by stick–slip motion of the air–liquid–substrate contact line. Inset: AFM height profile. (b) SEM zoom of a single stripe ridge. (c) Schematic of the stick–slip mechanism of stripe formation. Adapted from ref 674. Copyright 2011 American Chemical Society. (d) Optical micrograph overview of a striped film of 50 nm Ag nanocrystals coated with poly(vinylpyrrolidone) formed by the fingering instability. Inset: zoom of the drying front, showing stripes (circled) formed by nanoparticles carried toward the wet tips (arrows) of the growing stripes. (e) Spoke pattern formed by evaporation of a sessile droplet. Inset: schematic of the spoke pattern stripe formation. (f) Schematic of stripe formation by vertical deposition. Only nanoparticles at the water–substrate contact line (gold dots) are shown for clarity. Adapted with permission from ref 675. Copyright 2005 Nature Publishing Group.

parallel to the air–liquid–substrate contact line, and can be used to deposit lines of even single-particle thickness.⁶⁷³

Stripe-patterning perpendicular to the contact line was demonstrated by exploiting the fingering instability at the drying front. Uniform stripe formation by this mechanism has been achieved by withdrawing a dilute film of hydrophobic Ag nanocrystals floating on water surface (Figure S4d). In addition, stripes radiating from a central point have been produced by evaporating a standing water droplet covered with the same dilute nanocrystal film (Figure S4e). In these cases, the continuous line of particles at the air–liquid–substrate contact line segregates into more concentrated, periodically distributed domains of nanoparticles (Figure S4f).

12. UNIQUE PROPERTIES OF ORDERED NANOCRYSTAL SOLIDS

Nanocrystal self-assembly has presented researchers with several intriguing puzzles. Explaining the diversity of the observed structures made from nanocrystals (sections 5–11) requires a rationale that invokes a combination of hard and soft matter ordering principles as well as kinetic and environmental effects. Beyond the fundamental questions, however, lies a practical motivation: the structural hierarchy and compositional tunability of nanocrystal superlattices provides these materials with novel electronic, optical, mechanical, and catalytic functionality for nanotechnological applications. Realizing this potential remains the ultimate goal of nanoscience.^{23,676,677} Just as the factors governing crystal structures of bulk solids (e.g., atomic radius, chemical valence) are inextricably linked to properties of practical importance (e.g., electron affinity, ionization energy, polarizability), controlling the position, orientation, and chemical composition of nanocrystal components thus promises a versatile design platform for custom high-performance materials.

12.1. Controlled Mixing of Nanocrystal Electronic States

Semiconductor nanocrystal superlattices, for example from metal chalcogenide nanocrystals (quantum dots⁶⁷⁸), are candidates for materials with optoelectronic applications such as light-emitting devices (LEDs), photodetectors, and solar cells.^{676,679} Mixing of electronic states between nanocrystals, analogous to the development of molecular orbitals by overlap of atomic wave functions, is crucial for this purpose (Figure 55). Unfortunately, superlattices of nanocrystals with traditional hydrocarbon stabilizers cannot be directly used. The ligand bilayers separate the nanocrystals too far and act to electronically isolate neighboring particles from one another, creating a high tunnel barrier for charge transport among neighboring nanocrystals. As a result, the electronic and optical properties of the superlattices are often similar to those of the isolated building blocks. Weak coupling gives rise to Anderson localization,⁶⁸⁰ contributing to the presence of midgap electronic trap states. Stronger electronic coupling between nanocrystals is expected to improve charge carrier mobility by suppressing domain localization and may reveal experimental signatures for new collective phenomena in nanocrystal assemblies obscured so far by averaging over a range of coupling strengths.

A reduction in tunneling barrier height has been achieved by exchanging the hydrocarbon ligands used for synthesis with compact, nucleophilic species (e.g., $\text{Sn}_2\text{S}_6^{4-}$, SCN^- , S^{2-}) that offer electrostatic stabilization of nanocrystals in polar media and narrow interparticle separation in nanocrystal solids.^{39–41} Unfortunately, in contrast to nanocrystals stabilized by (nonconductive) charged aliphatic ligands, experimental

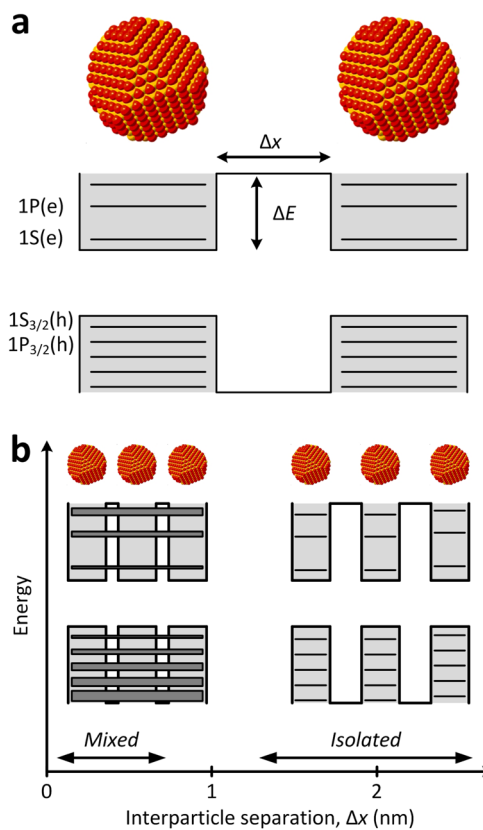


Figure 55. Control over the development of collective electronic states. (a) Sketch of two CdSe nanocrystals (top) and their quantized electronic states (bottom) separated by an interparticle matrix of barrier height ΔE and surface-to-surface distance Δx . (b) Schematic illustration of the spatial extension of electronic wave functions upon reduction in Δx . Adapted with permission from ref 679. Copyright 2015 Nature Publishing Group.

conditions for reliable assembly of nanocrystals stabilized with such compact, charged ligands have yet to be established. Current investigations are restricted to films of short-range-ordered particles. It was observed that this new class of surface ligands “silences” grain boundaries in nanostructured solids and enables mobility of charge carriers approaching that of single crystals.⁶⁸¹ Nevertheless, self-assembly of nanocrystals with novel ligand chemistries into ordered arrays remains the ultimate goal. Currently available superlattices have structural disorder that results in low-coordination sites that electronically couple weakly with their nearest neighbors.

A recent development is the creation of epitaxially connected quantum dot films that are obtained by removing the native ligands to induce neck formation (i.e., atomic connections) of specific nanocrystal facets.^{341,679,682,683} The generated percolating network of quantum dots connected by atomic bonds has an electronic structure that is distinct from that of arrays of quantum dots coupled by ligand molecules.⁶⁸⁴ Theoretical analysis in this work concludes that charges are coherently delocalized along segments with a length near 30 nm and charge transport occurs by incoherent charge transfer steps. The localization of electrons at defects⁶⁸⁵ has to be considered, and future work requires overcoming limitations, possibly through more uniform epitaxial connections to improve the properties of these quasi-two-dimensional quantum dot solids.

12.2. Orientational Ordering of Nanocrystals for Luminescence Applications

Self-assembly offers the ability to orient nanocrystals along a common crystallographic axis, a feature that may be exploited in device applications. For example, CdSe nanocrystals experience a sharp transition from plane polarized to linearly polarized emission when the nanocrystals are slightly elongated.⁶⁸⁶ Assembly of such nanocrystals into smectic superlattice films can be directed by shape anisotropy^{73,251} (sections 7.2 and 7.3), by solvent flow or external fields^{635,687} (section 10.7), alignment via direct mechanical rubbing of nanocrystal layer,⁶⁸⁸ dispersal in stretched polymer matrix^{689,690} (section 10.4), and nematic liquid crystal solvents.⁶⁹¹ Arrays of unidirectionally aligned nanorods are materials with strong polarization anisotropy across cm²-sized areas (Figure 56). Long-range orientational registry of nanocrystals with linearly polarized emission³⁵⁵ is useful for improving the efficiency of liquid crystal displays (LCDs). Current technology relies on filtering light from an unpolarized source, resulting in half the photons rejected by the first polarizer in the LCD stack. Orientationally aligning luminescent nanorods can increase the fraction of backlight photons reaching the viewer by absorbing unpolarized light and reemitting polarized light.

12.3. Plasmon Resonance under Electromagnetic Excitation

The collective oscillation of free electrons, typically in noble-metal nanocrystal superlattices, the so-called plasmon reso-

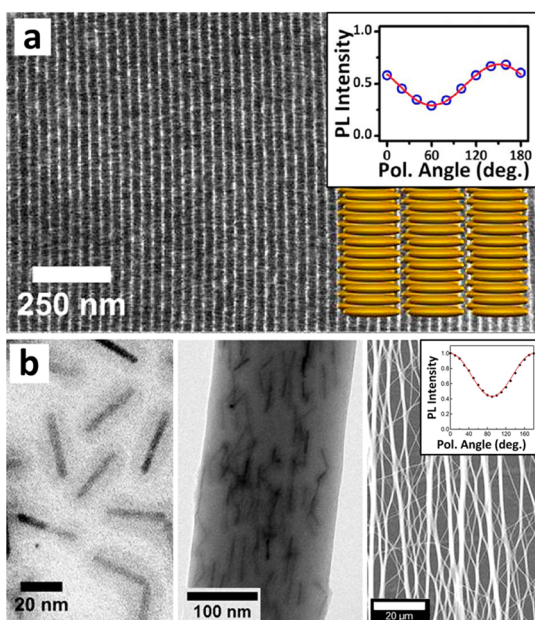


Figure 56. Long-range orientational alignment of anisotropic nanocrystals for lighting and display applications. (a) TEM overview of a horizontally oriented smectic B superlattice of 28 nm × 6 nm CdSe/CdS dot-in-rod nanocrystals capped with octadecylphosphonic acid ligands. Inset: measured photoluminescence intensity of an about 1- μm^2 -sized area of the superlattice under rotating, linearly polarized excitation source (top), and cartoon of horizontal rod packing orientation (bottom). Adapted from ref 251. Copyright 2015 American Chemical Society. (b) CdSe/CdS dot-in-rod nanocrystals encapsulated in a silica shell (left) align within electrospun polymer spindles (middle), which in turn have been aligned across cm² areas for polarized emission applications (right). Adapted from ref 690. Copyright 2015 American Chemical Society.

nance, provides a feasible way to realize light concentration and manipulation on a small scale.⁶⁹² The coupling of electromagnetic fields with a superlattice is mediated by surface plasmons, depends on the shape and arrangement of the nanocrystals,⁶⁹³ and is sensitive to the presence of local chirality in assemblies,⁶⁹⁴ as found for example in films formed by Au nanorod template by cholesteric (chiral) liquid crystalline cellulose nanocrystals.^{695,696} In another example, achiral Au/Ag core/shell nanocubes act as plasmonic reporters of chirality for attached DNA molecules by providing two orders of magnitude circular dichroism enhancement in the near-visible region.⁶⁹⁷ Furthermore, superparticles of polystyrene-stabilized noble metal nanocrystals can have optical properties that are highly sensitive or remarkably independent of cluster orientation,⁶⁹⁸ depending on particle number and cluster geometry.⁶⁹⁸ Superlattices of Au nanorods with plasmonic antennae enhancement of the electrical field can detect prions in biological media such as serum and blood.⁶⁹⁹ Similarly, in BNSLs the strength of near-field plasmonic coupling can be engineered by varying the nanocrystal size, composition, and the lattice symmetry of BNSLs, leading to broadband spectral tunability of the collective plasmonic response of BNSLs across the entire visible spectrum.⁷⁰⁰ An application of the plasmon resonance is the surface-enhanced Raman scattering (SERS) effect, which allows sensitive detection of trace chemical or biological species⁷⁰¹ and in Au nanostructures again depends on the nanocrystal core shape.^{702,703} Recent work included nanocrystal–polymer composites⁷⁰⁴ and expands the study of plasmonic coupling to semiconductor disks.⁷⁰⁵

DNA-based nanostructures are promising candidates for developing self-assembled plasmonic materials.^{706,707} Recently plasmonic photonic crystals have been explored as a way to couple light and plasmon interactions by independently adjusting lattice constants and Au nanocrystal diameters,⁷⁰⁸ as well as crystal habit (external shape)⁷⁰⁹. Two distinct optical modes can be controlled independently: a gap mode between the particle and the surface and a lattice mode that originates from cooperative scattering of many nanocrystals in the array.⁷¹⁰

12.4. Multicomponent Assemblies for Synergistic Effects

Colloidal nanocrystals have chemical and physical functionality of the inorganic core screened from the external environment by a passivating layer of surface ligands. Cocrystallization into a variety of superlattices with precise interparticle separation, stoichiometry, and lattice symmetry integrates this functionality and offers a compelling platform to explore interactions between chemically distinct nanocrystals.

One important class of multifunctional nanomaterials is the semiconductor–metal system. Interaction between luminescent semiconductor nanocrystals and plasmons from nearby metal nanostructures can lead to strong fluorescence enhancement or quenching of emission depending on the spatial arrangement of the components, as well as the energies of exciton and plasmon modes. For example, placement of luminescent CdSe/CdS nanocrystals within a polymer matrix atop a metallic film with nanoscale roughness increases the nanocrystal fluorescence intensity 30-fold when plasmonic and luminescent components are separated by about 35 nm.⁷¹¹ On the other hand, close-packing of semiconductor and metal nanocrystals into binary nanocrystal superlattices results in much narrower separations on the order of 2 nm (Figure 57a). Optical studies of AlB₂ BNSLs comprised of CdSe and Au nanocrystals revealed a

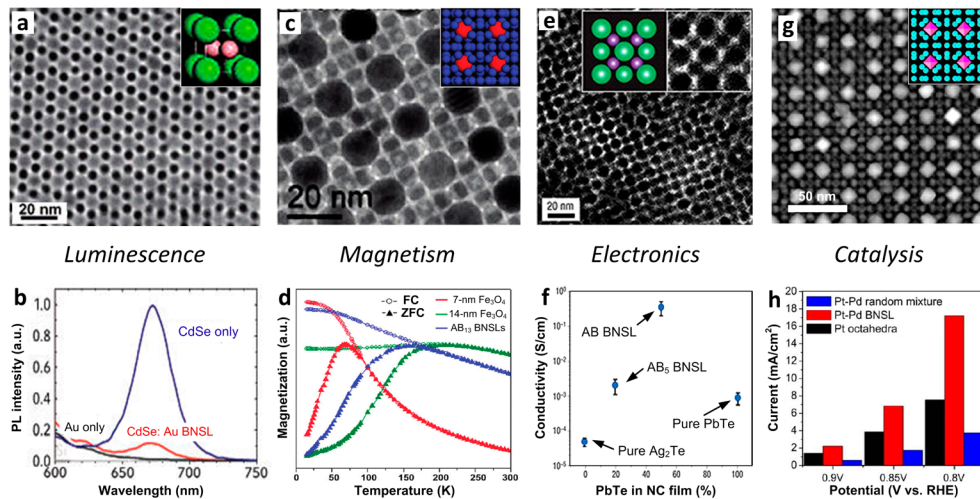


Figure 57. Nonadditive optical, magnetic, electronic, and catalytic properties of binary nanocrystal superlattices. (a) TEM image of an AlB_2 binary superlattice comprised of 9 nm CdSe and 6 nm Au nanocrystals capped with native hydrocarbon ligands. Inset: modeled AlB_2 unit cell. (b) Measured photoluminescence of Au (black trace), CdSe (blue), and CdSe + Au binary solid (red) under 405 nm excitation. Adapted from ref 715. Copyright 2008 American Chemical Society. (c) TEM image of a NaZn_{13} binary superlattice comprised of 14 and 7 nm Fe_3O_4 nanocrystals. Inset: modeled NaZn_{13} unit cell. (d) Field-cooled (FC) and zero-field-cooled (ZFC) magnetization curves of separate packings of 14 nm (green trace) and 7 nm Fe_3O_4 nanocrystals (red), and the two nanocrystal species packed together in a binary superlattice (blue). Adapted from ref 712. Copyright 2010 American Chemical Society. (e) TEM image of a NaCl-type binary superlattice comprised of 10 nm PbSe and 5 nm Ag_2Te after hydrazine and thermal annealing treatments. Inset: modeled NaCl unit cell (left) and TEM zoom of binary structure (right). (f) Conductivity of pure-phase Ag_2Te and PbSe nanocrystal superlattices, as well as AB and AB_5 binary superlattices, averaged over at least 12 devices. Adapted with permission from ref 716. Copyright 2007 Nature Publishing Group. (g) TEM image of NaZn_{13} binary superlattice comprised of 13 nm octahedral Pt nanocrystals and 6 nm spherical Pd nanocrystals. Inset: modeled unit cell. (h) Bar chart of the kinetic current density of the oxidation reduction reaction for single-component and binary nanocrystal films deposited on a rotating disk electrode. Adapted from ref 717. Copyright 2013 American Chemical Society.

fluorescence intensity of just 5–15% of that of pure CdSe superlattices when a similar number of quantum dots is excited (Figure 57b). Time-resolved emission transients show a considerably shorter emission lifetime for CdSe nanocrystals embedded in metal-containing arrays, suggesting creation of an additional nonradiative decay channel via energy transfer to the surrounding Au nanocrystals in the binary array.

Self-assembly of magnetic nanocrystals into ordered superlattices, with individual nanocrystals stable against spontaneous magnetization reversal at room temperature, is a promising approach to increase the density of magnetic data storage.⁸ Naturally, understanding the interactions between close-packed magnetic particles is important to the development of this field. Along these lines, cocrystallization of two sizes of magnetic nanocrystals has been shown to yield BNSLs (Figure 57c) with single-phase-like magnetization alignment⁷¹² and shows one-phase magnetization switching behavior and magnetoresistance switching behavior below 200 K.⁷¹³ Although separate arrays of the two nanocrystal components have different blocking temperatures, determined by the maximum in zero-field-cooled magnetization curves (Figure 57d), the BNSLs show zero-field-cooled curves with just a single peak. Such an effect is attributed to the collective dipolar interaction between nanocrystal components, suggesting magnetic moments of the smaller nanocrystals are pinned to those of the larger nanocrystal sublattice. Along these lines, BNSLs represent a promising route to produce exchange-spring magnets, nanocomposites in which grains of magnetically hard (high-coercivity) materials are embedded in a magnetically soft (low-coercivity) matrix. For example, cocrystallization of FePt and Fe_3O_4 nanocrystals and thermal annealing to remove organic ligands produced a binary solid of hard FePt and soft Fe_3Pt with significantly

higher magnetic performance than either material on its own.⁷¹⁴

Compositional mixing by cocrystallization of various nanocomponents also presents unique possibilities for tuning the electronic properties of nanocrystal solids. Generally, superlattices produced by self-assembly of nanocrystals capped with hydrocarbon surface ligands possess very low conductivity ($G < 10^{-11} \text{ S/cm}$, ref 60). Chemical activation of nanocrystal solids by treatment with small molecules that displace insulating native ligands and reduce interparticle spacing (e.g., hydrazine,⁶⁰ thiocyanate⁸⁵) is required to increase conductivity. In some cases, such treatment is sufficiently gentle to preserve the nanocrystal superlattice packing arrangement. However, significant volume contraction and concomitant cracking of nanocrystal films is generally unavoidable, though they may be partially addressed through repeated deposition steps.

The structure and composition of nanocrystal superlattices appear to strongly affect electronic properties such as conductivity by altering the number of charge carriers and/or carrier mobility through the solid. For example, following film exposure to hydrazine and mild thermal annealing at 150 °C, the conductivity of binary superlattices comprised of PbTe and Ag_2Te nanocrystals (Figure 57e) was found to be up to a factor of 10³ larger than that of corresponding single-component films treated the same way (Figure 57f).⁷¹⁶ It was suggested that intimate intermixing of the distinct nanocrystal components may give rise to surface transfer p-type doping. Structure-dependent conductivity has also been observed in thermally annealed BNSL membranes containing Fe_3O_4 and FePt nanocrystals across AlB_2 and NaZn_{13} packing arrangements.⁶⁴ Compositionally mixed, ordered nanocrystal solids also provide a platform for tuning conductivity via establishment of percolation networks through a host lattice. This concept was

demonstrated using PbSe nanocrystal superlattices containing metal nanocrystals in random positions as substitutional point defects within the PbSe matrix.⁸⁵ Following solid-state thiocyanate film treatment, the conductivity was modulated over six orders of magnitude, from 10^{-6} S/cm for pure PbSe films to 10^1 S/cm for PbSe containing about 17% metal nanocrystals, the number of nanocrystals required to establish long-range connectivity between randomly distributed metal nanocrystals.

Heterogeneous catalysis is another area that can greatly benefit from self-assembly of compositionally heterogeneous nanocrystal superlattices.⁷¹⁸ Contact with a metal oxide surface, for example, makes otherwise-inert Au nanocrystals highly catalytically active for the oxidation of carbon monoxide.⁷¹⁹ Binary superlattices with a high density of interfacial contact area offer an attractive platform for engineering such catalytic contacts, as demonstrated using Pd–Pt⁷¹⁷ and Au–Fe₃O₄⁷²⁰ material pairs. In the first example, hydrocarbon-capped octahedral Pt nanocrystals, terminated by catalytically active Pt(111) facets, were cocrystallized with spherical Pd nanocrystals into binary superlattices (Figure 57g). Treating these Pt–Pd binary superlattices with UV/ozone and thermal annealing at 180 °C removed the surface ligands and established contact between metal nanocrystal surfaces, yielding a nanostructured solid capable of catalyzing the reduction of oxygen to water several times faster than the largely phase-separated random mixture or sample with no Pd nanocrystals present (Figure 57h). In the second case, Au nanocrystals were cocrystallized with Fe₃O₄ nanocrystals to yield binary superlattices that are capable of catalyzing oxidation of carbon monoxide. Importantly, the superlattice structural framework provides spatial separation of Au nanocrystals by the more thermally stable metal oxide nanocrystals. For example, while heating to 200 °C is sufficient to initiate sintering, coalescence and loss of catalytic activity occur for close-packed Au nanocrystals or disordered binary solids. In contrast, when packed between Fe₃O₄ nanocrystals in binary superlattices, the size of Au nanocrystals is preserved up to 400 °C, a sufficient operating temperature for most industrial catalytic processes. Yet another example is the coassembly of Pt and CeO₂ nanocubes on a silica substrate to catalyze methanol decomposition to produce CO and H₂ on the CeO₂–Pt interface, which is subsequently used for ethylene hydroformylation catalysis by the nearby Pt–SiO₂ interface.⁷²¹ Furthermore, binary superlattices offer structural control over sintering, allowing coalescence within, but not across, clusters.³⁴⁵

Self-assembly has been proposed as a method to achieve Pt-around-Au nanocomposite⁷²² or to purify Pt nanocrystals by colloidal recrystallization for the isolation of high quality nanocrystals with narrow size and shape distributions.⁷²³ Catalytic activity can be enhanced significantly by eroding the interior of Pt₃Ni polyhedra, partially in a superlattice, leaving only open nanoframes behind.⁷²⁴

12.5. Beyond Quantum Phenomena: Classical Transport and Mechanical Properties

The collective mechanical response of ordered nanocrystal solids is comparable to nanocrystal-filled polymers or strong plastics. Ag nanocrystals self-organized into a fcc superlattice can couple mechanically to their neighbors. If excited, they vibrate coherently.⁷²⁵ While in the case of weak bonding, the ligands become the bottleneck for phonon transport, strong

bonding can transport distortion of the superlattice more efficiently. Furthermore, the film thickness itself can quantize phonons as observed with picosecond acoustic techniques.⁷²⁶

AFM nanoindentation has been a useful technique to probe the elasticity and hardness of nanocrystal superlattices. Such experiments revealed that, for close-packed superlattices comprised of oleic acid capped PbS nanocrystals, elastic modulus and hardness both increase with increasing size of the inorganic core. Similar changes to superlattice elasticity and hardness result when the organic volume fraction is reduced by exchanging oleic acid for shorter ligands.⁷²⁷ However, this softening effect of surface ligands does not apply to chains sufficiently long to impart mechanical rigidity through backbone entanglement. For example, entanglement has been implicated in the increase of Young's modulus and fracture toughness with increasing chain length of polymers grafted to nanoparticle surfaces.^{728,729} In addition, crystallographic defects and unbound ligands present within the superlattice can soften such structures.⁷³⁰

Molecular dynamics simulations also stress the importance of the ligand end group for a macroscopic mechanical response.⁷³¹ When long-chain dithiol ligands and spherical aggregates instead of individual nanocrystals were used for self-assembly, then the nanocomposite became plastic and moldable against arbitrarily shaped masters.⁷³² Thermal hardening produced polycrystalline metal structures of controllable porosity.

Unusual mechanical behavior of highly ordered monolayers of dodecanethiol-ligated Au nanocrystals⁶¹ has been demonstrated by Jaeger and co-workers. Free-standing sheets are flexible enough to bend while draping over edges⁷² and can be excited by vibration in the megahertz range into well-defined eigenmodes like drumhead resonators.⁷³³ Au nanocrystal monolayers curled up into hollow scrolls have been indented by atomic force microscopy to extract bending and stretching moduli.⁷³⁴ Although quite flexible, because they are so thin, the monolayers' resistance to bending is much larger than standard elasticity would predict based on the in-plane stretching behavior. When attached to elastomer substrates, the same monolayers and multilayers subjected to tensile stress can be forced to fracture.⁷³⁵ With increasing particle size, the fracture strength increases, while it decreases with film thickness.

Self-assembled membranes⁷³⁶ also demonstrate selective permeability (permselectivity⁷³⁷), which has potential for applications such as ultra- and nanofiltration and chemoselective separation. Molecular transport through Au nanocrystal membranes is two orders of magnitude faster than through polymer-based filters.⁷³⁸ Au nanocrystals can control ion transport through porous polycarbonate substrates by affecting the substrate electrostatic interactions with ions at the pores.⁷³⁹ Finally, nanocrystal membranes are interesting for high performance lithium ion battery anodes.⁷⁴⁰

13. CONCLUSION AND OUTLOOK

In 1989, Bentzon and colleagues published electron microscopy images of small ordered arrays of iron oxide nanoparticles, arguably the first example of man-made nanocrystal superlattices.⁷⁴¹ Since then, the library of nanocrystal shapes, sizes, and chemical compositions expanded dramatically. New experimental techniques to produce, characterize, and manipulate nanocrystal assemblies have unlocked a stunningly diverse set of new structures. Among these are, for example, binary and ternary nanocrystal superlattices, liquid crystalline phases of nanorods and nanoplates, dense and open lattices of polyhedral

nanocrystals, and interlocked, hierarchical arrangements of branched nanostructures. Increasingly sophisticated superlattice characterizations employ tomographic reconstruction and *in situ* microscopy techniques. These advanced techniques enable ever more accurate determinations of the structure of individual nanocrystals as well as their position and crystallographic orientation within self-assembled superlattices. Beyond the basic evaporation and destabilization approaches to superlattice preparation, new techniques such as self-assembly at immiscible liquid interfaces have opened up opportunities to prepare single-crystalline superlattices across cm² areas.

A combination of forces acting between colloidal nanocrystals can generate complex and counterintuitive nanocrystal assemblies. Even the most basic nanocrystals can pack themselves into ordered phases that defy explanation using principles borrowed from colloid and polymer fields. The extent to which concepts from ordered hard and soft particle systems (e.g., void volume and the Voronoi cell area minimizations) can be merged to rationalize, and ultimately to anticipate, the results of nanocrystal assembly experiments thus remains to be established. Compounding this challenge is the dynamic nature of nanocrystal surfaces including, for example, ligand binding equilibria and the possibility of atomic surface reconstruction. Beyond the structure and chemical composition of the nanocrystal building blocks, external factors (e.g., temperature, solvent–ligand interaction, meniscus dynamics at the drying front) can play an important role in determining which superstructures are formed. So far, key advances toward understanding the complexity of the nanocrystal phase diagram are arriving in the form of qualitative observations concerning the hierarchy of interaction strengths, packing properties of rigid particles with deformable surfaces, and optimal partitioning of interparticle matrix space. The ultimate goal, creation of a quantitative theoretical framework for predicting *de novo* the outcome of an assembly experiment, given only input parameters describing essential aspects of assembling particles and their environment, will require further extensive experimental, theoretical, and computational efforts. The development of algorithms for simulations of nanocrystal self-assembly needs to be paralleled with experimental verification of predicted structures and phase diagrams using well-understood nanocrystal model systems.

Relatively little is known about postsynthetic transformations of nanocrystal superlattices. Like any ordered solid, superlattices are expected to undergo various phase transitions. Recent *in situ* GISAXS studies revealed, somewhat unexpectedly, the multistage nature of PbS nanocrystal superlattice formation: nucleation of the fcc phase from a colloidal solution was followed by transformation to a superlattice with bcc packing of individual nanocrystals.^{98,99} This example emphasizes the power of *in situ* characterization techniques for tracking the dynamic evolution of complex systems under realistic experimental conditions.

Nanocrystals typically occupy only a fraction of the entire superlattice volume, leaving behind well-defined pores that either can be filled with another functional material, for example, by using gas-phase atomic layer deposition (ALD) reactions,^{742,743} or used for filtration and separation applications.⁷³⁸ If the voids in a nanoparticle superlattice are sufficiently large, as in case of DNA-coated nanoparticles, the nanocrystal superlattice can undergo topotactic transformations where other nanocrystals enter or leave the superlattice without destroying its long-range order.⁷⁴⁴ These proof-of-concept

examples introduce exciting avenues for future research and development.

To carry nanocrystal self-assembly from an intellectual curiosity to a practical toolset, researchers in the field must fully understand and elaborate its competitive advantages over other materials systems. For example, self-assembled multicomponent nanocrystal superlattices present a convenient platform to produce precisely intermixed inorganic materials of technologically relevant compositions, offering opportunities to engineer multicomponent heterogeneous catalysts and electronic heterojunctions at the nanoscale. Furthermore, self-assembly of colloidal nanocrystals introduces a general path toward organization of matter on the 2–20 nm length scale, a particularly difficult range for both bottom-up and top-down fabrication approaches. Nanocrystal assemblies offer arrangement of functional inorganic materials (metals, semiconductors, etc.) with three-dimensional precision that exceeds the resolution of current photolithography and imprint lithography. In this capacity, nanocrystal assemblies nicely complement block copolymers⁷⁴⁵ and DNA origami,⁵¹¹ the important methodologies that enable self-organization of organic matter on comparable length scales.

To take full advantage of nanocrystal self-assembly as a means to pattern materials with feature sizes currently inaccessible by photolithography or electron beam lithography, it will be important to establish robust methods for guiding the assembly process using external stimuli and boundary conditions. Here one can borrow ideas from innovations in block copolymer lithography, for instance, the self-assembly of nanoscale polymer domains inside microscopic trenches defined by traditional lithography. Such an approach to produce sublithographic patterns guided by lithographically defined features combines advantages of bottom-up and top-down processes.⁷⁴⁶

It has recently been recognized that colloidal nanocrystals represent an important class of materials for solution-processed electronic and optoelectronic devices.⁶⁷⁶ For instance, arrays of colloidal semiconductor nanocrystals have been utilized in field-effect-transistor channels⁴³ as well as absorber layers of solar cells⁷⁴⁷ and photodetectors.⁷⁴⁸ Similarly, assemblies of metallic and magnetic nanocrystals can be utilized as solution-processed elements of plasmonic circuits and magnetic inductors.⁷⁴⁹ In all these applications, the properties of individual nanocrystals should be complemented by suitable properties of the interparticle medium. It has been shown in numerous studies that charge³⁹ and heat⁷⁵⁰ transport in nanocrystal arrays is very sensitive to the interparticle medium. Along these lines, the development of electrically conductive inorganic ligands resulted in several breakthroughs in nanocrystal electronics and photovoltaics. At the same time, realization of robust self-assembly methods for colloidal nanocrystals with electrically conductive ligands is an important and currently unresolved challenge. Thinking a step further, one can envision sophisticated engineering of organic or inorganic nanocrystal ligands with chemical, electrical, optical, magnetic, or mechanical properties complementary to those of the nanocrystal cores. In parallel, there is a growing body of exciting experimental data showing that nanocrystals can be prearranged in a superlattice and epitaxially fused into a single crystalline domain spanning many nanocrystals.^{342,685} Mastering this approach may revolutionize the engineering of epitaxial nanoheterostructures for high-performance applications.

The future for nanocrystal assemblies looks diverse and bright. We are now on the verge of realizing all-nanocrystal electronic devices and components with solution-based deposition, patterning, and integration of metallic, semiconducting, and insulating colloidal nanocrystal inks. Continued development of nontraditional surface chemistries, techniques for superlattice preparation, rationalization of phase behavior, and control of the assembly environment will help to bridge fundamental research and practical applications, opening the door to a new generation of functional materials.

AUTHOR INFORMATION

Corresponding Author

*E-mail: dvtalapin@uchicago.edu.

Author Contributions

[†]M.A.B. and M.E. contributed equally to this work.

Notes

The authors declare no competing financial interest.

Biographies

Michael Boles is a graduate student in the Department of Chemistry at the University of Chicago. He received a B.S. in chemistry from the University of North Carolina at Chapel Hill in 2010. His current research interests span the synthesis of various shapes of colloidal nanocrystals, the atomic structure and chemistry of their surfaces, and the interplay between nanocrystal core and surface properties in controlling superlattice phase behavior.

Michael Engel received his doctorate degree in physics from the University of Stuttgart, Germany, in 2008. He then joined the group of Sharon Glotzer at the University of Michigan, Ann Arbor, where he worked first as a postdoctoral fellow and later as a research scientist on problems involving self-assembling shapes, packing, and aperiodic order. Since 2016 he has been an assistant professor in the Department of Chemical and Biological Engineering at the Friedrich-Alexander-University Erlangen-Nuremberg. His research interests include studying self-organization processes of molecules, nanoparticles, soft matter, and granular matter with the help of computer simulations.

Dmitri Talapin received his doctorate degree from the University of Hamburg, Germany, in 2002. In 2003 he joined the IBM Research Division at the T. J. Watson Research Center as a postdoctoral fellow to work with Chris Murray on synthesis and self-assembly of semiconductor nanostructures. In 2005 he moved to Lawrence Berkeley National Laboratory as a staff scientist at the Molecular Foundry, and in 2007 he accepted a faculty position at the University of Chicago. He is currently a professor in the Department of Chemistry and James Franck Institute at the University of Chicago and scientist at the Center for Nanoscale Materials at Argonne National Laboratory. His research interests focus on different aspects of chemistry, physics, and applications of inorganic nanomaterials.

ACKNOWLEDGMENTS

The authors thank Maryna Bodnarchuk, Sharon Glotzer, Elena Shevchenko, Alex Travesset, Tom Witten, and Xingchen Ye for many inspiring discussions and critical comments. They also thank Tanya Shpigel for assistance obtaining figure copyright permissions. M.A.B. and D.V.T. acknowledge support from MICCoM Center funded by the Department of Energy, Basic Energy Sciences, Air Force Office of Scientific Research, under Grant FA9550-14-1-0367, National Science Foundation (NSF)

under Award No. DMR-1611371, and NSF MRSEC Program under Award No. DMR-14-20703. M.E. acknowledges funding by Deutsche Forschungsgemeinschaft through the Cluster of Excellence Engineering of Advanced Materials and support from FPS and ZISC.

REFERENCES

- (1) Min, Y.; Akbulut, M.; Kristiansen, K.; Golan, Y.; Israelachvili, J. The Role of Interparticle and External Forces in Nanoparticle Assembly. *Nat. Mater.* **2008**, *7* (7), 527–538.
- (2) Pinheiro, A. V.; Han, D.; Shih, W. M.; Yan, H. Challenges and Opportunities for Structural DNA Nanotechnology. *Nat. Nanotechnol.* **2011**, *6* (12), 763–772.
- (3) Dill, K. A.; MacCallum, J. L. The Protein-Folding Problem, 50 Years On. *Science* **2012**, *338* (6110), 1042–1046.
- (4) Chen, I. A.; Walde, P. From Self-Assembled Vesicles to Protocols. *Cold Spring Harbor Perspect. Biol.* **2010**, *2* (7), a002170.
- (5) Bates, F. S.; Hillmyer, M. A.; Lodge, T. P.; Bates, C. M.; Delaney, K. T.; Fredrickson, G. H. Multiblock Polymers: Panacea or Pandora's Box? *Science* **2012**, *336* (6080), 434–440.
- (6) Kim, S.-H.; Lee, S. Y.; Yang, S.-M.; Yi, G.-R. Self-Assembled Colloidal Structures for Photonics. *NPG Asia Mater.* **2011**, *3* (1), 25–33.
- (7) Vogel, N.; Retsch, M.; Fustin, C.-A.; del Campo, A.; Jonas, U. Advances in Colloidal Assembly: The Design of Structure and Hierarchy in Two and Three Dimensions. *Chem. Rev.* **2015**, *115* (13), 6265–6311.
- (8) Sun, S.; Murray, C. B.; Weller, D.; Folks, L.; Moser, A. Monodisperse FePt Nanoparticles and Ferromagnetic FePt Nanocrystal Superlattices. *Science* **2000**, *287* (5460), 1989–1992.
- (9) Shevchenko, E. V.; Talapin, D. V. Self-Assembly of Semiconductor Nanocrystals into Ordered Superstructures. In *Semiconductor Nanocrystal Quantum Dots*; Springer: Vienna, 2008; pp 119–169.
- (10) Murray, C. B.; Kagan, C. R.; Bawendi, M. G. Synthesis and Characterization of Monodisperse Nanocrystals and Close-Packed Nanocrystal Assemblies. *Annu. Rev. Mater. Sci.* **2000**, *30* (1), 545–610.
- (11) Pileni, M. P. Nanocrystal Self-Assemblies: Fabrication and Collective Properties. *J. Phys. Chem. B* **2001**, *105* (17), 3358–3371.
- (12) Rogach, A. L.; Talapin, D. V.; Shevchenko, E. V.; Kornowski, A.; Haase, M.; Weller, H. Organization of Matter on Different Size Scales: Monodisperse Nanocrystals and Their Superstructures. *Adv. Funct. Mater.* **2002**, *12* (10), 653–664.
- (13) Liz-Marzán, L. M.; Mulvaney, P. The Assembly of Coated Nanocrystals. *J. Phys. Chem. B* **2003**, *107* (30), 7312–7326.
- (14) Daniel, M.-C.; Astruc, D. Gold Nanoparticles: Assembly, Supramolecular Chemistry, Quantum-Size-Related Properties, and Applications toward Biology, Catalysis, and Nanotechnology. *Chem. Rev.* **2004**, *104* (1), 293–346.
- (15) Bishop, K. J. M.; Wilmer, C. E.; Soh, S.; Grzybowski, B. A. Nanoscale Forces and Their Uses in Self-Assembly. *Small* **2009**, *5* (14), 1600–1630.
- (16) Velev, O. D.; Gupta, S. Materials Fabricated by Micro- and Nanoparticle Assembly - The Challenging Path from Science to Engineering. *Adv. Mater.* **2009**, *21* (19), 1897–1905.
- (17) Claridge, S. A.; Castleman, A. W.; Khanna, S. N.; Murray, C. B.; Sen, A.; Weiss, P. S. Cluster-Assembled Materials. *ACS Nano* **2009**, *3* (2), 244–255.
- (18) Vanmaekelbergh, D. Self-Assembly of Colloidal Nanocrystals as Route to Novel Classes of Nanostructured Materials. *Nano Today* **2011**, *6* (4), 419–437.
- (19) Li, F.; Josephson, D. P.; Stein, A. Colloidal Assembly: The Road from Particles to Colloidal Molecules and Crystals. *Angew. Chem., Int. Ed.* **2011**, *50* (2), 360–388.
- (20) Hanrath, T. Colloidal Nanocrystal Quantum Dot Assemblies as Artificial Solids. *J. Vac. Sci. Technol., A* **2012**, *30* (3), 030802.

- (21) Gong, J.; Li, G.; Tang, Z. Self-Assembly of Noble Metal Nanocrystals: Fabrication, Optical Property, and Application. *Nano Today* **2012**, *7* (6), 564–585.
- (22) Xu, L.; Ma, W.; Wang, L.; Xu, C.; Kuang, H.; Kotov, N. A. Nanoparticle Assemblies: Dimensional Transformation of Nanomaterials and Scalability. *Chem. Soc. Rev.* **2013**, *42* (7), 3114–3126.
- (23) Kovalenko, M. V.; Manna, L.; Cabot, A.; Hens, Z.; Talapin, D. V.; Kagan, C. R.; Klimov, V. I.; Rogach, A. L.; Reiss, P.; Milliron, D. J.; et al. Prospects of Nanoscience with Nanocrystals. *ACS Nano* **2015**, *9* (2), 1012–1057.
- (24) Murray, C. B.; Norris, D. J.; Bawendi, M. G. Synthesis and Characterization of Nearly Monodisperse CdE (E = Sulfur, Selenium, Tellurium) Semiconductor Nanocrystallites. *J. Am. Chem. Soc.* **1993**, *115* (19), 8706–8715.
- (25) Ulman, A. Formation and Structure of Self-Assembled Monolayers. *Chem. Rev.* **1996**, *96* (4), 1533–1554.
- (26) Templeton, A. C.; Wuelfing, W. P.; Murray, R. W. Monolayer-Protected Cluster Molecules. *Acc. Chem. Res.* **2000**, *33* (1), 27–36.
- (27) Schreiber, F. Structure and Growth of Self-Assembling Monolayers. *Prog. Surf. Sci.* **2000**, *65* (5–8), 151–257.
- (28) Love, J. C.; Estroff, L. A.; Kriebel, J. K.; Nuzzo, R. G.; Whitesides, G. M. Self-Assembled Monolayers of Thiols on Metals as a Form of Nanotechnology. *Chem. Rev.* **2005**, *105* (4), 1103–1170.
- (29) Vericat, C.; Vela, M. E.; Benitez, G.; Carro, P.; Salvarezza, R. C. Self-Assembled Monolayers of Thiols and Dithiols on Gold: New Challenges for a Well-Known System. *Chem. Soc. Rev.* **2010**, *39* (5), 1805–1834.
- (30) Häkkinen, H. The Gold–Sulfur Interface at the Nanoscale. *Nat. Chem.* **2012**, *4* (6), 443–455.
- (31) Tao, A. R.; Habas, S.; Yang, P. Shape Control of Colloidal Metal Nanocrystals. *Small* **2008**, *4* (3), 310–325.
- (32) Prasad, B. L. V.; Stoeva, S. I.; Sorensen, C. M.; Klabunde, K. J. Digestive Ripening of Thiolated Gold Nanoparticles: The Effect of Alkyl Chain Length. *Langmuir* **2002**, *18* (20), 7515–7520.
- (33) Wilcoxon, J. P.; Martin, J. E.; Provencio, P. Size Distributions of Gold Nanoclusters Studied by Liquid Chromatography. *Langmuir* **2000**, *16* (25), 9912–9920.
- (34) Silvera Batista, C. A.; Larson, R. G.; Kotov, N. A. Nonadditivity of Nanoparticle Interactions. *Science* **2015**, *350* (6257), 1242477.
- (35) Piner, R. D.; Zhu, J.; Xu, F.; Hong, S.; Mirkin, C. A. “Dip-Pen” Nanolithography. *Science* **1999**, *283* (5402), 661–663.
- (36) Zhrebetsky, D.; Scheele, M.; Zhang, Y.; Bronstein, N.; Thompson, C.; Britt, D.; Salmeron, M.; Alivisatos, P.; Wang, L.-W. Hydroxylation of the Surface of PbS Nanocrystals Passivated with Oleic Acid. *Science* **2014**, *344* (6190), 1380–1384.
- (37) Rupich, S. M.; Shevchenko, E. V.; Bodnarchuk, M. I.; Lee, B.; Talapin, D. V. Size-Dependent Multiple Twinning in Nanocrystal Superlattices. *J. Am. Chem. Soc.* **2010**, *132* (1), 289–296.
- (38) Boles, M. A.; Ling, D.; Hyeon, T.; Talapin, D. V. The Surface Science of Nanocrystals. *Nat. Mater.* **2016**, *15* (2), 141–153.
- (39) Kovalenko, M. V.; Scheele, M.; Talapin, D. V. Colloidal Nanocrystals with Molecular Metal Chalcogenide Surface Ligands. *Science* **2009**, *324* (5933), 1417–1420.
- (40) Fafarman, A. T.; Koh, W.; Diroll, B. T.; Kim, D. K.; Ko, D.-K.; Oh, S. J.; Ye, X.; Doan-Nguyen, V.; Crump, M. R.; Reifsnyder, D. C.; et al. Thiocyanate-Capped Nanocrystal Colloids: Vibrational Reporter of Surface Chemistry and Solution-Based Route to Enhanced Coupling in Nanocrystal Solids. *J. Am. Chem. Soc.* **2011**, *133* (39), 15753–15761.
- (41) Nag, A.; Kovalenko, M. V.; Lee, J.-S.; Liu, W.; Spokoyny, B.; Talapin, D. V. Metal-Free Inorganic Ligands for Colloidal Nanocrystals: S^{2-} , HS^{-} , Se^{2-} , HSe^{-} , Te^{2-} , HTe^{-} , TeS_3^{2-} , OH^{-} , and NH^{2-} as Surface Ligands. *J. Am. Chem. Soc.* **2011**, *133* (27), 10612–10620.
- (42) Turk, M. E.; Vora, P. M.; Fafarman, A. T.; Diroll, B. T.; Murray, C. B.; Kagan, C. R.; Kikkawa, J. M. Ultrafast Electron Trapping in Ligand-Exchanged Quantum Dot Assemblies. *ACS Nano* **2015**, *9* (2), 1440–1447.
- (43) Lee, J.-S.; Kovalenko, M. V.; Huang, J.; Chung, D. S.; Talapin, D. V. Band-Like Transport, High Electron Mobility and High Photoconductivity in All-Inorganic Nanocrystal Arrays. *Nat. Nanotechnol.* **2011**, *6* (6), 348–352.
- (44) Choi, J.-H.; Fafarman, A. T.; Oh, S. J.; Ko, D.-K.; Kim, D. K.; Diroll, B. T.; Muramoto, S.; Gillen, J. G.; Murray, C. B.; Kagan, C. R. Bandlike Transport in Strongly Coupled and Doped Quantum Dot Solids: A Route to High-Performance Thin-Film Electronics. *Nano Lett.* **2012**, *12* (5), 2631–2638.
- (45) Zhang, Y.; Lu, F.; Yager, K. G.; van der Lelie, D.; Gang, O. A General Strategy for the DNA-Mediated Self-Assembly of Functional Nanoparticles into Heterogeneous Systems. *Nat. Nanotechnol.* **2013**, *8* (11), 865–872.
- (46) Ye, X.; Zhu, C.; Ercius, P.; Raja, S. N.; He, B.; Jones, M. R.; Hauwiler, M. R.; Liu, Y.; Xu, T.; Alivisatos, A. P. Structural Diversity in Binary Superlattices Self-Assembled from Polymer-Grafted Nanocrystals. *Nat. Commun.* **2015**, *6*, 10052.
- (47) Lee, J.; Sundar, V. C.; Heine, J. R.; Bawendi, M. G.; Jensen, K. F. Full Color Emission from II-VI Semiconductor Quantum Dot-Polymer Composites. *Adv. Mater.* **2000**, *12* (15), 1102–1105.
- (48) Dreyer, A.; Feld, A.; Kornowski, A.; Yilmaz, E. D.; Noei, H.; Meyer, A.; Krekeler, T.; Jiao, C.; Stierle, A.; Abetz, V.; et al. Organically Linked Iron Oxide Nanoparticle Supercrystals with Exceptional Isotropic Mechanical Properties. *Nat. Mater.* **2016**, *15* (5), 522–528.
- (49) Boles, M. A.; Talapin, D. V. Many-Body Effects in Nanocrystal Superlattices: Departure from Sphere Packing Explains Stability of Binary Phases. *J. Am. Chem. Soc.* **2015**, *137* (13), 4494–4502.
- (50) Boles, M. A. Self-Assembly of Colloidal Nanocrystals: Surface Ligands Promote the Formation of Unexpected Superlattices, Ph.D. Thesis, University of Chicago, Chicago, IL, 2016.
- (51) Ye, X.; Jin, L.; Caglayan, H.; Chen, J.; Xing, G.; Zheng, C.; Doan-Nguyen, V.; Kang, Y.; Engheta, N.; Kagan, C. R.; et al. Improved Size-Tunable Synthesis of Monodisperse Gold Nanorods through the Use of Aromatic Additives. *ACS Nano* **2012**, *6* (3), 2804–2817.
- (52) de Nijs, B.; Dussi, S.; Smullenburg, F.; Meeldijk, J. D.; Groenendijk, D. J.; Filion, L.; Imhof, A.; van Blaaderen, A.; Dijkstra, M. Entropy-Driven Formation of Large Icosahedral Colloidal Clusters by Spherical Confinement. *Nat. Mater.* **2014**, *14* (1), 56–60.
- (53) Paik, T.; Ko, D.-K.; Gordon, T. R.; Doan-Nguyen, V.; Murray, C. B. Studies of Liquid Crystalline Self-Assembly of GdF_3 Nanoplates by In-Plane, Out-of-Plane SAXS. *ACS Nano* **2011**, *5* (10), 8322–8330.
- (54) Miszta, K.; de Graaf, J.; Bertoni, G.; Dorfs, D.; Brescia, R.; Marras, S.; Ceseracciu, L.; Cingolani, R.; van Roij, R.; Dijkstra, M.; et al. Hierarchical Self-Assembly of Suspended Branched Colloidal Nanocrystals into Superlattice Structures. *Nat. Mater.* **2011**, *10* (11), 872–876.
- (55) Singh, G.; Chan, H.; Baskin, A.; Gelman, E.; Repnin, N.; Kral, P.; Klajn, R. Self-Assembly of Magnetite Nanocubes into Helical Superstructures. *Science* **2014**, *345* (6201), 1149–1153.
- (56) Wang, T.; Zhuang, J.; Lynch, J.; Chen, O.; Wang, Z.; Wang, X.; LaMontagne, D.; Wu, H.; Wang, Z.; Cao, Y. C. Self-Assembled Colloidal Superparticles from Nanorods. *Science* **2012**, *338* (6105), 358–363.
- (57) Pelaz, B.; Jaber, S.; de Aberasturi, D. J.; Wulf, V.; Aida, T.; de la Fuente, J. M.; Feldmann, J.; Gaub, H. E.; Josephson, L.; Kagan, C. R.; et al. The State of Nanoparticle-Based Nanoscience and Biotechnology: Progress, Promises, and Challenges. *ACS Nano* **2012**, *6* (10), 8468–8483.
- (58) Murray, C. B.; Kagan, C. R.; Bawendi, M. G. Self-Organization of CdSe Nanocrystallites into Three-Dimensional Quantum Dot Superlattices. *Science* **1995**, *270* (5240), 1335–1338.
- (59) Lin, X. M.; Jaeger, H. M.; Sorensen, C. M.; Klabunde, K. J. Formation of Long-Range-Ordered Nanocrystal Superlattices on Silicon Nitride Substrates. *J. Phys. Chem. B* **2001**, *105* (17), 3353–3357.
- (60) Talapin, D. V.; Murray, C. B. PbSe Nanocrystal Solids for N- and P-Channel Thin Film Field-Effect Transistors. *Science* **2005**, *310* (5745), 86–89.
- (61) Bigioni, T. P.; Lin, X.-M.; Nguyen, T. T.; Corwin, E. I.; Witten, T. A.; Jaeger, H. M. Kinetically Driven Self Assembly of Highly Ordered Nanoparticle Monolayers. *Nat. Mater.* **2006**, *5* (4), 265–270.

- (62) Bodnarchuk, M. I.; Kovalenko, M. V.; Heiss, W.; Talapin, D. V. Energetic and Entropic Contributions to Self-Assembly of Binary Nanocrystal Superlattices: Temperature as the Structure-Directing Factor. *J. Am. Chem. Soc.* **2010**, *132* (34), 11967–11977.
- (63) Bodnarchuk, M. I.; Kovalenko, M. V.; Pichler, S.; Fritz-Popovski, G.; Hesser, G.; Heiss, W. Large-Area Ordered Superlattices from Magnetic Wüstite/Cobalt Ferrite Core/Shell Nanocrystals by Doctor Blade Casting. *ACS Nano* **2010**, *4* (1), 423–431.
- (64) Dong, A.; Chen, J.; Vora, P. M.; Kikkawa, J. M.; Murray, C. B. Binary Nanocrystal Superlattice Membranes Self-Assembled at the Liquid–Air Interface. *Nature* **2010**, *466* (7305), 474–477.
- (65) Aleksandrovic, V.; Greshnykh, D.; Randjelovic, I.; Frömsdorf, A.; Kornowski, A.; Roth, S. V.; Klinke, C.; Weller, H. Preparation and Electrical Properties of Cobalt–Platinum Nanoparticle Monolayers Deposited by the Langmuir–Blodgett Technique. *ACS Nano* **2008**, *2* (6), 1123–1130.
- (66) Talapin, D. V.; Shevchenko, E. V.; Kornowski, A.; Gaponik, N.; Haase, M.; Rogach, A. L.; Weller, H. A New Approach to Crystallization of CdSe Nanoparticles into Ordered Three-Dimensional Superlattices. *Adv. Mater.* **2001**, *13* (24), 1868–1871.
- (67) Jaeger, H. M.; Nagel, S. R.; Behringer, R. P. Granular Solids, Liquids, and Gases. *Rev. Mod. Phys.* **1996**, *68* (4), 1259–1273.
- (68) Henzie, J.; Grünwald, M.; Widmer-Cooper, A.; Geissler, P. L.; Yang, P. Self-Assembly of Uniform Polyhedral Silver Nanocrystals into Densest Packings and Exotic Superlattices. *Nat. Mater.* **2011**, *11* (2), 131–137.
- (69) ISO/TS 80004-2:2015 Nanotechnologies - Vocabulary - Part 2: Nano-Objects. <https://www.iso.org/obp/ui/#iso:std:iso:ts:80004-2:ed-1:v1:en> (accessed June 21, 2016).
- (70) Chayen, N. E. Turning Protein Crystallisation from an Art into a Science. *Curr. Opin. Struct. Biol.* **2004**, *14* (5), 577–583.
- (71) Diroll, B. T.; Doan-Nguyen, V. V. T.; Cargnello, M.; Gaulding, E. A.; Kagan, C. R.; Murray, C. B. X-Ray Mapping of Nanoparticle Superlattice Thin Films. *ACS Nano* **2014**, *8* (12), 12843–12850.
- (72) Mueggenburg, K. E.; Lin, X.-M.; Goldsmith, R. H.; Jaeger, H. M. Elastic Membranes of Close-Packed Nanoparticle Arrays. *Nat. Mater.* **2007**, *6* (9), 656–660.
- (73) Talapin, D. V.; Shevchenko, E. V.; Murray, C. B.; Kornowski, A.; Förster, S.; Weller, H. CdSe and CdSe/CdS Nanorod Solids. *J. Am. Chem. Soc.* **2004**, *126* (40), 12984–12988.
- (74) Abécassis, B.; Tessier, M. D.; Davidson, P.; Dubertret, B. Self-Assembly of CdSe Nanoplatelets into Giant Micrometer-Scale Needles Emitting Polarized Light. *Nano Lett.* **2014**, *14* (2), 710–715.
- (75) Klajn, R.; Bishop, K. J. M.; Grzybowski, B. A. Light-Controlled Self-Assembly of Reversible and Irreversible Nanoparticle Suprastructures. *Proc. Natl. Acad. Sci. U. S. A.* **2007**, *104* (25), 10305–10309.
- (76) Zhuang, J.; Wu, H.; Yang, Y.; Cao, Y. C. Supercrystalline Colloidal Particles from Artificial Atoms. *J. Am. Chem. Soc.* **2007**, *129* (46), 14166–14167.
- (77) Ge, G.; Brus, L. Evidence for Spinodal Phase Separation in Two-Dimensional Nanocrystal Self-Assembly. *J. Phys. Chem. B* **2000**, *104* (41), 9573–9575.
- (78) Haubold, D.; Reichhelm, A.; Weiz, A.; Borchardt, L.; Ziegler, C.; Bahrig, L.; Kaskel, S.; Ruck, M.; Eychmüller, A. The Formation and Morphology of Nanoparticle Supracrystals. *Adv. Funct. Mater.* **2016**, *26* (27), 4890–4895.
- (79) Rabani, E.; Reichman, D. R.; Geissler, P. L.; Brus, L. E. Drying-Mediated Self-Assembly of Nanoparticles. *Nature* **2003**, *426* (6964), 271–274.
- (80) Chen, J.; Ye, X.; Murray, C. B. Systematic Electron Crystallographic Studies of Self-Assembled Binary Nanocrystal Superlattices. *ACS Nano* **2010**, *4* (4), 2374–2381.
- (81) Midgley, P. A.; Weyland, M. 3D Electron Microscopy in the Physical Sciences: The Development of Z-Contrast and EFTEM Tomography. *Ultramicroscopy* **2003**, *96* (3–4), 413–431.
- (82) Evers, W. H.; Friedrich, H.; Filion, L.; Dijkstra, M.; Vanmaekelbergh, D. Observation of a Ternary Nanocrystal Superlattice and Its Structural Characterization by Electron Tomography. *Angew. Chem., Int. Ed.* **2009**, *48* (51), 9655–9657.
- (83) Friedrich, H.; Gommes, C. J.; Overgaag, K.; Meeldijk, J. D.; Evers, W. H.; de Nijls, B.; Boneschanscher, M. P.; de Jongh, P. E.; Verkleij, A. J.; de Jong, K. P.; et al. Quantitative Structural Analysis of Binary Nanocrystal Superlattices by Electron Tomography. *Nano Lett.* **2009**, *9* (7), 2719–2724.
- (84) Boneschanscher, M. P.; Evers, W. H.; Qi, W.; Meeldijk, J. D.; Dijkstra, M.; Vanmaekelbergh, D. Electron Tomography Resolves a Novel Crystal Structure in a Binary Nanocrystal Superlattice. *Nano Lett.* **2013**, *13* (3), 1312–1316.
- (85) Cargnello, M.; Johnston-Peck, A. C.; Diroll, B. T.; Wong, E.; Datta, B.; Damodhar, D.; Doan-Nguyen, V. V. T.; Herzing, A. A.; Kagan, C. R.; Murray, C. B. Substitutional Doping in Nanocrystal Superlattices. *Nature* **2015**, *524* (7566), 450–453.
- (86) Panthani, M. G.; Hessel, C. M.; Reid, D.; Casillas, G.; José-Yacamán, M.; Korgel, B. A. Graphene-Supported High-Resolution TEM and STEM Imaging of Silicon Nanocrystals and Their Capping Ligands. *J. Phys. Chem. C* **2012**, *116* (42), 22463–22468.
- (87) Ross, F. M. Opportunities and Challenges in Liquid Cell Electron Microscopy. *Science* **2015**, *350* (6267), aaa9886.
- (88) Park, J.; Zheng, H.; Lee, W. C.; Geissler, P. L.; Rabani, E.; Alivisatos, A. P. Direct Observation of Nanoparticle Superlattice Formation by Using Liquid Cell Transmission Electron Microscopy. *ACS Nano* **2012**, *6* (3), 2078–2085.
- (89) Liu, Y.; Lin, X.-M.; Sun, Y.; Rajh, T. In Situ Visualization of Self-Assembly of Charged Gold Nanoparticles. *J. Am. Chem. Soc.* **2013**, *135* (10), 3764–3767.
- (90) Sutter, E.; Sutter, P.; Tkachenko, A. V.; Krahe, R.; de Graaf, J.; Arciniegas, M.; Manna, L. In Situ Microscopy of the Self-Assembly of Branched Nanocrystals in Solution. *Nat. Commun.* **2016**, *7*, 11213.
- (91) Li, B.; Zhou, D.; Han, Y. Assembly and Phase Transitions of Colloidal Crystals. *Nat. Rev. Mater.* **2016**, *1* (2), 15011.
- (92) Swart, I.; Liljeroth, P.; Vanmaekelbergh, D. Scanning Probe Microscopy and Spectroscopy of Colloidal Semiconductor Nanocrystals and Assembled Structures. *Chem. Rev.* **2016**, DOI: 10.1021/acs.chemrev.5b00678.
- (93) Ye, X.; Chen, J.; Engel, M.; Millan, J. A.; Li, W.; Qi, L.; Xing, G.; Collins, J. E.; Kagan, C. R.; Li, J.; et al. Competition of Shape and Interaction Patchiness for Self-Assembling Nanoplates. *Nat. Chem.* **2013**, *5* (6), 466–473.
- (94) Talapin, D. V.; Shevchenko, E. V.; Bodnarchuk, M. I.; Ye, X.; Chen, J.; Murray, C. B. Quasicrystalline Order in Self-Assembled Binary Nanoparticle Superlattices. *Nature* **2009**, *461* (7266), 964–967.
- (95) Li, T.; Senesi, A. J.; Lee, B. Small Angle X-Ray Scattering for Nanoparticle Research. *Chem. Rev.* **2016**, DOI: 10.1021/acs.chemrev.5b00690.
- (96) Senesi, A.; Lee, B. Scattering Functions of Polyhedra. *J. Appl. Crystallogr.* **2015**, *48* (2), 565–577.
- (97) Yager, K. G.; Zhang, Y.; Lu, F.; Gang, O. Periodic Lattices of Arbitrary Nano-Objects: Modeling and Applications for Self-Assembled Systems. *J. Appl. Crystallogr.* **2014**, *47* (1), 118–129.
- (98) Bian, K.; Choi, J. J.; Kaushik, A.; Clancy, P.; Smilgies, D.-M.; Hanrath, T. Shape-Anisotropy Driven Symmetry Transformations in Nanocrystal Superlattice Polymorphs. *ACS Nano* **2011**, *5* (4), 2815–2823.
- (99) Weidman, M. C.; Smilgies, D.-M.; Tisdale, W. A. Kinetics of the Self-Assembly of Nanocrystal Superlattices Measured by Real-Time in Situ X-Ray Scattering. *Nat. Mater.* **2016**, *15* (7), 775–781.
- (100) Diroll, B. T.; Weigandt, K. M.; Jishkariani, D.; Cargnello, M.; Murphy, R. J.; Hough, L. A.; Murray, C. B.; Donnio, B. Quantifying “Softness” of Organic Coatings on Gold Nanoparticles Using Correlated Small-Angle X-Ray and Neutron Scattering. *Nano Lett.* **2015**, *15* (12), 8008–8012.
- (101) Fritz, G.; Schädler, V.; Willenbacher, N.; Wagner, N. J. Electrosteric Stabilization of Colloidal Dispersions. *Langmuir* **2002**, *18* (16), 6381–6390.
- (102) Witten, T. A.; Sander, L. M. Diffusion-Limited Aggregation, a Kinetic Critical Phenomenon. *Phys. Rev. Lett.* **1981**, *47* (19), 1400–1403.

- (103) Lu, P. J.; Zaccarelli, E.; Ciulla, F.; Schofield, A. B.; Sciortino, F.; Weitz, D. A. Gelation of Particles with Short-Range Attraction. *Nature* **2008**, *453* (7194), 499–503.
- (104) Ambrosetti, A.; Ferri, N.; DiStasio, R. A.; Tkatchenko, A. Wavelike Charge Density Fluctuations and Van Der Waals Interactions at the Nanoscale. *Science* **2016**, *351* (6278), 1171–1176.
- (105) Hamaker, H. C. The London—Van Der Waals Attraction between Spherical Particles. *Physica* **1937**, *4* (10), 1058–1072.
- (106) Derjaguin, B. Untersuchungen Über Die Reibung Und Adhäsion, IV. *Colloid Polym. Sci.* **1934**, *69* (2), 155–164.
- (107) Israelachvili, J. N. *Intermolecular and Surface Forces*; Elsevier: Oxford, U.K., 2011.
- (108) Vincent, B.; Edwards, J.; Emmett, S.; Jones, A. Depletion Flocculation in Dispersions of Sterically-Stabilised Particles (“Soft Spheres”). *Colloids Surf.* **1986**, *18* (2–4), 261–281.
- (109) Napper, D. Steric Stabilization. *J. Colloid Interface Sci.* **1977**, *58* (2), 390–407.
- (110) Boles, M. A.; Talapin, D. V. Self-Assembly of Tetrahedral CdSe Nanocrystals: Effective “Patchiness” via Anisotropic Steric Interaction. *J. Am. Chem. Soc.* **2014**, *136* (16), 5868–5871.
- (111) MattoSSI, H.; Cumming, A. W.; Murray, C. B.; Bawendi, M. G.; Ober, R. Properties of CdSe Nanocrystal Dispersions in the Dilute Regime: Structure and Interparticle Interactions. *Phys. Rev. B: Condens. Matter Mater. Phys.* **1998**, *58* (12), 7850–7863.
- (112) Yang, Y.; Qin, H.; Peng, X. Intramolecular Entropy and Size-Dependent Solution Properties of Nanocrystal–Ligands Complexes. *Nano Lett.* **2016**, *16* (4), 2127–2132.
- (113) Yang, Y.; Qin, H.; Jiang, M.; Lin, L.; Fu, T.; Dai, X.; Zhang, Z.; Niu, Y.; Cao, H.; Jin, Y.; et al. Entropic Ligands for Nanocrystals: From Unexpected Solution Properties to Outstanding Processability. *Nano Lett.* **2016**, *16* (4), 2133–2138.
- (114) Kim, J. U.; Matsen, M. W. Interaction between Polymer-Grafted Particles. *Macromolecules* **2008**, *41* (12), 4435–4443.
- (115) Schapotschnikow, P.; Pool, R.; Vlugt, T. J. H. Molecular Simulations of Interacting Nanocrystals. *Nano Lett.* **2008**, *8* (9), 2930–2934.
- (116) Fischer, S.; Salcher, A.; Kornowski, A.; Weller, H.; Förster, S. Completely Miscible Nanocomposites. *Angew. Chem., Int. Ed.* **2011**, *50* (34), 7811–7814.
- (117) Rubinstein, M.; Colby, R. *Polymer Physics*; Oxford University Press: 2003.
- (118) Salem, L. Attractive Forces between Long Saturated Chains at Short Distances. *J. Chem. Phys.* **1962**, *37* (9), 2100–2113.
- (119) Dubois, L. H.; Nuzzo, R. G. Synthesis, Structure, and Properties of Model Organic Surfaces. *Annu. Rev. Phys. Chem.* **1992**, *43* (1), 437–463.
- (120) Mancini, G. F.; Latychevskaia, T.; Pennacchio, F.; Reguera, J.; Stellacci, F.; Carbone, F. Order/Disorder Dynamics in a Dodecanethiol-Capped Gold Nanoparticles Supracrystal by Small-Angle Ultrafast Electron Diffraction. *Nano Lett.* **2016**, *16* (4), 2705–2713.
- (121) Luedtke, W. D.; Landman, U. Structure, Dynamics, and Thermodynamics of Passivated Gold Nanocrystallites and Their Assemblies. *J. Phys. Chem.* **1996**, *100* (32), 13323–13329.
- (122) Frederick, M. T.; Achtyl, J. L.; Knowles, K. E.; Weiss, E. A.; Geiger, F. M. Surface-Amplified Ligand Disorder in CdSe Quantum Dots Determined by Electron and Coherent Vibrational Spectroscopies. *J. Am. Chem. Soc.* **2011**, *133* (19), 7476–7481.
- (123) Badia, A.; Cuccia, L.; Demers, L.; Morin, F.; Lennox, R. B. Structure and Dynamics in Alkanethiolate Monolayers Self-Assembled on Gold Nanoparticles: A DSC, FT-IR, and Deuterium NMR Study. *J. Am. Chem. Soc.* **1997**, *119* (11), 2682–2692.
- (124) Lee, B.; Podsiadlo, P.; Rupich, S.; Talapin, D. V.; Rajh, T.; Shevchenko, E. V. Comparison of Structural Behavior of Nanocrystals in Randomly Packed Films and Long-Range Ordered Superlattices by Time-Resolved Small Angle X-Ray Scattering. *J. Am. Chem. Soc.* **2009**, *131* (45), 16386–16388.
- (125) Landman, U.; Luedtke, W. D. Small Is Different: Energetic, Structural, Thermal, and Mechanical Properties of Passivated Nano-cluster Assemblies. *Faraday Discuss.* **2004**, *125* (0), 1–22.
- (126) Schapotschnikow, P.; Vlugt, T. J. H. Understanding Interactions Between Capped Nanocrystals: Three-Body and Chain Packing Effects. *J. Chem. Phys.* **2009**, *131* (12), 124705.
- (127) Travesset, A. Topological Structure Prediction in Binary Nanoparticle Superlattices. *Soft Matter* **2016**, DOI: [10.1039/C6SM00713A](https://doi.org/10.1039/C6SM00713A).
- (128) Pool, R.; Schapotschnikow, P.; Vlugt, T. J. H. Solvent Effects in the Adsorption of Alkyl Thiols on Gold Structures: A Molecular Simulation Study. *J. Phys. Chem. C* **2007**, *111* (28), 10201–10212.
- (129) Kaushik, A. P.; Clancy, P. Solvent-Driven Symmetry of Self-Assembled Nanocrystal Superlattices-A Computational Study. *J. Comput. Chem.* **2013**, *34* (7), 523–532.
- (130) Ghorai, P. K.; Glotzer, S. C. Molecular Dynamics Simulation Study of Self-Assembled Monolayers of Alkanethiol Surfactants on Spherical Gold Nanoparticles †. *J. Phys. Chem. C* **2007**, *111* (43), 15857–15862.
- (131) Schapotschnikow, P.; Hommersom, B.; Vlugt, T. J. H. Adsorption and Binding of Ligands to CdSe Nanocrystals. *J. Phys. Chem. C* **2009**, *113* (29), 12690–12698.
- (132) Djebaili, T.; Richardi, J.; Abel, S.; Marchi, M. Atomistic Simulations of the Surface Coverage of Large Gold Nanocrystals. *J. Phys. Chem. C* **2013**, *117* (34), 17791–17800.
- (133) Djebaili, T.; Richardi, J.; Abel, S.; Marchi, M. Atomistic Simulations of Self-Assembled Monolayers on Octahedral and Cubic Gold Nanocrystals. *J. Phys. Chem. C* **2015**, *119* (36), 21146–21154.
- (134) Salerno, K. M.; Ismail, A. E.; Lane, J. M. D.; Grest, G. S. Coating Thickness and Coverage Effects on the Forces Between Silica Nanoparticles in Water. *J. Chem. Phys.* **2014**, *140* (19), 194904.
- (135) Kaushik, A. P.; Clancy, P. Explicit All-Atom Modeling of Realistically Sized Ligand-Capped Nanocrystals. *J. Chem. Phys.* **2012**, *136* (11), 114702.
- (136) Widmer-Cooper, A.; Geissler, P. Orientational Ordering of Passivating Ligands on CdS Nanorods in Solution Generates Strong Rod–Rod Interactions. *Nano Lett.* **2014**, *14* (1), 57–65.
- (137) Widmer-Cooper, A.; Geissler, P. L. Ligand-Mediated Interactions between Nanoscale Surfaces Depend Sensitively and Nonlinearly on Temperature, Facet Dimensions, and Ligand Coverage. *ACS Nano* **2016**, *10* (2), 1877–1887.
- (138) Schmid, G. Large Clusters and Colloids. Metals in the Embryonic State. *Chem. Rev.* **1992**, *92* (8), 1709–1727.
- (139) Gaponik, N.; Talapin, D. V.; Rogach, A. L.; Hoppe, K.; Shevchenko, E. V.; Kornowski, A.; Eychmüller, A.; Weller, H. Thiol-Capping of CdTe Nanocrystals: An Alternative to Organometallic Synthetic Routes. *J. Phys. Chem. B* **2002**, *106* (29), 7177–7185.
- (140) Walker, D. A.; Kowalczyk, B.; de la Cruz, M. O.; Grzybowski, B. A. Electrostatics at the Nanoscale. *Nanoscale* **2011**, *3* (4), 1316–1344.
- (141) Ohara, P. C.; Leff, D. V.; Heath, J. R.; Gelbart, W. M. Crystallization of Opals from Polydisperse Nanoparticles. *Phys. Rev. Lett.* **1995**, *75* (19), 3466–3469.
- (142) Shevchenko, E. V.; Talapin, D. V.; Kotov, N. A.; O'Brien, S.; Murray, C. B. Structural Diversity in Binary Nanoparticle Superlattices. *Nature* **2006**, *439* (7072), 55–59.
- (143) Saunders, A. E.; Korgel, B. A. Second Virial Coefficient Measurements of Dilute Gold Nanocrystal Dispersions Using Small-Angle X-Ray Scattering. *J. Phys. Chem. B* **2004**, *108* (43), 16732–16738.
- (144) Luo, D.; Yan, C.; Wang, T. Interparticle Forces Underlying Nanoparticle Self-Assemblies. *Small* **2015**, *11* (45), 5984–6008.
- (145) Pauling, L. The Principles Determining the Structure of Complex Ionic Crystals. *J. Am. Chem. Soc.* **1929**, *51* (4), 1010–1026.
- (146) Glotzer, S. C.; Solomon, M. J. Anisotropy of Building Blocks and Their Assembly into Complex Structures. *Nat. Mater.* **2007**, *6* (7), 557–562.
- (147) Cademartiri, L.; Bishop, K. J. M.; Snyder, P. W.; Ozin, G. A. Using Shape for Self-Assembly. *Philos. Trans. R. Soc., A* **2012**, *370* (1969), 2824–2847.
- (148) Kirkwood, J. G. Molecular Distribution in Liquids. *J. Chem. Phys.* **1939**, *7* (10), 919–925.

- (149) Alder, B. J.; Wainwright, T. E. Phase Transition for a Hard Sphere System. *J. Chem. Phys.* **1957**, *27* (5), 1208–1209.
- (150) Wood, W. W.; Jacobson, J. D. Preliminary Results from a Recalculation of the Monte Carlo Equation of State of Hard Spheres. *J. Chem. Phys.* **1957**, *27* (5), 1207–1208.
- (151) Pusey, P. N.; van Megen, W. Phase Behaviour of Concentrated Suspensions of Nearly Hard Colloidal Spheres. *Nature* **1986**, *320* (6060), 340–342.
- (152) Zhu, J.; Li, M.; Rogers, R.; Meyer, W.; Ottewill, R. H.; STS-73 Space Shuttle Crew; Russel, W. B.; Chaikin, P. M. Crystallization of Hard-Sphere Colloids in Microgravity. *Nature* **1997**, *387* (6636), 883–885.
- (153) Frenkel, D. Entropy-Driven Phase Transitions. *Phys. A* **1999**, *263* (1–4), 26–38.
- (154) Barrat, J. L.; Hansen, J. P. *Basic Concepts for Simple and Complex Liquids*; Cambridge University Press: 2003.
- (155) Eldridge, M. D.; Madden, P. A.; Frenkel, D. Entropy-Driven Formation of a Superlattice in a Hard-Sphere Binary Mixture. *Nature* **1993**, *365* (6441), 35–37.
- (156) Lekkerkerker, H. N. W.; Vroege, G. J. Liquid Crystal Phase Transitions in Suspensions of Mineral Colloids: New Life from Old Roots. *Philos. Trans. R. Soc., A* **2013**, *371* (1988), 20120263.
- (157) Onsager, L. The Effects of Shape on the Interaction of Colloidal Particles. *Ann. N. Y. Acad. Sci.* **1949**, *51* (4), 627–659.
- (158) Frenkel, D.; Mulder, B. M.; McTague, J. P. Phase Diagram of a System of Hard Ellipsoids. *Phys. Rev. Lett.* **1984**, *52* (4), 287–290.
- (159) Damasceno, P. F.; Engel, M.; Glotzer, S. C. Predictive Self-Assembly of Polyhedra into Complex Structures. *Science* **2012**, *337* (6093), 453–457.
- (160) Dijkstra, M. Entropy-Driven Phase Transitions in Colloids: From Spheres to Anisotropic Particles. In *Advances in Chemical Physics*; John Wiley & Sons, Inc.: 2014; Vol. 156, pp 35–71.
- (161) Anderson, J. A.; Eric Irrgang, M.; Glotzer, S. C. Scalable Metropolis Monte Carlo for Simulation of Hard Shapes. *Comput. Phys. Commun.* **2016**, *204*, 21–30.
- (162) Donev, A.; Torquato, S.; Stillinger, F. H. Neighbor List Collision-Driven Molecular Dynamics Simulation for Nonspherical Hard Particles. I. Algorithmic Details. *J. Comput. Phys.* **2005**, *202* (2), 737–764.
- (163) Bannerman, M. N.; Sargent, R.; Lue, L. DynamO: A Free O(N) General Event-Driven Molecular Dynamics Simulator. *J. Comput. Chem.* **2011**, *32* (15), 3329–3338.
- (164) de Graaf, J.; Filion, L.; Marechal, M.; van Roij, R.; Dijkstra, M. Crystal-Structure Prediction via the Floppy-Box Monte Carlo Algorithm: Method and Application to Hard (Non)convex Particles. *J. Chem. Phys.* **2012**, *137* (21), 214101.
- (165) Frenkel, D.; Ladd, A. J. C. New Monte Carlo Method to Compute the Free Energy of Arbitrary Solids. Application to the Fcc and Hcp Phases of Hard Spheres. *J. Chem. Phys.* **1984**, *81* (7), 3188–3193.
- (166) Frenkel, D.; Smit, B. *Understanding Molecular Simulation, Second Edition; From Algorithms to Applications*; Academic Press: 2001.
- (167) Schultz, B. A.; Damasceno, P. F.; Engel, M.; Glotzer, S. C. Symmetry Considerations for the Targeted Assembly of Entropically Stabilized Colloidal Crystals via Voronoi Particles. *ACS Nano* **2015**, *9* (3), 2336–2344.
- (168) Jiang, P.; Bertone, J. F.; Hwang, K. S.; Colvin, V. L. Single-Crystal Colloidal Multilayers of Controlled Thickness. *Chem. Mater.* **1999**, *11* (8), 2132–2140.
- (169) Anderson, V. J.; Lekkerkerker, H. N. W. Insights into Phase Transition Kinetics from Colloid Science. *Nature* **2002**, *416* (6883), 811–815.
- (170) Bolhuis, P.; Frenkel, D. Tracing the Phase Boundaries of Hard Spherocylinders. *J. Chem. Phys.* **1997**, *106* (2), 666–687.
- (171) Hilbert, D. Mathematical Problems. *Bull. Am. Math. Soc.* **1902**, *8* (10), 437–480.
- (172) Hales, T. C. Historical Overview of the Kepler Conjecture. *Discrete Comput. Geom.* **2006**, *36* (1), 5–20.
- (173) Bolhuis, P. G.; Frenkel, D.; Mau, S.-C.; Huse, D. A. Entropy Difference between Crystal Phases. *Nature* **1997**, *388* (6639), 235–236.
- (174) Elser, V. Phonon Contribution to the Entropy of Hard-Sphere Crystals. *Phys. Rev. E* **2014**, *89* (5), 052404.
- (175) Grunbaum, B.; Shephard, G. C. *Tilings and Patterns*; W. H. Freeman: New York, NY, 1990.
- (176) Kallus, Y. The 3-Ball Is a Local Pessimum for Packing. *Adv. Math. (N. Y.)* **2014**, *264* (0), 355–370.
- (177) Torquato, S.; Jiao, Y. Organizing Principles for Dense Packings of Nonspherical Hard Particles: Not All Shapes Are Created Equal. *Phys. Rev. E* **2012**, *86* (1), 011102.
- (178) Haji-Akbari, A.; Engel, M.; Keys, A. S.; Zheng, X.; Petschek, R. G.; Palffy-Muhoray, P.; Glotzer, S. C. Disordered, Quasicrystalline and Crystalline Phases of Densely Packed Tetrahedra. *Nature* **2009**, *462* (7274), 773–777.
- (179) Chen, E. R. A Dense Packing of Regular Tetrahedra. *Discrete Comput. Geom.* **2008**, *40* (2), 214–240.
- (180) Torquato, S.; Jiao, Y. Dense Packings of the Platonic and Archimedean Solids. *Nature* **2009**, *460* (7257), 876–879.
- (181) Quan, Z.; Fang, J. Superlattices with Non-Spherical Building Blocks. *Nano Today* **2010**, *5* (5), 390–411.
- (182) de Graaf, J.; van Roij, R.; Dijkstra, M. Dense Regular Packings of Irregular Nonconvex Particles. *Phys. Rev. Lett.* **2011**, *107* (15), 155501.
- (183) Damasceno, P. F.; Engel, M.; Glotzer, S. C. Crystalline Assemblies and Densest Packings of a Family of Truncated Tetrahedra and the Role of Directional Entropic Forces. *ACS Nano* **2012**, *6* (1), 609–614.
- (184) Gantapara, A. P.; de Graaf, J.; van Roij, R.; Dijkstra, M. Phase Diagram and Structural Diversity of a Family of Truncated Cubes: Degenerate Close-Packed Structures and Vacancy-Rich States. *Phys. Rev. Lett.* **2013**, *111* (1), 015501.
- (185) Chen, E. R.; Klotsa, D.; Engel, M.; Damasceno, P. F.; Glotzer, S. C. Complexity in Surfaces of Densest Packings for Families of Polyhedra. *Phys. Rev. X* **2014**, *4* (1), 011024.
- (186) Lagarias, J. C.; Zong, C. Mysteries in Packing Regular Tetrahedra. *Not. Am. Math. Soc.* **2012**, *59* (11), 1540–1549.
- (187) Conway, J. H.; Torquato, S. Packing, Tiling, and Covering with Tetrahedra. *Proc. Natl. Acad. Sci. U. S. A.* **2006**, *103* (28), 10612–10617.
- (188) Kallus, Y.; Elser, V.; Gravel, S. Dense Periodic Packings of Tetrahedra with Small Repeating Units. *Discrete Comput. Geom.* **2010**, *44* (2), 245–252.
- (189) Chen, E. R.; Engel, M.; Glotzer, S. C. Dense Crystalline Dimer Packings of Regular Tetrahedra. *Discrete Comput. Geom.* **2010**, *44* (2), 253–280.
- (190) Murray, M. J.; Sanders, J. V. Close-Packed Structures of Spheres of Two Different Sizes II. The Packing Densities of Likely Arrangements. *Philos. Mag. A* **1980**, *42* (6), 721–740.
- (191) Kummerfeld, J. K.; Hudson, T. S.; Harrowell, P. The Densest Packing of AB Binary Hard-Sphere Homogeneous Compounds across All Size Ratios. *J. Phys. Chem. B* **2008**, *112* (35), 10773–10776.
- (192) Filion, L.; Dijkstra, M. Prediction of Binary Hard-Sphere Crystal Structures. *Phys. Rev. E* **2009**, *79* (4), 046714.
- (193) O'Toole, P. I.; Hudson, T. S. New High-Density Packings of Similarly Sized Binary Spheres. *J. Phys. Chem. C* **2011**, *115* (39), 19037–19040.
- (194) Hopkins, A. B.; Stillinger, F. H.; Torquato, S. Densest Binary Sphere Packings. *Phys. Rev. E* **2012**, *85* (2), 021130.
- (195) Hynninen, A.-P.; Thijssen, J. H. J.; Vermolen, E. C. M.; Dijkstra, M.; van Blaaderen, A. Self-Assembly Route for Photonic Crystals with a Bandgap in the Visible Region. *Nat. Mater.* **2007**, *6* (3), 202–205.
- (196) Hynninen, A.-P.; Filion, L.; Dijkstra, M. Stability of LS and LS₂ Crystal Structures in Binary Mixtures of Hard and Charged Spheres. *J. Chem. Phys.* **2009**, *131* (6), 064902.

- (197) Adams, M.; Dogic, Z.; Keller, S. L.; Fraden, S. Entropically Driven Microphase Transitions in Mixtures of Colloidal Rods and Spheres. *Nature* **1998**, *393* (6683), 349–352.
- (198) Dogic, Z.; Frenkel, D.; Fraden, S. Enhanced Stability of Layered Phases in Parallel Hard Spherocylinders Due to Addition of Hard Spheres. *Phys. Rev. E: Stat. Phys., Plasmas, Fluids, Relat. Interdiscip. Top.* **2000**, *62* (3), 3925–3933.
- (199) Ye, X.; Millan, J. A.; Engel, M.; Chen, J.; Diroll, B. T.; Glotzer, S. C.; Murray, C. B. Shape Alloys of Nanorods and Nanospheres from Self-Assembly. *Nano Lett.* **2013**, *13* (10), 4980–4988.
- (200) Torquato, S.; Stillinger, F. H. Jammed Hard-Particle Packings: From Kepler to Bernal and Beyond. *Rev. Mod. Phys.* **2010**, *82* (3), 2633–2672.
- (201) Agarwal, U.; Escobedo, F. A. Mesophase Behaviour of Polyhedral Particles. *Nat. Mater.* **2011**, *10* (3), 230–235.
- (202) Isihara, A. Determination of Molecular Shape by Osmotic Measurement. *J. Chem. Phys.* **1950**, *18* (11), 1446–1449.
- (203) Hadwiger, H. Der Kinetische Radius Nichtkugelförmiger Moleküle. *Experientia* **1951**, *7* (10), 395–398.
- (204) Frank, F. C.; Kasper, J. S. Complex Alloy Structures Regarded as Sphere Packings. II. Analysis and Classification of Representative Structures. *Acta Crystallogr.* **1959**, *12* (7), 483–499.
- (205) Shoemaker, D. P.; Shoemaker, C. B. Concerning the Relative Numbers of Atomic Coordination Types in Tetrahedrally Close Packed Metal Structures. *Acta Crystallogr., Sect. B: Struct. Sci.* **1986**, *42* (1), 3–11.
- (206) Khadilkar, M. R.; Agarwal, U.; Escobedo, F. A. Phase Behavior of Binary Mixtures of Hard Convex Polyhedra. *Soft Matter* **2013**, *9* (48), 11557–11567.
- (207) Cadotte, A. T.; Dshemuchadse, J.; Damasceno, P. F.; Newman, R. S.; Glotzer, S. C. Self-Assembly of a Space-Tessellating Structure in the Binary System of Hard Tetrahedra and Octahedra. *Soft Matter* **2016**, DOI: 10.1039/C6SM01180B.
- (208) Young, K. L.; Personick, M. L.; Engel, M.; Damasceno, P. F.; Barnaby, S. N.; Bleher, R.; Glotzer, S. C.; Lee, B.; Mirkin, C. a.; Li, T. A Directional Entropic Force Approach to Assemble Anisotropic Nanoparticles into Superlattices. *Angew. Chem., Int. Ed.* **2013**, *52* (52), 13980–13984.
- (209) van Anders, G.; Klotsa, D.; Ahmed, N. K.; Engel, M.; Glotzer, S. C. Understanding Shape Entropy through Local Dense Packing. *Proc. Natl. Acad. Sci. U. S. A.* **2014**, *111* (45), E4812–E4821.
- (210) Smallenburg, F.; Filion, L.; Marechal, M.; Dijkstra, M. Vacancy-Stabilized Crystalline Order in Hard Cubes. *Proc. Natl. Acad. Sci. U. S. A.* **2012**, *109* (44), 17886–17890.
- (211) van Anders, G.; Ahmed, N. K.; Smith, R.; Engel, M.; Glotzer, S. C. Entropically Patchy Particles: Engineering Valence through Shape Entropy. *ACS Nano* **2014**, *8* (1), 931–940.
- (212) van Anders, G.; Klotsa, D.; Karas, A. S.; Dodd, P. M.; Glotzer, S. C. Digital Alchemy for Materials Design: Colloids and Beyond. *ACS Nano* **2015**, *9* (10), 9542–9553.
- (213) Damasceno, P. F.; Karas, A. S.; Schultz, B. A.; Engel, M.; Glotzer, S. C. Controlling Chirality of Entropic Crystals. *Phys. Rev. Lett.* **2015**, *115* (15), 158303.
- (214) Dussi, S.; Dijkstra, M. Entropy-Driven Formation of Chiral Nematic Phases by Computer Simulations. *Nat. Commun.* **2016**, *7*, 11175.
- (215) Xia, Y.; Xiong, Y.; Lim, B.; Skrabalak, S. E. Shape-Controlled Synthesis of Metal Nanocrystals: Simple Chemistry Meets Complex Physics? *Angew. Chem., Int. Ed.* **2009**, *48* (1), 60–103.
- (216) Sau, T. K.; Rogach, A. L. Nonspherical Noble Metal Nanoparticles: Colloid-Chemical Synthesis and Morphology Control. *Adv. Mater.* **2010**, *22* (16), 1781–1804.
- (217) Niu, W.; Xu, G. Crystallographic Control of Noble Metal Nanocrystals. *Nano Today* **2011**, *6* (3), 265–285.
- (218) Huang, M. H.; Lin, P.-H. Shape-Controlled Synthesis of Polyhedral Nanocrystals and Their Facet-Dependent Properties. *Adv. Funct. Mater.* **2012**, *22* (1), 14–24.
- (219) Xia, Y.; Xia, X.; Peng, H.-C. Shape-Controlled Synthesis of Colloidal Metal Nanocrystals: Thermodynamic versus Kinetic Products. *J. Am. Chem. Soc.* **2015**, *137* (25), 7947–7966.
- (220) Bates, F. S.; Fredrickson, G. H. Block Copolymers—Designer Soft Materials. *Phys. Today* **1999**, *52* (2), 32–38.
- (221) Ziherl, P.; Kamien, R. D. Maximizing Entropy by Minimizing Area: Towards a New Principle of Self-Organization. *J. Phys. Chem. B* **2001**, *105* (42), 10147–10158.
- (222) Leibler, L. Theory of Microphase Separation in Block Copolymers. *Macromolecules* **1980**, *13* (6), 1602–1617.
- (223) Whetten, R. L.; Shafiqullin, M. N.; Khouri, J. T.; Schaaff, T. G.; Vezmar, I.; Alvarez, M. M.; Wilkinson, A. Crystal Structures of Molecular Gold Nanocrystal Arrays. *Acc. Chem. Res.* **1999**, *32* (5), 397–406.
- (224) Weaire, D.; Phelan, R. A Counter-Example to Kelvin's Conjecture on Minimal Surfaces. *Philos. Mag. Lett.* **1994**, *69* (2), 107–110.
- (225) Ball, P. Scientists Make the “Perfect” Foam. <http://www.nature.com/news/scientists-make-the-perfect-foam-1.9504> (accessed July 6, 2016).
- (226) Lee, S.; Bluemle, M. J.; Bates, F. S. Discovery of a Frank-Kasper Phase in Sphere-Forming Block Copolymer Melts. *Science* **2010**, *330* (6002), 349–353.
- (227) Zeng, X.; Ungar, G.; Liu, Y.; Percec, V.; Dulcey, A. E.; Hobbs, J. K. Supramolecular Dendritic Liquid Quasicrystals. *Nature* **2004**, *428* (6979), 157–160.
- (228) Lee, S.; Leighton, C.; Bates, F. S. Sphericity and Symmetry Breaking in the Formation of Frank–Kasper Phases from One Component Materials. *Proc. Natl. Acad. Sci. U. S. A.* **2014**, *111* (50), 17723–17731.
- (229) Ungar, G.; Liu, Y.; Zeng, X.; Percec, V.; Cho, W.-D. Giant Supramolecular Liquid Crystal Lattice. *Science* **2003**, *299* (5610), 1208–1211.
- (230) Sakya, P.; Seddon, J. M.; Templer, R. H.; Mirkin, R. J.; Tiddy, G. J. T. Micellar Cubic Phases and Their Structural Relationships: The Nonionic Surfactant System $C_{12}EO_{12}$ /Water. *Langmuir* **1997**, *13* (14), 3706–3714.
- (231) Huang, M.; Hsu, C.-H.; Wang, J.; Mei, S.; Dong, X.; Li, Y.; Li, M.; Liu, H.; Zhang, W.-B.; Aida, T.; et al. Selective Assemblies of Giant Tetrahedra via Precisely Controlled Positional Interactions. *Science* **2015**, *348* (6233), 424–428.
- (232) Iacovella, C. R.; Keys, A. S.; Glotzer, S. C. Self-Assembly of Soft-Matter Quasicrystals and Their Approximants. *Proc. Natl. Acad. Sci. U. S. A.* **2011**, *108* (52), 20935–20940.
- (233) Travesset, A. Phase Diagram of Power Law and Lennard-Jones Systems: Crystal Phases. *J. Chem. Phys.* **2014**, *141* (16), 164501.
- (234) Alexander, S.; McTague, J. Should All Crystals Be Bcc? Landau Theory of Solidification and Crystal Nucleation. *Phys. Rev. Lett.* **1978**, *41* (10), 702–705.
- (235) Travesset, A. Binary Nanoparticle Superlattices of Soft-Particle Systems. *Proc. Natl. Acad. Sci. U. S. A.* **2015**, *112* (31), 9563–9567.
- (236) Horst, N.; Travesset, A. Prediction of Binary Nanoparticle Superlattices from Soft Potentials. *J. Chem. Phys.* **2016**, *144* (1), 014502.
- (237) Wang, Z.; Schliehe, C.; Bian, K.; Dale, D.; Bassett, W. A.; Hanrath, T.; Klinke, C.; Weller, H. Correlating Superlattice Polymorphs to Internanoparticle Distance, Packing Density, and Surface Lattice in Assemblies of PbS Nanoparticles. *Nano Lett.* **2013**, *13* (3), 1303–1311.
- (238) Goodfellow, B. W.; Korgel, B. A. Reversible Solvent Vapor-Mediated Phase Changes in Nanocrystal Superlattices. *ACS Nano* **2011**, *5* (4), 2419–2424.
- (239) Thaner, R. V.; Kim, Y.; Li, T. I. N. G.; Macfarlane, R. J.; Nguyen, S. T.; Olvera de la Cruz, M.; Mirkin, C. A. Entropy-Driven Crystallization Behavior in DNA-Mediated Nanoparticle Assembly. *Nano Lett.* **2015**, *15* (8), 5545–5551.
- (240) Hajiw, S.; Pansu, B.; Sadoc, J.-F. Evidence for a C14 Frank–Kasper Phase in One-Size Gold Nanoparticle Superlattices. *ACS Nano* **2015**, *9* (8), 8116–8121.

- (241) Goodfellow, B. W.; Rasch, M. R.; Hessel, C. M.; Patel, R. N.; Smilgies, D.-M.; Korgel, B. A. Ordered Structure Rearrangements in Heated Gold Nanocrystal Superlattices. *Nano Lett.* **2013**, *13* (11), 5710–5714.
- (242) Goodfellow, B. W.; Yu, Y.; Bosoy, C. A.; Smilgies, D.-M.; Korgel, B. A. The Role of Ligand Packing Frustration in Body-Centered Cubic (Bcc) Superlattices of Colloidal Nanocrystals. *J. Phys. Chem. Lett.* **2015**, *6* (13), 2406–2412.
- (243) Urban, J. J.; Talapin, D. V.; Shevchenko, E. V.; Murray, C. B. Self-Assembly of PbTe Quantum Dots into Nanocrystal Superlattices and Glassy Films. *J. Am. Chem. Soc.* **2006**, *128* (10), 3248–3255.
- (244) Demortière, A.; Launois, P.; Goubet, N.; Albouy, P.-A.; Petit, C. Shape-Controlled Platinum Nanocubes and Their Assembly into Two-Dimensional and Three-Dimensional Superlattices. *J. Phys. Chem. B* **2008**, *112* (46), 14583–14592.
- (245) Quan, Z.; Xu, H.; Wang, C.; Wen, X.; Wang, Y.; Zhu, J.; Li, R.; Sheehan, C. J.; Wang, Z.; Smilgies, D.-M.; et al. Solvent-Mediated Self-Assembly of Nanocube Superlattices. *J. Am. Chem. Soc.* **2014**, *136* (4), 1352–1359.
- (246) Disch, S.; Wetterskog, E.; Hermann, R. P.; Salazar-Alvarez, G.; Busch, P.; Brückel, T.; Bergström, L.; Kamali, S. Shape Induced Symmetry in Self-Assembled Mesocrystals of Iron Oxide Nanocubes. *Nano Lett.* **2011**, *11* (4), 1651–1656.
- (247) Choi, J. J.; Bian, K.; Baumgardner, W. J.; Smilgies, D.-M.; Hanrath, T. Interface-Induced Nucleation, Orientational Alignment and Symmetry Transformations in Nanocube Superlattices. *Nano Lett.* **2012**, *12* (9), 4791–4798.
- (248) Zhang, Y.; Lu, F.; van der Lelie, D.; Gang, O. Continuous Phase Transformation in Nanocube Assemblies. *Phys. Rev. Lett.* **2011**, *107* (13), 135701.
- (249) Zhang, J.; Luo, Z.; Quan, Z.; Wang, Y.; Kumbhar, A.; Smilgies, D.-M.; Fang, J. Low Packing Density Self-Assembled Superstructure of Octahedral Pt₃Ni Nanocrystals. *Nano Lett.* **2011**, *11* (7), 2912–2918.
- (250) Gordon, T. R.; Paik, T.; Klein, D. R.; Naik, G. V.; Caglayan, H.; Boltasseva, A.; Murray, C. B. Shape-Dependent Plasmonic Response and Directed Self-Assembly in a New Semiconductor Building Block, Indium-Doped Cadmium Oxide (ICO). *Nano Lett.* **2013**, *13* (6), 2857–2863.
- (251) Diroll, B. T.; Greybush, N. J.; Kagan, C. R.; Murray, C. B. Smectic Nanorod Superlattices Assembled on Liquid Subphases: Structure, Orientation, Defects, and Optical Polarization. *Chem. Mater.* **2015**, *27* (8), 2998–3008.
- (252) Peng, S.; Lee, Y.; Wang, C.; Yin, H.; Dai, S.; Sun, S. A Facile Synthesis of Monodisperse Au Nanoparticles and Their Catalysis of CO Oxidation. *Nano Res.* **2008**, *1* (3), 229–234.
- (253) Courty, A.; Richardi, J.; Albouy, P.-A.; Pilani, M.-P. How To Control the Crystalline Structure of Supracrystals of 5-Nm Silver Nanocrystals. *Chem. Mater.* **2011**, *23* (18), 4186–4192.
- (254) Norris, D. J.; Arlinghaus, E. G.; Meng, L.; Heiny, R.; Scriven, L. E. Opaline Photonic Crystals: How Does Self-Assembly Work? *Adv. Mater.* **2004**, *16* (16), 1393–1399.
- (255) Gasperino, D.; Meng, L.; Norris, D. J.; Derby, J. J. The Role of Fluid Flow and Convective Steering during the Assembly of Colloidal Crystals. *J. Cryst. Growth* **2008**, *310* (1), 131–139.
- (256) Talapin, D. V.; Shevchenko, E. V.; Murray, C. B.; Titov, A. V.; Král, P. Dipole–Dipole Interactions in Nanoparticle Superlattices. *Nano Lett.* **2007**, *7* (5), 1213–1219.
- (257) Portalès, H.; Goubet, N.; Sirokin, S.; Duval, E.; Mermet, A.; Albouy, P.-A.; Pilani, M.-P. Crystallinity Segregation upon Selective Self-Assembling of Gold Colloidal Single Nanocrystals. *Nano Lett.* **2012**, *12* (10), 5292–5298.
- (258) Li, R.; Bian, K.; Hanrath, T.; Bassett, W. A.; Wang, Z. Decoding the Superlattice and Interface Structure of Truncate PbS Nanocrystal-Assembled Supercrystal and Associated Interaction Forces. *J. Am. Chem. Soc.* **2014**, *136* (34), 12047–12055.
- (259) Liu, K.; Zhao, N.; Kumacheva, E. Self-Assembly of Inorganic Nanorods. *Chem. Soc. Rev.* **2011**, *40* (2), 656–671.
- (260) Zhang, S.-Y.; Regulacio, M. D.; Han, M.-Y. Self-Assembly of Colloidal One-Dimensional Nanocrystals. *Chem. Soc. Rev.* **2014**, *43* (7), 2301–2323.
- (261) Jana, N. R.; Gearheart, L.; Murphy, C. J. Wet Chemical Synthesis of High Aspect Ratio Cylindrical Gold Nanorods. *J. Phys. Chem. B* **2001**, *105* (19), 4065–4067.
- (262) Jana, N. R.; Gearheart, L.; Murphy, C. J. Wet Chemical Synthesis of Silver Nanorods and Nanowires of Controllable Aspect Ratio. *Chem. Commun.* **2001**, No. 7, 617–618.
- (263) Ye, X.; Zheng, C.; Chen, J.; Gao, Y.; Murray, C. B. Using Binary Surfactant Mixtures To Simultaneously Improve the Dimensional Tunability and Monodispersity in the Seeded Growth of Gold Nanorods. *Nano Lett.* **2013**, *13* (2), 765–771.
- (264) Ye, X.; Gao, Y.; Chen, J.; Reifsnyder, D. C.; Zheng, C.; Murray, C. B. Seeded Growth of Monodisperse Gold Nanorods Using Bromide-Free Surfactant Mixtures. *Nano Lett.* **2013**, *13* (5), 2163–2171.
- (265) Peng, X.; Manna, L.; Yang, W.; Wickham, J.; Scher, E.; Kadavanich, A.; Alivisatos, A. P. Shape Control of CdSe Nanocrystals. *Nature* **2000**, *404* (6773), 59–61.
- (266) Talapin, D. V.; Nelson, J. H.; Shevchenko, E. V.; Aloni, S.; Sadtler, B.; Alivisatos, A. P. Seeded Growth of Highly Luminescent CdSe/CdS Nanoheterostructures with Rod and Tetrapod Morphologies. *Nano Lett.* **2007**, *7* (10), 2951–2959.
- (267) Yin, Y.; Alivisatos, A. P. Colloidal Nanocrystal Synthesis and the Organic–Inorganic Interface. *Nature* **2005**, *437* (7059), 664–670.
- (268) Ithurria, S.; Tessier, M. D.; Mahler, B.; Lobo, R. P. S. M.; Dubertret, B.; Efros, A. L. Colloidal Nanoplatelets with Two-Dimensional Electronic Structure. *Nat. Mater.* **2011**, *10* (12), 936–941.
- (269) Ye, X.; Collins, J. E.; Kang, Y.; Chen, J.; Chen, D. T. N.; Yodh, A. G.; Murray, C. B. Morphologically Controlled Synthesis of Colloidal Upconversion Nanophosphors and Their Shape-Directed Self-Assembly. *Proc. Natl. Acad. Sci. U. S. A.* **2010**, *107* (52), 22430–22435.
- (270) Li, L.; Walda, J.; Manna, L.; Alivisatos, A. P. Semiconductor Nanorod Liquid Crystals. *Nano Lett.* **2002**, *2* (6), 557–560.
- (271) Chen, Q.; Cho, H.; Manthiram, K.; Yoshida, M.; Ye, X.; Alivisatos, A. P. Interaction Potentials of Anisotropic Nanocrystals from the Trajectory Sampling of Particle Motion Using in Situ Liquid Phase Transmission Electron Microscopy. *ACS Cent. Sci.* **2015**, *1* (1), 33–39.
- (272) Baranov, D.; Fiore, A.; van Huis, M.; Giannini, C.; Falqui, A.; Lafont, U.; Zandbergen, H.; Zanella, M.; Cingolani, R.; Manna, L. Assembly of Colloidal Semiconductor Nanorods in Solution by Depletion Attraction. *Nano Lett.* **2010**, *10* (2), 743–749.
- (273) Zhuang, J.; Shaller, A. D.; Lynch, J.; Wu, H.; Chen, O.; Li, A. D. Q.; Cao, Y. C. Cylindrical Superparticles from Semiconductor Nanorods. *J. Am. Chem. Soc.* **2009**, *131* (17), 6084–6085.
- (274) Huo, Z.; Tsung, C.-K.; Huang, W.; Fardy, M.; Yan, R.; Zhang, X.; Li, Y.; Yang, P. Self-Organized Ultrathin Oxide Nanocrystals. *Nano Lett.* **2009**, *9* (3), 1260–1264.
- (275) Rowland, C. E.; Fedin, I.; Zhang, H.; Gray, S. K.; Govorov, A. O.; Talapin, D. V.; Schaller, R. D. Picosecond Energy Transfer and Multiexciton Transfer Outpaces Auger Recombination in Binary CdSe Nanoplatelet Solids. *Nat. Mater.* **2015**, *14* (5), 484–489.
- (276) Millan, J. A.; Ortiz, D.; van Anders, G.; Glotzer, S. C. Self-Assembly of Archimedean Tilings with Enthalpically and Entropically Patchy Polygons. *ACS Nano* **2014**, *8* (3), 2918–2928.
- (277) Paik, T.; Diroll, B. T.; Kagan, C. R.; Murray, C. B. Binary and Ternary Superlattices Self-Assembled from Colloidal Nanodisks and Nanorods. *J. Am. Chem. Soc.* **2015**, *137* (20), 6662–6669.
- (278) Zhao, K.; Bruinsma, R.; Mason, T. G. Entropic Crystal–Crystal Transitions of Brownian Squares. *Proc. Natl. Acad. Sci. U. S. A.* **2011**, *108* (7), 2684–2687.
- (279) Zhao, K.; Bruinsma, R.; Mason, T. G. Local Chiral Symmetry Breaking in Triatic Liquid Crystals. *Nat. Commun.* **2012**, *3*, 801.
- (280) Young, K. L.; Jones, M. R.; Zhang, J.; Macfarlane, R. J.; Esquivel-Sirvent, R.; Nap, R. J.; Wu, J.; Schatz, G. C.; Lee, B.; Mirkin,

- C. A. Assembly of Reconfigurable One-Dimensional Colloidal Superlattices Due to a Synergy of Fundamental Nanoscale Forces. *Proc. Natl. Acad. Sci. U. S. A.* **2012**, *109* (7), 2240–2245.
- (281) Zhang, H.; Yang, J.; Hanrath, T.; Wise, F. W. Sub-10 nm Monodisperse PbS Cubes by Post-Synthesis Shape Engineering. *Phys. Chem. Chem. Phys.* **2014**, *16* (28), 14640–14643.
- (282) Dumestre, F.; Chaudret, B.; Amiens, C.; Renaud, P.; Fejes, P. Superlattices of Iron Nanocubes Synthesized from Fe[N(SiMe₃)₂]₂. *Science* **2004**, *303* (5659), 821–823.
- (283) Ren, J.; Tilley, R. D. Preparation, Self-Assembly, and Mechanistic Study of Highly Monodispersed Nanocubes. *J. Am. Chem. Soc.* **2007**, *129* (11), 3287–3291.
- (284) Wang, T.; Wang, X.; LaMontagne, D.; Wang, Z.; Wang, Z.; Cao, Y. C. Shape-Controlled Synthesis of Colloidal Superparticles from Nanocubes. *J. Am. Chem. Soc.* **2012**, *134* (44), 18225–18228.
- (285) Javon, E.; Gaceur, M.; Dachraoui, W.; Margeat, O.; Ackermann, J.; Saba, M. I.; Delugas, P.; Mattoni, A.; Bals, S.; Van Tendeloo, G. Competing Forces in the Self-Assembly of Coupled ZnO Nanopyramids. *ACS Nano* **2015**, *9* (4), 3685–3694.
- (286) Huang, M. H.; Thoka, S. Formation of Supercrystals through Self-Assembly of Polyhedral Nanocrystals. *Nano Today* **2015**, *10* (1), 81–92.
- (287) Nakagawa, Y.; Kageyama, H.; Oaki, Y.; Imai, H. Direction Control of Oriented Self-Assembly for 1D, 2D, and 3D Microarrays of Anisotropic Rectangular Nanoblocks. *J. Am. Chem. Soc.* **2014**, *136* (10), 3716–3719.
- (288) Liao, C.-W.; Lin, Y.-S.; Chanda, K.; Song, Y.-F.; Huang, M. H. Formation of Diverse Supercrystals from Self-Assembly of a Variety of Polyhedral Gold Nanocrystals. *J. Am. Chem. Soc.* **2013**, *135* (7), 2684–2693.
- (289) Blaak, R.; Mulder, B. M.; Frenkel, D. Cubatic Phase for Tetrapods. *J. Chem. Phys.* **2004**, *120* (11), 5486–5492.
- (290) Goodman, M. D.; Zhao, L.; DeRocher, K. A.; Wang, J.; Mallapragada, S. K.; Lin, Z. Self-Assembly of CdTe Tetrapods into Network Monolayers at the Air/Water Interface. *ACS Nano* **2010**, *4* (4), 2043–2050.
- (291) Deka, S.; Misztta, K.; Dorfs, D.; Genovese, A.; Bertoni, G.; Manna, L. Octapod-Shaped Colloidal Nanocrystals of Cadmium Chalcogenides via “One-Pot” Cation Exchange and Seeded Growth. *Nano Lett.* **2010**, *10* (9), 3770–3776.
- (292) Qi, W.; Graaf, J. de; Qiao, F.; Marras, S.; Manna, L.; Dijkstra, M. Ordered Two-Dimensional Superstructures of Colloidal Octapod-Shaped Nanocrystals on Flat Substrates. *Nano Lett.* **2012**, *12* (10), 5299–5303.
- (293) Arciniegas, M. P.; Kim, M. R.; De Graaf, J.; Brescia, R.; Marras, S.; Misztta, K.; Dijkstra, M.; van Roij, R.; Manna, L. Self-Assembly of Octapod-Shaped Colloidal Nanocrystals into a Hexagonal Ballerina Network Embedded in a Thin Polymer Film. *Nano Lett.* **2014**, *14* (2), 1056–1063.
- (294) Costi, R.; Saunders, A. E.; Banin, U. Colloidal Hybrid Nanostructures: A New Type of Functional Materials. *Angew. Chem., Int. Ed.* **2010**, *49* (29), 4878–4897.
- (295) Carbone, L.; Cozzoli, P. D. Colloidal Heterostructured Nanocrystals: Synthesis and Growth Mechanisms. *Nano Today* **2010**, *5* (5), 449–493.
- (296) Reiss, P.; Protière, M.; Li, L. Core/Shell Semiconductor Nanocrystals. *Small* **2009**, *5* (2), 154–168.
- (297) De Trizio, L.; Manna, L. Forging Colloidal Nanostructures via Cation Exchange Reactions. *Chem. Rev.* **2016**, DOI: [10.1021/acs.chemrev.5b00739](https://doi.org/10.1021/acs.chemrev.5b00739).
- (298) Figuerola, A.; Franchini, I. R.; Fiore, A.; Mastria, R.; Falqui, A.; Bertoni, G.; Bals, S.; Van Tendeloo, G.; Kudera, S.; Cingolani, R.; et al. End-to-End Assembly of Shape-Controlled Nanocrystals via a Nanowelding Approach Mediated by Gold Domains. *Adv. Mater.* **2009**, *21* (5), 550–554.
- (299) Zhao, N.; Vickery, J.; Guerin, G.; Park, J. Il; Winnik, M. A.; Kumacheva, E. Self-Assembly of Single-Tip Metal-Semiconductor Nanorods in Selective Solvents. *Angew. Chem., Int. Ed.* **2011**, *50* (20), 4606–4610.
- (300) Zhao, N.; Liu, K.; Greener, J.; Nie, Z.; Kumacheva, E. Close-Packed Superlattices of Side-by-Side Assembled Au-CdSe Nanorods. *Nano Lett.* **2009**, *9* (8), 3077–3081.
- (301) Tan, R.; Zhu, H.; Cao, C.; Chen, O. Multi-Component Superstructures Self-Assembled from Nanocrystal Building Blocks. *Nanoscale* **2016**, *8* (19), 9944–9961.
- (302) Sanders, J. V. Close-Packed Structures of Spheres of Two Different Sizes I. Observations on Natural Opal. *Philos. Mag. A* **1980**, *42* (6), 705–720.
- (303) Bartlett, P.; Ottewill, R. H.; Pusey, P. N. Superlattice Formation in Binary Mixtures of Hard-Sphere Colloids. *Phys. Rev. Lett.* **1992**, *68* (25), 3801–3804.
- (304) Vogel, N.; de Viguerie, L.; Jonas, U.; Weiss, C. K.; Landfester, K. Wafer-Scale Fabrication of Ordered Binary Colloidal Monolayers with Adjustable Stoichiometries. *Adv. Funct. Mater.* **2011**, *21* (16), 3064–3073.
- (305) Vogel, N.; Weiss, C. K.; Landfester, K. From Soft to Hard: The Generation of Functional and Complex Colloidal Monolayers for Nanolithography. *Soft Matter* **2012**, *8* (15), 4044–4061.
- (306) Yang, Z.; Wei, J.; Bonville, P.; Pilani, M.-P. Beyond Entropy: Magnetic Forces Induce Formation of Quasicrystalline Structure in Binary Nanocrystal Superlattices. *J. Am. Chem. Soc.* **2015**, *137* (13), 4487–4493.
- (307) Ye, X.; Chen, J.; Murray, C. B. Polymorphism in Self-Assembled AB₆ Binary Nanocrystal Superlattices. *J. Am. Chem. Soc.* **2011**, *133* (8), 2613–2620.
- (308) Dong, A.; Ye, X.; Chen, J.; Murray, C. B. Two-Dimensional Binary and Ternary Nanocrystal Superlattices: The Case of Monolayers and Bilayers. *Nano Lett.* **2011**, *11* (4), 1804–1809.
- (309) Bodnarchuk, M. I.; Erni, R.; Krumeich, F.; Kovalenko, M. V. Binary Superlattices from Colloidal Nanocrystals and Giant Polyoxometalate Clusters. *Nano Lett.* **2013**, *13* (4), 1699–1705.
- (310) Shevchenko, E. V.; Talapin, D. V.; Murray, C. B.; O’Brien, S. Structural Characterization of Self-Assembled Multifunctional Binary Nanoparticle Superlattices. *J. Am. Chem. Soc.* **2006**, *128* (11), 3620–3637.
- (311) Shevchenko, E. V.; Talapin, D. V.; O’Brien, S.; Murray, C. B. Polymorphism in AB₁₃ Nanoparticle Superlattices: An Example of Semiconductor–Metal Metamaterials. *J. Am. Chem. Soc.* **2005**, *127* (24), 8741–8747.
- (312) Evers, W. H.; de Nijs, B.; Filion, L.; Castillo, S.; Dijkstra, M.; Vanmaekelbergh, D. Entropy-Driven Formation of Binary Semiconductor-Nanocrystal Superlattices. *Nano Lett.* **2010**, *10* (10), 4235–4241.
- (313) Chen, Z.; O’Brien, S. Structure Direction of II–VI Semiconductor Quantum Dot Binary Nanoparticle Superlattices by Tuning Radius Ratio. *ACS Nano* **2008**, *2* (6), 1219–1229.
- (314) Redl, F. X.; Cho, K.-S.; Murray, C. B.; O’Brien, S. Three-Dimensional Binary Superlattices of Magnetic Nanocrystals and Semiconductor Quantum Dots. *Nature* **2003**, *423* (6943), 968–971.
- (315) Likos, C. N. Effective Interactions in Soft Condensed Matter Physics. *Phys. Rep.* **2001**, *348* (4–5), 267–439.
- (316) Ben-Simon, A.; Eshet, H.; Rabani, E. On the Phase Behavior of Binary Mixtures of Nanoparticles. *ACS Nano* **2013**, *7* (2), 978–986.
- (317) Leunissen, M. E.; Christova, C. G.; Hynninen, A.-P.; Royall, C. P.; Campbell, A. I.; Imhof, A.; Dijkstra, M.; van Roij, R.; van Blaaderen, A. Ionic Colloidal Crystals of Oppositely Charged Particles. *Nature* **2005**, *437* (7056), 235–240.
- (318) Paik, T.; Murray, C. B. Shape-Directed Binary Assembly of Anisotropic Nanoplates: A Nanocrystal Puzzle with Shape-Complementary Building Blocks. *Nano Lett.* **2013**, *13* (6), 2952–2956.
- (319) Paik, T.; Gordon, T. R.; Prantner, A. M.; Yun, H.; Murray, C. B. Designing Tripodal and Triangular Gadolinium Oxide Nanoplates and Self-Assembled Nanofibrils as Potential Multimodal Bioimaging Probes. *ACS Nano* **2013**, *7* (3), 2850–2859.
- (320) Castelli, A.; de Graaf, J.; Prato, M.; Manna, L.; Arciniegas, M. P. Tic-Tac-Toe Binary Lattices from the Interfacial Self-Assembly of Branched and Spherical Nanocrystals. *ACS Nano* **2016**, *10* (4), 4345–4353.

- (321) Thérien-Aubin, H.; Lukach, A.; Pitch, N.; Kumacheva, E. Coassembly of Nanorods and Nanospheres in Suspensions and in Stratified Films. *Angew. Chem., Int. Ed.* **2015**, *54* (19), 5618–5622.
- (322) Bodnarchuk, M. I.; Shevchenko, E. V.; Talapin, D. V. Structural Defects in Periodic and Quasicrystalline Binary Nanocrystal Superlattices. *J. Am. Chem. Soc.* **2011**, *133* (51), 20837–20849.
- (323) Smith, D. K.; Goodfellow, B.; Smilgies, D.-M.; Korgel, B. A. Self-Assembled Simple Hexagonal AB₂ Binary Nanocrystal Superlattices: SEM, GISAXS, and Defects. *J. Am. Chem. Soc.* **2009**, *131* (9), 3281–3290.
- (324) Bausch, A. R.; Bowick, M. J.; Cacciuto, A.; Dinsmore, A. D.; Hsu, M. F.; Nelson, D. R.; Nikolaides, M. G.; Travisset, A.; Weitz, D. A. Grain Boundary Scars and Spherical Crystallography. *Science* **2003**, *299* (5613), 1716–1718.
- (325) Irvine, W. T. M.; Vitelli, V.; Chaikin, P. M. Pleats in Crystals on Curved Surfaces. *Nature* **2010**, *468* (7326), 947–951.
- (326) Alexander, G. P.; Chen, B. G.; Matsumoto, E. A.; Kamien, R. D. Colloquium: Disclination Loops, Point Defects, and All That in Nematic Liquid Crystals. *Rev. Mod. Phys.* **2012**, *84* (2), 497–514.
- (327) Petit-Garrido, N.; Trivedi, R. P.; Sagüés, F.; Ignés-Mullol, J.; Smalyukh, I. I. Topological Defects in Cholesteric Liquid Crystals Induced by Monolayer Domains with Orientational Chirality. *Soft Matter* **2014**, *10* (41), 8163–8170.
- (328) Korkidi, L.; Barkan, K.; Lifshitz, R. Analysis of Dislocations in Quasicrystals Composed of Self-Assembled Nanoparticles. In *Aperiodic Crystals*; Springer: Dordrecht, Netherlands, 2013; pp 117–124.
- (329) Pileni, M. P. Supracrystals of Inorganic Nanocrystals: An Open Challenge for New Physical Properties. *Acc. Chem. Res.* **2008**, *41* (12), 1799–1809.
- (330) Li, R.; Zhang, J.; Tan, R.; Gerdes, F.; Luo, Z.; Xu, H.; Hollingsworth, J. A.; Klinke, C.; Chen, O.; Wang, Z. Competing Interactions between Various Entropic Forces toward Assembly of Pt₃Ni Octahedra into a Body-Centered Cubic Superlattice. *Nano Lett.* **2016**, *16* (4), 2792–2799.
- (331) Choi, J. J.; Bealing, C. R.; Bian, K.; Hughes, K. J.; Zhang, W.; Smilgies, D.-M.; Hennig, R. G.; Engstrom, J. R.; Hanrath, T. Controlling Nanocrystal Superlattice Symmetry and Shape-Anisotropic Interactions through Variable Ligand Surface Coverage. *J. Am. Chem. Soc.* **2011**, *133* (9), 3131–3138.
- (332) Zheng, H.; Smith, R. K.; Jun, Y. -w.; Kisielowski, C.; Dahmen, U.; Alivisatos, A. P. Observation of Single Colloidal Platinum Nanocrystal Growth Trajectories. *Science* **2009**, *324* (5932), 1309–1312.
- (333) Penn, R. L.; Banfield, J. F. Imperfect Oriented Attachment: Dislocation Generation in Defect-Free Nanocrystals. *Science* **1998**, *281* (5379), 969–971.
- (334) Niederberger, M.; Cölfen, H. Oriented Attachment and Mesocrystals: Non-Classical Crystallization Mechanisms Based on Nanoparticle Assembly. *Phys. Chem. Chem. Phys.* **2006**, *8* (28), 3271–3287.
- (335) De Yoreo, J. J.; Gilbert, P. U. P. A.; Somerdijk, N. A. J. M.; Penn, R. L.; Whitelam, S.; Joester, D.; Zhang, H.; Rimer, J. D.; Navrotsky, A.; Banfield, J. F.; et al. Crystallization by Particle Attachment in Synthetic, Biogenic, and Geologic Environments. *Science* **2015**, *349* (6247), aaa6760.
- (336) Li, D.; Nielsen, M. H.; Lee, J. R. I.; Frandsen, C.; Banfield, J. F.; De Yoreo, J. J. Direction-Specific Interactions Control Crystal Growth by Oriented Attachment. *Science* **2012**, *336* (6084), 1014–1018.
- (337) Niu, K.-Y.; Liao, H.-G.; Zheng, H. Visualization of the Coalescence of Bismuth Nanoparticles. *Microsc. Microanal.* **2014**, *20* (02), 416–424.
- (338) Anand, U.; Lu, J.; Loh, D.; Aabdin, Z.; Mirsaidov, U. Hydration Layer-Mediated Pairwise Interaction of Nanoparticles. *Nano Lett.* **2016**, *16* (1), 786–790.
- (339) Cho, K.-S.; Talapin, D. V.; Gaschler, W.; Murray, C. B. Designing PbSe Nanowires and Nanorings through Oriented Attachment of Nanoparticles. *J. Am. Chem. Soc.* **2005**, *127* (19), 7140–7147.
- (340) Schliehe, C.; Juarez, B. H.; Pelletier, M.; Jander, S.; Greshnykh, D.; Nagel, M.; Meyer, A.; Foerster, S.; Kornowski, A.; Klinke, C.; et al. Ultrathin PbS Sheets by Two-Dimensional Oriented Attachment. *Science* **2010**, *329* (5991), 550–553.
- (341) Evers, W. H.; Goris, B.; Bals, S.; Casavola, M.; de Graaf, J.; van Roij, R.; Dijkstra, M.; Vanmaekelbergh, D. Low-Dimensional Semiconductor Superlattices Formed by Geometric Control over Nanocrystal Attachment. *Nano Lett.* **2013**, *13* (6), 2317–2323.
- (342) Boneschanscher, M. P.; Evers, W. H.; Geuchies, J. J.; Altantzis, T.; Goris, B.; Rabouw, F. T.; van Rossum, S. A. P.; van der Zant, H. S. J.; Siebbeles, L. D. A.; Van Tendeloo, G.; et al. Long-Range Orientation and Atomic Attachment of Nanocrystals in 2D Honeycomb Superlattices. *Science* **2014**, *344* (6190), 1377–1380.
- (343) Nakamura, K.; Nakagawa, Y.; Kageyama, H.; Oaki, Y.; Imai, H. Orientation-Selective Alignments of Hydroxyapatite Nanoblocks through Epitaxial Attachment in a and c Directions. *Langmuir* **2016**, *32* (16), 4066–4070.
- (344) Podsiadlo, P.; Lee, B.; Prakapenka, V. B.; Krylova, G. V.; Schaller, R. D.; Demortière, A.; Shevchenko, E. V. High-Pressure Structural Stability and Elasticity of Supercrystals Self-Assembled from Nanocrystals. *Nano Lett.* **2011**, *11* (2), 579–588.
- (345) Treml, B. E.; Lukose, B.; Clancy, P.; Smilgies, D.-M.; Hanrath, T. Connecting the Particles in the Box - Controlled Fusion of Hexamer Nanocrystal Clusters within an AB₆ Binary Nanocrystal Superlattice. *Sci. Rep.* **2014**, *4*, 6731.
- (346) Hui, C. M.; Pietrasik, J.; Schmitt, M.; Mahoney, C.; Choi, J.; Bockstaller, M. R.; Matyjaszewski, K. Surface-Initiated Polymerization as an Enabling Tool for Multifunctional (Nano-)Engineered Hybrid Materials. *Chem. Mater.* **2014**, *26* (1), 745–762.
- (347) Choi, J.; Hui, C. M.; Schmitt, M.; Pietrasik, J.; Margel, S.; Matyjaszewski, K.; Bockstaller, M. R. Effect of Polymer-Graft Modification on the Order Formation in Particle Assembly Structures. *Langmuir* **2013**, *29* (21), 6452–6459.
- (348) Paul, D. R.; Robeson, L. M. Polymer Nanotechnology: Nanocomposites. *Polymer* **2008**, *49* (15), 3187–3204.
- (349) Ofir, Y.; Samanta, B.; Rotello, V. M. Polymer and Biopolymer Mediated Self-Assembly of Gold Nanoparticles. *Chem. Soc. Rev.* **2008**, *37* (9), 1814–1825.
- (350) Kumar, S. K.; Jouault, N.; Benicewicz, B.; Neely, T. Nanocomposites with Polymer Grafted Nanoparticles. *Macromolecules* **2013**, *46* (9), 3199–3214.
- (351) Corbierre, M. K.; Cameron, N. S.; Sutton, M.; Laaziri, K.; Lennox, R. B. Gold Nanoparticle/Polymer Nanocomposites: Dispersion of Nanoparticles as a Function of Capping Agent Molecular Weight and Grafting Density. *Langmuir* **2005**, *21* (13), 6063–6072.
- (352) Akcora, P.; Liu, H.; Kumar, S. K.; Moll, J.; Li, Y.; Benicewicz, B. C.; Schadler, L. S.; Acehan, D.; Panagiotopoulos, A. Z.; Pryamitsyn, V.; et al. Anisotropic Self-Assembly of Spherical Polymer-Grafted Nanoparticles. *Nat. Mater.* **2009**, *8* (4), 354–359.
- (353) Gao, B.; Arya, G.; Tao, A. R. Self-Orienting Nanocubes for the Assembly of Plasmonic Nanojunctions. *Nat. Nanotechnol.* **2012**, *7* (7), 433–437.
- (354) Gurunatha, K. L.; Marvi, S.; Arya, G.; Tao, A. R. Computationally Guided Assembly of Oriented Nanocubes by Modulating Grafted Polymer–Surface Interactions. *Nano Lett.* **2015**, *15* (11), 7377–7382.
- (355) Pérez-Juste, J.; Rodríguez-González, B.; Mulvaney, P.; Liz-Marzán, L. M. Optical Control and Patterning of Gold-Nanorod-Poly(vinyl Alcohol) Nanocomposite Films. *Adv. Funct. Mater.* **2005**, *15* (7), 1065–1071.
- (356) Wang, Y. A.; Li, J. J.; Chen, H.; Peng, X. Stabilization of Inorganic Nanocrystals by Organic Dendrons. *J. Am. Chem. Soc.* **2002**, *124* (10), 2293–2298.
- (357) Guo, W.; Li, J. J.; Wang, Y. A.; Peng, X. Conjugation Chemistry and Bioapplications of Semiconductor Box Nanocrystals Prepared via Dendrimer Bridging. *Chem. Mater.* **2003**, *15* (16), 3125–3133.
- (358) Bronstein, L. M.; Shifrina, Z. B. Dendrimers as Encapsulating, Stabilizing, or Directing Agents for Inorganic Nanoparticles. *Chem. Rev.* **2011**, *111* (9), 5301–5344.

- (359) Jishkariani, D.; Diroll, B. T.; Cargnello, M.; Klein, D. R.; Hough, L. A.; Murray, C. B.; Donnio, B. Dendron-Mediated Engineering of Interparticle Separation and Self-Assembly in Dendronized Gold Nanoparticles Superlattices. *J. Am. Chem. Soc.* **2015**, *137* (33), 10728–10734.
- (360) Nikolic, M. S.; Olsson, C.; Salcher, A.; Kornowski, A.; Rank, A.; Schubert, R.; Frömsdorf, A.; Weller, H.; Förster, S. Micelle and Vesicle Formation of Amphiphilic Nanoparticles. *Angew. Chem., Int. Ed.* **2009**, *48* (15), 2752–2754.
- (361) Liu, Y.; Liu, Y.; Yin, J.-J.; Nie, Z. Self-Assembly of Amphiphilic Block Copolymer-Tethered Nanoparticles: A New Approach to Nanoscale Design of Functional Materials. *Macromol. Rapid Commun.* **2015**, *36* (8), 711–725.
- (362) Sánchez-Iglesias, A.; Grzelczak, M.; Altantzis, T.; Goris, B.; Pérez-Juste, J.; Bals, S.; Van Tendeloo, G.; Donaldson, S. H.; Chmelka, B. F.; Israelachvili, J. N.; et al. Hydrophobic Interactions Modulate Self-Assembly of Nanoparticles. *ACS Nano* **2012**, *6* (12), 11059–11065.
- (363) He, J.; Liu, Y.; Babu, T.; Wei, Z.; Nie, Z. Self-Assembly of Inorganic Nanoparticle Vesicles and Tubules Driven by Tethered Linear Block Copolymers. *J. Am. Chem. Soc.* **2012**, *134* (28), 11342–11345.
- (364) He, J.; Wei, Z.; Wang, L.; Tomova, Z.; Babu, T.; Wang, C.; Han, X.; Fourkas, J. T.; Nie, Z. Hydrodynamically Driven Self-Assembly of Giant Vesicles of Metal Nanoparticles for Remote-Controlled Release. *Angew. Chem., Int. Ed.* **2013**, *52* (9), 2463–2468.
- (365) Liu, Y.; He, J.; Yang, K.; Yi, C.; Liu, Y.; Nie, L.; Khashab, N. M.; Chen, X.; Nie, Z. Folding Up of Gold Nanoparticle Strings into Plasmonic Vesicles for Enhanced Photoacoustic Imaging. *Angew. Chem., Int. Ed.* **2015**, *54* (52), 15809–15812.
- (366) Liu, Y.; Li, Y.; He, J.; Duelge, K. J.; Lu, Z.; Nie, Z. Entropy-Driven Pattern Formation of Hybrid Vesicular Assemblies Made from Molecular and Nanoparticle Amphiphiles. *J. Am. Chem. Soc.* **2014**, *136* (6), 2602–2610.
- (367) Liu, Y.; Liu, B.; Nie, Z. Concurrent Self-Assembly of Amphiphiles into Nanoarchitectures with Increasing Complexity. *Nano Today* **2015**, *10* (3), 278–300.
- (368) He, J.; Huang, X.; Li, Y.-C.; Liu, Y.; Babu, T.; Aronova, M. A.; Wang, S.; Lu, Z.; Chen, X.; Nie, Z. Self-Assembly of Amphiphilic Plasmonic Micelle-Like Nanoparticles in Selective Solvents. *J. Am. Chem. Soc.* **2013**, *135* (21), 7974–7984.
- (369) Thompson, R. B.; Ginzburg, V. V.; Matsen, M. W.; Balazs, A. C. Predicting the Mesophases of Copolymer-Nanoparticle Composites. *Science* **2001**, *292* (5526), 2469–2472.
- (370) Yan, L.-T.; Xie, X.-M. Computational Modeling and Simulation of Nanoparticle Self-Assembly in Polymeric Systems: Structures, Properties and External Field Effects. *Prog. Polym. Sci.* **2013**, *38* (2), 369–405.
- (371) Ganeshan, V.; Jayaraman, A. Theory and Simulation Studies of Effective Interactions, Phase Behavior and Morphology in Polymer Nanocomposites. *Soft Matter* **2014**, *10* (1), 13–38.
- (372) Marson, R. L.; Nguyen, T. D.; Glotzer, S. C. Rational Design of Nanomaterials from Assembly and Reconfigurability of Polymer-Tethered Nanoparticles. *MRS Commun.* **2015**, *5* (03), 397–406.
- (373) Karatrantos, A.; Clarke, N.; Kröger, M. Modeling of Polymer Structure and Conformations in Polymer Nanocomposites from Atomistic to Mesoscale: A Review. *Polym. Rev.* **2016**, *56* (3), 385–428.
- (374) Starr, F. W.; Schroder, T. B.; Glotzer, S. C. Molecular Dynamics Simulation of a Polymer Melt with a Nanoscopic Particle. *Macromolecules* **2002**, *35* (11), 4481–4492.
- (375) Starr, F. W.; Douglas, J. F.; Glotzer, S. C. Origin of Particle Clustering in a Simulated Polymer Nanocomposite and Its Impact on Rheology. *J. Chem. Phys.* **2003**, *119* (3), 1777–1788.
- (376) Lin, J.-Q.; Zhang, H.-W.; Chen, Z.; Zheng, Y.-G.; Zhang, Z.-Q.; Ye, H.-F. Simulation Study of Aggregations of Monolayer-Protected Gold Nanoparticles in Solvents. *J. Phys. Chem. C* **2011**, *115* (39), 18991–18998.
- (377) Patra, T. K.; Singh, J. K. Coarse-Grain Molecular Dynamics Simulations of Nanoparticle-Polymer Melt: Dispersion vs. Agglomeration. *J. Chem. Phys.* **2013**, *138* (14), 144901.
- (378) de Moura, A. F.; Bernardino, K.; Dalmaschio, C. J.; Leite, E. R.; Kotov, N. A. Thermodynamic Insights into the Self-Assembly of Capped Nanoparticles Using Molecular Dynamic Simulations. *Phys. Chem. Chem. Phys.* **2015**, *17* (5), 3820–3831.
- (379) Fan, H.; Resasco, D. E.; Striolo, A. Amphiphilic Silica Nanoparticles at the Decane–Water Interface: Insights from Atomistic Simulations. *Langmuir* **2011**, *27* (9), 5264–5274.
- (380) Luu, X.-C.; Yu, J.; Striolo, A. Nanoparticles Adsorbed at the Water/Oil Interface: Coverage and Composition Effects on Structure and Diffusion. *Langmuir* **2013**, *29* (24), 7221–7228.
- (381) Schwenke, K.; Isa, L.; Cheung, D. L.; Del Gado, E. Conformations and Effective Interactions of Polymer-Coated Nanoparticles at Liquid Interfaces. *Langmuir* **2014**, *30* (42), 12578–12586.
- (382) Quan, X.; Peng, C.; Dong, J.; Zhou, J. Structural Properties of Polymer-Brush-Grafted Gold Nanoparticles at the Oil–Water Interface: Insights from Coarse-Grained Simulations. *Soft Matter* **2016**, *12* (14), 3352–3359.
- (383) Posel, Z.; Posocco, P.; Lísal, M.; Fermeglia, M.; Prich, S. Highly Grafted Polystyrene/Polyvinylpyridine Polymer Gold Nanoparticles in a Good Solvent: Effects of Chain Length and Composition. *Soft Matter* **2016**, *12* (15), 3600–3611.
- (384) Detcheverry, F. A.; Kang, H.; Daoulas, K. C.; Müller, M.; Nealey, P. F.; de Pablo, J. J. Monte Carlo Simulations of a Coarse Grain Model for Block Copolymers and Nanocomposites. *Macromolecules* **2008**, *41* (13), 4989–5001.
- (385) Hoheisel, T. N.; Hur, K.; Wiesner, U. B. Block Copolymer-Nanoparticle Hybrid Self-Assembly. *Prog. Polym. Sci.* **2015**, *40*, 3–32.
- (386) Riest, J.; Athanasopoulou, L.; Egorov, S. A.; Likos, C. N.; Ziherl, P. Elasticity of Polymeric Nanocolloidal Particles. *Sci. Rep.* **2015**, *5*, 15854.
- (387) Chen, K.; Li, H.; Zhang, B.-K.; Li, J.; Tian, W.-D. A New Self-Consistent Field Model of Polymer/Nanoparticle Mixture. *Sci. Rep.* **2016**, *6*, 20355.
- (388) Yan, L.-T.; Maresov, E.; Buxton, G. A.; Balazs, A. C. Self-Assembly of Mixtures of Nanorods in Binary, Phase-Separating Blends. *Soft Matter* **2011**, *7* (2), 595–607.
- (389) Haley, J. D.; Iacovella, C. R.; Cummings, P. T.; McCabe, C. Examining the Aggregation Behavior of Polymer Grafted Nanoparticles Using Molecular Simulation and Theory. *J. Chem. Phys.* **2015**, *143* (5), 054904.
- (390) Zhang; Horsch, M. A.; Lamm, M. H.; Glotzer, S. C. Tethered Nano Building Blocks: Toward a Conceptual Framework for Nanoparticle Self-Assembly. *Nano Lett.* **2003**, *3* (10), 1341–1346.
- (391) Schultz, A. J.; Hall, C. K.; Genzer, J. Computer Simulation of Block Copolymer/Nanoparticle Composites. *Macromolecules* **2005**, *38* (7), 3007–3016.
- (392) Iacovella, C. R.; Horsch, M. A.; Zhang, Z.; Glotzer, S. C. Phase Diagrams of Self-Assembled Mono-Tethered Nanospheres from Molecular Simulation and Comparison to Surfactants. *Langmuir* **2005**, *21* (21), 9488–9494.
- (393) Iacovella, C. R.; Keys, A. S.; Horsch, M. A.; Glotzer, S. C. Icosahedral Packing of Polymer-Tethered Nanospheres and Stabilization of the Gyroid Phase. *Phys. Rev. E* **2007**, *75* (4), 040801.
- (394) Iacovella, C. R.; Glotzer, S. C. Complex Crystal Structures Formed by the Self-Assembly of Ditethered Nanospheres. *Nano Lett.* **2009**, *9* (3), 1206–1211.
- (395) Marson, R. L.; Phillips, C. L.; Anderson, J. A.; Glotzer, S. C. Phase Behavior and Complex Crystal Structures of Self-Assembled Tethered Nanoparticle Telechelics. *Nano Lett.* **2014**, *14* (4), 2071–2078.
- (396) Chan, E. R.; Zhang, X.; Lee, C.-Y.; Neurock, M.; Glotzer, S. C. Simulations of Tetra-Tethered Organic/Inorganic Nanocube–Polymer Assemblies. *Macromolecules* **2005**, *38* (14), 6168–6180.
- (397) Zhang, W.-B.; Yu, X.; Wang, C.-L.; Sun, H.-J.; Hsieh, I.-F.; Li, Y.; Dong, X.-H.; Yue, K.; Van Horn, R.; Cheng, S. Z. D. Molecular Nanoparticles Are Unique Elements for Macromolecular Science:

- From “Nanoatoms” to Giant Molecules. *Macromolecules* **2014**, *47* (4), 1221–1239.
- (398) Horsch, M. A.; Zhang, Z.; Glotzer, S. C. Self-Assembly of Polymer-Tethered Nanorods. *Phys. Rev. Lett.* **2005**, *95* (5), 056105.
- (399) Horsch, M. A.; Zhang, Z.; Glotzer, S. C. Self-Assembly of Laterally-Tethered Nanorods. *Nano Lett.* **2006**, *6* (11), 2406–2413.
- (400) Nguyen, T. D.; Glotzer, S. C. Switchable Helical Structures Formed by the Hierarchical Self-Assembly of Laterally Tethered Nanorods. *Small* **2009**, *5* (18), 2092–2098.
- (401) Nguyen, T. D.; Jankowski, E.; Glotzer, S. C. Self-Assembly and Reconfigurability of Shape-Shifting Particles. *ACS Nano* **2011**, *5* (11), 8892–8903.
- (402) Guo, R.; Liu, Z.; Xie, X.-M.; Yan, L.-T. Harnessing Dynamic Covalent Bonds in Patchy Nanoparticles: Creating Shape-Shifting Building Blocks for Rational and Responsive Self-Assembly. *J. Phys. Chem. Lett.* **2013**, *4* (8), 1221–1226.
- (403) Phillips, C. L.; Glotzer, S. C. Effect of Nanoparticle Polydispersity on the Self-Assembly of Polymer Tethered Nanspheres. *J. Chem. Phys.* **2012**, *137* (10), 104901.
- (404) Zhang; Glotzer, S. C. Self-Assembly of Patchy Particles. *Nano Lett.* **2004**, *4* (8), 1407–1413.
- (405) Pawar, A. B.; Kretzschmar, I. Fabrication, Assembly, and Application of Patchy Particles. *Macromol. Rapid Commun.* **2010**, *31* (2), 150–168.
- (406) Bianchi, E.; Blaak, R.; Likos, C. N. Patchy Colloids: State of the Art and Perspectives. *Phys. Chem. Chem. Phys.* **2011**, *13* (14), 6397–6410.
- (407) Lunn, D. J.; Finnegan, J. R.; Manners, I. Self-Assembly of “Patchy” Nanoparticles: A Versatile Approach to Functional Hierarchical Materials. *Chem. Sci.* **2015**, *6* (7), 3663–3673.
- (408) Kern, N.; Frenkel, D. Fluid–Fluid Coexistence in Colloidal Systems with Short-Ranged Strongly Directional Attraction. *J. Chem. Phys.* **2003**, *118* (21), 9882–9889.
- (409) Sciortino, F.; Bianchi, E.; Douglas, J. F.; Tartaglia, P. Self-Assembly of Patchy Particles into Polymer Chains: A Parameter-Free Comparison between Wertheim Theory and Monte Carlo Simulation. *J. Chem. Phys.* **2007**, *126* (19), 194903.
- (410) Noya, E. G.; Vega, C.; Doye, J. P. K.; Louis, A. A. Phase Diagram of Model Anisotropic Particles with Octahedral Symmetry. *J. Chem. Phys.* **2007**, *127* (5), 054501.
- (411) Zhang; Keys, A. S.; Chen, T.; Glotzer, S. C. Self-Assembly of Patchy Particles into Diamond Structures through Molecular Mimicry. *Langmuir* **2005**, *21* (25), 11547–11551.
- (412) Noya, E. G.; Vega, C.; Doye, J. P. K.; Louis, A. A. The Stability of a Crystal with Diamond Structure for Patchy Particles with Tetrahedral Symmetry. *J. Chem. Phys.* **2010**, *132* (23), 234511.
- (413) Romano, F.; Sanz, E.; Sciortino, F. Crystallization of Tetrahedral Patchy Particles in Silico. *J. Chem. Phys.* **2011**, *134* (17), 174502.
- (414) Smallenburg, F.; Sciortino, F. Liquids More Stable Than Crystals in Particles with Limited Valence and Flexible Bonds. *Nat. Phys.* **2013**, *9* (9), 554–558.
- (415) Newton, A. C.; Groenewold, J.; Kegel, W. K.; Bolhuis, P. G. Rotational Diffusion Affects the Dynamical Self-Assembly Pathways of Patchy Particles. *Proc. Natl. Acad. Sci. U. S. A.* **2015**, *112* (50), 15308–15313.
- (416) Asai, M.; Cacciuto, A.; Kumar, S. K. Quantitative Analogy between Polymer-Grafted Nanoparticles and Patchy Particles. *Soft Matter* **2015**, *11* (4), 793–797.
- (417) Mahynski, N. A.; Panagiotopoulos, A. Z. Grafted Nanoparticles as Soft Patchy Colloids: Self-Assembly versus Phase Separation. *J. Chem. Phys.* **2015**, *142* (7), 074901.
- (418) Walther, A.; Müller, A. H. E. Janus Particles: Synthesis, Self-Assembly, Physical Properties, and Applications. *Chem. Rev.* **2013**, *113* (7), 5194–5261.
- (419) Lattuada, M.; Hatton, T. A. Synthesis, Properties and Applications of Janus Nanoparticles. *Nano Today* **2011**, *6* (3), 286–308.
- (420) Zhang, J.; Luijten, E.; Granick, S. Toward Design Rules of Directional Janus Colloidal Assembly. *Annu. Rev. Phys. Chem.* **2015**, *66* (1), 581–600.
- (421) Vácha, R.; Frenkel, D. Relation between Molecular Shape and the Morphology of Self-Assembling Aggregates: A Simulation Study. *Biophys. J.* **2011**, *101* (6), 1432–1439.
- (422) Preisler, Z.; Vissers, T.; Munaò, G.; Smallenburg, F.; Sciortino, F. Equilibrium Phases of One-Patch Colloids with Short-Range Attractions. *Soft Matter* **2014**, *10* (28), 5121–5128.
- (423) Mao, X.; Chen, Q.; Granick, S. Entropy Favours Open Colloidal Lattices. *Nat. Mater.* **2013**, *12* (3), 217–222.
- (424) Alexeev, A.; Uspal, W. E.; Balazs, A. C. Harnessing Janus Nanoparticles to Create Controllable Pores in Membranes. *ACS Nano* **2008**, *2* (6), 1117–1122.
- (425) Sacanna, S.; Irvine, W. T. M.; Chaikin, P. M.; Pine, D. J. Lock and Key Colloids. *Nature* **2010**, *464* (7288), 575–578.
- (426) Chen, Q.; Bae, S. C.; Granick, S. Directed Self-Assembly of a Colloidal Kagome Lattice. *Nature* **2011**, *469* (7330), 381–384.
- (427) Kraft, D. J.; Ni, R.; Smallenburg, F.; Hermes, M.; Yoon, K.; Weitz, D. A.; van Blaaderen, A.; Groenewold, J.; Dijkstra, M.; Kegel, W. K. Surface Roughness Directed Self-Assembly of Patchy Particles into Colloidal Micelles. *Proc. Natl. Acad. Sci. U. S. A.* **2012**, *109* (27), 10787–10792.
- (428) Wang, Y.; Wang, Y.; Breed, D. R.; Manoharan, V. N.; Feng, L.; Hollingsworth, A. D.; Weck, M.; Pine, D. J. Colloids with Valence and Specific Directional Bonding. *Nature* **2012**, *491* (7422), 51–55.
- (429) Wang, Y.; Hollingsworth, A. D.; Yang, S. K.; Patel, S.; Pine, D. J.; Weck, M. Patchy Particle Self-Assembly via Metal Coordination. *J. Am. Chem. Soc.* **2013**, *135* (38), 14064–14067.
- (430) Shah, A. A.; Schultz, B.; Zhang, W.; Glotzer, S. C.; Solomon, M. J. Actuation of Shape-Memory Colloidal Fibres of Janus Ellipsoids. *Nat. Mater.* **2014**, *14* (1), 117–124.
- (431) Meester, V.; Verweij, R. W.; van der Wel, C.; Kraft, D. J. Colloidal Recycling: Reconfiguration of Random Aggregates into Patchy Particles. *ACS Nano* **2016**, *10* (4), 4322–4329.
- (432) Evers, C. H. J.; Luiken, J. A.; Bolhuis, P. G.; Kegel, W. K. Self-Assembly of Microcapsules via Colloidal Bond Hybridization and Anisotropy. *Nature* **2016**, *534* (7607), 364–368.
- (433) Gröschel, A. H.; Schacher, F. H.; Schmalz, H.; Borisov, O. V.; Zhulina, E. B.; Walther, A.; Müller, A. H. E. Precise Hierarchical Self-Assembly of Multicompartment Micelles. *Nat. Commun.* **2012**, *3*, 710.
- (434) Qiu, H.; Russo, G.; Rupar, P. A.; Chabanne, L.; Winnik, M. A.; Manners, I. Tunable Supramicelle Architectures from the Hierarchical Self-Assembly of Amphiphilic Cylindrical B-A-B Triblock Co-Micelles. *Angew. Chem., Int. Ed.* **2012**, *51* (47), 11882–11885.
- (435) Gröschel, A. H.; Walther, A.; Löbling, T. I.; Schacher, F. H.; Schmalz, H.; Müller, A. H. E. Guided Hierarchical Co-Assembly of Soft Patchy Nanoparticles. *Nature* **2013**, *503* (7475), 247–251.
- (436) Ma, C.; Wu, H.; Huang, Z.-H.; Guo, R.-H.; Hu, M.-B.; Kübel, C.; Yan, L.-T.; Wang, W. A Filled-Honeycomb-Structured Crystal Formed by Self-Assembly of a Janus Polyoxometalate-Silsesquioxane (POM-POSS) Co-Cluster. *Angew. Chem., Int. Ed.* **2015**, *54* (52), 15699–15704.
- (437) Dogic, Z.; Fraden, S. Development of Model Colloidal Liquid Crystals and the Kinetics of the Isotropic-Smectic Transition. *Philos. Trans. R. Soc., A* **2001**, *359* (1782), 997–1015.
- (438) Sharma, P.; Ward, A.; Gibaud, T.; Hagan, M. F.; Dogic, Z. Hierarchical Organization of Chiral Rafts in Colloidal Membranes. *Nature* **2014**, *513* (7516), 77–80.
- (439) Chen, Q.; Whitmer, J. K.; Jiang, S.; Bae, S. C.; Luijten, E.; Granick, S. Supracolloidal Reaction Kinetics of Janus Spheres. *Science* **2011**, *331* (6014), 199–202.
- (440) Burrows, N. D.; Vartanian, A. M.; Abadeer, N. S.; Grzincic, E. M.; Jacob, L. M.; Lin, W.; Li, J.; Dennison, J. M.; Hinman, J. G.; Murphy, C. J. Anisotropic Nanoparticles and Anisotropic Surface Chemistry. *J. Phys. Chem. Lett.* **2016**, *7* (4), 632–641.
- (441) Talapin, D. V.; Rogach, A. L.; Kornowski, A.; Haase, M.; Weller, H. Highly Luminescent Monodisperse CdSe and CdSe/ZnS

- Nanocrystals Synthesized in a Hexadecylamine–Trioctylphosphine Oxide–Trioctylphosphine Mixture. *Nano Lett.* **2001**, *1* (4), 207–211.
- (442) Jackson, A. M.; Myerson, J. W.; Stellacci, F. Spontaneous Assembly of Subnanometre-Ordered Domains in the Ligand Shell of Monolayer-Protected Nanoparticles. *Nat. Mater.* **2004**, *3* (5), 330–336.
- (443) Singh, C.; Ghorai, P. K.; Horsch, M. A.; Jackson, A. M.; Larson, R. G.; Stellacci, F.; Glotzer, S. C. Entropy-Mediated Patterning of Surfactant-Coated Nanoparticles and Surfaces. *Phys. Rev. Lett.* **2007**, *99* (22), 226106.
- (444) Cesbron, Y.; Shaw, C. P.; Birchall, J. P.; Free, P.; Lévy, R. Stripy Nanoparticles Revisited. *Small* **2012**, *8* (24), 3714–3719.
- (445) Nie, Z.; Fava, D.; Kumacheva, E.; Zou, S.; Walker, G. C.; Rubinstein, M. Self-Assembly of Metal–Polymer Analogues of Amphiphilic Triblock Copolymers. *Nat. Mater.* **2007**, *6* (8), 609–614.
- (446) Nie, Z.; Fava, D.; Rubinstein, M.; Kumacheva, E. Supramolecular Assembly of Gold Nanorods End-Terminated with Polymer “Pom-Poms”: Effect of Pom-Pom Structure on the Association Modes. *J. Am. Chem. Soc.* **2008**, *130* (11), 3683–3689.
- (447) McLeish, T. C. B.; Larson, R. G. Molecular Constitutive Equations for a Class of Branched Polymers: The Pom-Pom Polymer. *J. Rheol. (Melville, NY, U. S.)* **1998**, *42* (1), 81–110.
- (448) Liu, K.; Nie, Z.; Zhao, N.; Li, W.; Rubinstein, M.; Kumacheva, E. Step-Growth Polymerization of Inorganic Nanoparticles. *Science* **2010**, *329* (5988), 197–200.
- (449) Choueiri, R. M.; Klinkova, A.; Thérien-Aubin, H.; Rubinstein, M.; Kumacheva, E. Structural Transitions in Nanoparticle Assemblies Governed by Competing Nanoscale Forces. *J. Am. Chem. Soc.* **2013**, *135* (28), 10262–10265.
- (450) Lee, H.-Y.; Shin, S. H. R.; Drews, A. M.; Chirisan, A. M.; Lewis, S. A.; Bishop, K. J. M. Self-Assembly of Nanoparticle Amphiphiles with Adaptive Surface Chemistry. *ACS Nano* **2014**, *8* (10), 9979–9987.
- (451) Petukhova, A.; Greener, J.; Liu, K.; Nykypanchuk, D.; Nicolay, R.; Matyjaszewski, K.; Kumacheva, E. Standing Arrays of Gold Nanorods End-Tethered with Polymer Ligands. *Small* **2012**, *8* (5), 731–737.
- (452) Stewart, A. F.; Lee, A.; Ahmed, A.; Ip, S.; Kumacheva, E.; Walker, G. C. Rational Design for the Controlled Aggregation of Gold Nanorods via Phospholipid Encapsulation for Enhanced Raman Scattering. *ACS Nano* **2014**, *8* (6), 5462–5467.
- (453) Zhou, T.; Dong, B.; Qi, H.; Mei, S.; Li, C. Y. Janus Hybrid Hairy Nanoparticles. *J. Polym. Sci., Part B: Polym. Phys.* **2014**, *52* (24), 1620–1640.
- (454) Urban, M.; Freisinger, B.; Ghazy, O.; Staff, R.; Landfester, K.; Crespy, D.; Musyanovych, A. Polymer Janus Nanoparticles with Two Spatially Segregated Functionalizations. *Macromolecules* **2014**, *47* (20), 7194–7199.
- (455) Nepal, D.; Park, K.; Vaia, R. A. High-Yield Assembly of Soluble and Stable Gold Nanorod Pairs for High-Temperature Plasmonics. *Small* **2012**, *8* (7), 1013–1020.
- (456) Grzelczak, M.; Sánchez-Iglesias, A.; Mezerji, H. H.; Bals, S.; Pérez-Juste, J.; Liz-Marzán, L. M. Steric Hindrance Induces Crosslike Self-Assembly of Gold Nanodumbbells. *Nano Lett.* **2012**, *12* (8), 4380–4384.
- (457) Bian, T.; Shang, L.; Yu, H.; Perez, M. T.; Wu, L.-Z.; Tung, C.-H.; Nie, Z.; Tang, Z.; Zhang, T. Spontaneous Organization of Inorganic Nanoparticles into Nanovesicles Triggered by UV Light. *Adv. Mater.* **2014**, *26* (32), 5613–5618.
- (458) Tang, Z.; Kotov, N. A.; Giersig, M. Spontaneous Organization of Single CdTe Nanoparticles into Luminescent Nanowires. *Science* **2002**, *297* (5579), 237–240.
- (459) Tang, Z.; Zhang, Z.; Wang, Y.; Glotzer, S. C.; Kotov, N. A. Self-Assembly of CdTe Nanocrystals into Free-Floating Sheets. *Science* **2006**, *314* (5797), 274–278.
- (460) Zhang, Z.; Tang, Z.; Kotov, N. A.; Glotzer, S. C. Simulations and Analysis of Self-Assembly of CdTe Nanoparticles into Wires and Sheets. *Nano Lett.* **2007**, *7* (6), 1670–1675.
- (461) Walker, D. A.; Browne, K. P.; Kowalczyk, B.; Grzybowski, B. A. Self-Assembly of Nanotriangle Superlattices Facilitated by Repulsive Electrostatic Interactions. *Angew. Chem., Int. Ed.* **2010**, *49* (38), 6760–6763.
- (462) Kovalenko, M. V.; Bodnarchuk, M. I.; Talapin, D. V. Nanocrystal Superlattices with Thermally Degradable Hybrid Inorganic–Organic Capping Ligands. *J. Am. Chem. Soc.* **2010**, *132* (43), 15124–15126.
- (463) Bodnarchuk, M. I.; Yakunin, S.; Piveteau, L.; Kovalenko, M. V. Host–Guest Chemistry for Tuning Colloidal Solubility, Self-Organization and Photoconductivity of Inorganic-Capped Nanocrystals. *Nat. Commun.* **2015**, *6*, 10142.
- (464) Bartlett, P.; Campbell, A. I. Three-Dimensional Binary Superlattices of Oppositely Charged Colloids. *Phys. Rev. Lett.* **2005**, *95* (12), 128302.
- (465) Hynninen, A.-P.; Christova, C. G.; van Roij, R.; van Blaaderen, A.; Dijkstra, M. Prediction and Observation of Crystal Structures of Oppositely Charged Colloids. *Phys. Rev. Lett.* **2006**, *96* (13), 138308.
- (466) Kalsin, A. M.; Kowalczyk, B.; Smoukov, S. K.; Klajn, R.; Grzybowski, B. A. Ionic-like Behavior of Oppositely Charged Nanoparticles. *J. Am. Chem. Soc.* **2006**, *128* (47), 15046–15047.
- (467) Kalsin, A. M.; Fialkowski, M.; Paszewski, M.; Smoukov, S. K.; Bishop, K. J. M.; Grzybowski, B. A. Electrostatic Self-Assembly of Binary Nanoparticle Crystals with a Diamond-Like Lattice. *Science* **2006**, *312* (5772), 420–424.
- (468) Pillai, P. P.; Kowalczyk, B.; Grzybowski, B. A. Self-Assembly of Like-Charged Nanoparticles into Microscopic Crystals. *Nanoscale* **2016**, *8* (1), 157–161.
- (469) Kowalczyk, B.; Kalsin, A. M.; Orlik, R.; Bishop, K. J. M.; Patashinskii, A. Z.; Mitus, A.; Grzybowski, B. A. Size Selection During Crystallization of Oppositely Charged Nanoparticles. *Chem. - Eur. J.* **2009**, *15* (9), 2032–2035.
- (470) Piccinini, E.; Pallarola, D.; Battaglini, F.; Azzaroni, O. Self-Limited Self-Assembly of Nanoparticles into Supraparticles: Towards Supramolecular Colloidal Materials by Design. *Mol. Syst. Des. Eng.* **2016**, *1*, 155–162, DOI: 10.1039/C6ME00016A.
- (471) Xia, Y.; Nguyen, T. D.; Yang, M.; Lee, B.; Santos, A.; Podsiadlo, P.; Tang, Z.; Glotzer, S. C.; Kotov, N. A. Self-Assembly of Self-Limiting Monodisperse Supraparticles from Polydisperse Nanoparticles. *Nat. Nanotechnol.* **2011**, *6* (9), 580–587.
- (472) Nguyen, T. D.; Schultz, B. A.; Kotov, N. A.; Glotzer, S. C. Generic, Phenomenological, On-The-Fly Renormalized Repulsion Model for Self-Limited Organization of Terminal Supraparticle Assemblies. *Proc. Natl. Acad. Sci. U. S. A.* **2015**, *112* (25), E3161–E3168.
- (473) Demirörs, A. F.; Stiefelhagen, J. C. P.; Vissers, T.; Smallenburg, F.; Dijkstra, M.; Imhof, A.; van Blaaderen, A. Long-Ranged Oppositely Charged Interactions for Designing New Types of Colloidal Clusters. *Phys. Rev. X* **2015**, *5* (2), 021012.
- (474) Kowalczyk, B.; Bishop, K. J. M.; Lagzi, I.; Wang, D.; Wei, Y.; Han, S.; Grzybowski, B. A. Charged Nanoparticles as Supramolecular Surfactants for Controlling the Growth and Stability of Microcrystals. *Nat. Mater.* **2012**, *11* (3), 227–232.
- (475) Cabane, B.; Li, J.; Artzner, F.; Botet, R.; Labbez, C.; Bareigt, G.; Sztucki, M.; Goehring, L. Hiding in Plain View: Colloidal Self-Assembly from Polydisperse Populations. *Phys. Rev. Lett.* **2016**, *116* (20), 208001.
- (476) Fasolo, M.; Sollich, P. Equilibrium Phase Behavior of Polydisperse Hard Spheres. *Phys. Rev. Lett.* **2003**, *91* (6), 068301.
- (477) Sollich, P.; Wilding, N. B. Crystalline Phases of Polydisperse Spheres. *Phys. Rev. Lett.* **2010**, *104* (11), 118302.
- (478) Botet, R.; Cabane, B.; Goehring, L.; Li, J.; Artzner, F. How Do Polydisperse Repulsive Colloids Crystallize? *Faraday Discuss.* **2016**, *186* (0), 229–240.
- (479) Kostiainen, M. A.; Hiekataipale, P.; Laiho, A.; Lemieux, V.; Seitsonen, J.; Ruokolainen, J.; Ceci, P. Electrostatic Assembly of Binary Nanoparticle Superlattices Using Protein Cages. *Nat. Nanotechnol.* **2012**, *8* (1), 52–56.
- (480) Walker, D. A.; Leitsch, E. K.; Nap, R. J.; Szleifer, I.; Grzybowski, B. A. Geometric Curvature Controls the Chemical

- Patchiness and Self-Assembly of Nanoparticles. *Nat. Nanotechnol.* **2013**, *8* (9), 676–681.
- (481) Pothorszky, S.; Zámbó, D.; Deák, T.; Deák, A. Assembling Patchy Nanorods with Spheres: Limitations Imposed by Colloidal Interactions. *Nanoscale* **2016**, *8* (6), 3523–3529.
- (482) Jones, M. R.; Seeman, N. C.; Mirkin, C. A. Programmable Materials and the Nature of the DNA Bond. *Science* **2015**, *347* (6224), 1260901.
- (483) Rogers, W. B.; Shih, W. M.; Manoharan, V. N. Using DNA to Program the Self-Assembly of Colloidal Nanoparticles and Microparticles. *Nat. Rev. Mater.* **2016**, *1* (3), 16008.
- (484) Ke, Y.; Ong, L. L.; Shih, W. M.; Yin, P. Three-Dimensional Structures Self-Assembled from DNA Bricks. *Science* **2012**, *338* (6111), 1177–1183.
- (485) Jin, R.; Wu, G.; Li, Z.; Mirkin, C. A.; Schatz, G. C. What Controls the Melting Properties of DNA-Linked Gold Nanoparticle Assemblies? *J. Am. Chem. Soc.* **2003**, *125* (6), 1643–1654.
- (486) O'Brien, M. N.; Brown, K. A.; Mirkin, C. A. Critical Undercooling in DNA-Mediated Nanoparticle Crystallization. *ACS Nano* **2016**, *10* (1), 1363–1368.
- (487) Dreyfus, R.; Leunissen, M. E.; Sha, R.; Tkachenko, A. V.; Seeman, N. C.; Pine, D. J.; Chaikin, P. M. Simple Quantitative Model for the Reversible Association of DNA Coated Colloids. *Phys. Rev. Lett.* **2009**, *102* (4), 048301.
- (488) Varilly, P.; Angioletti-Uberti, S.; Mognetti, B. M.; Frenkel, D. A General Theory of DNA-Mediated and Other Valence-Limited Colloidal Interactions. *J. Chem. Phys.* **2012**, *137* (9), 094108.
- (489) Estephan, Z. G.; Qian, Z.; Lee, D.; Crocker, J. C.; Park, S.-J. Responsive Multidomain Free-Standing Films of Gold Nanoparticles Assembled by DNA-Directed Layer-by-Layer Approach. *Nano Lett.* **2013**, *13* (9), 4449–4455.
- (490) Angioletti-Uberti, S.; Mognetti, B. M.; Frenkel, D. Re-Entrant Melting as a Design Principle for DNA-Coated Colloids. *Nat. Mater.* **2012**, *11* (6), 518–522.
- (491) Rogers, W. B.; Manoharan, V. N. Programming Colloidal Phase Transitions with DNA Strand Displacement. *Science* **2015**, *347* (6222), 639–642.
- (492) Seo, S. E.; Wang, M. X.; Shade, C. M.; Rouge, J. L.; Brown, K. A.; Mirkin, C. A. Modulating the Bond Strength of DNA–Nanoparticle Superlattices. *ACS Nano* **2016**, *10* (2), 1771–1779.
- (493) Wang, H.; Li, Y.; Liu, M.; Gong, M.; Deng, Z. Overcoming the Coupling Dilemma in DNA-Programmable Nanoparticle Assemblies by “Ag⁺ Soldering. *Small* **2015**, *11* (19), 2247–2251.
- (494) Nykypanchuk, D.; Maye, M. M.; van der Lelie, D.; Gang, O. DNA-Guided Crystallization of Colloidal Nanoparticles. *Nature* **2008**, *451* (7178), 549–552.
- (495) Park, S. Y.; Lytton-Jean, A. K. R.; Lee, B.; Weigand, S.; Schatz, G. C.; Mirkin, C. A. DNA-Programmable Nanoparticle Crystallization. *Nature* **2008**, *451* (7178), 553–556.
- (496) Xiong, H.; van der Lelie, D.; Gang, O. Phase Behavior of Nanoparticles Assembled by DNA Linkers. *Phys. Rev. Lett.* **2009**, *102* (1), 015504.
- (497) Kim, Y.; Macfarlane, R. J.; Jones, M. R.; Mirkin, C. A. Transmutable Nanoparticles with Reconfigurable Surface Ligands. *Science* **2016**, *351* (6273), 579–582.
- (498) Casey, M. T.; Scarlett, R. T.; Benjamin Rogers, W.; Jenkins, I.; Sinn, T.; Crocker, J. C. Driving Diffusionless Transformations in Colloidal Crystals Using DNA Handshaking. *Nat. Commun.* **2012**, *3*, 1209.
- (499) Macfarlane, R. J.; Lee, B.; Jones, M. R.; Harris, N.; Schatz, G. C.; Mirkin, C. A. Nanoparticle Superlattice Engineering with DNA. *Science* **2011**, *334* (6053), 204–208.
- (500) O'Brien, M. N.; Jones, M. R.; Lee, B.; Mirkin, C. A. Anisotropic Nanoparticle Complementarity in DNA-Mediated Co-Crystallization. *Nat. Mater.* **2015**, *14* (8), 833–839.
- (501) Liu, W.; Tagawa, M.; Xin, H. L.; Wang, T.; Emamy, H.; Li, H.; Yager, K. G.; Starr, F. W.; Tkachenko, A. V.; Gang, O. Diamond Family of Nanoparticle Superlattices. *Science* **2016**, *351* (6273), 582–586.
- (502) Auyeung, E.; Cutler, J. I.; Macfarlane, R. J.; Jones, M. R.; Wu, J.; Liu, G.; Zhang, K.; Osberg, K. D.; Mirkin, C. A. Synthetically Programmable Nanoparticle Superlattices Using a Hollow Three-Dimensional Spacer Approach. *Nat. Nanotechnol.* **2011**, *7* (1), 24–28.
- (503) Zhang, Y.; Pal, S.; Srinivasan, B.; Vo, T.; Kumar, S.; Gang, O. Selective Transformations between Nanoparticle Superlattices via the Reprogramming of DNA-Mediated Interactions. *Nat. Mater.* **2015**, *14* (8), 840–847.
- (504) Maye, M. M.; Kumara, M. T.; Nykypanchuk, D.; Sherman, W. B.; Gang, O. Switching Binary States of Nanoparticle Superlattices and Dimer Clusters by DNA Strands. *Nat. Nanotechnol.* **2010**, *5* (2), 116–120.
- (505) Radha, B.; Senesi, A. J.; O'Brien, M. N.; Wang, M. X.; Auyeung, E.; Lee, B.; Mirkin, C. A. Reconstitutable Nanoparticle Superlattices. *Nano Lett.* **2014**, *14* (4), 2162–2167.
- (506) Feng, L.; Dreyfus, R.; Sha, R.; Seeman, N. C.; Chaikin, P. M. DNA Patchy Particles. *Adv. Mater.* **2013**, *25* (20), 2779–2783.
- (507) Xu, L.; Kuang, H.; Xu, C.; Ma, W.; Wang, L.; Kotov, N. A. Regiospecific Plasmonic Assemblies for in Situ Raman Spectroscopy in Live Cells. *J. Am. Chem. Soc.* **2012**, *134* (3), 1699–1709.
- (508) Xing, H.; Wang, Z.; Xu, Z.; Wong, N. Y.; Xiang, Y.; Liu, G. L.; Lu, Y. DNA-Directed Assembly of Asymmetric Nanoclusters Using Janus Nanoparticles. *ACS Nano* **2012**, *6* (1), 802–809.
- (509) Dhakal, S.; Kohlstedt, K. L.; Schatz, G. C.; Mirkin, C. A.; Olvera de la Cruz, M. Growth Dynamics for DNA-Guided Nanoparticle Crystallization. *ACS Nano* **2013**, *7* (12), 10948–10959.
- (510) Macfarlane, R. J.; Lee, B.; Jones, M. R.; Harris, N.; Schatz, G. C.; Mirkin, C. A. Nanoparticle Superlattice Engineering with DNA. *Science* **2011**, *334* (6053), 204–208.
- (511) Rothmund, P. W. K. Folding DNA to Create Nanoscale Shapes and Patterns. *Nature* **2006**, *440* (7082), 297–302.
- (512) Weizmann, Y.; Braunschweig, A. B.; Wilner, O. I.; Cheglakov, Z.; Willner, I. A Polycatenated DNA Scaffold for the One-Step Assembly of Hierarchical Nanostructures. *Proc. Natl. Acad. Sci. U. S. A.* **2008**, *105* (14), 5289–5294.
- (513) Endo, M.; Yang, Y.; Emura, T.; Hidaka, K.; Sugiyama, H. Programmed Placement of Gold Nanoparticles onto a Slit-Type DNA Origami Scaffold. *Chem. Commun.* **2011**, *47* (38), 10743.
- (514) Pilo-Pais, M.; Goldberg, S.; Samano, E.; LaBean, T. H.; Finkelstein, G. Connecting the Nanodots: Programmable Nanofabrication of Fused Metal Shapes on DNA Templates. *Nano Lett.* **2011**, *11* (8), 3489–3492.
- (515) Kuzyk, A.; Schreiber, R.; Fan, Z.; Pardatscher, G.; Roller, E.-M.; Högele, A.; Simmel, F. C.; Govorov, A. O.; Liedl, T. DNA-Based Self-Assembly of Chiral Plasmonic Nanostructures with Tailored Optical Response. *Nature* **2012**, *483* (7389), 311–314.
- (516) Schreiber, R.; Do, J.; Roller, E.-M.; Zhang, T.; Schüller, V. J.; Nickels, P. C.; Feldmann, J.; Liedl, T. Hierarchical Assembly of Metal Nanoparticles, Quantum Dots and Organic Dyes Using DNA Origami Scaffolds. *Nat. Nanotechnol.* **2013**, *9* (1), 74–78.
- (517) Tian, Y.; Wang, T.; Liu, W.; Xin, H. L.; Li, H.; Ke, Y.; Shih, W. M.; Gang, O. Prescribed Nanoparticle Cluster Architectures and Low-Dimensional Arrays Built Using Octahedral DNA Origami Frames. *Nat. Nanotechnol.* **2015**, *10* (7), 637–644.
- (518) Sharma, J.; Chhabra, R.; Cheng, A.; Brownell, J.; Liu, Y.; Yan, H. Control of Self-Assembly of DNA Tubules through Integration of Gold Nanoparticles. *Science* **2009**, *323* (5910), 112–116.
- (519) Cheng, W.; Campolongo, M. J.; Cha, J. J.; Tan, S. J.; Umbach, C. C.; Muller, D. A.; Luo, D. Free-Standing Nanoparticle Superlattice Sheets Controlled by DNA. *Nat. Mater.* **2009**, *8* (6), 519–525.
- (520) Liu, W.; Halverson, J.; Tian, Y.; Tkachenko, A. V.; Gang, O. Self-Organized Architectures from Assorted DNA-Framed Nanoparticles. *Nat. Chem.* **2016**, DOI: 10.1038/nchem.2540.
- (521) Yao, G.; Li, J.; Chao, J.; Pei, H.; Liu, H.; Zhao, Y.; Shi, J.; Huang, Q.; Wang, L.; Huang, W.; et al. Gold-Nanoparticle-Mediated Jigsaw-Puzzle-like Assembly of Supersized Plasmonic DNA Origami. *Angew. Chem., Int. Ed.* **2015**, *54* (10), 2966–2969.

- (522) Tian, Y.; Zhang, Y.; Wang, T.; Xin, H. L.; Li, H.; Gang, O. Lattice Engineering through Nanoparticle–DNA Frameworks. *Nat. Mater.* **2016**, *15* (6), 654–661.
- (523) Helmi, S.; Ziegler, C.; Kauert, D. J.; Seidel, R. Shape-Controlled Synthesis of Gold Nanostructures Using DNA Origami Molds. *Nano Lett.* **2014**, *14* (11), 6693–6698.
- (524) Vial, S.; Nykypanchuk, D.; Yager, K. G.; Tkachenko, A. V.; Gang, O. Linear Mesostructures in DNA–Nanorod Self-Assembly. *ACS Nano* **2013**, *7* (6), 5437–5445.
- (525) Lu, F.; Yager, K. G.; Zhang, Y.; Xin, H.; Gang, O. Superlattices Assembled through Shape-Induced Directional Binding. *Nat. Commun.* **2015**, *6*, 6912.
- (526) Theodorakis, P. E.; Fytas, N. G.; Kahl, G.; Dellago, C. Self-Assembly of DNA-Functionalized Colloids. *Condens. Matter Phys.* **2015**, *18*, 22801.
- (527) Angioletti-Uberti, S.; Mognetti, B. M.; Frenkel, D. Theory and Simulation of DNA-Coated Colloids: A Guide for Rational Design. *Phys. Chem. Chem. Phys.* **2016**, *18* (9), 6373–6393.
- (528) Knorowski, C.; Burleigh, S.; Traverset, A. Dynamics and Statics of DNA-Programmable Nanoparticle Self-Assembly and Crystallization. *Phys. Rev. Lett.* **2011**, *106* (21), 215501.
- (529) Knorowski, C.; Traverset, A. Self-Assembly and Crystallization of Hairy (F-Star) and DNA-Grafted Nanocubes. *J. Am. Chem. Soc.* **2014**, *136* (2), 653–659.
- (530) Li, T. I. N. G.; Sknepnek, R.; Olvera de la Cruz, M. Thermally Active Hybridization Drives the Crystallization of DNA-Functionalized Nanoparticles. *J. Am. Chem. Soc.* **2013**, *135* (23), 8535–8541.
- (531) Cademartiri, L.; Bishop, K. J. M. Programmable Self-Assembly. *Nat. Mater.* **2014**, *14* (1), 2–9.
- (532) Huntley, M. H.; Murugan, A.; Brenner, M. P. Information Capacity of Specific Interactions. *Proc. Natl. Acad. Sci. U. S. A.* **2016**, *113* (21), 5841–5846.
- (533) Wu, K.-T.; Feng, L.; Sha, R.; Dreyfus, R.; Grosberg, A. Y.; Seeman, N. C.; Chaikin, P. M. Polygamous Particles. *Proc. Natl. Acad. Sci. U. S. A.* **2012**, *109* (46), 18731–18736.
- (534) Grünwald, M.; Geissler, P. L. Patterns without Patches: Hierarchical Self-Assembly of Complex Structures from Simple Building Blocks. *ACS Nano* **2014**, *8* (6), 5891–5897.
- (535) Angioletti-Uberti, S.; Varilly, P.; Mognetti, B. M.; Frenkel, D. Mobile Linkers on DNA-Coated Colloids: Valency without Patches. *Phys. Rev. Lett.* **2014**, *113* (12), 128303.
- (536) Halverson, J. D.; Tkachenko, A. V. DNA-Programmed Mesoscopic Architecture. *Phys. Rev. E* **2013**, *87* (6), 062310.
- (537) Zeravcic, Z.; Manoharan, V. N.; Brenner, M. P. Size Limits of Self-Assembled Colloidal Structures Made Using Specific Interactions. *Proc. Natl. Acad. Sci. U. S. A.* **2014**, *111* (45), 15918–15923.
- (538) Zeravcic, Z.; Brenner, M. P. Self-Replicating Colloidal Clusters. *Proc. Natl. Acad. Sci. U. S. A.* **2014**, *111* (5), 1748–1753.
- (539) Murugan, A.; Zeravcic, Z.; Brenner, M. P.; Leibler, S. Multifarious Assembly Mixtures: Systems Allowing Retrieval of Diverse Stored Structures. *Proc. Natl. Acad. Sci. U. S. A.* **2015**, *112* (1), 54–59.
- (540) Hormoz, S.; Brenner, M. P. Design Principles for Self-Assembly with Short-Range Interactions. *Proc. Natl. Acad. Sci. U. S. A.* **2011**, *108* (13), 5193–5198.
- (541) Hedges, L. O.; Mannige, R. V.; Whitelam, S. Growth of Equilibrium Structures Built from a Large Number of Distinct Component Types. *Soft Matter* **2014**, *10* (34), 6404–6416.
- (542) Tkachenko, A. V. Theory of Programmable Hierarchic Self-Assembly. *Phys. Rev. Lett.* **2011**, *106* (25), 255501.
- (543) Reinhardt, A.; Frenkel, D. Numerical Evidence for Nucleated Self-Assembly of DNA Brick Structures. *Phys. Rev. Lett.* **2014**, *112* (23), 238103.
- (544) Whitelam, S. Hierarchical Assembly May Be a Way to Make Large Information-Rich Structures. *Soft Matter* **2015**, *11* (42), 8225–8235.
- (545) Klajn, R.; Stoddart, J. F.; Grzybowski, B. A. Nanoparticles Functionalised with Reversible Molecular and Supramolecular Switches. *Chem. Soc. Rev.* **2010**, *39* (6), 2203–2237.
- (546) Klajn, R. Spiropyran-Based Dynamic Materials. *Chem. Soc. Rev.* **2014**, *43* (1), 148–184.
- (547) Beharry, A. A.; Woolley, G. A. Azobenzene Photoswitches for Biomolecules. *Chem. Soc. Rev.* **2011**, *40* (8), 4422–4437.
- (548) Zhao, H.; Sen, S.; Udayabaskarao, T.; Sawczyk, M.; Kućanda, K.; Manna, D.; Kundu, P. K.; Lee, J.-W.; Král, P.; Klajn, R. Reversible Trapping and Reaction Acceleration within Dynamically Self-Assembling Nanoflasks. *Nat. Nanotechnol.* **2015**, *11* (1), 82–88.
- (549) Grzelczak, M.; Vermant, J.; Furst, E. M.; Liz-Marzán, L. M. Directed Self-Assembly of Nanoparticles. *ACS Nano* **2010**, *4* (7), 3591–3605.
- (550) Jones, M. R.; Osberg, K. D.; Macfarlane, R. J.; Langille, M. R.; Mirkin, C. A. Templated Techniques for the Synthesis and Assembly of Plasmonic Nanostructures. *Chem. Rev.* **2011**, *111* (6), 3736–3827.
- (551) Ge, G.; Brus, L. E. Fast Surface Diffusion of Large Disk-Shaped Nanocrystal Aggregates. *Nano Lett.* **2001**, *1* (4), 219–222.
- (552) Luedtke, W. D.; Landman, U. Slip Diffusion and Lévy Flights of an Adsorbed Gold Nanocluster. *Phys. Rev. Lett.* **1999**, *82* (19), 3835–3838.
- (553) Wei, J.; Schaeffer, N.; Pilani, M.-P. Solvent-Mediated Crystallization of Nanocrystal 3D Assemblies of Silver Nanocrystals: Unexpected Superlattice Ripening. *Chem. Mater.* **2016**, *28* (1), 293–302.
- (554) Thapar, V.; Hanrath, T.; Escobedo, F. A. Entropic Self-Assembly of Freely Rotating Polyhedral Particles Confined to a Flat Interface. *Soft Matter* **2015**, *11* (8), 1481–1491.
- (555) Boniello, G.; Blanc, C.; Fedorenko, D.; Medfai, M.; Mbarek, N. B.; In, M.; Gross, M.; Stocco, A.; Nobili, M. Brownian Diffusion of a Partially Wetted Colloid. *Nat. Mater.* **2015**, *14* (9), 908–911.
- (556) Zhang, Y.; Liu, F.-M. Self-Assembly of Three Shapes of Anatase TiO₂ Nanocrystals into Horizontal and Vertical Two-Dimensional Superlattices. *RSC Adv.* **2015**, *5* (82), 66934–66939.
- (557) van der Stam, W.; Gantapara, A. P.; Akkerman, Q. a; Soligno, G.; Meeldijk, J. D.; van Roij, R.; Dijkstra, M.; de Mello Donega, C. Self-Assembly of Colloidal Hexagonal Bipyramid- and Bifrustum-Shaped ZnS Nanocrystals into Two-Dimensional Superstructures. *Nano Lett.* **2014**, *14* (2), 1032–1037.
- (558) Lee, Y. H.; Shi, W.; Lee, H. K.; Jiang, R.; Phang, I. Y.; Cui, Y.; Isa, L.; Yang, Y.; Wang, J.; Li, S.; et al. Nanoscale Surface Chemistry Directs the Tunable Assembly of Silver Octahedra into Three Two-Dimensional Plasmonic Superlattices. *Nat. Commun.* **2015**, *6*, 6990.
- (559) Yang, Y.; Lee, Y. H.; Phang, I. Y.; Jiang, R.; Sim, H. Y. F.; Wang, J.; Ling, X. Y. A Chemical Approach To Break the Planar Configuration of Ag Nanocubes into Tunable Two-Dimensional Metasurfaces. *Nano Lett.* **2016**, *16* (6), 3872–3878.
- (560) Jiang, Z.; He, J.; Deshmukh, S. A.; Kanjanaboos, P.; Kamath, G.; Wang, Y.; Sankaranarayanan, S. K. R. S.; Wang, J.; Jaeger, H. M.; Lin, X.-M. Subnanometre Ligand-Shell Asymmetry Leads to Janus-Like Nanoparticle Membranes. *Nat. Mater.* **2015**, *14* (9), 912–917.
- (561) Cui, Y.; Björk, M. T.; Liddle, J. A.; Sönnichsen, C.; Boussert, B.; Alivisatos, A. P. Integration of Colloidal Nanocrystals into Lithographically Patterned Devices. *Nano Lett.* **2004**, *4* (6), 1093–1098.
- (562) Zhou, Y.; Zhou, X.; Park, D. J.; Torabi, K.; Brown, K. A.; Jones, M. R.; Zhang, C.; Schatz, G. C.; Mirkin, C. A. Shape-Selective Deposition and Assembly of Anisotropic Nanoparticles. *Nano Lett.* **2014**, *14* (4), 2157–2161.
- (563) Jiang, L.; Chen, X.; Lu, N.; Chi, L. Spatially Confined Assembly of Nanoparticles. *Acc. Chem. Res.* **2014**, *47* (10), 3009–3017.
- (564) Fan, J. A.; Bao, K.; Sun, L.; Bao, J.; Manoharan, V. N.; Nordlander, P.; Capasso, F. Plasmonic Mode Engineering with Templated Self-Assembled Nanoclusters. *Nano Lett.* **2012**, *12* (10), 5318–5324.
- (565) Greybush, N. J.; Saboktakin, M.; Ye, X.; Della Giovampaola, C.; Oh, S. J.; Berry, N. E.; Engheta, N.; Murray, C. B.; Kagan, C. R. Plasmon-Enhanced Upconversion Luminescence in Single Nanophosphor–Nanorod Heterodimers Formed through Template-Assisted Self-Assembly. *ACS Nano* **2014**, *8* (9), 9482–9491.

- (566) Rupich, S. M.; Castro, F. C.; Irvine, W. T. M.; Talapin, D. V. Soft Epitaxy of Nanocrystal Superlattices. *Nat. Commun.* **2014**, *5*, 5045.
- (567) Wang, X.; Feng, J.; Bai, Y.; Zhang, Q.; Yin, Y. Synthesis, Properties, and Applications of Hollow Micro-/Nanostructures. *Chem. Rev.* **2016**, DOI: 10.1021/acs.chemrev.5b00731.
- (568) Dinsmore, A. D.; Hsu, M. F.; Nikolaides, M. G.; Marquez, M.; Bausch, A. R.; Weitz, D. A. Colloidosomes: Selectively Permeable Capsules Composed of Colloidal Particles. *Science* **2002**, *298* (5595), 1006–1009.
- (569) Thompson, K. L.; Williams, M.; Armes, S. P. Colloidosomes: Synthesis, Properties and Applications. *J. Colloid Interface Sci.* **2015**, *447*, 217–228.
- (570) Böker, A.; He, J.; Emrick, T.; Russell, T. P. Self-Assembly of Nanoparticles at Interfaces. *Soft Matter* **2007**, *3* (10), 1231–1248.
- (571) de Folter, J. W. J.; Hutter, E. M.; Castillo, S. I. R.; Klop, K. E.; Philipse, A. P.; Kegel, W. K. Particle Shape Anisotropy in Pickering Emulsions: Cubes and Peanuts. *Langmuir* **2014**, *30* (4), 955–964.
- (572) Neubauer, M. P.; Poehlmann, M.; Fery, A. Microcapsule Mechanics: From Stability to Function. *Adv. Colloid Interface Sci.* **2014**, *207*, 65–80.
- (573) Meng, G.; Paulose, J.; Nelson, D. R.; Manoharan, V. N. Elastic Instability of a Crystal Growing on a Curved Surface. *Science* **2014**, *343* (6171), 634–637.
- (574) Schwenke, K.; Isa, L.; Del Gado, E. Assembly of Nanoparticles at Liquid Interfaces: Crowding and Ordering. *Langmuir* **2014**, *30* (11), 3069–3074.
- (575) Cui, M.; Emrick, T.; Russell, T. P. Stabilizing Liquid Drops in Nonequilibrium Shapes by the Interfacial Jamming of Nanoparticles. *Science* **2013**, *342* (6157), 460–463.
- (576) Pouliche, V.; Garbin, V. Ultrafast Desorption of Colloidal Particles from Fluid Interfaces. *Proc. Natl. Acad. Sci. U. S. A.* **2015**, *112* (19), 5932–5937.
- (577) Park, J. Il; Nie, Z.; Kumachev, A.; Abdelrahman, A. I.; Binks, B. P.; Stone, H. A.; Kumacheva, E. A Microfluidic Approach to Chemically Driven Assembly of Colloidal Particles at Gas-Liquid Interfaces. *Angew. Chem.* **2009**, *121* (29), 5404–5408.
- (578) Gorgoll, R. M.; Tsubota, T.; Harano, K.; Nakamura, E. Cooperative Self-Assembly of Gold Nanoparticles on the Hydrophobic Surface of Vesicles in Water. *J. Am. Chem. Soc.* **2015**, *137* (24), 7568–7571.
- (579) Yang, Z.; Altantzis, T.; Zanaga, D.; Bals, S.; Van Tendeloo, G.; Pileni, M.-P. Supracrystalline Colloidal Eggs: Epitaxial Growth and Freestanding Three-Dimensional Supracrystals in Nanoscaled Colloidosomes. *J. Am. Chem. Soc.* **2016**, *138* (10), 3493–3500.
- (580) Wei, J.; Niikura, K.; Higuchi, T.; Kimura, T.; Mitomo, H.; Jinnai, H.; Joti, Y.; Bessho, Y.; Nishino, Y.; Matsuo, Y.; et al. Yolk/Shell Assembly of Gold Nanoparticles by Size Segregation in Solution. *J. Am. Chem. Soc.* **2016**, *138* (10), 3274–3277.
- (581) Smallenburg, F.; Löwen, H. Close Packing of Rods on Spherical Surfaces. *J. Chem. Phys.* **2016**, *144* (16), 164903.
- (582) Liu, B.; Zeng, H. C. Mesoscale Organization of CuO Nanoribbons: Formation of “Dandelions. *J. Am. Chem. Soc.* **2004**, *126* (26), 8124–8125.
- (583) Cao, A.-M.; Hu, J.-S.; Liang, H.-P.; Wan, L.-J. Self-Assembled Vanadium Pentoxide (V_2O_5) Hollow Microspheres from Nanorods and Their Application in Lithium-Ion Batteries. *Angew. Chem., Int. Ed.* **2005**, *44* (28), 4391–4395.
- (584) Ciszek, J. W.; Huang, L.; Tsonev, S.; Wang, Y.; Shull, K. R.; Ratner, M. A.; Schatz, G. C.; Mirkin, C. A. Assembly of Nanorods into Designer Superstructures: The Role of Templating, Capillary Forces, Adhesion, and Polymer Hydration. *ACS Nano* **2010**, *4* (1), 259–266.
- (585) Pang, M.; Cairns, A. J.; Liu, Y.; Belmabkhout, Y.; Zeng, H. C.; Eddaoudi, M. Synthesis and Integration of Fe-Soc-MOF Cubes into Colloidosomes via a Single-Step Emulsion-Based Approach. *J. Am. Chem. Soc.* **2013**, *135* (28), 10234–10237.
- (586) Bahng, J. H.; Yeom, B.; Wang, Y.; Tung, S. O.; Hoff, J. D.; Kotov, N. Anomalous Dispersions of “Hedgehog” Particles. *Nature* **2015**, *517* (7536), 596–599.
- (587) Chhour, P.; Gallo, N.; Cheheltani, R.; Williams, D.; Al-Zaki, A.; Paik, T.; Nichol, J. L.; Tian, Z.; Naha, P. C.; Witschey, W. R.; et al. Nanodisco Balls: Control over Surface versus Core Loading of Diagnostically Active Nanocrystals into Polymer Nanoparticles. *ACS Nano* **2014**, *8* (9), 9143–9153.
- (588) Lu, Z.; Yin, Y. Colloidal Nanoparticle Clusters: Functional Materials by Design. *Chem. Soc. Rev.* **2012**, *41* (21), 6874–6887.
- (589) Wang, T.; LaMontagne, D.; Lynch, J.; Zhuang, J.; Cao, Y. C. Colloidal Superparticles from Nanoparticle Assembly. *Chem. Soc. Rev.* **2013**, *42* (7), 2804–2823.
- (590) Bai, F.; Wang, D.; Huo, Z.; Chen, W.; Liu, L.; Liang, X.; Chen, C.; Wang, X.; Peng, Q.; Li, Y. A Versatile Bottom-up Assembly Approach to Colloidal Spheres from Nanocrystals. *Angew. Chem., Int. Ed.* **2007**, *46* (35), 6650–6653.
- (591) Bodnarchuk, M. I.; Li, L.; Fok, A.; Nachtergael, S.; Ismagilov, R. F.; Talapin, D. V. Three-Dimensional Nanocrystal Superlattices Grown in Nanoliter Microfluidic Plugs. *J. Am. Chem. Soc.* **2011**, *133* (23), 8956–8960.
- (592) Lacava, J.; Born, P.; Kraus, T. Nanoparticle Clusters with Lennard-Jones Geometries. *Nano Lett.* **2012**, *12* (6), 3279–3282.
- (593) Galván-Moya, J. E.; Altantzis, T.; Nelissen, K.; Peeters, F. M.; Grzelczak, M.; Liz-Marzán, L. M.; Bals, S.; Van Tendeloo, G. Self-Organization of Highly Symmetric Nanoassemblies: A Matter of Competition. *ACS Nano* **2014**, *8* (4), 3869–3875.
- (594) Wales, D. J.; Doye, J. P. K. Global Optimization by Basin-Hopping and the Lowest Energy Structures of Lennard-Jones Clusters Containing up to 110 Atoms. *J. Phys. Chem. A* **1997**, *101* (28), 5111–5116.
- (595) Kuo, K. H. Mackay, Anti-Mackay, Double-Mackay, Pseudo-Mackay, and Related Icosahedral Shell Clusters. *Struct. Chem.* **2002**, *13* (3/4), 221–230.
- (596) Erickson, J. D.; Mednikov, E. G.; Ivanov, S. A.; Dahl, L. F. Isolation and Structural Characterization of a Mackay 55-Metal-Atom Two-Shell Icosahedron of Pseudo-Ih Symmetry, $Pd_{55}L_{12}(\mu_3\text{-CO})_{20}$ ($L = PR_3$, $R = \text{Isopropyl}$). *J. Am. Chem. Soc.* **2016**, *138* (5), 1502–1505.
- (597) Zanaga, D.; Bleichrodt, F.; Altantzis, T.; Winckelmans, N.; Palenstijn, W. J.; Sijbers, J.; de Nijs, B.; van Huis, M. A.; Sánchez-Iglesias, A.; Liz-Marzán, L. M.; et al. Quantitative 3D Analysis of Huge Nanoparticle Assemblies. *Nanoscale* **2016**, *8* (1), 292–299.
- (598) Teich, E. G.; van Anders, G.; Klotsa, D.; Dshemuchadse, J.; Glotzer, S. C. Clusters of Polyhedra in Spherical Confinement. *Proc. Natl. Acad. Sci. U. S. A.* **2016**, *113* (6), E669–E678.
- (599) Kister, T.; Mravlak, M.; Schilling, T.; Kraus, T. Pressure-Controlled Formation of Crystalline, Janus, and Core–Shell Supraparticles. *Nanoscale* **2016**, *8* (27), 13377–13384.
- (600) Lin, G.; Zhu, X.; Anand, U.; Liu, Q.; Lu, J.; Aabdin, Z.; Su, H.; Mirsaidov, U. Nanodroplet-Mediated Assembly of Platinum Nanoparticle Rings in Solution. *Nano Lett.* **2016**, *16* (2), 1092–1096.
- (601) Li, W.; Zhang, P.; Dai, M.; He, J.; Babu, T.; Xu, Y.-L.; Deng, R.; Liang, R.; Lu, M.-H.; Nie, Z.; et al. Ordering of Gold Nanorods in Confined Spaces by Directed Assembly. *Macromolecules* **2013**, *46* (6), 2241–2248.
- (602) Thorkelsson, K.; Nelson, J. H.; Alivisatos, A. P.; Xu, T. End-to-End Alignment of Nanorods in Thin Films. *Nano Lett.* **2013**, *13* (10), 4908–4913.
- (603) Cong, V. T.; Ganbold, E.-O.; Saha, J. K.; Jang, J.; Min, J.; Choo, J.; Kim, S.; Song, N. W.; Son, S. J.; Lee, S. B.; et al. Gold Nanoparticle Silica Nanopeapods. *J. Am. Chem. Soc.* **2014**, *136* (10), 3833–3841.
- (604) Liang, R.; Xu, J.; Deng, R.; Wang, K.; Liu, S.; Li, J.; Zhu, J. Assembly of Polymer-Tethered Gold Nanoparticles under Cylindrical Confinement. *ACS Macro Lett.* **2014**, *3* (5), 486–490.
- (605) Fu, L.; Steinhardt, W.; Zhao, H.; Socolar, J. E. S.; Charbonneau, P. Hard Sphere Packings within Cylinders. *Soft Matter* **2016**, *12* (9), 2505–2514.
- (606) Mann, S. Self-Assembly and Transformation of Hybrid Nano-Objects and Nanostructures under Equilibrium and Non-Equilibrium Conditions. *Nat. Mater.* **2009**, *8* (10), 781–792.

- (607) Lin, Y.; Böker, A.; He, J.; Sill, K.; Xiang, H.; Abetz, C.; Li, X.; Wang, J.; Emrick, T.; Long, S.; et al. Self-Directed Self-Assembly of Nanoparticle/Copolymer Mixtures. *Nature* **2005**, *434* (7029), 55–59.
- (608) Shenhar, R.; Norsten, T. B.; Rotello, V. M. Polymer-Mediated Nanoparticle Assembly: Structural Control and Applications. *Adv. Mater.* **2005**, *17* (6), 657–669.
- (609) Balazs, A. C.; Emrick, T.; Russell, T. P. Nanoparticle Polymer Composites: Where Two Small Worlds Meet. *Science* **2006**, *314* (5802), 1107–1110.
- (610) Euliss, L. E.; Grancharov, S. G.; O'Brien, S.; Deming, T. J.; Stucky, G. D.; Murray, C. B.; Held, G. A. Cooperative Assembly of Magnetic Nanoparticles and Block Copolypeptides in Aqueous Media. *Nano Lett.* **2003**, *3* (11), 1489–1493.
- (611) Zhao, Y.; Thorkelsson, K.; Mastroianni, A. J.; Schilling, T.; Luther, J. M.; Rancatore, B. J.; Matsunaga, K.; Jinnai, H.; Wu, Y.; Poulsen, D.; et al. Small-Molecule-Directed Nanoparticle Assembly Towards Stimuli-Responsive Nanocomposites. *Nat. Mater.* **2009**, *8* (12), 979–985.
- (612) Kao, J.; Xu, T. Nanoparticle Assemblies in Supramolecular Nanocomposite Thin Films: Concentration Dependence. *J. Am. Chem. Soc.* **2015**, *137* (19), 6356–6365.
- (613) Warren, S. C.; Messina, L. C.; Slaughter, L. S.; Kamperman, M.; Zhou, Q.; Gruner, S. M.; DiSalvo, F. J.; Wiesner, U. Ordered Mesoporous Materials from Metal Nanoparticle-Block Copolymer Self-Assembly. *Science* **2008**, *320* (5884), 1748–1752.
- (614) Jang, S. G.; Kramer, E. J.; Hawker, C. J. Controlled Supramolecular Assembly of Micelle-Like Gold Nanoparticles in PS-B-P2VP Diblock Copolymers via Hydrogen Bonding. *J. Am. Chem. Soc.* **2011**, *133* (42), 16986–16996.
- (615) Buonsanti, R.; Pick, T. E.; Krins, N.; Richardson, T. J.; Helms, B. A.; Milliron, D. J. Assembly of Ligand-Stripped Nanocrystals into Precisely Controlled Mesoporous Architectures. *Nano Lett.* **2012**, *12* (7), 3872–3877.
- (616) Ong, G. K.; Williams, T. E.; Singh, A.; Schaible, E.; Helms, B. A.; Milliron, D. J. Ordering in Polymer Micelle-Directed Assemblies of Colloidal Nanocrystals. *Nano Lett.* **2015**, *15* (12), 8240–8244.
- (617) Rauda, I. E.; Buonsanti, R.; Saldarriaga-Lopez, L. C.; Benjauthrit, K.; Schelhas, L. T.; Stefik, M.; Augustyn, V.; Ko, J.; Dunn, B.; Wiesner, U.; et al. General Method for the Synthesis of Hierarchical Nanocrystal-Based Mesoporous Materials. *ACS Nano* **2012**, *6* (7), 6386–6399.
- (618) Vamvasakis, I.; Subrahmanyam, K. S.; Kanatzidis, M. G.; Armatas, G. S. Template-Directed Assembly of Metal–Chalcogenide Nanocrystals into Ordered Mesoporous Networks. *ACS Nano* **2015**, *9* (4), 4419–4426.
- (619) Lapointe, C. P.; Mason, T. G.; Smalyukh, I. I. Shape-Controlled Colloidal Interactions in Nematic Liquid Crystals. *Science* **2009**, *326* (5956), 1083–1086.
- (620) Mundoor, H.; Senyuk, B.; Smalyukh, I. I. Triclinic Nematic Colloidal Crystals from Competing Elastic and Electrostatic Interactions. *Science* **2016**, *352* (6281), 69–73.
- (621) Musevic, I.; Skarabot, M.; Tkalec, U.; Ravnik, M.; Zumer, S. Two-Dimensional Nematic Colloidal Crystals Self-Assembled by Topological Defects. *Science* **2006**, *313* (5789), 954–958.
- (622) Ognysta, U.; Nych, A.; Nazarenko, V.; Mušević, I.; Škarabot, M.; Ravnik, M.; Žumer, S.; Poberaj, I.; Babić, D. 2D Interactions and Binary Crystals of Dipolar and Quadrupolar Nematic Colloids. *Phys. Rev. Lett.* **2008**, *100* (21), 217803.
- (623) Binder, K.; Virnau, P.; Statt, A. Perspective: The Asakura Oosawa Model: A Colloid Prototype for Bulk and Interfacial Phase Behavior. *J. Chem. Phys.* **2014**, *141* (14), 140901.
- (624) Asakura, S.; Oosawa, F. On Interaction between Two Bodies Immersed in a Solution of Macromolecules. *J. Chem. Phys.* **1954**, *22* (7), 1255–1256.
- (625) Park, K.; Koerner, H.; Vaia, R. A. Depletion-Induced Shape and Size Selection of Gold Nanoparticles. *Nano Lett.* **2010**, *10* (4), 1433–1439.
- (626) Li, R.; Bian, K.; Wang, Y.; Xu, H.; Hollingsworth, J. A.; Hanrath, T.; Fang, J.; Wang, Z. An Obtuse Rhombohedral Superlattice Assembled by Pt Nanocubes. *Nano Lett.* **2015**, *15* (9), 6254–6260.
- (627) Ni, R.; Gantapara, A. P.; de Graaf, J.; van Roij, R.; Dijkstra, M. Phase Diagram of Colloidal Hard Superballs: From Cubes via Spheres to Octahedra. *Soft Matter* **2012**, *8* (34), 8826–8834.
- (628) Rossi, L.; Soni, V.; Ashton, D. J.; Pine, D. J.; Philipse, A. P.; Chaikin, P. M.; Dijkstra, M.; Sacanna, S.; Irvine, W. T. M. Shape-Sensitive Crystallization in Colloidal Superball Fluids. *Proc. Natl. Acad. Sci. U. S. A.* **2015**, *112* (17), 5286–5290.
- (629) Karas, A. S.; Glaser, J.; Glotzer, S. C. Using Depletion to Control Colloidal Crystal Assemblies of Hard Cuboctahedra. *Soft Matter* **2016**, *12* (23), 5199–5204.
- (630) Rossi, L.; Sacanna, S.; Irvine, W. T. M.; Chaikin, P. M.; Pine, D. J.; Philipse, A. P. Cubic Crystals from Cubic Colloids. *Soft Matter* **2011**, *7* (9), 4139–4142.
- (631) Mahynski, N. A.; Panagiotopoulos, A. Z.; Meng, D.; Kumar, S. K. Stabilizing Colloidal Crystals by Leveraging Void Distributions. *Nat. Commun.* **2014**, *5*, 4472.
- (632) Mahynski, N. A.; Rovigatti, L.; Likos, C. N.; Panagiotopoulos, A. Z. Bottom-Up Colloidal Crystal Assembly with a Twist. *ACS Nano* **2016**, *10* (5), 5459–5467.
- (633) Song, R.-Q.; Cölfen, H. Additive Controlled Crystallization. *CrystEngComm* **2011**, *13* (5), 1249–1276.
- (634) Lalatonne, Y.; Richardi, J.; Pileni, M. P. Van Der Waals versus Dipolar Forces Controlling Mesoscopic Organizations of Magnetic Nanocrystals. *Nat. Mater.* **2004**, *3* (2), 121–125.
- (635) Ryan, K. M.; Mastroianni, A.; Stancil, K. A.; Liu, H.; Alivisatos, A. P. Electric-Field-Assisted Assembly of Perpendicularly Oriented Nanorod Superlattices. *Nano Lett.* **2006**, *6* (7), 1479–1482.
- (636) Yanai, N.; Sindoro, M.; Yan, J.; Granick, S. Electric Field-Induced Assembly of Monodisperse Polyhedral Metal–Organic Framework Crystals. *J. Am. Chem. Soc.* **2013**, *135* (1), 34–37.
- (637) Yanai, N.; Granick, S. Directional Self-Assembly of a Colloidal Metal–Organic Framework. *Angew. Chem., Int. Ed.* **2012**, *51* (23), 5638–5641.
- (638) Barsotti, R. J.; Vahey, M. D.; Wartena, R.; Chiang, Y.-M.; Voldman, J.; Stellacci, F. Assembly of Metal Nanoparticles into Nanogaps. *Small* **2007**, *3* (3), 488–499.
- (639) Smalleenburg, F.; Vutukuri, H. R.; Imhof, A.; van Blaaderen, A.; Dijkstra, M. Self-Assembly of Colloidal Particles into Strings in a Homogeneous External Electric or Magnetic Field. *J. Phys.: Condens. Matter* **2012**, *24* (46), 464113.
- (640) Ye, L.; Pearson, T.; Cordeau, Y.; Mefford, O. T.; Crawford, T. M. Triggered Self-Assembly of Magnetic Nanoparticles. *Sci. Rep.* **2016**, *6*, 23145.
- (641) Srivastava, S.; Santos, A.; Critchley, K.; Kim, K.-S.; Podsiadlo, P.; Sun, K.; Lee, J.; Xu, C.; Lilly, G. D.; Glotzer, S. C.; et al. Light-Controlled Self-Assembly of Semiconductor Nanoparticles into Twisted Ribbons. *Science* **2010**, *327* (5971), 1355–1359.
- (642) Yeom, J.; Yeom, B.; Chan, H.; Smith, K. W.; Dominguez-Medina, S.; Bahng, J. H.; Zhao, G.; Chang, W.-S.; Chang, S.-J.; Chuvalin, A.; et al. Chiral Templating of Self-Assembling Nanostructures by Circularly Polarized Light. *Nat. Mater.* **2014**, *14* (1), 66–72.
- (643) Snir, Y.; Kamien, R. D. Entropically Driven Helix Formation. *Science* **2005**, *307* (5712), 1067.
- (644) Gibaud, T.; Barry, E.; Zakhary, M. J.; Henglin, M.; Ward, A.; Yang, Y.; Berciu, C.; Oldenbourg, R.; Hagan, M. F.; Nicastro, D.; et al. Reconfigurable Self-Assembly through Chiral Control of Interfacial Tension. *Nature* **2012**, *481* (7381), 348–351.
- (645) Chen, C.-L.; Zhang, P.; Rosi, N. L. A New Peptide-Based Method for the Design and Synthesis of Nanoparticle Superstructures: Construction of Highly Ordered Gold Nanoparticle Double Helices. *J. Am. Chem. Soc.* **2008**, *130* (41), 13555–13557.
- (646) Zhou, Y.; Marson, R. L.; van Anders, G.; Zhu, J.; Ma, G.; Ercius, P.; Sun, K.; Yeom, B.; Glotzer, S. C.; Kotov, N. A. Biomimetic Hierarchical Assembly of Helical Supraparticles from Chiral Nanoparticles. *ACS Nano* **2016**, *10* (3), 3248–3256.

- (647) Yu, S.-H.; Cölfen, H.; Tauer, K.; Antonietti, M. Tectonic Arrangement of BaCO₃ Nanocrystals into Helices Induced by a Racemic Block Copolymer. *Nat. Mater.* **2004**, *4* (1), 51–55.
- (648) Tang, Z.; Kotov, N. A. One-Dimensional Assemblies of Nanoparticles: Preparation, Properties, and Promise. *Adv. Mater.* **2005**, *17* (8), 951–962.
- (649) Zhang, X.; Zhang, Z.; Glotzer, S. C. Simulation Study of Dipole-Induced Self-Assembly of Nanocubes. *J. Phys. Chem. C* **2007**, *111* (11), 4132–4137.
- (650) Mehdizadeh Taheri, S.; Michaelis, M.; Friedrich, T.; Förster, B.; Drechsler, M.; Römer, F. M.; Bösecke, P.; Narayanan, T.; Weber, B.; Rehberg, I.; et al. Self-Assembly of Smallest Magnetic Particles. *Proc. Natl. Acad. Sci. U. S. A.* **2015**, *112* (47), 14484–14489.
- (651) Donaldson, J. G.; Kantorovich, S. S. Directional Self-Assembly of Permanently Magnetised Nanocubes in Quasi Two Dimensional Layers. *Nanoscale* **2015**, *7* (7), 3217–3228.
- (652) Huang, S.; Pessot, G.; Cremer, P.; Weeber, R.; Holm, C.; Nowak, J.; Odenbach, S.; Menzel, A. M.; Auernhammer, G. K. Buckling of Paramagnetic Chains in Soft Gels. *Soft Matter* **2016**, *12* (1), 228–237.
- (653) Kantorovich, S. S.; Ivanov, A. O.; Rovigatti, L.; Tavares, J. M.; Sciotino, F. Temperature-Induced Structural Transitions in Self-Assembling Magnetic Nanocolloids. *Phys. Chem. Chem. Phys.* **2015**, *17* (25), 16601–16608.
- (654) Esquivel-Sirvent, R.; Schatz, G. C. Van Der Waals Torque Coupling between Slabs Composed of Planar Arrays of Nanoparticles. *J. Phys. Chem. C* **2013**, *117* (10), 5492–5496.
- (655) Yasui, K.; Kato, K. Oriented Attachment of Cubic or Spherical BaTiO₃ Nanocrystals by van Der Waals Torque. *J. Phys. Chem. C* **2015**, *119* (43), 24597–24605.
- (656) Kundu, P. K.; Samanta, D.; Leizrowice, R.; Margulis, B.; Zhao, H.; Börner, M.; Udayabhaskararao, T.; Manna, D.; Klajn, R. Light-Controlled Self-Assembly of Non-Photoresponsive Nanoparticles. *Nat. Chem.* **2015**, *7* (8), 646–652.
- (657) Yu, Y.; Jain, A.; Guillaussier, A.; Voggu, V. R.; Truskett, T. M.; Smilgies, D.-M.; Korgel, B. A. Nanocrystal Superlattices That Exhibit Improved Order on Heating: An Example of Inverse Melting? *Faraday Discuss.* **2015**, *181* (0), 181–192.
- (658) Lewandowski, W.; Fruhnert, M.; Mieczkowski, J.; Rockstuhl, C.; Górecka, E. Dynamically Self-Assembled Silver Nanoparticles as a Thermally Tunable Metamaterial. *Nat. Commun.* **2015**, *6*, 6590.
- (659) Denkov, N.; Velev, O.; Kralchevski, P.; Ivanov, I.; Yoshimura, H.; Nagayama, K. Mechanism of Formation of Two-Dimensional Crystals from Latex Particles on Substrates. *Langmuir* **1992**, *8* (12), 3183–3190.
- (660) Meijer, J.-M.; Hagemans, F.; Rossi, L.; Byelov, D. V.; Castillo, S. I. R.; Snigirev, A.; Snigireva, I.; Philipse, A. P.; Petukhov, A. V. Self-Assembly of Colloidal Cubes via Vertical Deposition. *Langmuir* **2012**, *28* (20), 7631–7638.
- (661) Malaquin, L.; Kraus, T.; Schmid, H.; Delamarche, E.; Wolf, H. Controlled Particle Placement through Convective and Capillary Assembly. *Langmuir* **2007**, *23* (23), 11513–11521.
- (662) Brewer, D. D.; Allen, J.; Miller, M. R.; de Santos, J. M.; Kumar, S.; Norris, D. J.; Tsapatsis, M.; Scriven, L. E. Mechanistic Principles of Colloidal Crystal Growth by Evaporation-Induced Convective Steering. *Langmuir* **2008**, *24* (23), 13683–13693.
- (663) Born, P.; Munoz, A.; Cavelius, C.; Kraus, T. Crystallization Mechanisms in Convective Particle Assembly. *Langmuir* **2012**, *28* (22), 8300–8308.
- (664) Deegan, R. D.; Bakajin, O.; Dupont, T. F.; Huber, G.; Nagel, S. R.; Witten, T. A. Capillary Flow as the Cause of Ring Stains from Dried Liquid Drops. *Nature* **1997**, *389* (6653), 827–829.
- (665) Deegan, R. D.; Bakajin, O.; Dupont, T. F.; Huber, G.; Nagel, S. R.; Witten, T. A. Contact Line Deposits in an Evaporating Drop. *Phys. Rev. E: Stat. Phys., Plasmas, Fluids, Relat. Interdiscip. Top.* **2000**, *62* (1), 756–765.
- (666) Narayanan, S.; Wang, J.; Lin, X.-M. Dynamical Self-Assembly of Nanocrystal Superlattices during Colloidal Droplet Evaporation by in Situ Small Angle X-Ray Scattering. *Phys. Rev. Lett.* **2004**, *93* (13), 135503.
- (667) Bray, A. J. Theory of Phase-Ordering Kinetics. *Adv. Phys.* **1994**, *43* (3), 357–459.
- (668) Khanal, B. P.; Zubarev, E. R. Rings of Nanorods. *Angew. Chem., Int. Ed.* **2007**, *46* (13), 2195–2198.
- (669) Varanakkottu, S. N.; Anyfantakis, M.; Morel, M.; Rudiuk, S.; Baigl, D. Light-Directed Particle Patterning by Evaporative Optical Marangoni Assembly. *Nano Lett.* **2016**, *16* (1), 644–650.
- (670) Ohara, P. C.; Heath, J. R.; Gelbart, W. M. Self-Assembly of Submicrometer Rings of Particles from Solutions of Nanoparticles. *Angew. Chem., Int. Ed.* **1997**, *36* (10), 1078–1080.
- (671) Stowell, C.; Korgel, B. A. Self-Assembled Honeycomb Networks of Gold Nanocrystals. *Nano Lett.* **2001**, *1* (11), 595–600.
- (672) Maillard, M.; Motte, L.; Ngo, A. T.; Pilani, M. P. Rings and Hexagons Made of Nanocrystals: A Marangoni Effect. *J. Phys. Chem. B* **2000**, *104* (50), 11871–11877.
- (673) Huang, J.; Tao, A. R.; Connor, S.; He, R.; Yang, P. A General Method for Assembling Single Colloidal Particle Lines. *Nano Lett.* **2006**, *6* (3), 524–529.
- (674) Dong, A.; Chen, J.; Oh, S. J.; Koh, W.; Xiu, F.; Ye, X.; Ko, D.-K.; Wang, K. L.; Kagan, C. R.; Murray, C. B. Multiscale Periodic Assembly of Striped Nanocrystal Superlattice Films on a Liquid Surface. *Nano Lett.* **2011**, *11* (2), 841–846.
- (675) Huang, J.; Kim, F.; Tao, A. R.; Connor, S.; Yang, P. Spontaneous Formation of Nanoparticle Stripe Patterns through Dewetting. *Nat. Mater.* **2005**, *4* (12), 896–900.
- (676) Talapin, D. V.; Lee, J.-S.; Kovalenko, M. V.; Shevchenko, E. V. Prospects of Colloidal Nanocrystals for Electronic and Optoelectronic Applications. *Chem. Rev.* **2010**, *110* (1), 389–458.
- (677) Nie, Z.; Petukhova, A.; Kumacheva, E. Properties and Emerging Applications of Self-Assembled Structures Made from Inorganic Nanoparticles. *Nat. Nanotechnol.* **2010**, *5* (1), 15–25.
- (678) Kershaw, S. V.; Susha, A. S.; Rogach, A. L. Narrow Bandgap Colloidal Metal Chalcogenide Quantum Dots: Synthetic Methods, Heterostructures, Assemblies, Electronic and Infrared Optical Properties. *Chem. Soc. Rev.* **2013**, *42* (7), 3033–3087.
- (679) Kagan, C. R.; Murray, C. B. Charge Transport in Strongly Coupled Quantum Dot Solids. *Nat. Nanotechnol.* **2015**, *10* (12), 1013–1026.
- (680) Shabaev, A.; Efros, A. L.; Efros, A. L. Dark and Photo-Conductivity in Ordered Array of Nanocrystals. *Nano Lett.* **2013**, *13* (11), 5454–5461.
- (681) Dolzhnikov, D. S.; Zhang, H.; Jang, J.; Son, J. S.; Panthani, M. G.; Shibata, T.; Chattopadhyay, S.; Talapin, D. V. Composition-Matched Molecular “Solders” for Semiconductors. *Science* **2015**, *347* (6220), 425–428.
- (682) Baumgardner, W. J.; Whitham, K.; Hanrath, T. Confined-but-Connected Quantum Solids via Controlled Ligand Displacement. *Nano Lett.* **2013**, *13* (7), 3225–3231.
- (683) Sandeep, C. S. S.; Azpiroz, J. M.; Evers, W. H.; Boehme, S. C.; Moreels, I.; Kinge, S.; Siebbeles, L. D. A.; Infante, I.; Houtepen, A. J. Epitaxially Connected PbSe Quantum-Dot Films: Controlled Neck Formation and Optoelectronic Properties. *ACS Nano* **2014**, *8* (11), 11499–11511.
- (684) Evers, W. H.; Schins, J. M.; Aerts, M.; Kulkarni, A.; Capiod, P.; Berthe, M.; Grandidier, B.; Delerue, C.; van der Zant, H. S. J.; van Overbeek, C.; et al. High Charge Mobility in Two-Dimensional Percolative Networks of PbSe Quantum Dots Connected by Atomic Bonds. *Nat. Commun.* **2015**, *6*, 8195.
- (685) Whitham, K.; Yang, J.; Savitzky, B. H.; Kourkoutis, L. F.; Wise, F.; Hanrath, T. Charge Transport and Localization in Atomically Coherent Quantum Dot Solids. *Nat. Mater.* **2016**, *15* (5), 557–563.
- (686) Hu, J.; Li, L.-S.; Yang, W.; Manna, L.; Wang, L.-W.; Alivisatos, A. P. Linearly Polarized Emission from Colloidal Semiconductor Quantum Rods. *Science* **2001**, *292* (5524), 2060–2063.
- (687) Carbone, L.; Nobile, C.; De Giorgi, M.; Sala, F. D.; Morello, G.; Pompa, P.; Hytch, M.; Snoeck, E.; Fiore, A.; Franchini, I. R.; et al. Synthesis and Micrometer-Scale Assembly of Colloidal CdSe/CdS

- Nanorods Prepared by a Seeded Growth Approach. *Nano Lett.* **2007**, *7* (10), 2942–2950.
- (688) Amit, Y.; Faust, A.; Lieberman, I.; Yedidya, L.; Banin, U. Semiconductor Nanorod Layers Aligned through Mechanical Rubbing. *Phys. Status Solidi A* **2012**, *209* (2), 235–242.
- (689) Roskov, K. E.; Kozek, K. A.; Wu, W.-C.; Chhetri, R. K.; Oldenburg, A. L.; Spontak, R. J.; Tracy, J. B. Long-Range Alignment of Gold Nanorods in Electrospun Polymer Nano/Microfibers. *Langmuir* **2011**, *27* (23), 13965–13969.
- (690) Aubert, T.; Palangetic, L.; Mohammadimasioudi, M.; Neyts, K.; Beeckman, J.; Clasen, C.; Hens, Z. Large-Scale and Electroswitchable Polarized Emission from Semiconductor Nanorods Aligned in Polymeric Nanofibers. *ACS Photonics* **2015**, *2* (5), 583–588.
- (691) Liu, Q.; Cui, Y.; Gardner, D.; Li, X.; He, S.; Smalyukh, I. I. Self-Alignment of Plasmonic Gold Nanorods in Reconfigurable Anisotropic Fluids for Tunable Bulk Metamaterial Applications. *Nano Lett.* **2010**, *10* (4), 1347–1353.
- (692) Klinkova, A.; Choueiri, R. M.; Kumacheva, E. Self-Assembled Plasmonic Nanostructures. *Chem. Soc. Rev.* **2014**, *43* (11), 3976–3991.
- (693) Tao, A.; Sinsermsuksakul, P.; Yang, P. Tunable Plasmonic Lattices of Silver Nanocrystals. *Nat. Nanotechnol.* **2007**, *2* (7), 435–440.
- (694) Fan, Z.; Govorov, A. O. Plasmonic Circular Dichroism of Chiral Metal Nanoparticle Assemblies. *Nano Lett.* **2010**, *10* (7), 2580–2587.
- (695) Querejeta-Fernández, A.; Chauve, G.; Methot, M.; Bouchard, J.; Kumacheva, E. Chiral Plasmonic Films Formed by Gold Nanorods and Cellulose Nanocrystals. *J. Am. Chem. Soc.* **2014**, *136* (12), 4788–4793.
- (696) Querejeta-Fernández, A.; Kopera, B.; Prado, K. S.; Klinkova, A.; Methot, M.; Chauve, G.; Bouchard, J.; Helmy, A. S.; Kumacheva, E. Circular Dichroism of Chiral Nematic Films of Cellulose Nanocrystals Loaded with Plasmonic Nanoparticles. *ACS Nano* **2015**, *9* (10), 10377–10385.
- (697) Lu, F.; Tian, Y.; Liu, M.; Su, D.; Zhang, H.; Govorov, A. O.; Gang, O. Discrete Nanocubes as Plasmonic Reporters of Molecular Chirality. *Nano Lett.* **2013**, *13* (7), 3145–3151.
- (698) Urban, A. S.; Shen, X.; Wang, Y.; Large, N.; Wang, H.; Knight, M. W.; Nordlander, P.; Chen, H.; Halas, N. J. Three-Dimensional Plasmonic Nanoclusters. *Nano Lett.* **2013**, *13* (9), 4399–4403.
- (699) Alvarez-Puebla, R. A.; Agarwal, A.; Manna, P.; Khanal, B. P.; Aldeanueva-Potel, P.; Carbo-Argibay, E.; Pazos-Perez, N.; Vigderman, L.; Zubarev, E. R.; Kotov, N. A.; et al. Gold Nanorods 3D-Superocrystals as Surface Enhanced Raman Scattering Spectroscopy Substrates for the Rapid Detection of Scrambled Prions. *Proc. Natl. Acad. Sci. U. S. A.* **2011**, *108* (20), 8157–8161.
- (700) Ye, X.; Chen, J.; Diroll, B. T.; Murray, C. B. Tunable Plasmonic Coupling in Self-Assembled Binary Nanocrystal Superlattices Studied by Correlated Optical Microspectrophotometry and Electron Microscopy. *Nano Lett.* **2013**, *13* (3), 1291–1297.
- (701) Nie, S.; Emory, S. R. Probing Single Molecules and Single Nanoparticles by Surface-Enhanced Raman Scattering. *Science* **1997**, *275* (5303), 1102–1106.
- (702) Zhu, Z.; Meng, H.; Liu, W.; Liu, X.; Gong, J.; Qiu, X.; Jiang, L.; Wang, D.; Tang, Z. Superstructures and SERS Properties of Gold Nanocrystals with Different Shapes. *Angew. Chem., Int. Ed.* **2011**, *50* (7), 1593–1596.
- (703) Liu, Y.; Zhou, J.; Zhou, L.; Yue-Bun Pun, E.; Jiang, T.; Petti, L.; Mormile, P. Self-Assembled Structures of Polyhedral Gold Nanocrystals: Shape-Directive Arrangement and Structure-Dependence Plasmonic Enhanced Characteristics. *RSC Adv.* **2016**, *6* (62), 57320–57326.
- (704) Gao, B.; Rozin, M. J.; Tao, A. R. Plasmonic Nanocomposites: Polymer-Guided Strategies for Assembling Metal Nanoparticles. *Nanoscale* **2013**, *5* (13), 5677–5691.
- (705) Hsu, S.-W.; Ngo, C.; Tao, A. R. Tunable and Directional Plasmonic Coupling within Semiconductor Nanodisk Assemblies. *Nano Lett.* **2014**, *14* (5), 2372–2380.
- (706) Young, K. L.; Ross, M. B.; Blaber, M. G.; Rycenga, M.; Jones, M. R.; Zhang, C.; Senesi, A. J.; Lee, B.; Schatz, G. C.; Mirkin, C. A. Using DNA to Design Plasmonic Metamaterials with Tunable Optical Properties. *Adv. Mater.* **2014**, *26* (4), 653–659.
- (707) Chao, J.; Lin, Y.; Liu, H.; Wang, L.; Fan, C. DNA-Based Plasmonic Nanostructures. *Mater. Today* **2015**, *18* (6), 326–335.
- (708) Park, D. J.; Zhang, C.; Ku, J. C.; Zhou, Y.; Schatz, G. C.; Mirkin, C. A. Plasmonic Photonic Crystals Realized through DNA-Programmable Assembly. *Proc. Natl. Acad. Sci. U. S. A.* **2015**, *112* (4), 977–981.
- (709) Ross, M. B.; Ku, J. C.; Vaccarezza, V. M.; Schatz, G. C.; Mirkin, C. A. Nanoscale Form Dictates Mesoscale Function in Plasmonic DNA–Nanoparticle Superlattices. *Nat. Nanotechnol.* **2015**, *10* (5), 453–458.
- (710) Lin, Q.-Y.; Li, Z.; Brown, K. A.; O'Brien, M. N.; Ross, M. B.; Zhou, Y.; Butun, S.; Chen, P.-C.; Schatz, G. C.; Dravid, V. P.; et al. Strong Coupling between Plasmonic Gap Modes and Photonic Lattice Modes in DNA-Assembled Gold Nanocube Arrays. *Nano Lett.* **2015**, *15* (7), 4699–4703.
- (711) Pompa, P. P.; Martiradonna, L.; Torre, A.; Sala, F. D.; Manna, L.; De Vittorio, M.; Calabi, F.; Cingolani, R.; Rinaldi, R. Metal-Enhanced Fluorescence of Colloidal Nanocrystals with Nanoscale Control. *Nat. Nanotechnol.* **2006**, *1* (2), 126–130.
- (712) Chen, J.; Dong, A.; Cai, J.; Ye, X.; Kang, Y.; Kikkawa, J. M.; Murray, C. B. Collective Dipolar Interactions in Self-Assembled Magnetic Binary Nanocrystal Superlattice Membranes. *Nano Lett.* **2010**, *10* (12), 5103–5108.
- (713) Chen, J.; Ye, X.; Oh, S. J.; Kikkawa, J. M.; Kagan, C. R.; Murray, C. B. Bistable Magnetoresistance Switching in Exchange-Coupled CoFe_2O_4 – Fe_3O_4 Binary Nanocrystal Superlattices by Self-Assembly and Thermal Annealing. *ACS Nano* **2013**, *7* (2), 1478–1486.
- (714) Zeng, H.; Li, J.; Liu, J. P.; Wang, Z. L.; Sun, S. Exchange-Coupled Nanocomposite Magnets by Nanoparticle Self-Assembly. *Nature* **2002**, *420* (6914), 395–398.
- (715) Shevchenko, E. V.; Ringler, M.; Schwemer, A.; Talapin, D. V.; Klar, T. A.; Rogach, A. L.; Feldmann, J.; Alivisatos, A. P. Self-Assembled Binary Superlattices of CdSe and Au Nanocrystals and Their Fluorescence Properties. *J. Am. Chem. Soc.* **2008**, *130* (11), 3274–3275.
- (716) Urban, J. J.; Talapin, D. V.; Shevchenko, E. V.; Kagan, C. R.; Murray, C. B. Synergism in Binary Nanocrystal Superlattices Leads to Enhanced P-Type Conductivity in Self-Assembled PbTe/Ag₂Te Thin Films. *Nat. Mater.* **2007**, *6* (2), 115–121.
- (717) Kang, Y.; Ye, X.; Chen, J.; Cai, Y.; Diaz, R. E.; Adzic, R. R.; Stach, E. A.; Murray, C. B. Design of Pt–Pd Binary Superlattices Exploiting Shape Effects and Synergistic Effects for Oxygen Reduction Reactions. *J. Am. Chem. Soc.* **2013**, *135* (1), 42–45.
- (718) Kleijn, S. E. F.; Lai, S. C. S.; Koper, M. T. M.; Unwin, P. R. Electrochemistry of Nanoparticles. *Angew. Chem., Int. Ed.* **2014**, *53* (14), 3558–3586.
- (719) Wang, C.; Yin, H.; Dai, S.; Sun, S. A General Approach to Noble Metal–Metal Oxide Dumbbell Nanoparticles and Their Catalytic Application for CO Oxidation. *Chem. Mater.* **2010**, *22* (10), 3277–3282.
- (720) Kang, Y.; Ye, X.; Chen, J.; Qi, L.; Diaz, R. E.; Doan-Nguyen, V.; Xing, G.; Kagan, C. R.; Li, J.; Gorte, R. J.; et al. Engineering Catalytic Contacts and Thermal Stability: Gold/Iron Oxide Binary Nanocrystal Superlattices for CO Oxidation. *J. Am. Chem. Soc.* **2013**, *135* (4), 1499–1505.
- (721) Yamada, Y.; Tsung, C.-K.; Huang, W.; Huo, Z.; Habas, S. E.; Soejima, T.; Aliaga, C. E.; Somorjai, G. A.; Yang, P. Nanocrystal Bilayer for Tandem Catalysis. *Nat. Chem.* **2011**, *3* (5), 372–376.
- (722) Zhang, S.; Shao, Y.; Yin, G.; Lin, Y. Electrostatic Self-Assembly of a Pt-around-Au Nanocomposite with High Activity towards Formic Acid Oxidation. *Angew. Chem., Int. Ed.* **2010**, *49* (12), 2211–2214.
- (723) Kang, Y.; Li, M.; Cai, Y.; Cargnello, M.; Diaz, R. E.; Gordon, T. R.; Wieder, N. L.; Adzic, R. R.; Gorte, R. J.; Stach, E. A.; et al. Heterogeneous Catalysts Need Not Be so “Heterogeneous”:

- Monodisperse Pt Nanocrystals by Combining Shape-Controlled Synthesis and Purification by Colloidal Recrystallization. *J. Am. Chem. Soc.* **2013**, *135* (7), 2741–2747.
- (724) Chen, C.; Kang, Y.; Huo, Z.; Zhu, Z.; Huang, W.; Xin, H. L.; Snyder, J. D.; Li, D.; Herron, J. A.; Mavrikakis, M.; et al. Highly Crystalline Multimetallic Nanoframes with Three-Dimensional Electrocatalytic Surfaces. *Science* **2014**, *343* (6177), 1339–1343.
- (725) Courty, A.; Mermet, A.; Albouy, P. A.; Duval, E.; Pilani, M. P. Vibrational Coherence of Self-Organized Silver Nanocrystals in F.C.C. Supra-Crystals. *Nat. Mater.* **2005**, *4* (5), 395–398.
- (726) Poyser, C. L.; Czerniuk, T.; Akimov, A.; Diroll, B. T.; Gaulding, E. A.; Salasyuk, A. S.; Kent, A. J.; Yakovlev, D. R.; Bayer, M.; Murray, C. B. Coherent Acoustic Phonons in Colloidal Semiconductor Nanocrystal Superlattices. *ACS Nano* **2016**, *10* (1), 1163–1169.
- (727) Podsiadlo, P.; Krylova, G.; Lee, B.; Critchley, K.; Gosztola, D. J.; Talapin, D. V.; Ashby, P. D.; Shevchenko, E. V. The Role of Order, Nanocrystal Size, and Capping Ligands in the Collective Mechanical Response of Three-Dimensional Nanocrystal Solids. *J. Am. Chem. Soc.* **2010**, *132* (26), 8953–8960.
- (728) Choi, J.; Hui, C. M.; Pietrasik, J.; Dong, H.; Matyjaszewski, K.; Bockstaller, M. R. Toughening Fragile Matter: Mechanical Properties of Particle Solids Assembled from Polymer-Grafted Hybrid Particles Synthesized by ATRP. *Soft Matter* **2012**, *8* (15), 4072–4082.
- (729) Schmitt, M.; Choi, J.; Min Hui, C.; Chen, B.; Korkmaz, E.; Yan, J.; Margel, S.; Burak Ozdoganlar, O.; Matyjaszewski, K.; Bockstaller, M. R. Processing Fragile Matter: Effect of Polymer Graft Modification on the Mechanical Properties and Processibility of (Nano-)Particulate Solids. *Soft Matter* **2016**, *12* (15), 3527–3537.
- (730) Gauvin, M.; Wan, Y.; Arfaoui, I.; Pilani, M.-P. Mechanical Properties of Au Supracrystals Tuned by Flexible Ligand Interactions. *J. Phys. Chem. C* **2014**, *118* (9), 5005–5012.
- (731) Salerno, K. M.; Bolintineanu, D. S.; Lane, J. M. D.; Grest, G. S. Ligand Structure and Mechanical Properties of Single-Nanoparticle-Thick Membranes. *Phys. Rev. E* **2015**, *91* (6), 062403.
- (732) Klajn, R.; Bishop, K. J. M.; Fialkowski, M.; Paszewski, M.; Campbell, C. J.; Gray, T. P.; Grzybowski, B. A. Plastic and Moldable Metals by Self-Assembly of Sticky Nanoparticle Aggregates. *Science* **2007**, *316* (5822), 261–264.
- (733) Kanjanaboos, P.; Lin, X.-M.; Sader, J. E.; Rupich, S. M.; Jaeger, H. M.; Guest, J. R. Self-Assembled Nanoparticle Drumhead Resonators. *Nano Lett.* **2013**, *13* (5), 2158–2162.
- (734) Wang, Y.; Liao, J.; McBride, S. P.; Efrati, E.; Lin, X.-M.; Jaeger, H. M. Strong Resistance to Bending Observed for Nanoparticle Membranes. *Nano Lett.* **2015**, *15* (10), 6732–6737.
- (735) Wang, Y.; Kanjanaboos, P.; Barry, E.; McBride, S.; Lin, X.-M.; Jaeger, H. M. Fracture and Failure of Nanoparticle Monolayers and Multilayers. *Nano Lett.* **2014**, *14* (2), 826–830.
- (736) van Rijn, P.; Tutus, M.; Kathrein, C.; Zhu, L.; Wessling, M.; Schwaneberg, U.; Böker, A. Challenges and Advances in the Field of Self-Assembled Membranes. *Chem. Soc. Rev.* **2013**, *42* (16), 6578–6592.
- (737) Green, E.; Fullwood, E.; Selden, J.; Zharov, I. Functional Membranes via Nanoparticle Self-Assembly. *Chem. Commun.* **2015**, *51* (37), 7770–7780.
- (738) He, J.; Lin, X.-M.; Chan, H.; Vuković, L.; Král, P.; Jaeger, H. M. Diffusion and Filtration Properties of Self-Assembled Gold Nanocrystal Membranes. *Nano Lett.* **2011**, *11* (6), 2430–2435.
- (739) Barry, E.; McBride, S. P.; Jaeger, H. M.; Lin, X.-M. Ion Transport Controlled by Nanoparticle-Functionalized Membranes. *Nat. Commun.* **2014**, *5*, 5847.
- (740) Jang, B.; Park, M.; Chae, O. B.; Park, S.; Kim, Y.; Oh, S. M.; Piao, Y.; Hyeon, T. Direct Synthesis of Self-Assembled Ferrite/Carbon Hybrid Nanosheets for High Performance Lithium-Ion Battery Anodes. *J. Am. Chem. Soc.* **2012**, *134* (36), 15010–15015.
- (741) Bentzon, M. D.; van Wonterghem, J.; Mørup, S.; Thölén, A.; Koch, C. J. W. Ordered Aggregates of Ultrafine Iron Oxide Particles: "Super Crystals." *Philos. Mag. B* **1989**, *60* (2), 169–178.
- (742) Pourret, A.; Guyot-Sionnest, P.; Elam, J. W. Atomic Layer Deposition of ZnO in Quantum Dot Thin Films. *Adv. Mater.* **2009**, *21* (2), 232–235.
- (743) Liu, Y.; Tolentino, J.; Gibbs, M.; Ihly, R.; Perkins, C. L.; Liu, Y.; Crawford, N.; Hemminger, J. C.; Law, M. PbSe Quantum Dot Field-Effect Transistors with Air-Stable Electron Mobilities above 7 cm² V⁻¹ s⁻¹. *Nano Lett.* **2013**, *13* (4), 1578–1587.
- (744) Macfarlane, R. J.; Jones, M. R.; Lee, B.; Auyeung, E.; Mirkin, C. A. Topotactic Interconversion of Nanoparticle Superlattices. *Science* **2013**, *341* (6151), 1222–1225.
- (745) Hawker, C. J.; Russell, T. P. Block Copolymer Lithography: Merging "Bottom-Up" with "Top-Down" Processes. *MRS Bull.* **2005**, *30* (12), 952–966.
- (746) Ruiz, R.; Kang, H.; Detcheverry, F. A.; Dobisz, E.; Kercher, D. S.; Albrecht, T. R.; de Pablo, J. J.; Nealey, P. F. Density Multiplication and Improved Lithography by Directed Block Copolymer Assembly. *Science* **2008**, *321* (5891), 936–939.
- (747) Lan, X.; Voznyy, O.; García de Arquer, F. P.; Liu, M.; Xu, J.; Proppe, A. H.; Walters, G.; Fan, F.; Tan, H.; Liu, M.; et al. 10.6% Certified Colloidal Quantum Dot Solar Cells via Solvent-Polarity-Engineered Halide Passivation. *Nano Lett.* **2016**, *16* (7), 4630–4634.
- (748) Konstantatos, G.; Sargent, E. H. Nanostructured Materials for Photon Detection. *Nat. Nanotechnol.* **2010**, *5* (6), 391–400.
- (749) Choi, J.-H.; Wang, H.; Oh, S. J.; Paik, T.; Sung, P.; Sung, J.; Ye, X.; Zhao, T.; Diroll, B. T.; Murray, C. B.; et al. Exploiting the Colloidal Nanocrystal Library to Construct Electronic Devices. *Science* **2016**, *352* (6282), 205–208.
- (750) Ong, W.-L.; Rupich, S. M.; Talapin, D. V.; McGaughey, A. J. H.; Malen, J. A. Surface Chemistry Mediates Thermal Transport in Three-Dimensional Nanocrystal Arrays. *Nat. Mater.* **2013**, *12* (5), 410–415.